

INFORMATION TO USERS

This manuscript has been reproduced from the microfilm master. UMI films the text directly from the original or copy submitted. Thus, some thesis and dissertation copies are in typewriter face, while others may be from any type of computer printer.

The quality of this reproduction is dependent upon the quality of the copy submitted. Broken or indistinct print, colored or poor quality illustrations and photographs, print bleedthrough, substandard margins, and improper alignment can adversely affect reproduction.

In the unlikely event that the author did not send UMI a complete manuscript and there are missing pages, these will be noted. Also, if unauthorized copyright material had to be removed, a note will indicate the deletion.

Oversize materials (e.g., maps, drawings, charts) are reproduced by sectioning the original, beginning at the upper left-hand corner and continuing from left to right in equal sections with small overlaps.

Photographs included in the original manuscript have been reproduced xerographically in this copy. Higher quality 6" x 9" black and white photographic prints are available for any photographs or illustrations appearing in this copy for an additional charge. Contact UMI directly to order.

**Bell & Howell Information and Learning
300 North Zeeb Road, Ann Arbor, MI 48106-1346 USA
800-521-0600**

UMI[®]



**ANALYSIS OF LAMINATED GENERAL SHELLS
UNDERGOING FINITE ROTATIONS
AND LARGE MOTION**

BY
MOHAMED BALAH

A Dissertation Presented to the
DEANSHIP OF GRADUATE STUDIES

KING FAHD UNIVERSITY OF PETROLEUM & MINERALS

DHAHRAN, SAUDI ARABIA

In Partial Fulfillment of the
Requirements for the Degree of

DOCTOR OF PHILOSOPHY

In

CIVIL ENGINEERING

MAY 2000

UMI Number: 9983984

UMI[®]

UMI Microform 9983984

Copyright 2000 by Bell & Howell Information and Learning Company.

All rights reserved. This microform edition is protected against
unauthorized copying under Title 17, United States Code.

Bell & Howell Information and Learning Company
300 North Zeeb Road
P.O. Box 1346
Ann Arbor, MI 48106-1346

**KING FAHD UNIVERSITY OF PETROLEUM & MINERALS
DHAHRAN 31261, SAUDI ARABIA**

DEANSHIP OF GRADUATE STUDIES

This dissertation, written by

MOHAMED BALAH

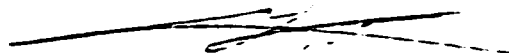
under the direction of his Dissertation Advisor and approved by his Dissertation Committee, has been presented to and accepted by the Dean of Graduate Studies, in partial fulfillment of the requirements of the degree of

DOCTOR OF PHILOSOPHY IN CIVIL ENGINEERING

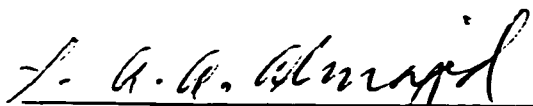
Dissertation Committee



**Dr. Hamdan N. Al-Ghamedy
Dissertation Advisor**



**Prof. Sahel N. Abduljawwad
Member**



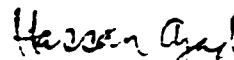
**Prof. Hamad I. Al-Abdulwahhab
Department Chairman**



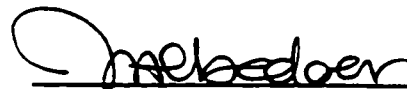
**Dr. Abdallah M. Al-Shehri
Dean of Graduate Studies**



**Dr. Hussein J. Al-Gahtani
Member**



**Prof. Hassan Azad
Member**



**Dr. Bassem O. Al-Bedoor
Member**

Date: 23/07/2000



*This Dissertation is dedicated
to my Parents, my Wife
and my Children*

ACKNOWLEDGEMENTS

First and foremost, all praise is to Almighty **ALLAH** Who gave me the courage and patience to carry out this work, and peace and blessings be upon the Prophet Muhammed.

Acknowledgement is due to the King Fahd University of Petroleum and Minerals for providing support for this research.

My deep appreciation goes to my Dissertation advisor Dr. Hamdan N. Al-Ghamedy for his valuable guidance and continuous help throughout the course of this work. Thanks are also due to my dissertation committee members, Dr. Sahel N. Abduljawwad, Dr. Hassan Azad, Dr. Hussein J. Al-Gahtany and Dr. Bassem A. Al-Bedoor for their constructive criticism, comments and suggestions.

My heartfelt thanks and gratefulness are due to my parents, for their moral support and encouragement throughout my academic career. They suffered my absence for many years.

Finally, I am deeply indebted to my wife and children for their patience, understanding and above all their constant support.

TABLE OF CONTENTS

	Page
LIST OF TABLES	xi
LIST OF FIGURES.....	xii
ABSTRACT(ENGLISH).....	xvi
ABSTRACT (ARABIC).....	xvii
CHAPTER 1	
INTRODUCTION	1
1.1 General	1
1.2 Objectives	4
1.3 Dissertation Overview	6
CHAPTER 2	
LITERATURE REVIEW	8
2.1 Formulation Methods	8
2.2 Approaches for Constructing Multilayered Shell Theories	10
2.2.1 Equivalent Single Layer Theories	11
2.2.2 Discrete Layer theories	17
2.3 Large Rotation Formulations	19
2.3.1 General	19
2.3.2 Rotation Parametrization	21
2.3.2.1 Direction Cosines	21
2.3.2.2 Rotation bout Some Axis	22
2.3.2.3 Euler Angles	24
2.3.2.4 Euler Parameters (Quaternions)	27

2.3.2.5	Rotational Vector	28
2.4	Shell Elements	30
2.5	Dynamic Effects	34
2.6	Current State of the Art	35

CHAPTER 3

SHELL THEORY	37	
3.1	General	37
3.2	Curvilinear Coordinates	38
3.3	Shell Kinematics	43
3.3.1	Introduction	43
3.3.2	Undeformed Geometry	46
3.3.3	Deformed State	49
3.3.4	Present Rotation Parametrization	50
3.3.5	Strain Measures	51
3.3.6	Stress Measures	56
3.3.7	Constitutive Equations	60
3.3.7.1	General	60
3.3.7.2	Isotropic Material	61
3.3.7.3	Orthotropic Lamina	63

CHAPTER 4

STATIC FORMULATION.....	73	
4.1	Introduction	73
4.2	Principle of Virtual Work	74
4.2.1	Virtual Work of Internal Forces	75
4.2.2	Virtual Work of External Forces	78
4.2.3	Variation of Strain Measures	80
4.2.4	Variation of Kinematic Variables	81
4.2.5	Matrix Formulation of the Internal Virtual Work	83

4.3	Finite Element Discretization	86
4.3.1	Midsurface Interpolation	86
4.3.2	Interpolation of Director Fields d_1 and d_3	87
4.3.3	Configuration Update	90
4.3.4	Transverse Shear Interpolation	94
4.3.5	Matrix Formulation of the Discretized Internal Virtual Work	96
4.4	Linearization and Tangent Operators	98
4.4.1	Second Variation of Kinematic Variables	99
4.4.2	Material Stiffness Operator	102
4.4.3	Geometric Stiffness Operator	103

CHAPTER 5

STATIC SOLUTION PROCEDURE	106
5.1 Introduction.....	106
5.2 Basic Newton-Raphson Method	107
5.3 Arc-Length Method	109
5.4 Implementation	117
5.4.1 Reference Configuration	117
5.4.1.1 Construction of Nodal Normals	117
5.4.1.2 Identification of Nodal Reference Directions (Axes)	118
5.4.1.3 Construction of the Initial Nodal Rotation Matrices	119
5.4.1.4 Construction of Cartesian Reference Frames at Integration points for Composite Materials.....	124
5.4.1.5 Computation of Metric Tensor Coefficients at Integration Points.....	125
5.4.1.6 Construction of Stiffness Coefficient Matrices	126
5.4.2 Current Configuration	127
5.4.3 Description of the Program STLSHEL7	129

CHAPTER 6

DYNAMIC FORMUALTION	137
6.1 Introduction	137
6.2 Continuum Form of the Equation of Motion	138
6.2.1 Total Linear and Angular Momenta	139
6.2.2 Kinetic and Potential Energies	141
6.2.3 Formulation of the Weak Form of the Equations of Motion	143
6.3 Conservation Laws of the Shell Motion	145
6.3.1 Conservation of the Total Energy	146
6.3.2 Conservation of the Total Linear and Angular momenta	147
6.4 Time Discretization: Energy-Momentum Conserving Algorithm	148
6.4.1 Approximation of Configuration and Momenta	149
6.4.2 Time Discretization of the Weak Form	150
6.4.3 Momenta Conservation of the Algorithm	151
6.4.4 Exact Momentum-Energy Conserving Scheme	152
6.5 Spatial Finite Element Discretization	153
6.5.1 Interpolation of the Kinematic and Momenta Fields	154
6.5.2 Admissible Test Functions	155
6.5.3 Strain Variations	156
6.6 Linearization	158
6.6.1 Second Variation of the Kinematic Variables	159
6.6.2 Inertia Part of the Tangent Stiffness Operator	160
6.6.3 Material Part of the Tangent Stiffness Operator	160
6.6.4 Geometric Part of the Tangent Stiffness Operator	161
6.7 Implementation Notes.....	162

CHAPTER 7

NUMERICAL SIMULATIONS	164
7.1 Introduction	164
7.2 Static Simulations	165

7.2.1	Linear Problems	165
7.2.1.1	Pinched Isotropic Cylinder with End Diaphragms	165
7.2.1.2	Pinched Isotropic Hemisphere	169
7.2.1.3	Sandwich Plate under Sinusoidal Transverse Loads	173
7.2.1.4	Laminated Rectangular Plate under Sinusoidal Transverse Loads	177
7.2.1.5	Laminated Cylindrical Panel under Sinusoidal Transverse Loads	182
7.2.1.6	Laminated Spherical Panel under Sinusoidal Transverse Loads	186
7.2.2	Nonlinear Problems	188
7.2.2.1	Pinching of a Clamped Isotropic Cylinder	188
7.2.2.2	Pinching of a Hemispherical Shell with a Hole	197
7.2.2.3	Composite Shallow Cylindrical Shell with a Central Point Load	203
7.2.2.4	Composite Hyperboloidal Shell under two Pairs of Opposite Loads	208
7.2.2.5	Cylindrical Bending of an Asymmetric Cross Plyed Laminate under Uniformly Distributed Transverse load.....	226
7.2.2.6	Bending of a Nine Layer Cross-ply (0o/90o/0o/..) Simply Supported Spherical Shell Subjected to a Uniformly Distributed Load.....	229
7.3	Dynamic simulations	231
7.3.1	Dynamics of a Short Cylinder under Impulsive Loading	231
7.3.2	Free Large Motion of a Cylindrical Panel	238
7.3.3	Dynamic Snap Through of a Pseudo-Spherical Cap under Impulsive Ring Loading	240
7.3.4	'Snap-Through' of a Cylindrical Shell under a Concentrated Vertex Load	247
7.3.5	Ideal Sandwich Cylindrical Shell under Impulsive Load	251

CHAPTER 8

CONCLUSIONS AND RECOMMENDATIONS	258
8.1 Summary.....	258
8.2 Conclusions.....	262
8.3 Recommendations.....	264
APPENDIX I GEOMETRIC STIFFNESS MATRICES.....	267
REFERENCES.....	273
CURRICULUM VITAE.....	288

LIST OF TABLES

Table		Page
7.1	Displacement Results of The Pinched Cylinder with Diaphragms.....	167
7.2	Pinched Cylinder with End Diaphragms: Maximum Stresses with Mesh Refinement.....	169
7.3	Pinched Hemisphere: Displacement along the Applied Load.....	171
7.4	Pinched Hemisphere: Maximum Stresses with Mesh Refinement.....	171
7.5	Simply Supported Square Sandwich Plate: Maximum Stresses and Deflection for (a/h=100).....	176
7.6	Simply Supported Square Sandwich Plate: Maximum Stresses and Deflection for (a/h=10).....	177
7.7	Simply Supported Square Sandwich Plate: Maximum Stresses and Deflection for (a/h=4).....	177
7.8	Laminated Plate under Sinusoidal Loading (a/h=10, N=5): Nondimensional Results with Mesh Refinement.....	179
7.9	Laminated Plate under Sinusoidal Loading: Nondimensional Inplane Displacements \bar{u} and \bar{v}	179
7.10	Laminated Plate under Sinusoidal Loading: Nondimensional Inplane Stresses $\bar{\sigma}_x$, $\bar{\sigma}_y$ and $\bar{\sigma}_{xy}$	180
7.11	Laminated Plate under Sinusoidal Loading: Nondimensional Transverse Stresses $\bar{\sigma}_z$ and $\bar{\sigma}_{yz}$	180
7.12	Laminated Cylindrical Panel under Sinusoidal Loading: Nondimensional Inplane Stresses $\bar{\sigma}_x$, $\bar{\sigma}_y$ and $\bar{\sigma}_{xy}$	185
7.13	Laminated Cylindrical Panel under Sinusoidal Loading: Nondimensional Transverse Stresses $\bar{\sigma}_z$ and $\bar{\sigma}_{yz}$	185
7.14	Short Cylinder under Impulsive Loading: Nodal loads.....	234
7.15	Pseudo-Spherical Panel: Loading Intensity Variation.....	244

LIST OF FIGURES

Figure	Page
2.1	Spherical coordinates : Three different possibilities defining the director with respect to the orthonormal basis..... 26
3.1	Position vector of a point P with Cartesian and curvilinear coordinates..... 39
3.2	Volume and surface elements..... 42
3.3	Geometry and kinematics of the shell element 44
3.4	Orthotropic laminae (flat and curved) with principal and nonprincipal coordinate systems..... 64
4.1	Shell bounding surface in the deformed state and bounding curve of the reference surface in the reference state 79
4.2	Location of assumed strain points 88
5.1	Various load/deflection curves : (a) snap through ; (b) snap back ; (c) 'brittle' collapse; (d) 'ductile collapse' 111
5.2	Arc-length procedure and notation for one degree of freedom system (with $\psi=1$) 113
5.3	Sign convention for the stacking sequence of a laminate 120
5.4	Examples of laminate stacking sequences and the corresponding laminate orientation code 121
5.5	(a) Nodal bases in case $d_{1(t)}^0 = -E_3$, (b) Local frames for skewed boundary conditions 123
5.6	Structure of STLSHEL7 program containing primary and some secondary subroutines 130
5.7	Flowchart for the computer program STLSHEL7 134
7.1	Pinched cylinder with end diaphragms: Geometry and loading conditions..... 166
7.2	Pinched cylinder: Normalized displacement in load direction 168

7.3	Pinched hemispherical shell: Geometry and loading	170
7.4	Pinched hemisphere: Convergence versus mesh refinement	172
7.5	Simply supported sandwich plate under sinusoidal loading	174
7.6	Laminated plate under sinusoidal loading ($a/h=5$): Nondimensional center deflection	181
7.7	Laminated plate under sinusoidal loading ($a/h=10$): Nondimensional center deflection	181
7.8	Laminated cylindrical panel under sinusoidal loading ($R/a=1$, $a/h=50$): Nondimensional center deflection	183
7.9	Laminated cylindrical panel under sinusoidal loading ($R/a=1$, $a/h=10$): Nondimensional center deflection	183
7.10	Laminated cylindrical panel under sinusoidal loading ($R/a=4$, $a/h=5$): Nondimensional center deflection	184
7.11	Laminated cylindrical panel under sinusoidal loading ($R/a=4$, $a/h=10$): Nondimensional center deflection	184
7.12	Laminated spherical panel under sinusoidal loading ($R/a=2$, $a/h=10$): Nondimensional center deflection	187
7.13	Laminated spherical panel under sinusoidal loading ($R/a=5$, $a/h=5$): Nondimensional center deflection	187
7.14	Pinching of a clamped cylinder: Geometry and loading	189
7.15	Pinching of a clamped cylinder: Displacement at the load location	190
7.16	Pinching of a clamped cylinder: Maximum normal stresses	192
7.17	Pinching of a clamped cylinder: Maximum shear stresses	193
7.18	Pinching of a clamped cylinder: Maximum normal Green strains.....	194
7.19	Pinching of a clamped cylinder: Maximum shear strains	195
7.20	Pinching of a clamped cylinder: Vertical displacement load location versus Green strains	196
7.21	Pinching of a hemispherical shell with a hole: Geometry and loading	198
7.22	Pinching of a hemispherical shell with a hole. Deflection-load plots	199
7.23	Pinching of a hemispherical shell with a hole. Maximum stresses-load plots ...	200

7.24	Pinching of a hemispherical shell with a hole. Green strains-load plots	201
7.25	Pinching of a hemispherical shell with a hole. Green strains versus X displacement of point A	202
7.26	Composite shallow cylindrical shell with a central point load	204
7.27	Composite cylindrical shell, $t=12.6\text{mm}$: Load-displacement variation	206
7.28	Composite cylindrical shell, $t=6.3\text{mm}$: Load-displacement variation	207
7.29	Composite cylindrical shell, (0/90/0), $t=12.6\text{mm}$: Stress-Load variation	209
7.30	Composite cylindrical shell, (0/90/0), $t=12.6\text{mm}$: Normal Green strains-load variation	210
7.31	Composite cylindrical shell, (0/90/0), $t=12.6\text{mm}$: Green strains-displacement variation	211
7.32	Composite cylindrical shell, (90/0/90), $t=12.6\text{mm}$: Green strains-displacement variation	212
7.33	Composite cylindrical shell, (0/90/0), $t=6.3\text{mm}$: Green strains-displacement variation	213
7.34	Composite cylindrical shell, (90/0/90), $t=6.3\text{mm}$: Green strains-displacement variation	214
7.35	Composite hyperboloidal shell : Geometry and loading conditions	216
7.36	Composite hyperboloidal shell, [0/90/0], Displacements of A and D	217
7.37	Composite hyperboloidal shell, [0/90/0], Displacements of B and C	218
7.38	Composite hyperboloidal shell, [90/0/90], Displacements of A and D	219
7.39	Composite hyperboloidal shell, [90/0/90], Displacements of B and C	220
7.40	Composite hyperboloidal shell, [0/90/0], Stresses-Displacement UA variations.....	222
7.41	Composite hyperboloidal shell, [90/0/90], Stresses-Displacement UA variations	223
7.42	Composite hyperboloidal shell, [0/90/0], Strains-Displacement UA variations	224
7.43	Composite hyperboloidal shell, [90/0/90], Strains-Displacement UA variations	225

7.44	Asymmetric cross-plyed laminate under uniform transverse loading: Geometry and loading	227
7.45	Asymmetric cross-plyed laminate under uniform transverse loading: Hinged case: Load-displacement plot	228
7.46	Asymmetric cross-plyed laminate under uniform transverse loading: Pinned case: Load-displacement plot	228
7.47	Bending of a nine layer cross-ply simply supported spherical shell under uniform loading: Geometry and loading	230
7.48	Nine layer cross-ply simply supported spherical shell under uniform loading: Load-deflection variation.....	232
7.49	Short cylinder : Geometry description	233
7.50	Short cylinder: Time history of the total linear momentum	235
7.51	Short cylinder: Time history of the total angular momentum	236
7.52	Short cylinder: Time history of the energy	237
7.53	Free cylindrical panel: Geometry and loading	239
7.54	Free cylindrical panel: Time history of the total linear momentum	241
7.55	Free cylindrical panel: Time history of the total angular momentum	242
7.56	Free cylindrical panel: variation of kinetic, internal and total energies	243
7.57	Pseudo-spherical cap: Geometry and loading conditions	245
7.58	Pseudo-spherical cap: variation of kinetic, internal and total energies	246
7.59	Cylindrical shell 'Snap through': Geometry, and loading conditions	248
7.60	Cylindrical shell: vertex displacement before and after 'snap-through'	250
7.61	Ideal sandwich cylindrical shell: Geometry and loading description	252
7.62	Ideal sandwich cylindrical shell: Displacement of A along X axis (TOSDT and FOSDT models)	254
7.63	Ideal sandwich cylindrical shell: Displacement of A along Z axis (TOSDT and FOSDT models)	255
7.64	Ideal sandwich cylindrical shell: Kinetic and total energies (TOSDT and FOSDT models)	256
7.65	Ideal sandwich cylindrical shell: Internal energy (TOSDT and FOSDT models)	257

DISSERTATION ABSTRACT

Full Name **MOHAMED BALAH**
Title of Study **ANALYSIS OF LAMINATED GENERAL SHELLS
UNDERGOING FINITE ROTATIONS AND LARGE MOTION**
Major Field **STRUCTURAL ENGINEERING**
Date of Degree **May, 2000**

The primary objective of this dissertation is the development of a modeling tool, using the finite element method, for static and dynamic analysis of general refined laminated shell structures undergoing finite rotations and large motion with strains assumed to remain small.

A kinematic model based on the material representation is presented leading to a third order shear deformation theory with large rotation capabilities and quadratic transverse shear stress distribution across the thickness. A singularity-free parametrization of the rotation field is adopted with it the exponential mapping for configuration update. A Total Lagrangian formulation is used with the second Piola-Kirchhoff stresses, Green-Lagrange strains and constitutive equations defined with respect to laminate general curvilinear coordinates. The developed shell element is composed of an arbitrary number of layers where the fiber directions are allowed to vary in any way from layer to layer.

The finite element discretization is carried out using a four-node isoparametric laminated shell element with seven degrees of freedom per node. The transverse shear locking problem is avoided by applying the Assumed Natural Strain concept to the constant part of the transverse shear strain. A consistent linearization of the weak form of equilibrium equations (static case) or equations of motion (dynamic case) is undertaken to achieve a quadratic rate of convergence.

The dynamic part consists of designing and implementing an energy-momentum conserving time stepping algorithm. This algorithm is based on a general methodology for the design of exact energy-momentum schemes, which was recently proposed in the literature and applied successfully to nonlinear shells based on the first order shear deformation theory. Here it is extended, for the first time, to the third order shear deformation theory.

The developed finite rotation shell element is then implemented in two independent computer programs, one for static and the other for dynamic analysis. Then it is tested on some challenging linear and nonlinear problems, recently reported in the literature, and the results show its excellent performance and robustness. A couple of examples show the discrepancy in prediction between third and first order shear deformation theories and this raises the need for such refined theories.

ملخص بحث

درجة الدكتوراه في الفلسفة

الإسم : محمد بالخ

عنوان الرسالة : تحليل المنشآت القشرية العامة المصفحة المعرضه لدوران وحركة كبيرين

التخصص : هندسة الإنشائية

تاريخ التخرج : مايو ٢٠٠٠م

إن الهدف الأساسي من هذه الرسالة هو تطوير نموذج يتركز على طريقة العناصر المحدودة للدراسة المحسنة للمنشآت القشرية العامة المصفحة في حال سكونها وحركتها ، علما بأن هذه المنشآت تتعرض لدوران غير محدود وحركة كبيرة غير أن الإنفعالات يفترض بقاؤها صغيرة .

تبدأ هذه الدراسة بطرح طريقة لإنشاء نموذج حركي حيث تمدد المكونات الثلاثة للإزاحة إلى متسلسلة القوى من الدرجة الثالثة في اتجاه إحداثيات السُمك . تنتج عن هذه الصياغة نظرية للتشوه القصي من الدرجة الثالثة تتمتع بإدراج دوران كبير و إجهادات قص عرضية موزعة بصفة تربيعية عبر سمك القشرة . لقد استعملت طريقة خالية من الأفراد لتمثيل مجال الدوران ومعها طريقة هندسية دقيقة لتحديث شكل المنشأ تعتمد على التطبيق الآسي . أعمدت صياغة لاقرانجيان (Lagrangian) الكلية مع إجهادات بيولا كيركوف (Piola-Kirchhoff) الثانية وانفعالات قريسن لاقرانج (Green-Lagrange) المرتبطة ببعضها البعض بمعادلات تكوينية مرجعيتها إحداثيات انحنائية عامة معرفة على سطح المصنوع . يتكون العنصر القشري المطور من عدد غير محدود من الطبقات حيث يمكن تغيير اتجاه الألياف بطريقة اختيارية من طبقة إلى أخرى.

نقدت التجزئة إلى عناصر محدودة باستخدام عنصر قشري مصنوع سوي المعام ذي أربعة عقد تتمتع كل واحدة منها بسبع درجات حرية . لتجنب معضلة الإنفعال القصي العرضي ، طُبّق مفهوم الإنفعال الطبيعي المفترض على مكونة الإنفعال القصي العرضي الثابتة . وقد كرست هذه الدراسة أهمية خاصة للتخطيط المتوافق للشكل الضعيف لمعادلات الإتران (عند السكون) أو معادلات الحركة (في

حالة الحركة) وذلك لإحراز معدل تلاقي تربيعي والذي يعتبر نموذجي بالنسبة لطريقة نيوتن رافسون (Newton-Raphson).

يتكون الجزء الحركي من هذه الرسالة من تصميم وتنفيذ خوارزمية للتدرج الزمني خاصيتها حفظ الطاقة وكمية الحركة . تعتمد هذه الخوارزمية على طريقة عامة لتصميم خطط للحفاظ التام للطاقة وكمية الحركة والتي طرحت في الأبحاث العلمية الحديثة وطبقت بنجاح على القشرات الغير خطية المبينة على نظرية التشوه القصي من الدرجة الأولى . تم في هذا البحث ولأول مرة تمديد هذه الطريقة إلى نظرية التشوه القصي من الدرجة الثالثة .

بعد تطوير العنصر القشري المصفح القابل للدوران الكبير ، تم إدراجه بنجاح في برنامجين منفصلين للحاسب الآلي ؛ أحدهما للتحميل الساكن والآخر لتحليل الحركي . وقد تم اختبار العنصر بعد ذلك على بعض المسائل الخطية والغير خطية المتوفرة في النشرات العلمية والتي تعتبر تحدي لأداء العناصر المحدودة المطورة . لقد بينت النتائج الأداء الممتاز للعنصر المطور وقوته كما أظهرت نتائج بعض الأمثلة التعارض في التنبؤ بين نظريات التشوه القصي ذوات الدرجة الأولى والثالثة . هذا التعارض يرفع من الحاجة إلى مثل هذه النظريات المحسنة.

جامعة الملك فهد للبترول والمعادن

مايو ٢٠٠٠ م

CHAPTER 1

INTRODUCTION

1.1 General

The advent of composite materials with their appealing characteristics of high strength-to-weight and high stiffness-to-weight ratios and the evolution of their technology have increased their use in many industries such as aircraft, spacecraft, automotive, shipbuilding and building construction. They are also finding applications in a number of areas in the medical sector in addition to consumer products such as skis, golf clubs, tennis rackets etc. Among composite materials, fiber reinforced composites are used extensively. In order to achieve the desirable structural properties offered by these materials, they have to be of laminated construction.

Laminated fibrous composites are made of two or more bonded layers. Each layer (lamina) is composed of unidirectional fibers, which are the principal reinforcing or load-carrying agent, embedded in a matrix material. This matrix, which can be organic, ceramic, or metallic, holds the fibers together in a structural unit and protects them from external damage. It also serves to transfer and distribute the applied loads to the fibers.

and in many cases it contributes some needed property such as ductility, toughness and electrical insulation. Polymers are unquestionably the most widely used matrix materials. The enormous possibilities presented by laminated composite structures in the combination of layer materials, fiber orientation within each layer and the ply stacking sequence may enhance considerably the design process of such structures. They represent in many respects a good example of the principle of 'material design'. In such situations, the concept of tailoring materials at a fundamental level, to meet specific design requirements, is fully incorporated in the overall product development process. While these materials offer many advantages over conventional isotropic ones, they also present challenging technical problems in modeling their structural behavior.

The analysis and design of structures made of laminated composites become complex because of three reasons. Firstly, the basic lamina involves additional elastic constants, five against two for isotropic materials. Secondly, the laminated construction induces various types of coupling in their structural behavior such as bending-extension, twisting-extension, and bending-twisting. Thirdly, the great difference in elastic properties between fibers and matrix material leads to a high ratio of in-plane Young's modulus to transverse shear modulus and this makes transverse shear deformation important in such structures even in the case of small thickness. The increased use of laminated structures in modern technologies has stimulated interest in the development of theories and computational models for predicting as fairly as possible their response to different loading conditions. One of the most important structural configurations made of composite materials is the shell type structure.

Laminated composite shells used in weight-sensitive applications are very flexible and can experience large elastic deformations and rotations. Accordingly, the consideration of geometric nonlinearities is of great relevance for the analysis and design of this type of structures. Simplified nonlinear models even of moderate rotation type may introduce significant errors in the analysis and are, moreover, not necessarily much more timesaving than finite rotation models. Thus finite rotation models may be considered as the only reliable models permitting an accurate prediction of the structure response in the whole nonlinear range. The sensitivity of laminated composites to transverse shear deformation makes the classical Kirchhoff-Love theory inadequate in predicting their responses.

Modeling approaches, which take into consideration transverse shear deformation, have been the topic of serious research in the last three decades. The two dimensional theories based on the method of hypotheses [1], where a certain displacement, strain or stress field is postulated in the thickness direction, are preferred in practice. Among these theories, the ones based on the assumed displacement field across the shell thickness are the most popular. The general classification adopted in Reference 2 distinguishes three classes of theories of laminated composites: the equivalent single layer (ESL) theories, the layerwise theories and the continuum based three-dimensional theories. The ESL (global) theories, which are the most economical of all laminate theories, have been found to be adequate in predicting global response characteristics of laminates, like maximum deflection, maximum stresses, fundamental frequencies and critical loads [3]. Many global shear deformation theories have been proposed over the years. The

implementation of these theories, using the displacement-based finite element approach. suffers from a defect known as the transverse shear locking phenomenon. This defect appears when thin shells are analyzed. A current successful remedy to this problem uses mixed interpolation of tensorial transverse shear strain components proposed by Dvorkin and Bathe[4,5]. The application of the developed laminated shell elements to simulate large dynamic motion necessitates some criterion to assess the stability of the time integration scheme. Algorithms that conserve constants of motion are important for two fundamental reasons. Firstly, constants of motion, such as energy and momenta, are often primary physical quantities of direct engineering interest. Secondly, in an algorithmic context, conservation properties lead to rigorous notions of nonlinear stability. A general methodology proposed recently by Simo and Tarnow [6] enables the design of time integration algorithms that conserve exactly energy and momenta.

After assessment of the previous research work published in the literature, as will be seen in chapter two, concerning geometrically nonlinear laminated shells, we notice that the static and dynamic analyses of such structures where simultaneous consideration of higher order shear deformation models and finite rotations are scarce.

1.2 Objectives

The primary objective of this study is the development of an element for static and dynamic analyses of general laminated composite shells undergoing finite (unlimited in size) spatial rotations and large overall motion. Strains are assumed to be small, i.e., the material stays in the elastic region. A cubic displacement field over the thickness of the shell is proposed. The Total Lagrangian formulation with the second Piola-Kirchhoff

stresses and Green strains is adopted. A numerical procedure is developed, and a computer program is written. This software, which represents advancement in the state-of-the-art analysis of laminated shells, may be utilized by researchers and designers for a diverse spectrum of problems. To achieve this objective, the finite element method is used for space discretization followed by time integration of the resulting nonlinear ordinary differential equations of motion. More specifically, the following objectives are within the scope of the present dissertation:

- ◆ To develop a laminated finite shell element based on a proposed cubic displacement model;
- ◆ To allow for modeling of laminates with arbitrary variation of fiber directions from layer to layer;
- ◆ To use the economical thickness pre-integration concept to reduce the computational effort;
- ◆ To use singularity-free parametrization for the rotation field;
- ◆ To update the rotation field in an exact manner using the exponential mapping;
- ◆ To alleviate the shear locking problem by using mixed interpolation of tensorial transverse shear strain components;
- ◆ To utilize the general methodology alluded to previously, to design an exact energy-momentum conserving algorithm for the nonlinear dynamic response of shell structures using the developed model;
- ◆ To implement the above features in a modular and efficient software package;
- ◆ To assess the performance of the developed model by running numerical simulations

concerning some challenging test problems reported recently in the literature.

1.3 Dissertation Overview

This chapter describes the problem and the objectives of this study.

Chapter 2 presents an extensive review of the previous work involving various issues related to geometrically nonlinear analysis of laminated shells such as formulation methods, different approaches for constructing multilayered shell theories, large rotation parametrization, shells elements and dynamic effects.

Chapter 3 reviews some mathematical preliminaries related to differential shell geometry, then it derives the shell theory based on the proposed kinematic model and using general convective curvilinear coordinates. Constitutive equations relating the stress and strain measures for both isotropic and orthotropic materials, are shown in chapter 3.

In chapter 4, the virtual work principle is used to derive the weak form of the equations of equilibrium. The finite element discretization of these equations is implemented via a four-noded isoparametric shell element. The linearization of the fully discrete equilibrium equations, which is performed in the last part of this chapter, leads to the formation of the tangent stiffness matrices.

Chapter 5 presents the basic Newton Raphson method and its adaptive variant, the arc-length method, with their respective algorithmic counterparts for the advancement of the global solution procedure at the structure level. Afterwards, it presents the implementation details for the different tasks presented in chapters 4 and 3. The nesting of all such tasks with the global solution algorithm leads to the design of the computer

program **STLSHEL7** which is also described.

In chapter 6, which concerns the dynamic formulation, the weak form of the equations of motion are derived using Hamiltonian formulation. Time and spatial finite element discretizations are then introduced leading to a time integration algorithm which conserves exactly momenta and energy. This is followed by a consistent linearization of the fully discrete equations of motion. The last section of this chapter highlights the implementation notes which lead to the design of the computer program for the nonlinear dynamic analysis of laminated shells

The numerical evaluation of the developed static and dynamic shell models is carried out in chapter 7. A set of severe test problems, available in the literature, is considered ranging from linear static to nonlinear dynamic problems. The predictions of the numerical simulations are compared to those of the literature and discussed.

Chapter 8 starts by a summary of the achievements attained during this study, followed by some conclusions based on the performance of the developed model in the numerical simulations and finishing by suggesting some directions for future research.

CHAPTER 2

LITERATURE REVIEW

The approach towards the development of reliable laminated general shell elements capable of performing well in the whole geometrically nonlinear range requires a careful consideration of many aspects. In this regard, the issues which are believed to be of utmost importance from a theoretical and computational standpoint will be discussed in the following sections.

2.1 Formulation Methods

When considering the geometric nonlinear behavior of a structure, a consistent continuum mechanics-based approach should be employed to define its motion. In solid mechanics analysis, we follow all particles of the body in their motion, from the original to the final configuration of the body, which means that a Lagrangian (material) formulation of the problem is adopted. This approach stands in contrast to an Eulerian formulation which is usually used in the analysis of fluid mechanics problems, in which attention is focused on the motion of the material through a stationary control volume.

In the finite element approach applied to solids, the total Lagrangian (TL), updated

Lagrangian (UL) and co-rotational (CR) formulations are the most widely used ones [7-9]. These formulations are identical from a continuum mechanics point of view, the only difference resides in the choice of a reference configuration. In the TL formulation, also referred to as Lagrangian formulation, all static and kinematic variables are referred to the initial configuration that the body occupies at time $t=0$. The UL formulation is based on the same procedures that are used in the TL formulation, except that all static and kinematic variables are referred to the configuration at time t . In the CR formulation, which is less popular than the two previous formulations, a local cartesian coordinate system is attached to each finite element, and it is continuously translated and rotated with the element as the deformations proceed. The intent of this formulation is to eliminate the rigid body motion from the total displacement field. As a result, the linear finite element theory can still be used in element corotational coordinate system. This puts restrictions on the size of the element and the load step in each increment for the linear theory to be applicable. This formulation has both, total (CR-TL) and updated (CR-UL) forms.

In the analysis of structures, the stress and strain measures need to be objective and work-conjugate. Work-conjugate stresses and strains are pairs of stress and strain measures that fully account for the internal elastic energy. For example, the engineering strains and stresses, the infinitesimal strains and the Cauchy stresses, the Green-Lagrange strains and the second Piola-Kirchhoff stresses are work-conjugate pairs of strain and stress measures. Objective strains and stresses are invariant under finite rigid body motions and no stresses or strains arise from finite pure rigid body rotations. For

example, the Green-Lagrange strain, and the second Piola-Kirchhoff stresses are objective measures. On the other hand, the engineering stresses, the engineering strains, the Cauchy stresses, and the infinitesimal strains are non-objective measures. Alternative stress and conjugate strain measures can be found in reference [10].

Most of the recent research work concerning shell type structures undergoing finite rotations is based on the Total Lagrangian formulation with Green-Lagrange strains and the second Piola-Kirchhoff stresses as work-conjugates [11-33]. Nevertheless, we cite some representative research work done using the Updated Lagrangian formulation [7,29,34-36]. The co-rotational formulation has also attracted some researchers who succeeded in applying it for large rotation analysis [9,37-45]. The rigid body invariance of the second Piola-Kirchhoff stresses and their work conjugate Green-Lagrange strains make them an ideal choice for this study where the rigid body motion contributes largely to the overall deformation of the structure.

2.2 Approaches for Constructing Multilayered Shell Theories

Composite materials, presently used in laminated structures, exhibit high sensitivity to transverse shear deformation even in the case of thin shells. This sensitivity is due to the great difference in elastic properties between fibers and matrix materials, which leads

to a low ratio of transverse shear to inplane Young's moduli $\left(\frac{G_{TT}}{E_L} \approx \frac{G_{ZZ}}{E_L} = \frac{1}{10} \text{ to } \frac{1}{200} \right)$

where L denotes the fiber directions, whereas T and Z are two directions orthogonal to L [46]. This in turn leads to higher transverse shear deformability in comparison to isotropic cases.

Many of the classical theories, which were developed initially for thin isotropic shells, are based of the Love-Kirchhoff theory; it assumes that straight lines normal to the undeformed middle surface remain straight and normal to the deformed middle surface without undergoing thickness stretching [47]. This assumption implies that the transverse shear strain is ignored. The application of such theories to layered anisotropic composite shells could lead to an error up to 30% or more in deflections, stresses and frequencies [48].

The need for more accurate computational models for multilayered laminated shells has led to the development of a variety of two dimensional shear deformation theories [1-3, 49-53]. From a theoretical point of view, one of the central issues of various theories is how to account for the effects of the transverse shear deformation which plays a remarkable role in affecting the mechanical behavior of laminated shells. As seen in chapter one, the two dimensional theories are the equivalent single layer (ESL) and the layerwise theories. Their classification is based on the nature of the approximations made in reducing the three dimensional problem into a two dimensional one.

2.2.1 Equivalent Single Layer Theories

In the ESL theories, the displacement field is expanded as a linear combination of the thickness coordinate and undetermined functions of position in the reference surface (i.e. a separation of variables approach). The three components of the displacement vector are given by [54]

$$u_i(\xi, \eta, \zeta) = u_i^0(\xi, \eta) + \zeta u_i^1(\xi, \eta) + \zeta^2 u_i^2(\xi, \eta) + \dots = \sum_{j=0}^{N_i} (\zeta)^j u_i^j(\xi, \eta) \quad (2.1)$$

where $u_i(\xi, \eta, \zeta)$ ($i=1,2,3$) denotes a displacement component in the shell. (ξ, η) are surface coordinates. ζ is the thickness coordinate and $u_i^j(\xi, \eta)$ ($j=1,2,\dots,N_i$) are functions of ξ and η coordinates.

In these theories, the displacement field is assumed to be continuously and smoothly distributed across the entire thickness, and the laminated shell is actually replaced by an equivalent single layer anisotropic shell. The order of the governing equations is independent of the number of layers. Since the constitutive properties of each layer are different, the stresses are discontinuous at the layer interfaces. The simplest of these shear deformation theories is the first order shear deformation theory (FOSDT), which was proposed by Reissner [55] for the linear analysis of isotropic plates and then extended to laminated plates and shells. This theory has been used extensively in modeling the response of laminated thin plates/shells; the components of the displacement vector are given by

$$\begin{aligned} u_\alpha(x, y, z) &= u_\alpha^0(x, y) + z u_\alpha^1(x, y) \\ u_3(x, y, z) &= u_3^0(x, y) \end{aligned} \quad (2.2)$$

for the case of plates, and

$$\begin{aligned} u_1(\xi, \eta, \zeta) &= u_1^0(\xi, \eta) \left(1 + \frac{\zeta}{R_1} \right) + \zeta \psi_1(\xi, \eta) \\ u_2(\xi, \eta, \zeta) &= u_2^0(\xi, \eta) \left(1 + \frac{\zeta}{R_2} \right) + \zeta \psi_2(\xi, \eta) \\ u_3(\xi, \eta, \zeta) &= u_3^0(\xi, \eta) \end{aligned} \quad (2.3)$$

for the case of shells defined by means of two orthogonal curvilinear middle surface coordinates ξ and η and a third coordinate ζ normal to the surface[56]. R_1 and R_2 are

two radii of curvature along ξ and η , respectively. This theory, which yields a constant transverse shear strain, has been used extensively in modeling plates and shells within the finite element method (FEM). Noor and Mathers [57] performed linear static, stability and vibration analysis of laminated plates and shells based on FOSDT. Ahmad et al.[58] introduced a degenerated isoparametric finite shell element whose kinematic assumption is analogous to the FOSDT. The composite formulation of this type of element (see for example [36]) requires a numerical integration through the thickness which is uneconomical when the number of layers is high, which is the case for laminated structures. An explicit integration through the thickness can be performed, as reported by some authors [26,35,59,60], and thus the model is reduced to a more economical resultant form. Palmerio et al.[54,61] used this theory with moderate rotations to study the nonlinear bending, buckling and postbuckling of anisotropic rectangular plates, circular cylindrical and spherical shells. A lot of recent research work has been devoted to the development of shell elements based on the FOSDT where finite rotations (unlimited in size) can be modeled. Representative works can be found in References [1,14,22,23,25,32,33,62-67] for the case of isotropic shells and in references [12,15,17,19,20,31,68] for the case of laminated composite shells. The kinematic model used in most of these works describes the deformed shell continuum by

$$x(\xi, \eta, \zeta) = \varphi(\xi, \eta) + \zeta d(\xi, \eta) , \quad d(\xi, \eta) \cdot d(\xi, \eta) = 1 \quad (2.4)$$

where $x(\xi, \eta, \zeta)$ is the position vector of a generic point in the shell medium, $\varphi(\xi, \eta)$ maps the middle surface of the shell, and $d(\xi, \eta)$ is a unit vector (inextensible shell director) initially normal to the shell middle surface but, after deformation, this

orthogonality condition is lost because of transverse shear deformation. Pandya and Kant [69], among others, have conducted comparative studies which have shown that classical plate/shell models, even of Mindlin-Reissner type, are unable to predict the deformation behavior with sufficient accuracy if the side length-thickness ratio or layer stiffness discontinuities exceed some limits. To improve the prediction capability of ESL theories, researchers developed higher order shear deformation theories (HOSDT).

The most popular theory among HOSDT are the third order shear deformation theories (TOSDT). In recent years, several third order theories have been developed by different authors [70-79]. The displacement field present by Lo et al.[74] and Reddy[52], for the case of plates, is

$$\begin{aligned} u_{\beta}(\xi, \eta, \zeta) &= u_{\beta}^0(\xi, \eta) + \zeta u_{\beta}^1(\xi, \eta) + \zeta^2 u_{\beta}^2(\xi, \eta) + \zeta^3 u_{\beta}^3(\xi, \eta) \\ u_3(\xi, \eta, \zeta) &= u_3^0(\xi, \eta) + \zeta u_3^1(\xi, \eta) + \zeta^2 u_3^2(\xi, \eta) \end{aligned} \quad (2.5)$$

Reddy [52] reviewed third order theories which satisfy vanishing of transverse stresses on the bounding planes (case of plates) and showed that most third order theories are not new but duplicates of other theories. He also showed that all technical theories up to and including third order can be derived from generalized displacement field [51,80]. The transverse displacement in Equation (2.5) is expanded only to the second order in z for consistency of transverse shear strains [51]. Some of the above mentioned TOSDT accounted for the Von Karman nonlinear strains. Pandya and Kant [69] performed comparative studies for linear flexure of sandwich plates using the finite element method. They showed that TOSDT models, for which the zero transverse shear stress condition is not enforced, perform better than those similar to Reddy's model [78] where the zero

transverse shear stress condition is enforced at the bounding surfaces. Reddy's model [78] and similar ones lead to a formulation with five parameters, as in the first order shear deformation theory. A significant feature of these TOSDT is that the assumed displacement field leads to a parabolic distribution of the transverse shear stresses, thereby, removing the need for using a shear correction factor as used in the FOSDT. These kinematic models have then received a widespread use in modeling multilayered plates for different purposes, i.e., bending, stability and dynamic analysis [2,81-85]. Reddy and Liu [48] extended this theory to shell geometries in an analytical study to get deflections and natural frequencies for cross-ply laminated shells. The results were believed to be better than the FOSDT. The displacement field used in this theory, which is based on orthogonal curvilinear coordinates as was the case for Equations (2.3), is given by

$$\begin{aligned}
 u(\xi, \eta, \zeta) &= u^0(\xi, \eta) \left(1 + \frac{\zeta}{R_1} \right) + \zeta \phi_1(\xi, \eta) + \zeta^2 \psi_1(\xi, \eta) + \zeta^3 \theta_1(\xi, \eta) \\
 v(\xi, \eta, \zeta) &= v^0(\xi, \eta) \left(1 + \frac{\zeta}{R_2} \right) + \zeta \phi_2(\xi, \eta) + \zeta^2 \psi_2(\xi, \eta) + \zeta^3 \theta_2(\xi, \eta) \\
 w(\xi, \eta, \zeta) &= w^0(\xi, \eta)
 \end{aligned} \tag{2.6}$$

where u^0, v^0 and w^0 are the displacement along the (ξ, η, ζ) coordinates of a point on the middle surface and ϕ_1 and ϕ_2 are the rotations at $\zeta = 0$ of normals to the middle surface with respect to the η and ξ axes, respectively. The functions ψ_i and θ_i ($i=1,2$) are determined by enforcing the zero transverse strain condition on the bounding surfaces. After enforcing these conditions, Equations (2.6) reduce to

$$\begin{aligned}
u(\xi, \eta, \zeta) &= u^0 \left(1 + \frac{\zeta}{R_1} \right) + \zeta \phi_1 + \zeta^3 \frac{4}{3h^2} \left[-\phi_1 - \frac{\partial w^0}{\alpha_1 \partial \xi^1} \right] \\
v(\xi, \eta, \zeta) &= v^0 \left(1 + \frac{\zeta}{R_2} \right) + \zeta \phi_2 + \zeta^3 \frac{4}{3h^2} \left[-\phi_2 - \frac{\partial w^0}{\alpha_2 \partial \xi^2} \right] \\
w(\xi, \eta, \zeta) &= w^0
\end{aligned} \tag{2.7}$$

where α_1 and α_2 are the surface metrics and h is the total shell thickness. Now the theory has reduced to five parameters instead of seven as described in the first case. These parameters are u^0, v^0, w^0, ϕ_1 and ϕ_2 . Their dependence on ξ and η is not explicitly shown in Equations (2.7) for simplification. Soldatos has applied this theory to examine the stability and vibration of laminated circular [86] and non-circular [87] cylindrical shells. Dennis and Palazotto [24] used an initial kinematic model where the displacements along the midsurface coordinates were expanded to the fourth power in ζ coordinate and the transverse displacement was independent of ζ . After introducing some simplifying assumptions, their model was reduced to Reddy and Liu's model as presented in Equations (2.7). Their displacement-based finite element formulation was specialized to cylindrical shell geometry, and large rotations and displacements were incorporated using a simplified approach. The same model was used by Kumar and Singh [88] for the dynamic analysis of laminated shells using Bezier functions as admissible displacement fields to represent the shell's middle surface displacement and rotation components. Here also, it is valid for moderate rotations only. The true finite rotation model using a TOSDT was developed by Basar et al.[19] where the position vector of an arbitrary point in the deformed shell medium is given by

$$x(\xi, \eta, \zeta) = \varphi(\xi, \eta) + \zeta a_3(\xi, \eta) + \zeta^2 u(\xi, \eta) + \zeta^3 y(\xi, \eta) \tag{2.8}$$

After introducing the fiber inextensibility condition (transverse normal strain neglected) and assuming furthermore that the transverse shear deformation is distributed symmetrically with respect to the shell middle surface, they obtained a reduced equation with two kinematic constraints.

$$x(\xi, \eta, \zeta) = \varphi(\xi, \eta) + \zeta a_3(\xi, \eta) + \zeta^3 y(\xi, \eta) ; a_3 \cdot a_3 = 1 ; a_3 \cdot y = 0 \quad (2.9)$$

The first constraint was satisfied exactly using a certain decomposition for a_3 , but the second one was enforced in the finite element procedure at the element level.

2.2.2 Discrete Layer Theories

In the theories of this kind [1,2,49,50], piecewise, layer by layer displacement assumption through the thickness is introduced. Although the discrete layer approximation theories are very accurate in general, they are quite cumbersome in solving practical problems because the order of their governing equations depends on the number of layers (NL) of the laminated shell, which is very high in real laminated composite shells. The theoretical model developed on this basis contains $2*NL+3$ parameters making them the most expensive ones. In addition, since in these theories the transverse shear stresses are constant within each layer, the shear stresses are also discontinuous at the layer interfaces. In view of these reasons, Di Sciuva [89] has proposed a simplified discrete layer theory with only five unknowns for describing the deformation of shells. His model was based on firstly assuming the in-plane displacements to be piecewise linearly distributed through the thickness, and then imposing the continuity of transverse shear stresses at layer interfaces. A similar

laminated shell theory, incorporating the geometrical nonlinearities in the spirit of the Von Karman's small strain and moderately small rotation approximation, has been proposed by Librescu and Shmidt [90]. In these theories the transverse shear stresses are uniform across the entire thickness of the shell, therefore the zero shear stresses on the bounding surfaces are not fulfilled. The displacement assumption proposed by Di Sciuva [89] was modified later, to develop third order shear deformation plate [91] and shell [92] theories with continuous interlaminar stresses. Some finite rotation models using layerwise theory can be found in references [16,19,93-95]. Braun et al.[16] used a so-called multi-director theory, which was described in References [96-99], to develop a layerwise shell model with extensible director, i.e., allowing for transverse shear and normal strains within each layer. This model was applied to laminated plates under uniform and sinusoidal loads. A similar model was used by Basar and Ding [94] where a constant stretch of the layer director is allowed and this model is based on a multiplicative decomposition proposed originally by Simo et al.[100], but in References [19,93], the layer shell director was based on the inextensible director assumption. Because of the expensiveness and accuracy of these models, they should be used to model localized three-dimensional effects where the predictions of ESL theories are inadequate. A number of simultaneous multiple model methods have been reported in the literature [101] where different subregions of the laminate are described with different types of mathematical models. A review of such models can be found in Reference [101].

2.3 Large Rotation Formulations

2.3.1 General

The theoretical background for the parametrization of finite rotations has reached a very advanced level which is documented in many textbooks [102-104] and in many papers [11, 105-114]. From the algebraic point of view, finite rotations may be regarded as linear transformations with invariance properties. They can be described by a set of parameters, the choice of which is very wide. Euler was the first to recognize the importance of spherical motion defined as the pure rotation motion occurring in a body fixed at one point. He also observed that a spherical motion could always be described by a unique rotation about an axis of a given orientation in space. The geometrical point of view, which is found in most textbooks on classical dynamics [102], consists of describing an arbitrary rotation in terms of elementary rotations about fixed axes. Euler himself introduced a set of angles, known as Euler angles, which is well suited for the study of spinning bodies such as tops and gyroscopes. Another set of angles, known as Bryant or nautical angles, has been adopted by the community of flight mechanics [115]. These quantities are called roll, pitch and yaw. Although these angles have straightforward physical meaning, they may lead to singularities in specific situations and their trigonometric nature make them computationally inefficient in describing arbitrary large rotations which may be encountered in very complex systems [111]. The development of the algebraic approach is based on the fundamental observation that rotation preserves the length of the position vector of any point undergoing the rotation.

This induces the well-known orthonormality condition of the rotation operator and allows its presentation in terms of its invariants [104]. These invariants were described by many sets of parameters, the most important among them are the Euler parameters and the Rodrigues parameters. Euler parameters were successfully used in the simulation of rigid multibody dynamics [116] and later on extended to flexible multibody systems by several authors [117].

The interest of the continuum mechanics community for the kinematic description of rotational motion is more recent. Among the contribution of continuum mechanics experts, we can cite the remarkable synthesis works of Argyris [106] and Atluri and Cazzani [112]. However, it was only with the recent development by Simo and co-workers of the so-called geometrically exact structural theories for beams [118,119] and shells [64-66] that the urgent need to address the pertinent computational issues, has arisen.

Many nonlinear shell theories, capable of capturing finite rotations, have been developed recently. These theories are characterized by being geometrically exact and by including a rotation tensor. They are either based on the Green-Lagrange strain tensor or the stretch tensor as a strain measure. In the first case, which is more popular, the rotation tensor is part of a geometric description of the displacement field. It describes the rotation of the shell director (normal vector to the shell middle surface in the undeformed state). In this type of formulation, the rotation about the normal (drilling degree of freedom) is excluded at the onset thus resulting in a two-parameter rotation tensor instead of three. Examples of Research works representing this category can be

found in References [12,14,15,17,18-20, 22,23,25,31-33,64,66,121]. In the second case, when stretch type of strain tensors are used, the rotation tensor enters the formulation based on its definition, i.e., by means of polar decomposition of the deformation gradient [8, 120]. This rotation tensor can be three-parametric with a natural inclusion of the drilling degree of freedom. A representative work of this category can be found in Reference [67].

2.3.2 Rotation Parametrization

Many possibilities exist for an explicit representation of the rotation tensor \mathbf{R} . This has been described for example by Spring [108] in his review paper. Recently, Betsch et al. [11] reviewed the computational treatment of finite rotations based on various rotational parametrizations, used in the computational mechanics field, and classified them with respect to their update structure as either additive or multiplicative. The main parametrizations, used frequently in the literature, will be briefly presented and then focus is placed on the one adopted in this study.

2.3.2.1 Direction Cosines

Even though the direction cosines are rarely used in describing the three dimensional rotations, this method is discussed for the completeness of the presentation. Considering two coordinate systems $x_1x_2x_3$ and $x'_1x'_2x'_3$ with, respectively, (e_1, e_2, e_3) and (t_1, t_2, t_3) as unit base vectors in these coordinate systems. $x'_1x'_2x'_3$ is obtained by rotating $x_1x_2x_3$ about its origin. In this case, the rotation tensor can be expressed as

$$\mathbf{R} = \mathbf{t}_i \otimes \mathbf{e}_i \quad (2.10)$$

where ' \otimes ' represents the tensor product.

The components of \mathbf{R} , i.e., R_{ij} are obtained in the initial coordinate system x_1, x_2, x_3 as follows

$$R_{ij} = \mathbf{e}_i \cdot (\mathbf{t}_k \otimes \mathbf{e}_k) \cdot \mathbf{e}_j = (\mathbf{e}_i \cdot \mathbf{t}_k)(\mathbf{e}_k \cdot \mathbf{e}_j) = \mathbf{e}_i \cdot \mathbf{t}_j \quad (2.11)$$

Equation (2.11) shows that column j of \mathbf{R} represents the direction cosines of the base vector \mathbf{t}_j . The orthogonality of the rotation tensor is shown in the following equation

$$\mathbf{R}\mathbf{R}^T = (\mathbf{t}_i \otimes \mathbf{e}_i)(\mathbf{e}_j \otimes \mathbf{t}_j) = \delta_{ij}(\mathbf{t}_i \otimes \mathbf{t}_j) = \mathbf{t}_i \otimes \mathbf{t}_i = \mathbf{I} \quad (2.12)$$

This implies that the inverse of \mathbf{R} is equal to its transpose. The nine direction cosines in \mathbf{R} are not independent and Equation (2.12) contains nine constraints where three of them are repeated twice, thus six independent constraints exist between the direction cosines. This will reduce the number of independent parameters, to characterize the rotation tensor, to three. It is evident from above that carrying out nine parameters with six constraints to explicitly express the rotation tensor is not practical.

2.3.2.2 Rotation about some Axis

The well-known Euler's theorem states that the general displacement of a rigid body with one point fixed can be always described as a unique rotation about an axis of a given orientation in space. Let us consider a finite rotation with an angle $\theta = |\theta|$ about an axis

given by a unit vector $\mathbf{n} = \frac{\boldsymbol{\theta}}{\theta}$ where

$$\boldsymbol{\theta} = \theta \mathbf{n} \quad (2.13)$$

is called the rotation vector. The corresponding rotation tensor $\mathbf{R}(\boldsymbol{\theta} \mathbf{n})$ defines the conical transformation $\mathbf{R}(\boldsymbol{\theta} \mathbf{n})\mathbf{a}$ of a vector \mathbf{a} which moves on a cone around the rotation axis \mathbf{n} . Simple geometric considerations lead to the so-called Rodrigues formula [102, 104-106],

$$\mathbf{R}(\boldsymbol{\theta} \mathbf{n}) = \cos \theta \mathbf{I} + (1 - \cos \theta) \mathbf{n} \otimes \mathbf{n} + \sin \theta \hat{\mathbf{n}} \quad (2.14)$$

where $\hat{\mathbf{n}}$ denotes the skew symmetric matrix associated with the axial vector \mathbf{n} and satisfies the following condition

$$\hat{\mathbf{n}} \mathbf{v} = \mathbf{n} \times \mathbf{v} \quad \text{for any } \mathbf{v} \in \mathfrak{R}^3 \quad (2.15)$$

and 'x' stands for cross product.

The components of \mathbf{n} and $\hat{\mathbf{n}}$, expressed with respect to fixed three dimensional orthonormal base vectors $\mathbf{e}_i, i=1,2,3$, are

$$\mathbf{n} = n_i \mathbf{e}_i \quad ; \quad \hat{\mathbf{n}} = \hat{n}_{ij} \mathbf{e}_i \otimes \mathbf{e}_j \quad (2.16a,b)$$

The matrix representation of these quantities is given by

$$\{\mathbf{n}\} = \begin{Bmatrix} n_1 \\ n_2 \\ n_3 \end{Bmatrix} \quad [\hat{\mathbf{n}}] = \begin{bmatrix} 0 & -n_3 & n_2 \\ n_3 & 0 & -n_1 \\ -n_2 & n_1 & 0 \end{bmatrix} \quad (2.17a,b)$$

The Rodrigues formula (2.14) can be identified with the exponential of the skew symmetric tensor $\hat{\theta}$ that has the explicit expression [103.106]

$$\text{Exp}[\hat{\theta}] = I + \frac{\sin \theta}{\theta} \hat{\theta} + \frac{1}{2} \left(\frac{\sin \theta/2}{\theta/2} \right)^2 \hat{\theta}^2 \quad (2.18)$$

We can go from Equation (2.14) to Equation (2.18) by using the standard relations

$$\hat{\theta}^2 = \theta \otimes \theta - \theta^2 I \quad 2 \sin^2 \theta/2 = 1 - \cos \theta \quad (2.19a,b)$$

Equations (2.14) or (2.18) can be used to construct elementary rotations about fixed coordinate axes such as $\theta_1 = \theta_1 e_1$, $\theta_2 = \theta_2 e_2$ and $\theta_3 = \theta_3 e_3$. Accordingly, we obtain

$$R(\theta_1 e_1) = \begin{bmatrix} 1 & 0 & 0 \\ 0 & \cos \theta_1 & -\sin \theta_1 \\ 0 & \sin \theta_1 & \cos \theta_1 \end{bmatrix} \quad (2.20)$$

$$R(\theta_2 e_2) = \begin{bmatrix} \cos \theta_2 & 0 & \sin \theta_2 \\ 0 & 1 & 0 \\ -\sin \theta_2 & 0 & \cos \theta_2 \end{bmatrix} \quad (2.21)$$

$$R(\theta_3 e_3) = \begin{bmatrix} \cos \theta_3 & -\sin \theta_3 & 0 \\ \sin \theta_3 & \cos \theta_3 & 0 \\ 0 & 0 & 1 \end{bmatrix} \quad (2.22)$$

2.3.2.3 Euler Angles

One of the most common and widely used parameters in rigid body rotations are the

three independent Euler angles. This parametrization relies on the use of successive elementary rotations about three axes that are not orthogonal in general (follower axes). Euler angles, however, are not unique; the most widely used set is given by Goldstein [102] where the Euler angles are defined with respect to the follower axes (3.1.3) with the respective rotation angles of ϕ, θ, ψ . Argyris [106] pointed out that a sequence of rotations about follower axes is equivalent to the same sequence of rotations about fixed axes except that the order of application of the rotations is inverted. Thus, the above sequence is equivalent to a rotation ψ about e_3 axis, followed by a rotation θ about e_1 axis and concluded by a rotation ϕ about e_3 axis. The resulting rotation matrix is given by

$$\mathbf{R} = \mathbf{R}(\phi e_3) \mathbf{R}(\theta e_1) \mathbf{R}(\psi e_3) \quad (2.23)$$

After substituting the elementary rotations by their expressions, based on Equations (2.20)- (2.22), the final expression of \mathbf{R} is

$$\mathbf{R} = \begin{bmatrix} \cos \phi \sin \psi - \sin \phi \cos \theta \sin \psi & -\cos \phi \sin \psi - \sin \phi \cos \theta \cos \psi & \sin \phi \sin \theta \\ \sin \phi \cos \psi + \cos \phi \cos \theta \sin \psi & -\sin \phi \sin \psi + \cos \phi \cos \theta \cos \psi & -\cos \phi \sin \theta \\ \sin \theta \sin \psi & \sin \theta \cos \psi & \cos \theta \end{bmatrix} \quad (2.24)$$

Euler angles are a special version of formulations based on elementary rotations. Lee and Kanok-Nukulchai [12] used three elementary rotations leading to a rotation matrix similar to that derived by Surana and Sorem [122]. This formulation includes drilling rotations which will cause singularity in case the elements meeting at the same node are

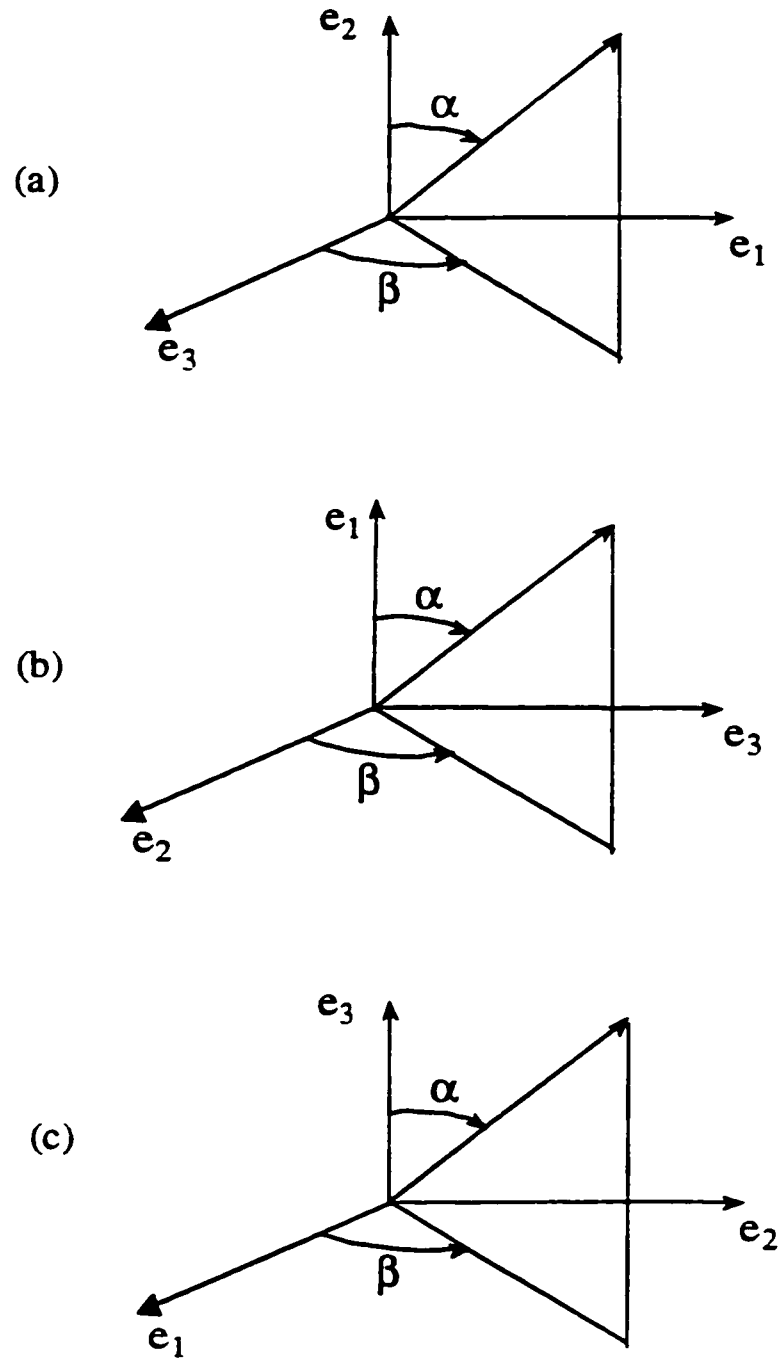


Figure 2.1. Spherical coordinates : Three different possibilities defining the director with respect to the orthonormal basis

coplanar.

The spherical coordinates, consisting of two independent angles used to describe the position vector d of a point on the unit sphere, have been used in finite rotation shell formulations [121,25,19,17,15] to define the direction of the shell director in case drilling degrees of freedom are excluded. Figure (2.1) shows different possibilities to define these angles. The formulations in References [121,25,15] used the definition shown in Figure (2.1a) and those in References [19,17] adopted that of Figure (2.1c). Unfortunately all these formulations are not free of singularities and, as mentioned above, due to their trigonometric nature they are not computationally efficient.

2.3.2.4 Euler Parameters (Quaternions)

An alternative parametrization of the rotation about an axis n with angle θ , which offers a very attractive scheme for the multiplication of two sequential rotations, is based on the so-called Euler, or sometimes referred to as Euler-Rodrigues, parameters defined by

$$q_0 = \cos \theta / 2 \quad q = [\sin \theta / 2]n \quad (2.25a,b)$$

Since the norm of n is equal to unity, the four Euler parameters (q_0, q) have to satisfy the constraint condition

$$q_0^2 + q \cdot q = 1 \quad (2.26)$$

In this case, the rotation matrix leads to the alternative parametrization

$$R(q_0, q) = (2q_0^2 - 1)I + 2q \otimes q + 2q_0 \hat{q} \quad (2.27)$$

in terms of Euler parameters (q_0, \mathbf{q}) . This rotation tensor does not require any trigonometric functions. Euler parameters are especially well suited for the composition of two successive rotations. Given two sequential finite rotations with corresponding Euler parameters $(q_{0(1)}, \mathbf{q}_1)$ and $(q_{0(2)}, \mathbf{q}_2)$, there is a single compound rotation with parameters

$$q_{0(3)} = q_{0(1)}q_{0(2)} - \mathbf{q}_1 \cdot \mathbf{q}_2 \quad (2.28)$$

$$\mathbf{q}_3 = q_{0(1)}\mathbf{q}_2 + q_{0(2)}\mathbf{q}_1 - \mathbf{q}_1 \times \mathbf{q}_2 \quad (2.29)$$

so that the rotation tensor $\mathbf{R}(q_{0(3)}, \mathbf{q}_3)$ is identical to

$$\mathbf{R}(q_{0(3)}, \mathbf{q}_3) = \mathbf{R}(q_{0(2)}, \mathbf{q}_2)\mathbf{R}(q_{0(1)}, \mathbf{q}_1) \quad (2.30)$$

The multiplication rule defined by Equations (2.28) and (2.29) is often accredited to Rodrigues [123]. This will lead to the identification of Euler parameters with quaternions. This parametrization has been used by Simo et al.[124] for the update of the rotation matrix which is composed of two finite rotation. The use of quaternions in the parametrization of a rotation requires less storage i.e. four parameters compared to the nine coefficients used in a rotation matrix including drilling degrees of freedom or six in the one excluding, by design, the drilling degrees of freedom.

2.3.2.5 Rotational Vector

Formulations based on the rotational vector θ are very close to Euler parameters.

except that they use only three parameters, which are the components of the vector θ , or some scaling of the unit vector n , which is parallel to θ . Other alternatives used by some researchers are presented here with the resulting rotation matrix corresponding to each scaled rotation vector [22,107].

$$\theta = \theta n \quad ; \quad \mathbf{R}(\theta) = I + \frac{\sin\theta}{\theta} \hat{\theta} + \frac{1 - \cos\theta}{\theta^2} \hat{\theta} \hat{\theta} \quad (2.31a,b)$$

$$\mathbf{w} = [\tan \theta / 2] n \quad ; \quad \mathbf{R}(\mathbf{w}) = I + \frac{2}{1 + \mathbf{w} \cdot \mathbf{w}} [\hat{\mathbf{w}} + \hat{\mathbf{w}} \hat{\mathbf{w}}] \quad (2.32a,b)$$

$$\mathbf{v} = \sin \theta n \quad ; \quad \mathbf{R}(\mathbf{v}) = I + \hat{\mathbf{v}} + \frac{1}{2 \cos^2 \frac{\theta}{2}} \hat{\mathbf{v}} \hat{\mathbf{v}} \quad (2.33a,b)$$

where $\hat{\theta}$, $\hat{\mathbf{w}}$ and $\hat{\mathbf{v}}$ are skew symmetric matrices satisfying Equations (2.17). Equations (2.31) are the Rodrigues equations which can be obtained from Equation (2.18) with the help of the trigonometric identity (2.19b). The rotation matrix obtained using the parametrization of Equation (2.32) does not require any trigonometric functions, as was the case for the rotation tensor based on Euler parameters. The relation of \mathbf{w} to Euler parameters is given by

$$\mathbf{w} = \frac{\mathbf{q}}{q_0} \quad (2.34)$$

The compound rotation that results from two sequential rotations, which are now given, respectively, by \mathbf{w}_1 and \mathbf{w}_2 , can be directly calculated based on Equations (2.28) and (2.29) to yield

$$\mathbf{w}_3 = \frac{\mathbf{w}_1 + \mathbf{w}_2 - \mathbf{w}_1 \times \mathbf{w}_2}{1 - \mathbf{w}_1 \cdot \mathbf{w}_2} \quad (2.35)$$

Note however that the scaled rotation vector \mathbf{w} introduces a singularity at $\theta = \pm\pi + 2k\pi$ since $\tan \theta / 2 \rightarrow \infty$. The third term of Equation (2.32b) also becomes unstable. Equation (2.31) is the only one without singularities in the range of $0 \leq \theta \leq 2\pi$ because

$$\lim_{\theta \rightarrow 0} \frac{\sin \theta}{\theta} = 1 \quad ; \quad \lim_{\theta \rightarrow 0} \frac{1 - \cos \theta}{\theta^2} = \frac{1}{2} \quad (2.36a,b)$$

Simo et al.[66] used the Rodrigues formula with a material parametrization which reduces the components of the rotation vector to two, i.e., excluding the drilling rotations. Sansour et al.[67] and Parisch[23] used the three components of the rotation vector which is normal in the formulation of Sansour et al., but induces singularities in the formulation of Parisch in case of coplanar elements. However Hughes and Liu [62] as well as Stanley [35] used different approximations of the Rodrigues formula. The formulation adopted in this study follows closely that of Simo et al. [66]

2.4 Shell Elements

Over the years many shell elements have been developed. Yang et al. [125] reviewed extensively the advances of the formulations for thin shell finite elements previous to 1990 and discussed the effects of geometric and material nonlinearities. Most of the developed elements can be put into three distinct classes according to the basic mathematical principles used.

Facet Elements:

In this kind of formulation, the shell surfaces are approximated by an assembly of flat elements. The behavior of the shell is modeled by superposition of stretching behavior (two dimensional membrane element) and bending behavior (plate bending element). At the element level, the in-plane stretching and bending stiffnesses are completely uncoupled. The coupling is accounted for at the structure level, i.e. while assembling the global stiffness matrix; such coupling is a major contributor towards load carrying mechanism in shells and other curved elements. Some notable flat displacement-based elements can be found in references [126-130]. Knowles et al.[131] observed that, in general, adequate performance of such elements can be obtained when the sought response is either membrane dominated or bending dominated. However, when there is strong coupling between them, the performance is extremely poor. Horigmoe and Bergan [42] and Madenci and Barut [45], who used the corotational formulation to remove the small rotation limitation, applied these elements to geometrically nonlinear problems.

Curved Shell Elements based on Classical Shell Theory

Curved shell elements have been developed to overcome the difficulties encountered by facet elements due to their flatness and the discontinuity in geometry caused while modeling curved surfaces. For elements based on classical shallow (thin) shell theories, their range of application is limited by the underlying shell theories employed. The problem encountered with early curved shell elements, based on classical shell theory, is their inadequacy in modeling rigid body modes [125]. Hansen and Heppler [132]

presented a method to enable the shell-coordinate (curvilinear) finite elements to exactly reproduce all of the six Cartesian rigid body modes. This was done by forcing the rigid body capability as an essential requirement for the derivation of the basis functions. The recent use of tensor mathematics in the formulation of quadrilateral shell elements [133-136,5,25] has removed the limitation of such elements to regular shapes, i.e., confined to orthogonal curvilinear coordinates where any two neighboring sides of an element must be orthogonal. The problem, which arises in this case, is the uniqueness requirement that these curvilinear coordinate systems and base vectors must be unique at each common nodal point [136].

Kirchhoff shell theory has been widely used in the formulation of curved thin shell elements due to its well-established nature. Irons and Drapeer [137] showed that the requirement of inter-element normal slope continuity, which is a requirement of Kirchhoff theory for the formulation of conforming shell elements, was incompatible with the requirement that the element must be able to represent states of constant stress. Such limitations have led to the development of 'degenerated' shell elements, which are degenerated from the three dimensional isoparametric formulation with additional kinematic assumptions.

Degenerated Shell Element

The degenerated shell element, first introduced by Ahmad et al.[58], is based on the 3-D continuum equations but with an isoparametric interpolation that in effect imposes the same kinematic constraints/restrictions as those of the FOSDT. The continuum based finite element development avoids the intermediate step of deriving 2-D plate or shell

equations and then using them to develop finite element models. The dissertation of Stanley [35] and the books of Bathe[8] and Hughes[138] offer comprehensive overviews of the degenerated solid approach and related methodologies involving some type of reduction to resultant form. Although the hypotheses underlying the degenerated solid approach and the classical shell theory, with a Reissner-Mindlin kinematic, are essentially the same, the reduction to resultant form is typically carried out numerically in the former and analytically in the latter. The recently developed finite rotation shell elements by Simo and co-workers [64-66] are very efficient and brought the two approaches closer to each other. They started their formulation from the strain definition of the classical shell theory, but a discretization similar to the degeneration concept was introduced in the finite element, i.e., the vectorial quantities were decomposed along fixed Cartesian axes rather than along local bases. Most of recent finite rotation models follow this approach [14,15,17,19,20,22,23]. We mention here also Stander et al.[25] who used curvilinear convective coordinates rather than cartesian coordinates within the degenerated approach.

The displacement-based finite element formulations suffer from the so-called shear locking, a phenomena which is closely connected with the underlying assumptions typical for the shell theories of the Mindlin-Reissner type when they become thin. Many procedures have been suggested to improve the behavior of these elements in thin shell situations. Some of these procedures alleviate the 'locking' problem by special treatment of the transverse shear strain components, while using full integration to preserve the correct rank of the element stiffness matrix. Among these proposed procedures, the one

based on mixed interpolation of tensorial transverse shear strain components, initially developed by Bathe and Dvorkin [4,5], is especially attractive.

The four node quadrilateral shell element has been a matter of performance investigation by many authors especially for shells undergoing finite rotations [15,17,19,23,25]. Extensive testing was done in Reference [25] to prove the robustness of this element. It is believed to have a weakness of poor coarse mesh geometric modeling. Its strengths lie with its inherent economy and its insensitivity to distortion. The former characteristic stems from the element's low nodal connectivity. In geometrically nonlinear analysis, distortion of higher order elements may reduce the quality of the analysis significantly, whereas four node elements are less sensitive[25].

2.5 Dynamic Effects

When dynamic effects are included, a temporal discretization method is needed. The Newmark family of implicit single step time integration schemes [139] are favored in structural dynamics. These algorithms are unconditionally stable for linear problems, but only conditionally stable for nonlinear problems. This has been demonstrated recently by Simo and co-workers [6,140-142] for the midpoint and the trapezoidal rules through numerical simulations considering rigid bodies, shells and rods. In their simulations, these two methods exhibit severe energy growth which suggest the loss of the 'unconditional stability'.

An attractive criterion for the stability of time integration algorithms is the conservation of energy. Hughes et al.[143] presented a modification of the trapezoidal rule to achieve conservation of energy which was enforced via Lagrange multiplier.

Their algorithm failed to conserve momentum. Simo et al.[124] modified the momentum conserving schemes to preserve energy for the case of nonlinear shells. Their designed algorithms achieved limited success in actual calculations. Afterwards, Simo and Tarnow [140] proposed a general methodology for the design of exact energy-momentum conserving algorithms within the context of nonlinear elastodynamics. This methodology has been extended by the same authors, in Reference [6], to the nonlinear dynamics of shells and by Simo et al.[141] to the nonlinear dynamics of three dimensional rods. Galvanetto and Crisfield [144] presented an energy-conserving procedure for nonlinear dynamic analysis of planar beam structures based on the co-rotational technique which was proposed by Rankin and Brogan[41] for the static case. Kuhl and Ram [33] presented the so-called constraint-energy momentum algorithm, which combines the positive features of algorithmic damping of higher frequencies with the enforcement of conservation of energy and momenta via Lagrange multipliers. Recently, Brank et al.[32] applied the energy-momentum algorithm developed by Simo and Tarnow [6] to first order shear deformation shell models with large rotations.

2.6 Current State of the Art

The noticeable work in laminated shells with reference to geometrically nonlinear behavior including finite (unlimited in size) rotations is limited compared to its counterpart in isotropic shells. The nature of fiber reinforced composites with their low transverse shear to inplane moduli and their fast transition from secondary to primary structural element in modern industries require the use of HOSDT to accurately predict the response of structures made of such materials. Among HOSDT, the TOSDT is the

most popular one. This refined theory has been extensively used in linear analysis laminated beams, plates and shells but rarely used in the analysis of laminated shells undergoing finite rotations. It is needed to assess the range of predictability of the FOSDT when applied to thin-to-thick laminated shells in highly nonlinear cases. The analytical solutions in such cases, even for isotropic shells, don't exist. The importance of composite materials in aerospace, outerspace and automotive structures motivates the consideration of dynamic analysis. The conservation of energy, linear and angular momenta, besides their physical foundations, represent attractive criteria for the stability of time integration algorithms. If one of these quantities blows up, it suggests that the time integration scheme becomes unstable. The exact energy-momentum conserving algorithm has only been applied to the nonlinear dynamic analysis of shell type structures undergoing finite rotations and using the FOSDT. Thus its extension to the TOSDT represents at the same time a need and advancement in state-of-the-art analysis of laminated composite shells.

CHAPTER 3

SHELL THEORY

3.1 General

This chapter aims at presenting the essential elements of a shell theory that will be used in subsequent chapters, within the framework of the finite element method (FEM), for numerical analysis of isotropic or laminated shell type structures subjected to static and dynamic loads. It starts by reviewing some important mathematical preliminaries pertaining to curvilinear coordinates and differential geometry of a surface, which are essential for the treatment of the shell theory. The construction of the present shell theory is approached from the three-dimensional theory by viewing the shell as a three-dimensional continuum body, then appropriate assumptions are introduced as a consequence of the thinness of the shell. The exposition of the shell theory itself starts by proposing a kinematic model, based on TOSDT, to trace the material particles during the deformation process which allows the shell body to undergo large motion and finite rotations. Then, using this kinematic model, Green-Lagrange strains are derived based on two configurations of the shell, which are the initial and current states. The

relationship of these strains to their work-conjugate second Piola-Kirchhoff stresses are then established through constitutive relations that are limited to small strains. These constitutive equations are derived directly with respect to curvilinear coordinates in case the layer is isotropic. Otherwise, when the layer is orthotropic, they are derived with respect material principal axes and then transformed to curvilinear laminate coordinates. These constitutive equations, which were initially three dimensional, are reduced to plane stress by imposing zero transverse normal stress condition.

3.2 Curvilinear Coordinates

The position vector of a generic point P (Figure 3.1) is given by the vector

$$\mathbf{x} = x_i \hat{\mathbf{i}}_i \quad (3.1)$$

where x_i are rectangular coordinates and $\hat{\mathbf{i}}_i$ are unit vectors directed as shown in Figure 3.1. In this work the Latin index (subscript or superscript) represents any of the numbers 1,2 or 3. In two dimensional problems, a Greek index is used to represent either of the numbers 1 or 2 only. Any term in which the same index is repeated, unless otherwise indicated, stands for the sum of all such terms obtained by giving this index its complete range of values.

Let θ^i denote arbitrary curvilinear coordinates. We assume the existence of equations which express the variables x_i in terms of θ^i and vice versa, that is

$$x_i = x_i(\theta^1, \theta^2, \theta^3) \quad , \quad \theta^i = \theta^i(x_1, x_2, x_3) \quad (3.2a,b)$$

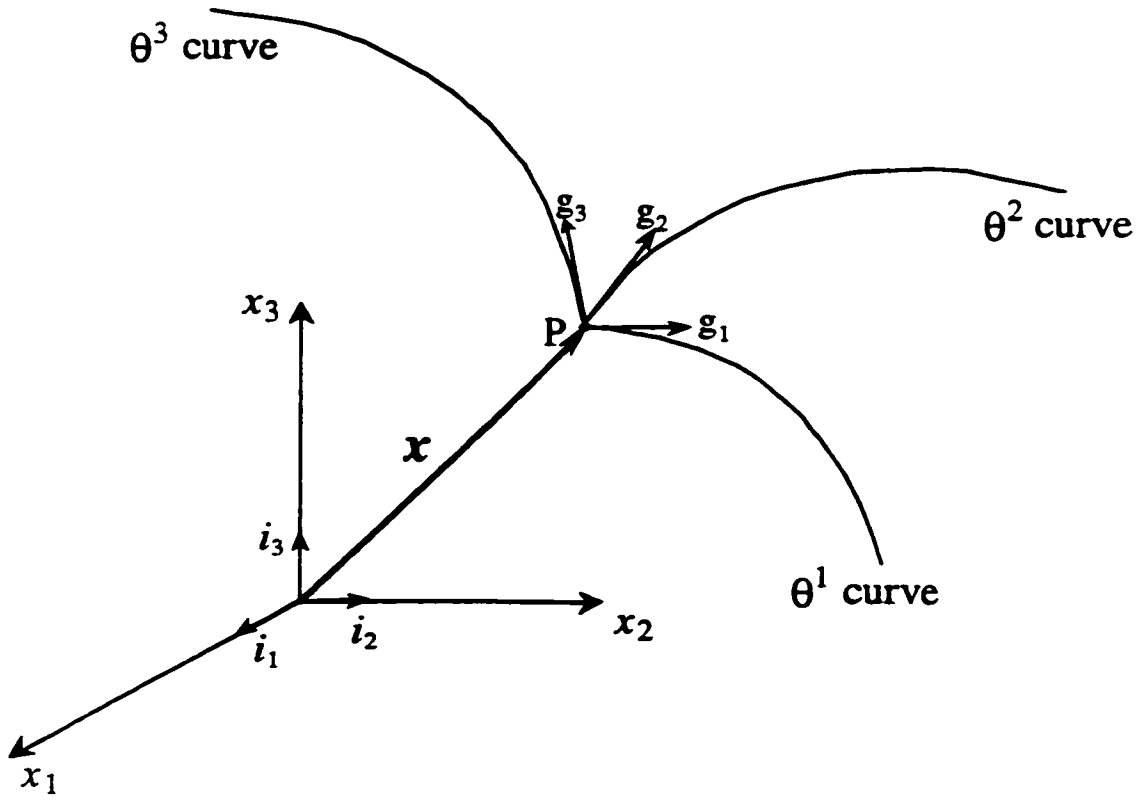


Figure 3.1 Position vector of a point P with cartesian and curvilinear coordinates

By means of Equations (3.2a). and (3.2b), the position vector \mathbf{x} can be expressed in alternative forms:

$$x_i = x_i(x_1, x_2, x_3) = x_i(\theta^1, \theta^2, \theta^3) \quad (3.3)$$

A differential change $d\theta^i$ is accompanied by a change $d\mathbf{x}$ tangent to the θ^i curve. It follows that the vector

$$\mathbf{G}_i = \frac{\partial \mathbf{x}}{\partial \theta^i} = \frac{\partial x_j}{\partial \theta^i} \hat{\mathbf{i}}_j \quad (3.4)$$

is tangent to the θ^i curve. The tangent vector \mathbf{G}_i is sometimes called a covariant base or shortly a base vector. We define another triad of vectors \mathbf{G}^i such that

$$\mathbf{G}_i \cdot \mathbf{G}^j = \delta_i^j \quad (3.5)$$

where \mathbf{G}^j is often called a contravariant or reciprocal base vector and δ_i^j is the Kronecker delta defined by the equation

$$\delta_{ij} = \delta^{ij} = \delta_i^j = \delta_j^i = \begin{cases} 0 & (i \neq j) \\ 1 & (i = j) \end{cases} \quad (3.6)$$

From Equation (3.5), it can be seen that the contravariant base vectors ($\mathbf{G}^1, \mathbf{G}^2, \mathbf{G}^3$) are respectively perpendicular to the planes $\mathbf{G}_2\mathbf{G}_3$, $\mathbf{G}_3\mathbf{G}_1$, $\mathbf{G}_1\mathbf{G}_2$. The triad \mathbf{G}_i can be expressed as a linear combination of the triad \mathbf{G}^i and vice versa i.e.

$$\mathbf{G}^i = G^{ij} \mathbf{G}_j \quad , \quad \mathbf{G}_i = G_{ij} \mathbf{G}^j \quad (3.7a,b)$$

where

$$\mathbf{G}^{\dot{i}} = \mathbf{G}^i \cdot \mathbf{G}^j \quad , \quad G_{ij} = \mathbf{G}_i \cdot \mathbf{G}_j \quad (3.8a.b)$$

and

$$G^{im} G_{mj} = \delta_j^i \quad (3.9)$$

Equation (3.9) can be solved to express the coefficients $G^{\dot{i}}$ in terms of G_{ij} .

The differential length ds of the differential vector $d\mathbf{x}$ is given by

$$ds^2 = d\mathbf{x} \cdot d\mathbf{x} = G_{ij} d\theta^i d\theta^j \quad (3.10)$$

The coefficients G_{ij} play an important role in differential geometry; they are the components of the metric tensor.

We introduce also the expression for volume and surface elements in general curvilinear coordinates. An elemental volume bounded by the coordinate surfaces through the points $(\theta^1, \theta^2, \theta^3)$ and $(\theta^1 + d\theta^1, \theta^2 + d\theta^2, \theta^3 + d\theta^3)$ is shown in Figure

3.2. In the limit the volume element approaches

$$\begin{aligned} dV &= d\mathbf{r}_1 \cdot (d\mathbf{r}_2 \times d\mathbf{r}_3) \\ &= \mathbf{G}_1 \cdot (\mathbf{G}_2 \times \mathbf{G}_3) d\theta^1 d\theta^2 d\theta^3 \\ &= \sqrt{G} d\theta^1 d\theta^2 d\theta^3 \end{aligned} \quad (3.11)$$

Where

$$G = |G_{ij}| \quad (3.12)$$

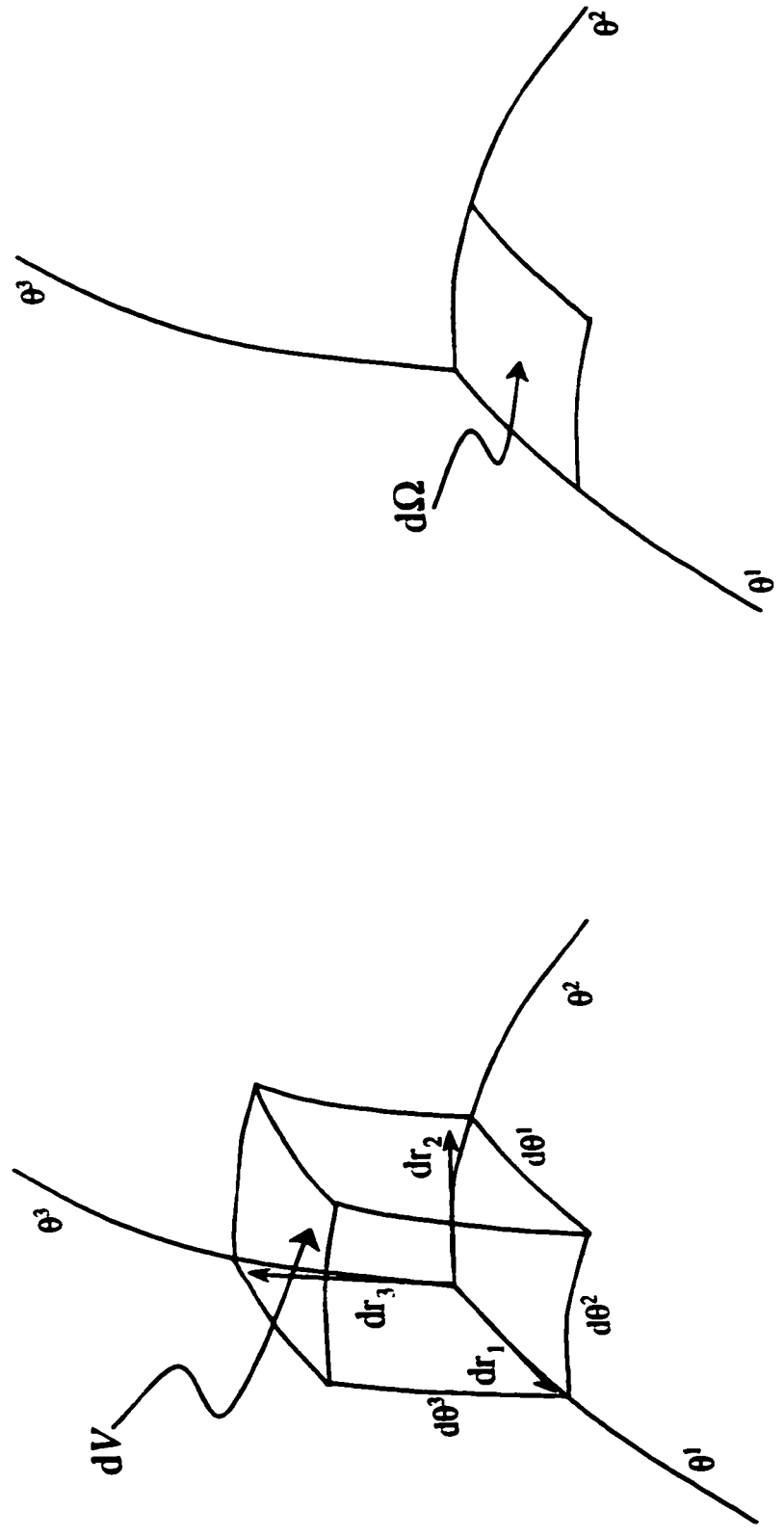


Figure 3.2 Volume and surface elements

represents the determinant of the metric tensor G_{ij} . The area element $d\Omega_3$ on the θ^3 -surface (surface obtained by keeping θ^3 constant and varying θ^1 and θ^2) is given by

$$d\Omega_3 = |dr_1 \times dr_2| = |G_1 \times G_2| d\theta^1 d\theta^2 = \sqrt{GG^{33}} d\theta^1 d\theta^2 \quad (3.13)$$

In general, the area element $d\Omega_i$ on the θ^i -surface is given by

$$d\Omega_i = \sqrt{GG^{ii}} d\theta^j d\theta^k \quad (i \text{ not summed, } i \neq j \neq k) \quad (3.14)$$

3.3 Shell Kinematics

3.3.1 Introduction

By a shell we understand a piece of solid matter bounded by two nearby curved surfaces. The distance between them defines the shell thickness h , which is supposed to be small compared to the other dimensions of the shell. The surface which halves the shell thickness everywhere is called the middle surface (midsurface) and it serves the same purpose as the midplane of a plate or the axis of a beam. In principle, the theory of shells can be derived as the theory of plates is derived. However, the shell theory is necessarily complicated by the initial curvature.

Figure 3.3 shows a shell element in its reference and deformed configurations. (ξ, η, ζ) represent general curvilinear (convected) coordinates attached to the shell body. Note here that, for convenience, (ξ, η, ζ) coordinates will be used instead of $(\theta^1, \theta^2, \theta^3)$ coordinates used in the previous section. We may imagine that this coordinate system

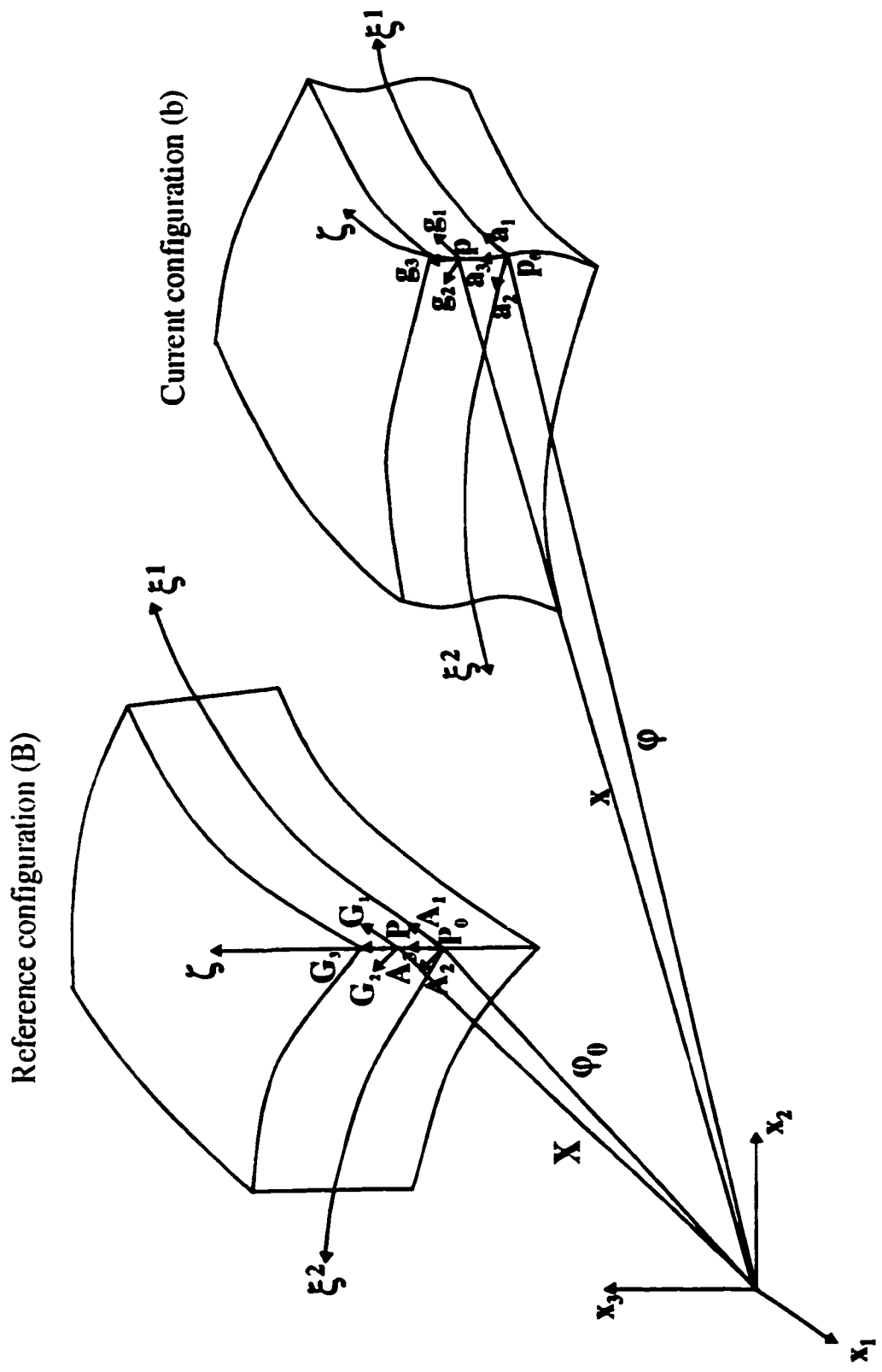


Figure 3.3 Geometry and kinematics of the shell element

moves and deforms continuously with the body as it passes from the original state 'B' to the deformed one 'b'. The values of these coordinates, defining a generic point P in 'B', remain constant as P moves from its position in 'B' to its new position, denoted by p , in 'b' (material representation). Fibers are lines of particles (material lines) in ζ direction extending from the bottom surface of the shell to its top surface. Thus, these fibers are represented by ζ lines in the reference configuration and ζ curves in the current (deformed) configuration. Initially, they are normal to the midsurface $\zeta = 0$ but, after deformation, they become curved and their tangents at $\zeta = 0$ are no longer orthogonal to the middle surface because of shear deformation. The set of all these fibers fully describes the shell body (medium).

Now that a coordinate system is set up for locating any material point in the shell medium, we need to describe geometrically the deformation process. This can be done by first assuming a kinematic model, which will be based on TOSDT with finite rotations, and then using the position vector of any point, defined with respect to a fixed cartesian coordinate system (X, Y, Z) , as a means to describe the geometry of the shell. Two states of the shell are of interest, as shown in Figure 3.3, the initial (reference) state and the current state, which represents the shape of the shell body after it has gone some deformation.

In each state of the shell body, two position vectors are used; i.e., (X, φ_0) in the initial configuration and (x, φ) which represent, respectively, the position vectors of points (P, P_0) and (p, p_0) . Thus, to each point on the shell medium, there is a corresponding point on the reference surface, and they both belong to the same fiber.

Noting here that points and vectorial quantities denoted by upper case letters refer to the undeformed configuration and those with lower case letters refer to the deformed configuration.

The position vector \mathbf{x} of point \mathbf{p} can be expressed by

$$\mathbf{x} = \boldsymbol{\varphi} + (\mathbf{x} - \boldsymbol{\varphi}) = \boldsymbol{\varphi} + \overline{\mathbf{p}_0\mathbf{p}} \quad (3.15)$$

where $\mathbf{x}(\xi, \eta, \zeta)$, $\boldsymbol{\varphi}(\xi, \eta)$ and $\overline{\mathbf{p}_0\mathbf{p}}(\xi, \eta, \zeta)$ are the vectorial quantities shown in Equation (3.15) with their dependence on the curvilinear coordinates. Since $\boldsymbol{\varphi}(\xi, \eta)$ is independent of ζ , the vector $\overline{\mathbf{p}_0\mathbf{p}}$ is the only quantity, which needs to be expanded in power series of ζ coordinate. The analytical expression of the proposed kinematic model is based on the following. In the first step, the vector $\overline{\mathbf{p}_0\mathbf{p}}$ is rotated back along with the fiber containing the points \mathbf{p}_0 and \mathbf{p} until the tangent to this fiber, at the midsurface level ($\zeta = 0$), becomes parallel to the Z axis. In the second step, a power series expansion, up to the third degree with respect to ζ coordinate, is used to approximate the components of the rotated vector $\overline{\mathbf{p}_0\mathbf{p}}$, in the cartesian coordinate system (X,Y,Z).

3.3.2 Undeformed Geometry

In the undeformed geometry, the fibers are straight and normal to the midsurface. In this case the tangents to the fibers are parallel to the fibers themselves and the expression for approximating the rotated $\overline{\mathbf{P}_0\mathbf{P}}$ vector is given by

$$\mathbf{R}_o^T (\mathbf{X} - \boldsymbol{\varphi}_o) = \zeta \mathbf{E}_3 \quad (3.16)$$

where

$\mathbf{X}(\xi, \eta, \zeta)$ and $\boldsymbol{\varphi}_o(\xi, \eta)$ have been defined previously. $\boldsymbol{\varphi}_o(\xi, \eta)$ totally defines the middle (reference) surface of the shell body

$-\frac{h}{2} \leq \zeta \leq \frac{h}{2}$ is the thickness coordinate as mentioned before with h being the thickness of the shell

$\mathbf{E}_3 = [0, 0, 1]^T$ is a unit vector of a fixed reference basis $\{\mathbf{E}_I\}, I = 1, 2, 3$

\mathbf{R}_o is the rotation matrix mapping \mathbf{E}_3 into a unit vector tangent to ζ coordinate at the midsurface level ($\zeta = 0$)

Equation (3.16) can be expanded to yield

$$\mathbf{X} = \boldsymbol{\varphi}_o + \zeta \mathbf{R}_o \mathbf{E}_3 = \boldsymbol{\varphi}_o + \zeta \mathbf{d}_1^{(o)} \quad (3.17)$$

where

$$\mathbf{d}_1^{(o)} = \mathbf{R}_o \mathbf{E}_3 \quad (3.18)$$

represents the unit vector tangent to ζ coordinate at $\zeta = 0$. But since ζ coordinates are straight lines in the reference configuration, then $\mathbf{d}_1^{(o)}$ is a unit vector along ζ axis and it is normal to the base vectors $\mathbf{G}_1, \mathbf{G}_2, \mathbf{A}_1$ and \mathbf{A}_2

Equation (3.18) implies the two following properties

$$\mathbf{d}_1^{(o)} \cdot \mathbf{d}_1^{(o)} = 1 \quad , \quad \mathbf{d}_1^{(o)} \cdot \mathbf{d}_{1,\alpha}^{(o)} = 0 \quad (3.19)$$

where $\mathbf{d}_{1,\alpha}^{(o)}$ represents a differentiation of $\mathbf{d}_1^{(o)}$ with respect to ξ ($\alpha=1$) and η ($\alpha=2$).

Figure 3.3 shows the covariant base vectors $(\mathbf{G}_1, \mathbf{G}_2, \mathbf{G}_3)$ at point P and covariant base vectors $(\mathbf{A}_1, \mathbf{A}_2, \mathbf{A}_3)$ at point P_0 (reference surface level); they are expressed as follow:

– At the middle surface ($\zeta = 0$)

$$\text{base vectors: } \mathbf{A}_\alpha = \boldsymbol{\varphi}_{0,\alpha} \quad (3.20a)$$

$$\mathbf{A}_3 = \mathbf{X}_{,3}|_{\zeta=0} = \mathbf{d}_1^{(o)} = \mathbf{A}_1 \times \mathbf{A}_2 / \|\mathbf{A}_1 \times \mathbf{A}_2\| \quad (3.20b)$$

$$\text{metric tensor } \mathbf{A}_{\alpha\beta} = \mathbf{A}_\alpha \cdot \mathbf{A}_\beta \quad \mathbf{A}_{\alpha 3} = 0 \quad \mathbf{A}_{33} = 1 \quad \mathbf{A} = \det|\mathbf{A}_{\alpha\beta}| \quad (3.21)$$

– At a distance ζ from the middle surface

$$\text{base vectors: } \mathbf{G}_\alpha = \mathbf{X}_{,\alpha} = \boldsymbol{\varphi}_{o,\alpha} + \zeta \mathbf{d}_{1,\alpha}^{(o)} \quad (3.22a)$$

$$\mathbf{G}_3 = \mathbf{d}_1^{(o)} \quad (3.22b)$$

$$\text{metric tensor } \mathbf{G}_{\alpha\beta} = \mathbf{G}_\alpha \cdot \mathbf{G}_\beta \quad \mathbf{G}_{\alpha 3} = 0 \quad \mathbf{G}_{33} = 1 \quad \mathbf{G} = \det|\mathbf{G}_{\alpha\beta}| \quad (3.23)$$

\mathbf{G} was defined in section (3.2) as the determinant of the metric tensor \mathbf{G}_{ij} , but since \mathbf{G}_3 is normal to \mathbf{G}_1 and \mathbf{G}_2 and the norm of \mathbf{G}_3 is unity, then the determinant of \mathbf{G}_{ij} is equal to the determinant of $\mathbf{G}_{\alpha\beta}$, as shown in Equation (3.23). The same reasoning applies to \mathbf{A} which represents the determinant of the metric tensor \mathbf{A}_{ij} .

3.3.3 Deformed State

After deformation, the points P_0 and P will move to new locations p_0 and p (Figure 3.3) having as position vectors $\boldsymbol{\varphi}$ and \boldsymbol{x} , respectively. The rotated vector $\overline{p_0 p}$ in the current configuration is approximated by

$$\boldsymbol{R}^T (\boldsymbol{x} - \boldsymbol{\varphi}) = \zeta \boldsymbol{E}_3 + \zeta^2 \boldsymbol{D}_2 + \zeta^3 \boldsymbol{D}_3 \quad (3.24)$$

where $\boldsymbol{x}(\xi, \eta, \zeta)$ and $\boldsymbol{\varphi}(\xi, \eta)$ are defined above. \boldsymbol{D}_2 and \boldsymbol{D}_3 are two vectors lying in the $(\boldsymbol{E}_1, \boldsymbol{E}_2)$ plane, i.e.,

$$\boldsymbol{D}_2 = D_2^1 \boldsymbol{E}_1 + D_2^2 \boldsymbol{E}_2 \quad (3.25)$$

$$\boldsymbol{D}_3 = D_3^1 \boldsymbol{E}_1 + D_3^2 \boldsymbol{E}_2 \quad (3.26)$$

\boldsymbol{R} is the rotation matrix mapping \boldsymbol{E}_3 into a unit vector tangent to ζ coordinate at the midsurface level ($\zeta = 0$) in the deformed configuration.

The expansion of Equation (3.24) yields

$$\boldsymbol{x} = \boldsymbol{\varphi} + \zeta \boldsymbol{d}_1 + \zeta^2 \boldsymbol{d}_2 + \zeta^3 \boldsymbol{d}_3 \quad (3.27)$$

where

$$\boldsymbol{d}_1 = \boldsymbol{R} \boldsymbol{E}_3 \quad , \quad \boldsymbol{d}_2 = \boldsymbol{R} \boldsymbol{D}_2 \quad , \quad \boldsymbol{d}_3 = \boldsymbol{R} \boldsymbol{D}_3 \quad (3.28a,b,c)$$

From Equations (3.28a,b,c), we deduce the following

$$\boldsymbol{d}_1 \cdot \boldsymbol{d}_1 = 1 \quad \boldsymbol{d}_1 \cdot \boldsymbol{d}_2 = 0 \quad \boldsymbol{d}_1 \cdot \boldsymbol{d}_3 = 0 \quad (3.29)$$

The covariant base vectors $(\mathbf{g}_1, \mathbf{g}_2, \mathbf{g}_3)$, shown at point \mathbf{p} (see Figure 3.3), and covariant base vectors $(\mathbf{a}_1, \mathbf{a}_2, \mathbf{a}_3)$, shown at point \mathbf{p}_0 , are as follow:

-- At the middle surface

$$\text{base vector: } \mathbf{a}_\alpha = \boldsymbol{\varphi}_{,\alpha} \quad (3.30a)$$

$$\mathbf{a}_3 = \mathbf{x}_{,3} \Big|_{\zeta=0} = \mathbf{d}_1 \quad (3.30b)$$

– At a distance ζ from the middle surface

$$\text{base vectors: } \mathbf{g}_\alpha = \mathbf{x}_{,\alpha} = \boldsymbol{\varphi}_{,\alpha} + \zeta \mathbf{d}_{1,\alpha} + \zeta^2 \mathbf{d}_{2,\alpha} + \zeta^3 \mathbf{d}_{3,\alpha} \quad (3.31a)$$

$$\mathbf{g}_3 = \mathbf{x}_{,3} = \mathbf{d}_1 + 2\zeta \mathbf{d}_2 + 3\zeta^2 \mathbf{d}_3 \quad (3.31b)$$

3.3.4. Present Rotation Parametrization

The parametrization adopted in this study follows closely that of Simo et al.[66]. It is based on the Rodrigues formula and a rotational vector both given by Equations (2,31a,b). It was mentioned in chapter two that, among the parametrizations based on the rotational vector, it is the only one free from singularities in the range $0 \leq \theta \leq 2\pi$. A material representation of the rotational vector will reduce the number of parameters from three to two, i.e. excluding the drilling rotation (rotation about the normal to the shell middle surface). The Rodrigues formula will be rewritten here for clarity:

$$\boldsymbol{\theta} = \theta \mathbf{n} \quad (3.32a)$$

$$\mathbf{R}(\boldsymbol{\theta}) = \mathbf{I} + \frac{\sin \theta}{\theta} \hat{\boldsymbol{\theta}} + \frac{1 - \cos \theta}{\theta^2} \hat{\boldsymbol{\theta}} \hat{\boldsymbol{\theta}} \quad (3.32b)$$

The quantities involved in Equations (3.32a) and (3.32b) have already been defined in chapter 2. \mathbf{R}_0 , described in section (3.3.1), represents the initial value of \mathbf{R} . It can be constructed based on the normals to the midsurface of the shell body in its reference configuration. \mathbf{R} however will be uniquely constructed incrementally during the solution procedure and Equation (3.32b) will be used for the parametrization of the incremental rotation as will be seen in the next chapter.

3.3.5. Strain Measures

Considering the points P and p , discussed above, with their respective position vectors \mathbf{X} and \mathbf{x} . Let

$$d\mathbf{X} = \mathbf{G}_i d\theta^i \qquad d\mathbf{x} = \mathbf{g}_i d\theta^i \qquad (3.33)$$

be two differential vectors in the reference and current configurations, respectively. The deformation gradient tensor \mathbf{F} can be written as

$$d\mathbf{x} = \mathbf{F} \cdot d\mathbf{X} = d\mathbf{X} \cdot \mathbf{F}^T \qquad (3.34)$$

$$d\mathbf{X} = \mathbf{F}^{-1} \cdot d\mathbf{x} = d\mathbf{x} \cdot \mathbf{F}^{-T} \qquad (3.35)$$

\mathbf{F} and \mathbf{F}^{-1} are given by

$$\mathbf{F} = \mathbf{g}_i \otimes \mathbf{G}^i \qquad \mathbf{F}^{-1} = \mathbf{G}_i \otimes \mathbf{g}^i \qquad (3.36)$$

Our attention now is focused on the definition of a strain tensor appropriate for the Total Lagrangian Formulation, i.e. Green-Lagrange strain tensor \mathbf{E} which is given by

$$\mathbf{E} = E_{ij} \mathbf{G}^i \otimes \mathbf{G}^j = \frac{1}{2} (\mathbf{F}^T \mathbf{F} - \mathbf{G}) = \frac{1}{2} (g_{ij} - G_{ij}) \mathbf{G}^i \otimes \mathbf{G}^j \quad (3.37)$$

where

$$\mathbf{G} = G_{ij} \mathbf{G}^i \otimes \mathbf{G}^j \quad (3.38)$$

represents the metric tensor in the undeformed configuration and

$$g_{ij} = \mathbf{g}_i \cdot \mathbf{g}_j \quad (3.39)$$

represents the components of the metric tensor \mathbf{g} in the deformed configuration. The components E_{ij} of the Green-Lagrange strain are given by (see Equation 3.37)

$$E_{ij} = \frac{1}{2} (g_{ij} - G_{ij}) \quad (3.40)$$

Before introducing the kinematic model, the strains in Equation (3.40) will be split into in-plane strains $E_{\alpha\beta}$, transverse shear strains $E_{\alpha 3}$ and out of plane normal strains E_{33} . Starting first by the out of plane normal strains.

$$E_{33} = \frac{1}{2} (g_{33} - G_{33}) \quad (3.41)$$

The kinematic model is now introduced through the covariant base vectors \mathbf{g}_i and \mathbf{G}_i as defined in Equations (3.31a,b) and (3.22a,b), respectively. Using Equations (3.23) and (3.39) for G_{ij} and g_{ij} , respectively, and neglecting terms with ζ -power higher than two, we get

$$E_{33} = 4\zeta^2 \mathbf{d}_2 \cdot \mathbf{d}_2 \quad (3.42)$$

Introducing the fiber inextensibility condition (i.e. $E_{33} = 0$), which is a common assumption for many shell theories, leads to

$$D_2 = 0 \quad (3.43)$$

This condition reduces the kinematic model to

$$x = \varphi + \zeta d_1 + \zeta^3 d_3 \quad (3.44)$$

Equation (3.44) represents the final form of our kinematic model. To the knowledge of the author, the only research work where the kinematic model is based on TOSDT and includes finite rotations (unlimited size) is that of Basar et al.[19]. But it is worthy to mention the differences between the two models. Their model started with the expansion to the third degree in ζ i.e.

$$x = \varphi + \zeta a_3 + \zeta^2 u + \zeta^3 y \quad (3.45)$$

this expansion is not something new as has been seen in chapter two. a_3 used in Equation (3.45) is given in Equation (3.30b) and it is equal to d_1 used in this study. Afterwards, they constrained the out of plane strain to zero, which is the usual assumption used in classical shell theory (fiber inextensibility) and it has also adopted here. Then, they supposed the transverse shear strain to be distributed symmetrically. In the present study, the second assumption used by Basar et al. is a result of the satisfaction of the first one i.e. fiber inextensibility. After enforcing the two constraints, the vector u vanished and the model was left with two kinematic constraints to be satisfied, which are

$$\mathbf{a}_j \cdot \mathbf{a}_j = 1 \quad \mathbf{a}_j \cdot \mathbf{y} = 0 \quad (3.46a,b)$$

The first constraint was satisfied by using two Euler angles, as indicated in chapter two, to denote the components of \mathbf{a}_j . However, the second constraint was not satisfied identically because the authors used the following decomposition for the vector \mathbf{y} , along with the difference vector \mathbf{w} between \mathbf{a}_j and \mathbf{A}_j ,

$$\mathbf{y} = y_i \mathbf{A}^i \quad \mathbf{w} = \mathbf{a}_j - \mathbf{A}_j = w_i \mathbf{A}^i = w^j \mathbf{A}_j \quad (3.47a,b)$$

where \mathbf{A}^i and \mathbf{A}_j are the contravariant and covariant base vectors, respectively. \mathbf{A}_j is obtained from Equations (3.20) and \mathbf{A}^i can be obtained from \mathbf{A}_j using Equation (3.5).

The decomposition used in Equations (3.47) is typical of classical shell theory. The use of Equations (3.47a,b) in (3.46b) will result in the following

$$y_3 = -\frac{1}{1 + w^3} w^\alpha y_\alpha \quad (3.48)$$

Basar et al. said that this equation will be used in the finite element procedure for the elimination of y_3 at the element level. After going through Basar et al. kinematic model, the following remarks can be drawn:

- The approaches used to construct the kinematic models are different, material in the present study and spatial in their study.
- The easiness in satisfying the fiber inextensibility constraint in the present model in contrast to their model where the constraint of Equation (3.48) is to be implemented at the element level

- The rotation parametrization used here is based on the rotation vector which is free from singularity however their parametrization is based on Euler angles. thus it suffers from singularity and may lead to ill-conditioning in certain situations

This ends the comparison between the two models.

By using Equation (3.44) for the kinematic model, the expressions for the in-plane and transverse shear strains will be presented, starting with the inplane strains

$$E_{\alpha\beta} = \frac{1}{2}(g_{\alpha\beta} - G_{\alpha\beta}) = \sum_{n=0}^3 \zeta^n E_{\alpha\beta}^{(n)} \quad (3.49)$$

where

$$E_{\alpha\beta}^{(0)} = \frac{1}{2} (\varphi_{,\alpha} \cdot \varphi_{,\beta} - \varphi_{o,\alpha} \cdot \varphi_{o,\beta}) \quad (3.50a)$$

$$E_{\alpha\beta}^{(1)} = \frac{1}{2} (\varphi_{,\alpha} \cdot d_{1,\beta} + \varphi_{,\beta} \cdot d_{1,\alpha} - \varphi_{o,\alpha} \cdot d_{1,\beta}^{(0)} - \varphi_{o,\beta} \cdot d_{1,\alpha}^{(0)}) \quad (3.50b)$$

$$E_{\alpha\beta}^{(2)} = \frac{1}{2} (d_{1,\alpha} \cdot d_{1,\beta} - d_{1,\alpha}^{(0)} \cdot d_{1,\beta}^{(0)}) \quad (3.50c)$$

$$E_{\alpha\beta}^{(3)} = \frac{1}{2} (\varphi_{,\alpha} \cdot d_{3,\beta} + \varphi_{,\beta} \cdot d_{3,\alpha}) \quad (3.50d)$$

then the transverse shear strain

$$E_{\alpha 3} = \frac{1}{2} (g_{\alpha 3} - G_{\alpha 3}) = \sum_{k=0,2} \zeta^k E_{\alpha 3}^{(k)} \quad (3.51)$$

where

$$E_{\alpha 3}^{(0)} = \frac{1}{2} (\varphi_{,\alpha} \cdot d_1) \quad (3.52a)$$

$$E_{\alpha 3}^{(2)} = \frac{3}{2} (\varphi_{,\alpha} \cdot d_3) \quad (3.52b)$$

The terms with ζ -power higher than three are neglected in $E_{\alpha\beta}$ and those higher than two are neglected in $E_{\alpha 3}$, and this in connection with the degree of approximation in $x_{,\alpha}$ (3rd degree) and $x_{,3}$ (second degree).

3.3.6. Stress Measures

In order to introduce expressions for the stress tensor, it is necessary to relate surface elements consisting of the same particles in the undeformed and deformed configurations.

Let

$$dX = G_k d\theta^k \quad \underline{dX} = G_l d\theta^l \quad (3.53)$$

and

$$dx = g_k d\theta^k \quad \underline{dx} = g_l d\theta^l \quad (3.54)$$

be the corresponding differentials of the position vectors in the undeformed and deformed states, respectively. The notations dX and \underline{dX} point out that $dX \neq \underline{dX}$. The surface elements NdA and nda , with N and n corresponding unit normals, spanned by the above differential vectors are determined by

$$NdA = dX \times \underline{dX} = G_k \times G_l d\theta^k d\theta^l = \sqrt{G} e_{klm} G^m d\theta^k d\theta^l \quad (3.55)$$

$$nda = dx \times dx = g_k \times g_l d\theta^k d\theta^l = \sqrt{g} e_{klm} g^m d\theta^k d\theta^l \quad (3.56)$$

where

e_{klm} represents the permutation symbol defined by the following rules

$$e_{klm} = \begin{cases} +1 & \text{if } k, l, m \text{ are an even permutation of } 1, 2, 3 \\ -1 & \text{if } k, l, m \text{ are an odd permutation of } 1, 2, 3 \\ 0 & \text{if any two indices are the number} \end{cases} \quad (3.57)$$

Multiplying the deformation gradient tensor by nda from the left we get

$$nda \cdot F = \sqrt{g} e_{klm} g^m \cdot (g_i \otimes G^i) d\theta^k d\theta^l = \sqrt{g} e_{klm} G^m d\theta^k d\theta^l \quad (3.58)$$

Comparing Equations (3.55) and (3.58), we get the following

$$NdA = \sqrt{\frac{G}{g}} n da \cdot F \quad (3.59)$$

Let the internal force acting on the differential area nda be df . The 'true' or Cauchy stress, as it is often called, is defined by the fundamental relation

$$df = dan \cdot \sigma \quad (3.60)$$

The component representation of the Cauchy stress tensor σ is

$$\sigma = \sigma^{ij} g_i \otimes g_j \quad (3.61)$$

Some alternative tensors of 'stress measures' will be introduced through their fundamental relations to the differential force vector df acting on an oriented area nda defined previously.

$$df = dan \cdot \sigma = dAN \cdot t = dAN \cdot S \cdot F^T = \sqrt{\frac{G}{g}} dan \cdot \hat{\sigma} \quad (3.62)$$

The physical interpretation of the various above 'stress' tensors can be given from the relations

$$dAN \cdot t = df \quad (3.63)$$

$$dAN \cdot S = df \cdot F^{-T} = F^{-1} \cdot df = d\hat{f} \quad (3.64)$$

$$df = dan \cdot \sigma = \sqrt{\frac{G}{g}} dan \cdot \hat{\sigma} \quad (3.65)$$

The newly introduced terms will be defined and explained each at a time. The tensor t is often referred to as the first Piola-Kirchhoff or the Piola-Lagrange stress tensor. It is derived by moving df , acting on nda , in parallel transport to the pre-image NdA in the undeformed configuration. In order to relate t to σ , Equations (3.59) and (3.60) are used to yield

$$\sqrt{\frac{G}{g}} dan \cdot F \cdot t = dan \cdot \sigma \quad (3.66)$$

Equation (3.66) implies the following relation between the Cauchy and first Piola-Kirchhoff stress tensors

$$t = \sqrt{\frac{g}{G}} F^{-1} \cdot \sigma \quad (3.67)$$

σ is symmetric, but t is in general unsymmetric. The component representation of t is

$$\mathbf{t} = t^{ij} \mathbf{G}_i \otimes \mathbf{g}_j = \sqrt{\frac{g}{G}} \sigma^{ij} \mathbf{G}_i \otimes \mathbf{g}_j \quad (3.68)$$

The tensor \mathbf{S} is often referred to as the **second Piola-Kirchhoff stress tensor**. It is derived by first creating a force vector $d\hat{\mathbf{f}}$ given by

$$d\hat{\mathbf{f}} = \mathbf{F}^{-1} \cdot d\mathbf{f} \quad (3.69)$$

and then moving $d\hat{\mathbf{f}}$ in parallel transport, on to the oriented area $Nd\mathbf{A}$ in the reference configuration. Using Equations (3.59), (3.60) and (3.64), we get

$$\sqrt{\frac{G}{g}} \mathbf{F} \cdot \mathbf{S} = \boldsymbol{\sigma} \cdot \mathbf{F}^{-T} \quad (3.70)$$

Premultiplying both terms of Equation (3.70) by \mathbf{F}^{-1} yields the expression for the second Piola-Kirchhoff stress tensor

$$\mathbf{S} = \sqrt{\frac{g}{G}} \mathbf{F}^{-1} \cdot \boldsymbol{\sigma} \cdot \mathbf{F}^{-T} = S^{ij} \mathbf{G}_i \otimes \mathbf{G}_j = \sqrt{\frac{g}{G}} \sigma^{ij} \mathbf{G}_i \otimes \mathbf{G}_j \quad (3.71)$$

It can be seen from Equation (3.71) that \mathbf{S} is symmetric

The tensor $\hat{\boldsymbol{\sigma}}$ shown in Equation (3.65) is often referred to as the **Kirchhoff stress**. It is simply a scalar $\sqrt{\frac{g}{G}}$ multiple of $\boldsymbol{\sigma}$.

The second Piola-Kirchhoff stress tensor \mathbf{S} is the work conjugate of the Green-Lagrange strain tensor \mathbf{E} whose components were described in the previous section. Together, they represent the stress and strain measures used in the Total Lagrangian

formulation. Since the second Piola Kirchhoff stresses have little physical meaning, the above transformations will be used to find Cauchy stresses whenever they are needed.

3.3.7 Constitutive Relations

3.3.7.1 General

In order to complete the formulation, we need to relate the Green-Lagrange strains to the second Piola Kirchhoff stresses through constitutive equations. This research will be limited to elastic materials. A simple and widely used elastic material description for the large deformation analysis is obtained by generalizing the linear elastic relations used for infinitesimal strains to the Total Lagrangian formulation.

$$S^{ij} = C^{ijkl} E_{kl} \quad (3.72)$$

where S^{ij} and E_{ij} are the components of the second Piola Kirchhoff stress and Green-Lagrange strain tensors, respectively, and C^{ijkl} are the components of the constant elasticity tensor. In large displacement and large rotation but small strain analysis, Equation (3.72) provides a natural material description, because the second Piola-Kirchhoff stress and Green Lagrange strain tensors are invariant under rigid body motion. Thus, only the actual straining of the material will yield an increase in the components of the stress tensor. This invariance observation implies that any material description, which has been developed for infinitesimal displacement analysis using engineering strain and stress measures, can be directly employed in large displacement and large rotation but small strain analysis. This can be achieved simply by substituting the second

Piola-Kirchhoff stress and Green Lagrange strains for the engineering stress and strain measures. We can cite the elasto-plastic and creep material models as examples.

3.3.7.2 Isotropic Material

Considering an isotropic material in three-dimensional conditions related to cartesian coordinates, we have

$$C^{ijkl} = \lambda \delta_{ij} \delta_{kl} + \mu (\delta_{ik} \delta_{jl} + \delta_{il} \delta_{jk}) \quad (3.73)$$

where λ and μ are Lamé's constants given by

$$\lambda = \frac{E\nu}{(1+\nu)(1-2\nu)} \quad \mu = G = \frac{E}{2(1+\nu)} \quad (3.74)$$

in terms of engineering constants E , ν and G . The latter constants represent respectively Young's modulus, Poisson's ratio and the shear modulus.

δ_{ij} represents the Kronecker delta.

Equation (3.73) can be generalized to curvilinear coordinates by replacing the Kronecker deltas with the proper components of the metric tensor [145]

$$C^{ijkl} = \lambda G^{ij} G^{kl} + \mu (G^{ik} G^{jl} + G^{il} G^{jk}) \quad (3.75)$$

where G^{ij} are given by Equations (3.8a).

Considering the condition of zero through the thickness stress ($S^{33}=0$), which is commonly used for shell theories, we get

$$S^{33} = C^{33\mu} E_{\mu} = C^{3333} E_{33} + C^{33mn} E_{mn} = 0 \quad , mn \neq 33 \quad (3.76)$$

From Equation (3.76), we solve for E_{33} to get

$$E_{33} = -\frac{C^{33mn}}{C^{3333}} E_{mn} \quad , mn \neq 33 \quad (3.77)$$

Substituting Equation (3.77) in the stress-strain relations of Equation (3.72), we obtain

$$S^{ij} = C^{ijkl} E_{kl} = C^{ijmn} E_{mn} + C^{ij33} E_{33} = \left(C^{ijmn} - \frac{C^{ij33} C^{33mn}}{C^{3333}} \right) E_{mn} = \bar{C}^{ijmn} E_{mn} \quad ij \neq 33 \quad , mn \neq 33 \quad (3.78)$$

where

$$\bar{C}^{ijmn} = C^{ijmn} - \frac{C^{ij33} C^{33mn}}{C^{3333}} \quad , ij \neq 33 \quad , mn \neq 33 \quad (3.79)$$

Equation (3.79) can be split into

$$\bar{C}^{\alpha\beta\rho\lambda} = C^{\alpha\beta\rho\lambda} - \frac{C^{\alpha\beta33} C^{33\rho\lambda}}{C^{3333}} \quad (3.80)$$

$$\bar{C}^{\alpha3\rho3} = C^{\alpha3\rho3} - \frac{C^{\alpha333} C^{33\rho3}}{C^{3333}} \quad (3.81)$$

Since the constitutive equations are defined with respect to the reference configuration (undeformed state), we have $\mathbf{G}^3 = \mathbf{G}_3 = \mathbf{d}_1^{(0)}$ which represents a unit vector normal to the shell midsurface. Thus, it is orthogonal to \mathbf{G}^α . Based on these conditions, Equations (3.80) and (3.81), with the help of Equations (3.74) and (3.8a), yield

$$\bar{C}^{\alpha\beta\rho\lambda} = \frac{2\lambda\mu}{\lambda + 2\mu} G^{\alpha\beta} G^{\rho\lambda} + \mu(G^{\alpha\rho} G^{\beta\lambda} + G^{\alpha\lambda} G^{\beta\rho}) \quad (3.82)$$

$$\bar{C}^{\alpha\beta\rho\beta} C^{\alpha\beta\rho\beta} = \mu G^{\alpha\beta} \quad (3.83)$$

Equations (3.82) and (3.83) can be given in terms of engineering constants E and ν as follows

$$\bar{C}^{\alpha\beta\rho\lambda} = \frac{E\nu}{1-\nu^2} G^{\alpha\beta} G^{\rho\lambda} + \frac{E}{2(1+\nu)} (G^{\alpha\rho} G^{\beta\lambda} + G^{\alpha\lambda} G^{\beta\rho}) \quad (3.84)$$

$$\bar{C}^{\alpha\beta\rho\beta} C^{\alpha\beta\rho\beta} = \frac{E}{2(1+\nu)} G^{\alpha\beta} \quad (3.85)$$

3.3.7.3. Orthotropic Lamina

A composite material is heterogeneous at the constituent material level (fibers and matrix), with properties possibly changing from point to point. A lamina is the basic building block in a laminated fiber reinforced composite. Thus, knowledge of the mechanical behavior of a lamina is essential to the understanding of laminated fiber reinforced structures. The 'macromechanical' stress-strain relationships of a lamina can be expressed in terms of average stresses and strains and effective properties of an equivalent homogeneous material. The analysis of effective composite properties in terms of constituent material properties is called 'micromechanics'.

A unidirectional composite lamina has three mutually orthogonal planes of material property symmetry (i.e. the 12, 23 and 13 planes) and is called orthotropic material. The 123 axes are referred to as the principal material coordinates since they are associated

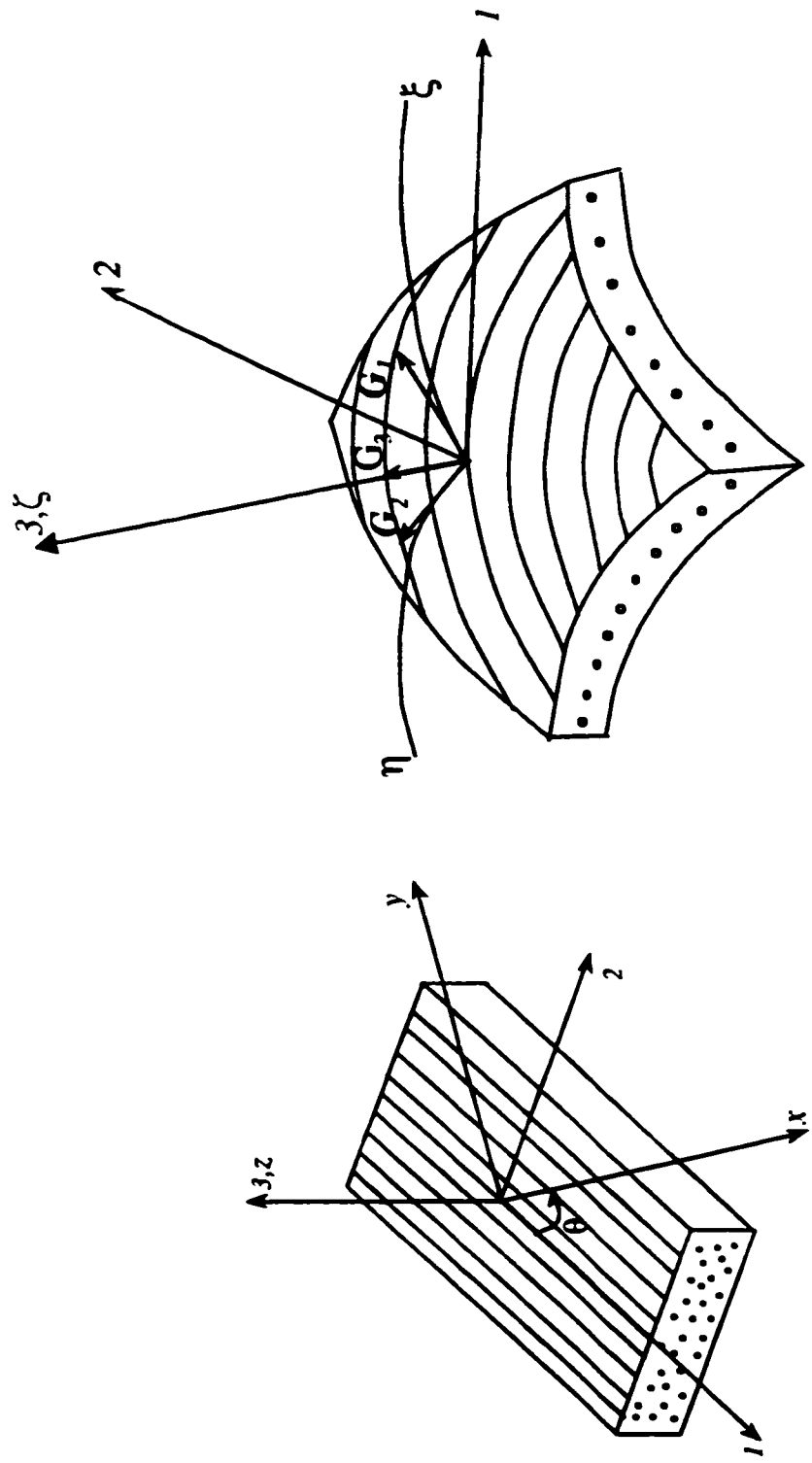


Figure 3.4 Orthotropic laminae (flat and curved) with principal and nonprincipal coordinate systems

with the reinforcement directions. Figure 3.4 shows a flat and curved orthotropic laminae with principal and non principal axes. We notice here that the angle θ between the 1 and x axes is constant for the whole flat lamina, but no such angle exist in the case of a curved lamina. For the latter case, the tangent plane at each point of the lamina contains the covariant base vectors G_1 and G_2 , which are tangent to the curvilinear coordinates ξ and η , respectively, and the local principal axes 1 and 2. The angles between G_1 and G_2 and the axes 1 and 2 may change from point to point and this adds to the complexity of curved fiber-reinforced laminates. Since the total Lagrangian formulation is based on the reference configuration, the third principal axis 3 is parallel to the third curvilinear coordinate ζ .

Our goal is to formulate a constitutive law to relate the second Piola-Kirchhoff stresses to the Green-Lagrange strains for the curved lamina. The stress-strain relations for a so-called specially orthotropic material (i.e. orthotropic material where constitutive equations are associated with material principal axes) is of the form

$$\hat{S}^{mn} = H^{mnlk} \hat{E}_k \quad (3.86)$$

or in matrix form

$$\begin{Bmatrix} \hat{S}_{11} \\ \hat{S}_{22} \\ \hat{S}_{33} \\ \hat{S}_{23} \\ \hat{S}_{31} \\ \hat{S}_{12} \end{Bmatrix} = \begin{bmatrix} H^{1111} & H^{1122} & H^{1133} & 0 & 0 & 0 \\ & H^{2222} & H^{2233} & 0 & 0 & 0 \\ & & H^{3333} & 0 & 0 & 0 \\ & & & H^{2323} & 0 & 0 \\ & SYM & & & H^{3131} & 0 \\ & & & & & H^{1212} \end{bmatrix} \begin{Bmatrix} \hat{E}_{11} \\ \hat{E}_{22} \\ \hat{E}_{33} \\ 2\hat{E}_{23} \\ 2\hat{E}_{31} \\ 2\hat{E}_{12} \end{Bmatrix} \quad (3.87)$$

The matrix H containing the coefficients H^{mnlk} is called the stiffness matrix. It has 12

nonzero elastic coefficients, which depend on nine independent constants.

In most composites, the fiber packing arrangement is statistically random in nature so that the properties are nearly the same in the direction perpendicular to the fibers (i.e. the properties along direction 2 are the same as those along direction 3). and the material is named transversally isotropic. For such a material, we would expect the following

$$H^{2222} = H^{3333} ; H^{1122} = H^{1133} ; H^{3131} = H^{1212} ; H^{2323} = \frac{1}{2}(H^{2222} - H^{2233}) \quad (3.88)$$

We note now that there are still 12 nonzero elastic constants, but that only five are independent.

The Green-Lagrange strains can be expressed in terms of the second Piola-Kirchhoff stresses by

$$\hat{E}_{ij} = D_{ijkl} \hat{S}^{kl} \quad (3.89)$$

The matrix D composed of the coefficients D_{ijkl} is the compliance matrix.

When a material is characterized experimentally, the so-called 'engineering constants' such as Young's modulus, shear modulus and Poisson's ratio are usually measured instead of the coefficients H^{ijkl} or D_{ijkl} . Considering a three-dimensional state of stress associated with the material principal axes 123, the compliance matrix D is given by

$$D = \begin{bmatrix} \frac{1}{E_1} & -\frac{\nu_{21}}{E_2} & -\frac{\nu_{31}}{E_3} & 0 & 0 & 0 \\ -\frac{\nu_{12}}{E_1} & \frac{1}{E_2} & -\frac{\nu_{32}}{E_3} & 0 & 0 & 0 \\ -\frac{\nu_{12}}{E_1} & -\frac{\nu_{23}}{E_2} & \frac{1}{E_3} & 0 & 0 & 0 \\ 0 & 0 & 0 & \frac{1}{G_{23}} & 0 & 0 \\ 0 & 0 & 0 & 0 & \frac{1}{G_{31}} & 0 \\ 0 & 0 & 0 & 0 & 0 & \frac{1}{G_{12}} \end{bmatrix} \quad (3.90)$$

where

E_i is Yong's modulus along direction i

$\nu_{ij} = -\frac{\hat{E}_{ij}}{\hat{E}_{ii}}$ is Poisson's ratio; it represents the ratio of the strain in the j direction to the strain in the perpendicular i direction when the applied stress is in the i direction.

G_{ij} is the shear modulus associated with plane ij .

The symmetry of the compliance matrix implies that

$$\frac{\nu_{ij}}{E_i} = \frac{\nu_{ji}}{E_j} \quad i, j = 1, 2, 3 \quad (3.91)$$

Thus, there are 3 reciprocal relations that must be satisfied for an orthotropic material. Moreover, only ν_{12}, ν_{13} and ν_{23} need be further considered since ν_{21}, ν_{31} and ν_{32} can be expressed in terms of the first mentioned Poisson's ratios and the Young moduli associated. The elastic behavior of an orthotropic material can be described by the following nine independent constants:

3 Young moduli E_1, E_2, E_3

3 Poisson's ratio's $\nu_{12}, \nu_{13}, \nu_{23}$

3 Shear moduli G_{12}, G_{13}, G_{23}

If the material is transversally isotropic, which is the case in fiber reinforced shells, the subscripts 2 and 3 can be interchanged and we have

$$G_{13} = G_{12}, \quad E_2 = E_3, \quad \nu_{12} = \nu_{13}, \quad \nu_{23} = \nu_{32} \quad (3.92)$$

In addition, the familiar relationship among the isotropic engineering constants [47,146,147] is now valid for the engineering constants associated with the 23 plane. so that

$$G_{23} = \frac{E_2}{2(1+\nu_{32})} \quad (3.93)$$

The five independent constants can now be $E_1, E_2, \nu_{12}, \nu_{23}$ and G_{12} .

Considering now the condition of zero through the thickness normal stress ($\hat{S}^{33} = 0$), which is commonly assumed in shell theories, the strain-stress relations will reduce to

$$\begin{Bmatrix} \hat{E}_{11} \\ \hat{E}_{22} \\ 2\hat{E}_{12} \\ 2\hat{E}_{13} \\ 2\hat{E}_{23} \end{Bmatrix} = \begin{bmatrix} \frac{1}{E_1} & -\frac{\nu_{12}}{E_1} & 0 & 0 & 0 \\ & \frac{1}{E_2} & 0 & 0 & 0 \\ & & \frac{1}{G_{12}} & 0 & 0 \\ & \text{SYM} & & \frac{1}{G_{13}} & 0 \\ & & & & \frac{1}{G_{23}} \end{bmatrix} \begin{Bmatrix} S^{11} \\ S^{22} \\ S^{12} \\ S^{13} \\ S^{23} \end{Bmatrix} \quad (3.94)$$

by inverting Equation (3.94), we get the stress-strain relations given by

$$\hat{S}^{mn} = \bar{H}^{mnkl} \hat{E}_k \quad , \quad mn \neq 33 \quad , \quad kl \neq 33 \quad (3.95)$$

where \bar{H}^{mnkl} are the reduced stiffness coefficients. Equation (3.95) can be represented in matrix form as

$$\begin{Bmatrix} \hat{S}^{11} \\ \hat{S}^{22} \\ \hat{S}^{12} \\ \hat{S}^{13} \\ \hat{S}^{23} \end{Bmatrix} = \begin{bmatrix} \bar{H}^{1111} & \bar{H}^{1122} & 0 & 0 & 0 \\ \bar{H}^{2211} & \bar{H}^{2222} & 0 & 0 & 0 \\ 0 & 0 & \bar{H}^{1212} & 0 & 0 \\ 0 & 0 & 0 & \bar{H}^{1313} & 0 \\ 0 & 0 & 0 & 0 & \bar{H}^{2323} \end{bmatrix} \begin{Bmatrix} \hat{E}^{11} \\ \hat{E}^{22} \\ 2\hat{E}^{12} \\ 2\hat{E}^{13} \\ 2\hat{E}^{23} \end{Bmatrix} \quad (3.96)$$

where

$$\begin{aligned} \bar{H}^{1111} &= \frac{E_1}{1 - \nu_{12}\nu_{21}} \quad , \quad \bar{H}^{1122} = \bar{H}^{2211} = \frac{\nu_{12}E_2}{1 - \nu_{12}\nu_{21}} = \frac{\nu_{21}E_1}{1 - \nu_{12}\nu_{21}} \\ \bar{H}^{2222} &= \frac{E_2}{1 - \nu_{12}\nu_{21}} \quad , \quad \bar{H}^{1212} = G_{12} \quad , \quad \bar{H}^{1313} = G_{13} \quad , \quad \bar{H}^{2323} = G_{23} \end{aligned} \quad (3.97)$$

Equations (3.96) represent the final form of the stress-strain relations with respect to the local principal axes 123 at each point of a lamina.

Composite structures are more likely to be in the form of laminates consisting of multiple laminae, or plies, oriented in the desired directions and bonded together in a structural unit. It is assumed that the individual laminae are perfectly bonded together so as to behave as a unitary, nonhomogeneous, anisotropic shell. Interfacial slip is not allowed and the interfacial bonds are not allowed to deform in shear, which supports the continuity of the displacement field across laminae interfaces. As we go from layer to layer along the thickness direction, the directions of the principal material axes will vary, but we need to refer all the constitutive equations to the same local coordinate system.

This system will be the laminate curvilinear coordinate system (ξ, η, ζ) with its respective covariant base vectors $(\mathbf{G}_1, \mathbf{G}_2, \mathbf{G}_3)$ as shown in Fig. 3.4. At each point of a layer L ($L=1, N$), where N is the total number of layers composing the laminate, the principal material axes $(123)_L$ have corresponding unit bases $(\hat{\mathbf{e}}_1, \hat{\mathbf{e}}_2, \hat{\mathbf{e}}_3)_L$. The transformation of Equation (3.95) to laminate coordinates (ξ, η, ζ) gives

$$\mathbf{S}^{\hat{ij}} = \mathbf{C}_L^{\hat{ijkl}} \mathbf{E}_{kl} \quad (3.98)$$

where

$S^{\hat{ij}}$ represent the contravariant components of the second Piola-Kirchhoff stress tensor

E_{ij} represent the covariant components of the Green-Lagrange strain tensor

These covariant and contravariant components can be shown using the dyadic notation for representing the Piola-Kirchhoff stress and Green-Lagrange tensors.

$$\mathbf{S} = \hat{S}^{\hat{ij}} \hat{\mathbf{e}}_i \otimes \hat{\mathbf{e}}_j = S^{\hat{ij}} \mathbf{G}_i \otimes \mathbf{G}_j \quad (3.99)$$

$$\mathbf{E} = \hat{E}_{\hat{ij}} \hat{\mathbf{e}}_i \otimes \hat{\mathbf{e}}_j = E_{\hat{ij}} \mathbf{G}^i \otimes \mathbf{G}^j \quad (3.100)$$

The same representation can be done for the stiffness tensors $\bar{\mathbf{H}}_L$ and \mathbf{C}_L giving

$$\bar{\mathbf{H}}_L = \bar{H}_L^{\hat{ijkl}} \hat{\mathbf{e}}_i \otimes \hat{\mathbf{e}}_j \otimes \hat{\mathbf{e}}_k \otimes \hat{\mathbf{e}}_l \quad (3.101)$$

$$\mathbf{C}_L = C_L^{\hat{ijkl}} \mathbf{G}_i \otimes \mathbf{G}_j \otimes \mathbf{G}_k \otimes \mathbf{G}_l \quad (3.102)$$

The subscript L in the above equations refer to layer L . It should be mentioned here that

for cartesian coordinates, which is the case for 123 axes, there is no difference between covariant and contravariant components of a tensor. Actually, the two tensors \overline{H}_L and C_L are identical except that they are represented in two different coordinate systems. Thus, we can equate Equations (3.101) and (3.102)

$$\overline{H}_L = \overline{H}_L^{ijkl} \hat{e}_i \otimes \hat{e}_j \otimes \hat{e}_k \otimes \hat{e}_l = C_L = C_L^{ijkl} G_i \otimes G_j \otimes G_k \otimes G_l \quad (3.103)$$

The transformation equations between the components \overline{H}_L^{mnsr} and C_L^{ijkl} can be found by simply expressing the unit base vectors ($\hat{e}_i, i=1,2,3$) in terms of the covariant base vectors ($G_k, k=1,2,3$). This expression is given by

$$\hat{e}_i = (\hat{e}_i \cdot G^k) G_k \quad (3.104)$$

where $G^k, k=1,2,3$ are the reciprocal bases given by the standard relation $G^i \cdot G_k = \delta_k^i$.

Thus, the first part of Equation (3.103) can be written as

$$\overline{H}_L^{mnsr} (\hat{e}_m \cdot G^i) (\hat{e}_n \cdot G^j) (\hat{e}_s \cdot G^k) (\hat{e}_r \cdot G^l) G_i \otimes G_j \otimes G_k \otimes G_l \quad (3.105)$$

By comparing Equations (3.105) and (3.102), we find the sought expression

$$C_L^{ijkl} = (G^i \cdot \hat{e}_m) (G^j \cdot \hat{e}_n) (G^k \cdot \hat{e}_s) (G^l \cdot \hat{e}_r) \overline{H}_L^{mnsr} \quad (3.106)$$

Using Equation (3.106), we provide the coefficients C^{ijkl} in detailed forms

$$C_L^{1111} = C_{11}^4 \overline{H}_L^{1111} + 2 C_{11}^2 C_{12}^2 (\overline{H}_L^{1122} + 2 \overline{H}_L^{1212}) + C_{12}^4 \overline{H}_L^{2222}$$

$$C_L^{1122} = C_{11}^2 C_{21}^2 \overline{H}_L^{1111} + (C_{11}^2 C_{22}^2 + C_{12}^2 C_{21}^2) \overline{H}_L^{1122} + 4 C_{11} C_{22} C_{12} C_{21} \overline{H}_L^{1212} + C_{12}^2 C_{22}^2 \overline{H}_L^{2222}$$

$$\begin{aligned}
C_L^{1112} &= C_{11}^3 C_{21} \bar{H}_L^{1111} + (C_{11}^2 C_{22} C_{12} + C_{11} C_{12}^2 C_{21}) (\bar{H}_L^{1122} + 2\bar{H}_L^{1212}) + C_{12}^3 C_{22} \bar{H}_L^{2222} \\
C_L^{2222} &= C_{21}^4 \bar{H}_L^{1111} + 2C_{21}^2 C_{22}^2 (\bar{H}_L^{1122} + 2\bar{H}_L^{1212}) + C_{22}^4 \bar{H}_L^{2222} \\
C_L^{2212} &= C_{21}^3 C_{11} \bar{H}_L^{1111} + (C_{11} C_{21} C_{22}^2 + C_{12} C_{21}^2 C_{22}) (\bar{H}_L^{1122} + 2\bar{H}_L^{1212}) + C_{12} C_{22}^3 \bar{H}_L^{2222} \\
C_L^{1212} &= C_{11}^2 C_{21}^2 \bar{H}_L^{1111} + 2C_{11} C_{12} C_{21} C_{22} \bar{H}_L^{1122} + (C_{11}^2 C_{22}^2 + 2C_{11} C_{12} C_{21} C_{22} + C_{12}^2 C_{21}^2) \bar{H}_L^{1212} \\
&\quad + C_{12}^2 C_{22}^2 \bar{H}_L^{2222} \\
C_L^{1313} &= C_{11}^2 \bar{H}_L^{1313} + C_{12}^2 \bar{H}_L^{2323} \\
C_L^{1323} &= C_{11} C_{21} \bar{H}_L^{1313} + C_{12} C_{22} \bar{H}_L^{2323} \\
C_L^{2323} &= C_{21}^2 \bar{H}_L^{1313} + C_{22}^2 \bar{H}_L^{2323} \\
C_L^{1113} &= C_L^{1123} = C_L^{2213} = C_L^{2223} = C_L^{1215} = C_L^{1223} = 0
\end{aligned} \tag{3.107}$$

where

$$C_{11} = G^1 \cdot \hat{e}_1 \quad , \quad C_{12} = G^1 \cdot \hat{e}_2 \quad , \quad C_{21} = G^2 \cdot \hat{e}_1 \quad , \quad C_{22} = G^2 \cdot \hat{e}_2 \tag{3.108}$$

The stiffness tensor \mathbf{C}_L , whose components are given in Equation (3.106), is symmetric.

Thus, only the elements of the upper triangular part of this matrix are given in Equations

(3.107). The rest of the coefficients can be deduced from symmetry considerations.

CHAPTER 4

STATIC FORMULATION

4.1 Introduction

In the previous chapter, a shell theory was presented based on a proposed kinematic model, which uses explicitly the rotation tensor and allows for TOSDT and finite rotations. Based on this model, Green-Lagrange strains were derived and reduced constitutive relations relating them to their work-conjugate second Piola-Kirchhoff stresses were defined with respect to laminate curvilinear coordinates. The purpose of this chapter is to cast this theory in the finite element framework so that it can be used to analyze laminated shell type structures subjected to static loads. It starts by applying the principle of virtual work to derive the weak form of the equations of motion, which are the equilibrium equations of motion in the static case. These equations are reduced to their two-dimensional form after performing the integration through the thickness analytically. The quantities involved in the virtual work expression such as the strain variations and variation of kinematic variables are evaluated. The finite element method is introduced by first approximating the middle surface area by a set of four noded

quadrilateral elements, then introducing interpolation functions at the element level to approximate kinematic variables. The constant part of the transverse shear strain is approximated using the Assumed Natural Strain (ANS) concept [4,5]. The configuration update, which is important in the incremental/iterative solution procedure, is addressed where a geometrically exact configuration update procedure based on the exponential mapping is developed. The discretization of the equations of equilibrium yields a system of highly nonlinear algebraic equations whose solution iteratively by the Newton-Raphson method requires a linearization. A consistent linearization of these equations yields the elemental tangent material and geometric stiffness matrices.

4.2 Principle of Virtual Work

The numerical treatment within the finite element framework is based on the principle of virtual work. This principle, which must be restricted to purely mechanical phenomena, states that the virtual work of a system of equilibrium forces vanishes on compatible virtual displacements. It was shown by Zienkiewicz and Taylor [148] that the virtual work statement is precisely the weak form of the equilibrium equations and is valid for linear and nonlinear stress-strain relations. The Finite Element Method (FEM) based on this principle may be considered as a Galerkin formulation of the weighted residual process applied to the equilibrium equations. The principle of virtual work can be expressed as

$$\delta w = \delta w_I - \delta w_E = 0 \quad (4.1)$$

where δw_I is the virtual work of the internal forces and δw_E the virtual work of the external forces.

4.2.1 Virtual Work of Internal Forces

Since we are concerned with the Total Lagrangian formulation, the conjugate tensors giving the internal virtual work are the second Piola-Kirchhoff stresses S^{ij} and the virtual Green-Lagrange strains δE_{ij} . The virtual work of the internal forces can be expressed as

$$\delta w_I = \int_{v^0} S^{ij} \delta E_{ij} dv^0 \quad (4.2)$$

The integration in Equation (4.2) is carried out over the undeformed shell body. dv^0 is the volume element given by

$$dv^0 = \sqrt{G} d\xi d\eta d\zeta \quad (4.3)$$

G is given by Equation (3.23). Making use of the determinant A of the metric tensor of the reference surface Ω^0 given in Equation (3.21), dv^0 becomes

$$dv^0 = \sqrt{\frac{G}{A}} \sqrt{A} d\xi d\eta d\zeta = \mu d\Omega^0 d\zeta \quad (4.4)$$

where

$$\mu = \sqrt{\frac{G}{A}} \quad , \quad d\Omega^0 = \sqrt{A} d\xi d\eta \quad (4.5)$$

With the help of Equations (3.49) and (3.51), the term $S^{ij} \delta E_{ij}$ can be written in the following form

$$S^{ij} \delta E_{ij} = S^{\alpha\beta} \delta E_{\alpha\beta} + 2S^{\alpha 3} \delta E_{\alpha 3} = S^{\alpha\beta} \sum_{n=0}^3 \zeta^n \delta E_{\alpha\beta}^{(n)} + 2S^{\alpha 3} \sum_{k=0,2} \zeta^k \delta E_{\alpha 3}^{(k)} \quad (4.6)$$

Substituting Equations (4.6) and (4.4) into Equation (4.2), we get

$$\delta W_I = \iint_{\Omega^c} \left(\sum_{n=0}^3 m^{\alpha\beta} \delta E_{\alpha\beta}^{(n)} + 2 \sum_{k=0,2} Q^\alpha \delta E_{\alpha 3}^{(k)} \right) d\Omega^c \quad (4.7)$$

where the stress resultants $m^{\alpha\beta}$ and Q^α are given by

$$m^{\alpha\beta} = \int_{-h/2}^{h/2} \mu S^{\alpha\beta} \zeta^n d\zeta, \quad n = 0,1,2,3 \quad (4.8)$$

$$Q^\alpha = \int_{-h/2}^{h/2} \mu S^{\alpha 3} \zeta^k d\zeta, \quad k = 0,2 \quad (4.9)$$

We will elaborate more on the stress resultants by using the constitutive Equation (3.98)

with Equations (3.49) and (3.51)

$$\begin{aligned} m^{\alpha\beta} &= \int_{-h/2}^{h/2} \mu C^{\alpha\beta\rho\lambda} E_{\rho\lambda} \zeta^n d\zeta = \sum_{L=1}^{NL} \int_{h_{L-1}}^{h_L} \mu C_L^{\alpha\beta\rho\lambda} \left(\sum_{i=0}^3 \zeta^i E_{\rho\lambda}^{(i)} \right) \zeta^n d\zeta \\ &= \sum_{i=0}^3 C^{\alpha\beta\rho\lambda} E_{\rho\lambda}^{(i)}, \quad n = 0,1,2,3 \end{aligned} \quad (4.10)$$

where

$$C^{\alpha\beta\rho\lambda} = \sum_{L=1}^{NL} \left(\int_{h_{L-1}}^{h_L} \mu C_L^{\alpha\beta\rho\lambda} \zeta^k d\zeta \right), \quad k = 0,1,2,\dots,6 \quad (4.11)$$

h_{L-1} and h_L are the limits of integration for layer L .

$$Q^\alpha = 2 \int_{-h/2}^{h/2} \mu C^{\alpha 3\rho 3} E_{\rho 3} \zeta^k d\zeta = \sum_{L=1}^{NL} \int_{h_{L-1}}^{h_L} \mu C_L^{\alpha 3\rho 3} \left(\sum_{j=0,2} \zeta^j E_{\rho 3}^{(j)} \right) \zeta^k d\zeta$$

$$= \sum_{j=0,2}^{j+k} \bar{C}^{\alpha 3 \rho 3} \left(2 \bar{E}_{\rho 3}^{(j)} \right) , \quad k = 0, 2 \quad (4.12)$$

where

$$\bar{C}^m{}^{\alpha 3 \rho 3} = \sum_{L=1}^{NL} \left(\int_{h_{L-1}}^{h_L} \mu C_L^{\alpha 3 \rho 3} \zeta^m d\zeta \right) , \quad m = 0, 2, 4 \quad (4.13)$$

The coefficients $\bar{C}^k{}^{\alpha \beta \rho \lambda}$ and $\bar{C}^m{}^{\alpha 3 \rho 3}$ can be computed explicitly or numerically and this will be based on the assumptions made.

Case 1: The metric G of the laminate will be approximated by that of the reference surface Ω° (i.e. A).

$$G_{\alpha\beta} = A_{\alpha\beta} \quad , \quad \mu = 1 \quad (4.14)$$

The coefficients $C_{\alpha\beta} = (G^\alpha \cdot \hat{e}_\beta)$ are constant within each layer, thus Equations (4.11) and (4.13) become

$$\bar{C}^k{}^{\alpha \beta \rho \lambda} = \sum_{L=1}^{NL} C_L^{\alpha \beta \rho \lambda} \frac{h_L^{k+1} - h_{L-1}^{k+1}}{k+1} , \quad k = 0, 1, 2, \dots, 6 \quad (4.15)$$

$$\bar{C}^m{}^{\alpha 3 \rho 3} = \sum_{L=1}^{NL} C_L^{\alpha 3 \rho 3} \frac{h_L^{k+1} - h_{L-1}^{k+1}}{k+1} , \quad m = 0, 2, 4 \quad (4.16)$$

Case 2: The metric will be taken as constant within each layer and equated to the metric of the middle surface of that layer.

$$\mu_L = \sqrt{\frac{G_L}{A}} \quad ; \quad \bar{\zeta}_L = \frac{h_L + h_{L-1}}{2} , \quad L = 1, 2, \dots, NL \quad (4.17)$$

$\bar{\zeta}_L$ is the coordinate of the middle surface of layer L .

$${}^k C^{\alpha\beta\rho\lambda} = \sum_{L=1}^{NL} \mu_L C_L^{\alpha\beta\rho\lambda} \frac{h_L^{k+1} - h_{L-1}^{k+1}}{k+1}, \quad k=1,2,\dots,6 \quad (4.18)$$

$${}^m C^{\alpha\beta\rho\lambda} = \sum_{L=1}^{NL} \mu_L C_L^{\alpha\beta\rho\lambda} \frac{h_L^{k+1} - h_{L-1}^{k+1}}{k+1}, \quad m=0,2,4 \quad (4.19)$$

Case 3: In this case a direct numerical integration will be performed using Equations (4.11) and (4.13) with at least one Gauss point per layer.

4.2.2 Virtual Work of External Forces

The virtual work of the external loads consists of the virtual work of the traction forces, including concentrated forces, on the top and bottom shell surfaces at $\left(\zeta = \pm \frac{h}{2}\right)$ plus the virtual work of the traction forces on the edge surface plus the virtual work of the body forces. In equation form, we get

$$\begin{aligned} \delta W_E = & \int_{\Omega} (\sqrt{g} g^3 \cdot \sigma) \cdot (\delta \varphi + \zeta \delta d_1 + \zeta^3 \delta d_3) \Big|_{\zeta=-\frac{h}{2}}^{\zeta=\frac{h}{2}} d\xi d\eta + \int_{\Omega} \int_{-\frac{h}{2}}^{\frac{h}{2}} dm B \cdot (\delta \varphi + \zeta \delta d_1 + \zeta^3 \delta d_3) \\ & + \int_{\partial\Omega \times \left[\frac{h}{2}, \frac{h}{2}\right]} (nda \cdot \sigma) \cdot (\delta \varphi + \zeta \delta d_1 + \zeta^3 \delta d_3) \end{aligned} \quad (4.20)$$

where

$\sqrt{g} g^3 \Big|_{\zeta=-\frac{h}{2}}^{\zeta=\frac{h}{2}}$ represents the area elements on the top and bottom shell surfaces in the

deformed state (Figure 4.1 shows the area element at the top of the shell surface)

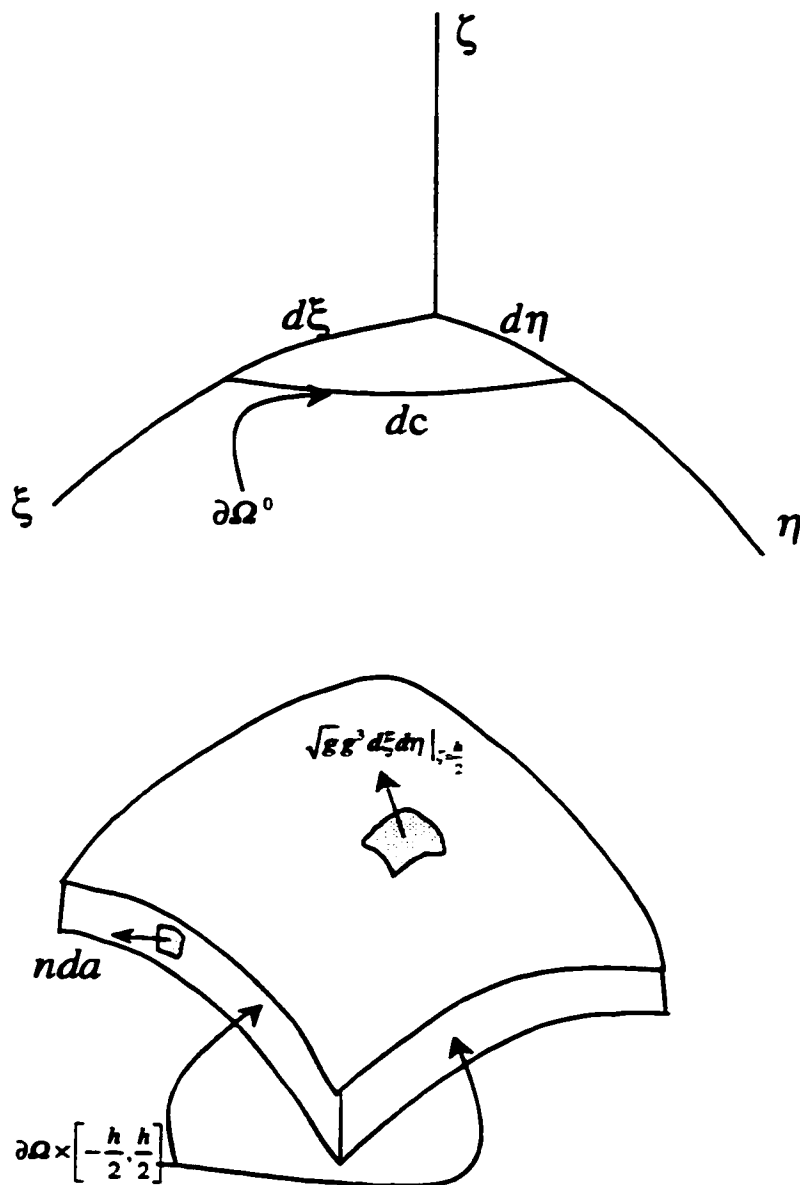


Figure 4.1 Shell bounding surface in the deformed state and bounding curve of the reference surface in the reference state

nda is an area element on the bounding surface $\partial\Omega \times \left[-\frac{h}{2}, \frac{h}{2}\right]$ as shown in Figure 4.1

$\delta\varphi + \zeta\delta d_1 + \zeta^3\delta d_3$, represents the displacement variation at the corresponding point

B represents body forces per unit mass

dm represents the mass of a volume element dv^0 (in the reference configuration) or dv (in the current configuration); it is given by

$$dm = \rho^0 dv^0 = \rho dv \quad (4.21)$$

where

ρ^0 and ρ are mass per unit volume in the initial and current configurations, respectively.

Since we are dealing, in this study, with concentrated external forces whose virtual work expression is simple, The expression of the virtual work of external forces will not be detailed any further.

4.2.3 Variation of Strain Measures

The expression of the virtual work of internal forces, shown in Equation (4.7), depends on the variation of the strain measures. Taking the variation of Equations (3.50) and (3.52), which represent the expressions of the inplane and transverse Green-Lagrange strains, we get

$$\delta E_{\alpha\beta}^{(0)} = \frac{1}{2} (\delta\varphi_{,\alpha} \cdot \varphi_{,\beta} + \varphi_{,\alpha} \cdot \delta\varphi_{,\beta}) \quad (4.22a)$$

$$\delta E_{\alpha\beta}^{(1)} = \frac{1}{2} (\delta\varphi_{,\alpha} \cdot d_{1,\beta} + \varphi_{,\alpha} \cdot \delta d_{1,\beta} + \delta\varphi_{,\beta} \cdot d_{1,\alpha} + \varphi_{,\beta} \cdot \delta d_{1,\alpha}) \quad (4.22b)$$

$$\delta E_{\alpha\beta}^{(2)} = \frac{1}{2} (\delta d_{1,\alpha} \cdot d_{1,\beta} + d_{1,\alpha} \cdot \delta d_{1,\beta}) \quad (4.22c)$$

$$\delta E_{\alpha\beta}^{(3)} = \frac{1}{2} (\delta \varphi_{,\alpha} \cdot d_{3,\beta} + \varphi_{,\alpha} \cdot \delta d_{3,\beta} + \delta \varphi_{,\beta} \cdot d_{3,\alpha} + \varphi_{,\beta} \cdot \delta d_{3,\alpha}) \quad (4.22d)$$

$$\delta E_{\alpha 3}^{(0)} = \frac{1}{2} (\delta \varphi_{,\alpha} \cdot d_1 + \varphi_{,\alpha} \cdot \delta d_1) \quad (4.23a)$$

$$\delta E_{\alpha 3}^{(2)} = \frac{3}{2} (\delta \varphi_{,\alpha} \cdot d_3 + \varphi_{,\alpha} \cdot \delta d_3) \quad (4.23b)$$

It can be seen from Equations (4.22a,b,c,d) and (4.23a,b) that the strain measure variations are based on the variation of the kinematic quantities φ , d_1 and d_3 which will be considered next.

4.2.4 Variation of Kinematic Variables

The displacement of a point on the middle surface is given by

$$\mathbf{u}(\xi, \eta) = \boldsymbol{\varphi}(\xi, \eta) - \boldsymbol{\varphi}_o(\xi, \eta) \quad (4.24)$$

Then

$$\delta \boldsymbol{\varphi} = \delta \mathbf{u} \quad (4.25)$$

For the variation of the vector d_1 we use Equation (3.28a)

$$\delta d_1 = \delta R E_3 = R R^T \delta R E_3 = R \delta \hat{\boldsymbol{\psi}} E_3 = R(\delta \boldsymbol{\psi} \times E_3) \quad (4.26)$$

where

$$\delta \hat{\boldsymbol{\psi}} = R^T \delta R \quad (4.27)$$

$\delta \hat{\boldsymbol{\psi}}$ represents a skew-symmetric matrix with $\delta \boldsymbol{\psi}$ as its axial vector.

For d_3 , we use Equation (3.28c) to get

$$\delta d_3 = \delta R D_3 + R \delta D_3 = R R^T \delta R D_3 + R \delta D_3 = R[\delta \psi \times D_3 + \delta D_3] \quad (4.28)$$

Our goal now is to find a relation between $\delta \psi$ and θ which represents our primary variable in the explicit representation of R . Using Equations (3.22b) and (4.27), and after some manipulations we get

$$\delta \hat{\psi} = \frac{\sin(\|\theta\|)}{\|\theta\|} \delta \hat{\theta} - \frac{1 - \cos(\|\theta\|)}{\|\theta\|} [\delta \theta \otimes e - e \otimes \delta \theta] + \frac{\|\theta\| - \sin(\|\theta\|)}{\|\theta\|} (\delta \theta \cdot e) \hat{e} \quad (4.29)$$

where

$e = \frac{\theta}{\|\theta\|}$ is a unit vector along the rotation axis θ

\hat{e} is a skew-symmetric matrix with e as its axial vector

$\delta \hat{\theta}$ is a skew-symmetric matrix with $\delta \theta$ as its axial vector

From Equation (4.29) we deduce the relation between the axial vectors $\delta \psi$ and $\delta \theta$

$$\delta \psi = \left[\frac{\sin(\|\theta\|)}{\|\theta\|} I - \frac{1 - \cos(\|\theta\|)}{\|\theta\|} \hat{e} + \frac{\|\theta\| - \sin(\|\theta\|)}{\|\theta\|} e \otimes e \right] \delta \theta = T(\theta) \delta \theta \quad (4.30)$$

The same expression is reported by Ibrahimbegovic [113].

In our case, the explicit representation is used for the incremental rotation and not for the total one, i.e. the above relation is needed at the limit when $\theta \rightarrow 0$. In this case Equation (4.30) reduces to the simple form

$$\delta \psi = \delta \theta \quad (4.31)$$

Substituting Equation (4.31) into Equation (4.26) we get

$$\delta \mathbf{d}_1 = \mathbf{R}(\delta \boldsymbol{\theta} \times \mathbf{E}_3) = \mathbf{R} \delta \mathbf{D}_1 \quad (4.32)$$

where

$$\delta \mathbf{D}_1 = \delta \boldsymbol{\theta} \times \mathbf{E}_3 \quad (4.33)$$

In the case of shells where there is no rotation about the normal (drilling rotation), $\delta \boldsymbol{\theta}$ will lie in the plane formed by \mathbf{E}_1 and \mathbf{E}_2 (material representation) and admits the following decomposition

$$\delta \boldsymbol{\theta} = \delta \theta^1 \mathbf{E}_1 + \delta \theta^2 \mathbf{E}_2 \quad (4.34)$$

From Equation (4.33) we see that $\delta \mathbf{D}_1$ is also normal to \mathbf{E}_3 ; thus

$$\delta \mathbf{D}_1 = \delta D_1^1 \mathbf{E}_1 + \delta D_1^2 \mathbf{E}_2 \quad (4.35)$$

Based on Equations (4.33) and (4.34) we find that

$$\delta \boldsymbol{\theta} = \mathbf{E}_3 \times \delta \mathbf{D}_1 \quad (4.36)$$

The variation of \mathbf{d}_3 becomes

$$\delta \mathbf{d}_3 = -(\mathbf{d}_1 \otimes \mathbf{d}_3) \bar{\mathbf{R}} \delta \mathbf{D}_1 + \bar{\mathbf{R}} \delta \mathbf{D}_3 \quad (4.37)$$

$\bar{\mathbf{R}}$ is a matrix containing the first two columns of the rotation matrix \mathbf{R} .

4.2.5. Matrix Formulation of The Internal Virtual Work

The matrix formulation of the virtual work of the internal forces is useful to get the equations in a compact way, especially in the implementation within the finite element method. Thus, we rewrite Equation (4.7) of the internal virtual work using matrix

notation

$$\delta w_I = \int_{\Omega^0} \left(\sum_{n=0}^3 \left\{ \delta \boldsymbol{\varepsilon}^{(n)} \right\}^T \left\{ \boldsymbol{m}^{(n)} \right\} + \sum_{k=0,2} \left\{ \delta \boldsymbol{\gamma}^{(k)} \right\}^T \left\{ \boldsymbol{Q}^{(k)} \right\} \right) d\Omega^0 \quad (4.38)$$

where

$$\left\{ \boldsymbol{m}^{(n)} \right\} = \sum_{i=0}^3 \left[\boldsymbol{C}_p^{n+i} \right] \left\{ \boldsymbol{\varepsilon}^{(i)} \right\}, \quad n=0,1,2,3 \quad (4.39)$$

$$\left[\boldsymbol{C}_p^k \right] = \begin{bmatrix} \boldsymbol{C}^k_{1111} & \boldsymbol{C}^k_{1122} & \boldsymbol{C}^k_{1112} \\ \boldsymbol{C}^k_{2211} & \boldsymbol{C}^k_{2222} & \boldsymbol{C}^k_{2212} \\ \boldsymbol{C}^k_{1211} & \boldsymbol{C}^k_{1222} & \boldsymbol{C}^k_{1212} \end{bmatrix}, \quad k=0,1,2,\dots,6, \quad \left\{ \boldsymbol{\varepsilon}^{(i)} \right\} = \begin{Bmatrix} \boldsymbol{E}_{11}^{(i)} \\ \boldsymbol{E}_{22}^{(i)} \\ 2\boldsymbol{E}_{12}^{(i)} \end{Bmatrix} \quad (4.40)$$

$$\left\{ \boldsymbol{Q}^{(k)} \right\} = \sum_{j=0,2} \left[\boldsymbol{C}_s^{k+j} \right] \left\{ \boldsymbol{\gamma}^{(j)} \right\}, \quad k=0,2 \quad (4.41)$$

$$\left[\boldsymbol{C}_s^m \right] = \begin{bmatrix} \boldsymbol{C}^m_{1313} & \boldsymbol{C}^m_{1323} \\ \boldsymbol{C}^m_{2313} & \boldsymbol{C}^m_{2323} \end{bmatrix}, \quad m=0,2,4, \quad \left\{ \boldsymbol{\gamma}^{(j)} \right\} = \begin{Bmatrix} 2\boldsymbol{E}_{13}^{(j)} \\ 2\boldsymbol{E}_{23}^{(j)} \end{Bmatrix} \quad (4.42)$$

From the variations of the strain measures and the kinematic variables presented in the previous sections, we deduce the strain-displacement operators, which are given by

$$\left\{ \delta \boldsymbol{\varepsilon}^{(o)} \right\} = \left[\boldsymbol{B}_p^{(o)} \right] \left\{ \delta \boldsymbol{\Phi} \right\} = \begin{bmatrix} (\boldsymbol{\varphi}_{.1})^T \frac{\partial}{\partial \xi^1} & \boldsymbol{O}_{1 \times 2} & \boldsymbol{O}_{1 \times 2} \\ (\boldsymbol{\varphi}_{.2})^T \frac{\partial}{\partial \xi^2} & \boldsymbol{O}_{1 \times 2} & \boldsymbol{O}_{1 \times 2} \\ (\boldsymbol{\varphi}_{.2})^T \frac{\partial}{\partial \xi^1} + (\boldsymbol{\varphi}_{.1})^T \frac{\partial}{\partial \xi^2} & \boldsymbol{O}_{1 \times 2} & \boldsymbol{O}_{1 \times 2} \end{bmatrix} \begin{Bmatrix} \delta \boldsymbol{u} \\ \delta \boldsymbol{D}_1 \\ \delta \boldsymbol{D}_3 \end{Bmatrix} \quad (4.43-a)$$

$$\left\{ \delta \varepsilon^{(1)} \right\} = \left[B_p^{(1)} \right] \{ \delta \Phi \} = \begin{bmatrix} (\mathbf{d}_{1,1})^T \frac{\partial}{\partial \xi^1} & (\boldsymbol{\varphi}_{1,1})^T \frac{\partial}{\partial \xi^1} \bar{\mathbf{R}}_{3 \times 2} & O_{1 \times 2} \\ (\mathbf{d}_{1,2})^T \frac{\partial}{\partial \xi^2} & (\boldsymbol{\varphi}_{1,2})^T \frac{\partial}{\partial \xi^2} \bar{\mathbf{R}}_{3 \times 2} & O_{1 \times 2} \\ (\mathbf{d}_{1,2})^T \frac{\partial}{\partial \xi^1} + (\mathbf{d}_{1,1})^T \frac{\partial}{\partial \xi^2} & \left[(\boldsymbol{\varphi}_{1,1})^T \frac{\partial}{\partial \xi^2} + (\boldsymbol{\varphi}_{1,2})^T \frac{\partial}{\partial \xi^1} \right] \bar{\mathbf{R}}_{3 \times 2} & O_{1 \times 2} \end{bmatrix} \begin{Bmatrix} \delta \mathbf{u} \\ \delta D_1 \\ \delta D_3 \end{Bmatrix} \quad (4.43b)$$

$$\left\{ \delta \varepsilon^{(2)} \right\} = \left[B_p^{(2)} \right] \{ \delta \Phi \} = \begin{bmatrix} O_{1 \times 3} & (\mathbf{d}_{1,1})^T \frac{\partial}{\partial \xi^1} \bar{\mathbf{R}}_{3 \times 2} & O_{1 \times 2} \\ O_{1 \times 3} & (\mathbf{d}_{1,2})^T \frac{\partial}{\partial \xi^2} \bar{\mathbf{R}}_{3 \times 2} & O_{1 \times 2} \\ O_{1 \times 3} & \left[(\mathbf{d}_{1,1})^T \frac{\partial}{\partial \xi^2} + (\mathbf{d}_{1,2})^T \frac{\partial}{\partial \xi^1} \right] \bar{\mathbf{R}}_{3 \times 2} & O_{1 \times 2} \end{bmatrix} \begin{Bmatrix} \delta \mathbf{u} \\ \delta D_1 \\ \delta D_3 \end{Bmatrix} \quad (4.43c)$$

$$\left\{ \delta \varepsilon^{(3)} \right\} = \left[B_p^{(3)} \right] \{ \delta \Phi \} = \begin{bmatrix} (\mathbf{d}_{3,1})^T \frac{\partial}{\partial \xi^1} & -(\boldsymbol{\varphi}_{1,1})^T \frac{\partial}{\partial \xi^1} (\mathbf{d}_1 \otimes \mathbf{d}_3) \bar{\mathbf{R}}_{3 \times 2} \\ (\mathbf{d}_{3,2})^T \frac{\partial}{\partial \xi^2} & -(\boldsymbol{\varphi}_{1,2})^T \frac{\partial}{\partial \xi^2} (\mathbf{d}_1 \otimes \mathbf{d}_3) \bar{\mathbf{R}}_{3 \times 2} \\ (\mathbf{d}_{3,1})^T \frac{\partial}{\partial \xi^2} + (\mathbf{d}_{3,2})^T \frac{\partial}{\partial \xi^1} & - \left[(\boldsymbol{\varphi}_{1,1})^T \frac{\partial}{\partial \xi^2} + (\boldsymbol{\varphi}_{1,2})^T \frac{\partial}{\partial \xi^1} \right] (\mathbf{d}_1 \otimes \mathbf{d}_3) \bar{\mathbf{R}}_{3 \times 2} \\ & (\boldsymbol{\varphi}_{1,1})^T \frac{\partial}{\partial \xi^1} \bar{\mathbf{R}}_{3 \times 2} \\ & (\boldsymbol{\varphi}_{1,2})^T \frac{\partial}{\partial \xi^2} \bar{\mathbf{R}}_{3 \times 2} \\ & \left[(\boldsymbol{\varphi}_{1,1})^T \frac{\partial}{\partial \xi^2} + (\boldsymbol{\varphi}_{1,2})^T \frac{\partial}{\partial \xi^1} \right] \bar{\mathbf{R}}_{3 \times 2} \end{bmatrix} \begin{Bmatrix} \delta \mathbf{u} \\ \delta D_1 \\ \delta D_3 \end{Bmatrix} \quad (4.43d)$$

$$\left\{ \delta \gamma^{(o)} \right\} = \left[B_s^{(o)} \right] \{ \delta \Phi \} = \begin{bmatrix} (\mathbf{d}_1)^T \frac{\partial}{\partial \xi^1} & (\boldsymbol{\varphi}_{1,1})^T \bar{\mathbf{R}}_{3 \times 2} & O_{1 \times 2} \\ (\mathbf{d}_1)^T \frac{\partial}{\partial \xi^2} & (\boldsymbol{\varphi}_{1,2})^T \bar{\mathbf{R}}_{3 \times 2} & O_{1 \times 2} \end{bmatrix} \begin{Bmatrix} \delta \mathbf{u} \\ \delta D_1 \\ \delta D_3 \end{Bmatrix} \quad (4.44a)$$

$$\left\{ \delta \gamma^{(2)} \right\} = \left[B_s^{(2)} \right] \{ \delta \Phi \} = 3 \begin{bmatrix} (d_3)^T \frac{\partial}{\partial \xi^1} & -(\varphi_{,1})^T (d_1 \otimes d_3) \bar{R}_{3 \times 2} & (\varphi_{,1})^T \bar{R}_{3 \times 2} \\ (d_3)^T \frac{\partial}{\partial \xi^2} & -(\varphi_{,2})^T (d_1 \otimes d_3) \bar{R}_{3 \times 2} & (\varphi_{,2})^T \bar{R}_{3 \times 2} \end{bmatrix} \begin{Bmatrix} \delta u \\ \delta D_1 \\ \delta D_3 \end{Bmatrix} \quad (4.44b)$$

$\bar{R}_{3 \times 2}$ is a three by two matrix representing the first two columns of matrix R .

4.3 Finite Element Discretization

The equations of motion, for shell type structures as a continuum, were presented in the previous section in their weak form (i.e. virtual work principle). A numerical procedure such as FEM appears to be the most viable tool to deal with such highly nonlinear differential equations. The most important formulation within the finite element method, which is widely used for the solution of practical problems, is the displacement based finite element method. Practically all major general; purpose analysis softwares have been developed using this formulation; e.g. see Bathe [8], because of its simplicity, generality and numerical properties. This formulation is adopted in this study based on a four-noded element whose features were discussed in chapter two.

4.3.1. Midsurface Interpolation

The finite element discretization is presented based on the isoparametric formulation using a four-noded quadrilateral shell element. The midsurface of the shell element is given by

$$\boldsymbol{\varphi}^k(\xi, \eta) = \sum_{I=1}^4 N^I(\xi, \eta) \boldsymbol{\varphi}_I^k \quad (4.45)$$

where

$\boldsymbol{\varphi}_I^k$ is the position vector of node I at iteration k .

$N^I(\xi, \eta)$ are standard bilinear shape functions given by

$$N^I(\xi, \eta) = \frac{1}{4}(1 + \xi\xi_I)(1 + \eta\eta_I) \quad (4.46)$$

with (ξ_I, η_I) taking the values $(-1, -1)$, $(1, -1)$, $(1, 1)$ and $(-1, 1)$ at, respectively, points 1, 2, 3 and 4 in Figure 4.2

Following the isoparametric concept, we get

$$\Delta\boldsymbol{\varphi}^k(\xi, \eta) = \sum_{I=1}^4 N^I(\xi, \eta) \Delta\boldsymbol{\varphi}_I^k = \sum_{I=1}^4 N^I(\xi, \eta) \Delta\mathbf{u}_I^k \quad (4.47)$$

$\Delta\mathbf{u}_I^k$ is the incremental displacement vector of node I at iteration k .

4.3.2. Interpolation of Director Fields \mathbf{d}_1 and \mathbf{d}_3

In the reference configuration, the director field $\mathbf{d}_1^{(o)}$ is interpolated by

$$\mathbf{d}_1^{(o)} = \frac{\tilde{\mathbf{d}}_1^{(o)}}{\|\tilde{\mathbf{d}}_1^{(o)}\|}, \quad \tilde{\mathbf{d}}_1^{(o)} = \sum_{I=1}^4 N^I(\xi, \eta) \mathbf{d}_{1(I)}^{(o)} \quad (4.48)$$

$\mathbf{d}_{1(I)}^{(o)}$ are the nodal directors in the reference configuration. They can be input by the user or computed internally by the program. If computed internally, the nodal normals are computed at the element level using the cross product. Then at each node, at the structure

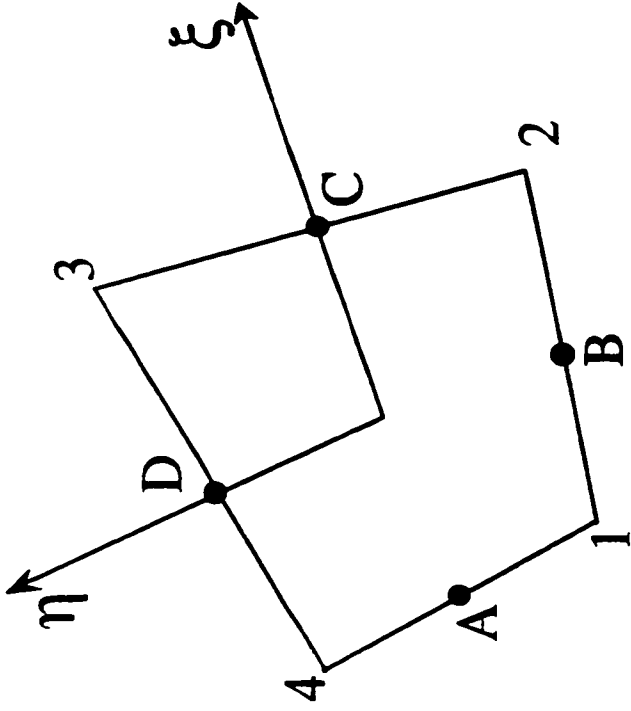


Figure 4.2 Location of assumed strain points

level, the average of the nodal normals of the adjoining elements is taken [23]. The field director $\mathbf{d}_3^{(\sigma)}$ is zero as shown in Equation (3.17). Equation (4.48) is used to compute the directors $\mathbf{d}_1^{(\sigma)}$ at Gauss points. $\mathbf{d}_{1,\alpha}^{(\sigma)}$, which represents the derivative of the director $\mathbf{d}_1^{(\sigma)}$ with respect to ξ ($\alpha=1$) and η ($\alpha=2$) is obtained by differentiating Equation (4.48) with respect to ξ and η . After differentiation, we get

$$\mathbf{d}_{1,\alpha}^{(\sigma)} = \frac{\bar{\mathbf{d}}_{1,\alpha}^{(\sigma)}}{\|\bar{\mathbf{d}}_1^{(\sigma)}\|} - \frac{(\bar{\mathbf{d}}_1^{(\sigma)} \cdot \bar{\mathbf{d}}_{1,\alpha}^{(\sigma)}) \bar{\mathbf{d}}_1^{(\sigma)}}{\|\bar{\mathbf{d}}_1^{(\sigma)}\|^3} = (\mathbf{I} - \mathbf{d}_1^{(\sigma)} \otimes \mathbf{d}_1^{(\sigma)}) \frac{\bar{\mathbf{d}}_{1,\alpha}^{(\sigma)}}{\|\bar{\mathbf{d}}_1^{(\sigma)}\|} \quad (4.49)$$

In the current configuration, we adopt the so-called continuum consistent interpolation as presented in Reference [66]. Here the isoparametric concept is applied to the spatial incremental directors $\Delta \mathbf{d}_1$ and $\Delta \mathbf{d}_3$.

$$\Delta \mathbf{d}_1^k = \sum_{I=1}^4 N^I(\xi, \eta) \Delta \mathbf{d}_{1(I)}^k, \quad \Delta \mathbf{d}_3^k = \sum_{I=1}^4 N^I(\xi, \eta) \Delta \mathbf{d}_{3(I)}^k \quad (4.50)$$

$\Delta \mathbf{d}_{1(I)}^k$ and $\Delta \mathbf{d}_{3(I)}^k$ are the nodal incremental directors.

At iteration k , $\boldsymbol{\varphi}_I^k$, $\mathbf{d}_{1(I)}^k$ and $\mathbf{d}_{3(I)}^k$ are known quantities. The solution of the linearized problem will yield the nodal discrete values $(\Delta \mathbf{u}_I^k, \Delta \mathbf{D}_{1(I)}^k, \Delta \mathbf{D}_{3(I)}^k)$. $\Delta \mathbf{D}_{1(I)}^k$ and $\Delta \mathbf{D}_{3(I)}^k$ are nodal material incremental vectors having two components each along the bases \mathbf{E}_1 and \mathbf{E}_2 , i.e. they are orthogonal to \mathbf{E}_3 basis. Next we compute the spatial nodal director increments $\Delta \mathbf{d}_{1(I)}^k$ and $\Delta \mathbf{d}_{3(I)}^k$ as follow

$$\Delta \mathbf{d}_{1(I)}^k = \bar{\mathbf{R}}_I^k \Delta \mathbf{D}_{1(I)}^k \quad (4.51)$$

$$\Delta d_{3(I)}^k = -(\mathbf{d}_{1(I)}^k \otimes \mathbf{d}_{3(I)}^k) \bar{\mathbf{R}}_I^k \Delta D_{1(I)}^k + \bar{\mathbf{R}}_I^k \Delta D_{3(I)}^k \quad (4.52)$$

\otimes denotes the standard tensor product

$\bar{\mathbf{R}}_I^k$ represents the first two columns of the rotation matrix \mathbf{R}_I^k

The nodal director increments $\Delta d_{1(I)}^k$ and $\Delta d_{3(I)}^k$, computed using Equations (4.51) and (4.52), along with $\Delta \mathbf{u}_I^k$ serve to update the configuration of the shell element which will be outlined in the next section.

4.3.3. Configuration Update

The update of the surface configuration is straightforward; it is

$$\boldsymbol{\varphi}_I^{k+1} = \boldsymbol{\varphi}_I^k + \Delta \mathbf{u}_I^k \quad (4.53)$$

The nodal directors $\mathbf{d}_{1(I)}$ and $\mathbf{d}_{3(I)}$ are updated using the spatial representation

$$\mathbf{d}_{1(I)}^{k+1} = \mathbf{R}_I^{k+1} \mathbf{E}_3 = \Delta \mathbf{R}_I^k \mathbf{R}_I^k \mathbf{E}_3 = \Delta \mathbf{R}_I^k \mathbf{d}_{1(I)}^k \quad (4.54)$$

The incremental rotation matrix $\Delta \mathbf{R}_I^k$ is given by

$$\Delta \mathbf{R}_I^k = \exp \left[\Delta \hat{\boldsymbol{\theta}}_I^k \right] \quad (4.55)$$

$\Delta \boldsymbol{\theta}_I^k$ represents the spatial incremental rotation vector given by

$$\Delta \boldsymbol{\theta}_I^k = \mathbf{R}_I^k (\mathbf{E}_3 \times \Delta \mathbf{D}_I^k) = \mathbf{d}_{1(I)}^k \times \Delta \mathbf{d}_{1(I)}^k \quad (4.56)$$

The incremental rotation matrix $\Delta \mathbf{R}_I^k$ is parametrized by

$$\Delta \mathbf{R}_I^k = \cos \left| \Delta \boldsymbol{\theta}_I^k \right| \mathbf{I} + \frac{\sin \left| \Delta \boldsymbol{\theta}_I^k \right|}{\left| \Delta \boldsymbol{\theta}_I^k \right|} \Delta \hat{\boldsymbol{\theta}}_I^k + \frac{1 - \cos \left| \Delta \boldsymbol{\theta}_I^k \right|}{\left| \Delta \boldsymbol{\theta}_I^k \right|^2} \Delta \boldsymbol{\theta}_I^k \otimes \Delta \boldsymbol{\theta}_I^k \quad (4.57)$$

$\Delta\hat{\theta}_I^k$ is a skew symmetric matrix related to $\Delta\theta_I^k$ by

$$\Delta\hat{\theta}_I^k \Delta\theta_I^k = 0 \quad \text{and} \quad \Delta\hat{\theta}_I^k V = \Delta\theta_I^k \times V \quad , \quad \forall V \in \mathfrak{R}^3 \quad (4.58)$$

From Equation (4.56), we deduce the following

$$\|\Delta\theta_I^k\| = \|\Delta d_{3(I)}^k\| \quad (4.59)$$

Substituting ΔR_I^k by its expression in Equation (4.54) and making use of Equation (4.59),

we get

$$d_{3(I)}^{k+1} = \cos \|\Delta d_{3(I)}^k\| d_{3(I)}^k + \frac{\sin \|\Delta d_{3(I)}^k\|}{\|\Delta d_{3(I)}^k\|} \Delta d_{3(I)}^k \quad (4.60)$$

$d_{3(I)}$ is updated by

$$d_{3(I)}^{k+1} = R_I^{k+1} D_{3(I)}^{k+1} = \Delta R_I^k (d_{3(I)}^k + R_I^k \Delta D_{3(I)}^k) \quad (4.61)$$

Finally, we update the nodal rotation matrices R_I by

$$R_I^{k+1} = \Delta R_I^k R_I^k \quad (4.62)$$

The updated surface configuration φ_I^{k+1} and nodal directors $d_{1(I)}^{k+1}$ and $d_{3(I)}^{k+1}$ will be used

to find field expressions for φ^{k+1} , d_1^{k+1} and d_3^{k+1} and their derivatives $\varphi_{,\alpha}^{k+1}$, $d_{1,\alpha}^{k+1}$ and

$d_{3,\alpha}^{k+1}$ ($\alpha = 1,2$) with respect to the curvilinear coordinates ξ and η . The derivation is

based on the interpolation Equations (4.45) and (4.50) and the details are shown next

In the updated configuration, φ^{k+1} is obtained directly from Equation (4.45); d_1^{k+1} is

given by

$$\mathbf{d}_1^{k+1} = \exp [\Delta \hat{\theta}^k] \mathbf{d}_1^k = \cos \|\Delta \mathbf{d}_1^k\| \mathbf{d}_1^k + \sin \|\Delta \mathbf{d}_1^k\| \bar{\mathbf{e}}^k \quad (4.63)$$

where

$$\bar{\mathbf{e}}^k = \frac{\Delta \mathbf{d}_1^k}{\|\Delta \mathbf{d}_1^k\|} \text{ is a unit vector in the direction of } \Delta \mathbf{d}_1^k.$$

In Equation (4.63), \mathbf{d}_1^k are known at Gauss points and $\Delta \mathbf{d}_1^k$ are obtained from Equation (4.49)

Since \mathbf{d}_3^{k+1} is normal to \mathbf{d}_1^{k+1} , we form an orthonormal basis $\{\mathbf{t}_1^{k+1}, \mathbf{t}_2^{k+1}\}$ in the plane normal to \mathbf{d}_1^{k+1} and represent \mathbf{d}_3^{k+1} using these bases

$$\mathbf{t}_1^{k+1} = \mathbf{d}_1^k \times \bar{\mathbf{e}}^k \quad (4.64)$$

$$\mathbf{t}_2^{k+1} = \mathbf{d}_1^{k+1} \times \mathbf{t}_1^{k+1} = \sin \|\Delta \mathbf{d}_1^k\| \mathbf{d}_1^k - \cos \|\Delta \mathbf{d}_1^k\| \bar{\mathbf{e}}^k \quad (4.65)$$

$$\mathbf{d}_3^{k+1} = \mathbf{R}^{k+1} \mathbf{D}_3^{k+1} = \exp [\Delta \hat{\theta}^k] \mathbf{R}^k (\mathbf{D}_3^k + \Delta \mathbf{D}_3^k) = \exp [\Delta \hat{\theta}^k] (\mathbf{d}_3^k + \mathbf{R}^k \Delta \mathbf{D}_3^k) \quad (4.66)$$

Applying Equation (4.52) for a field point, and putting $\mathbf{R}^k \Delta \mathbf{D}_3^k$ on one side of the equation, we get

$$\mathbf{R}^k \Delta \mathbf{D}_3^k = \Delta \mathbf{d}_3^k + (\mathbf{d}_1^k \otimes \mathbf{d}_3^k) \Delta \mathbf{d}_1^k = \Delta \mathbf{d}_3^k + (\Delta \mathbf{d}_1^k \cdot \mathbf{d}_3^k) \mathbf{d}_1^k \quad (4.67)$$

Using Equations (4.56) and (4.64), we find that

$$\mathbf{t}_1^{k+1} = \frac{\Delta \theta^k}{\|\Delta \theta^k\|} \quad (4.68)$$

In Equation (4.66), $\exp [\Delta \hat{\theta}^k]$ is represented by the following parametrization

$$\exp [\Delta \hat{\theta}^k] = I + \sin \|\Delta d_1^k\| \hat{t}_1^{k+1} + (1 - \cos \|\Delta d_1^k\|) \hat{t}_1^{k+1} \hat{t}_1^{k+1} \quad (4.69)$$

Equation (4.69) is obtained from Equations (3.32b) and (4.68)

Substituting Equations (4.69) and (4.67) into Equation (4.66) and after projecting d_3^{k+1} on the bases t_1^{k+1} and t_2^{k+1} we find

$$d_3^{k+1} = ((d_3^k + \Delta d_3^k) \cdot t_1^{k+1}) t_1^{k+1} - ((d_3^k + \Delta d_3^k) \cdot \bar{e}^k) t_2^{k+1} \quad (4.70)$$

The updated expressions for the derivatives of φ^{k+1} , d_1^{k+1} and d_3^{k+1} will be based on Equations (4.45), (4.63) and (4.70).

$$\varphi_{,\alpha}^{k+1} = \sum_{I=1}^4 N_{\alpha}^I \varphi_I^{k+1} \quad (4.71)$$

$$d_{1,\alpha}^{k+1} = \cos \|\Delta d_1^k\| d_{1,\alpha}^k - (\Delta d_{1,\alpha}^k \cdot \bar{e}^k) t_2^{k+1} + \sin \|\Delta d_1^k\| \bar{e}_{,\alpha}^k \quad (4.72)$$

where

$$\Delta d_{1,\alpha}^k = \sum_{I=1}^4 N_{\alpha}^I \Delta d_{1I}^k \quad (4.73)$$

$$\bar{e}_{,\alpha}^k = \frac{\Delta d_{1,\alpha}^k}{\|\Delta d_1^k\|} - \frac{(\Delta d_{1,\alpha}^k \cdot \bar{e}^k)}{\|\Delta d_1^k\|} \bar{e}^k \quad (4.74)$$

$$\begin{aligned} d_{3,\alpha}^{k+1} = & ((d_{3,\alpha}^k + \Delta d_{3,\alpha}^k) \cdot t_1^{k+1}) t_1^{k+1} + ((d_3^k + \Delta d_3^k) \cdot t_{1,\alpha}^{k+1}) t_1^{k+1} + ((d_3^k + \Delta d_3^k) \cdot t_1^{k+1}) t_{1,\alpha}^{k+1} \\ & - ((d_{3,\alpha}^k + \Delta d_{3,\alpha}^k) \cdot \bar{e}^k) t_2^{k+1} - ((d_3^k + \Delta d_3^k) \cdot \bar{e}_{,\alpha}^k) t_2^{k+1} - ((d_3^k + \Delta d_3^k) \cdot \bar{e}^k) t_{2,\alpha}^{k+1} \end{aligned} \quad (4.75)$$

where

$$\Delta d_{3,\alpha}^k = \sum_{I=1}^4 N_{\alpha}^I \Delta d_{3I}^k \quad (4.76)$$

$$\boldsymbol{t}_{1,\alpha}^{k+1} = \boldsymbol{d}_{1,\alpha}^k \times \bar{\boldsymbol{e}}^k + \boldsymbol{d}_1^k \times \bar{\boldsymbol{e}}_{,\alpha}^k \quad (4.77)$$

$$\boldsymbol{t}_{2,\alpha}^{k+1} = \boldsymbol{d}_{1,\alpha}^{k+1} \times \boldsymbol{t}_1^{k+1} + \boldsymbol{d}_1^{k+1} \times \boldsymbol{t}_{1,\alpha}^{k+1} \quad (4.78)$$

This ends up the updating procedure of the director fields and their derivatives.

4.3.4. Transverse Shear Interpolation

The performance of displacement finite elements deteriorates as the thickness of the plate/shell element gets smaller. This is attributed to the fact that the assumed displacement interpolation functions impose excessive amounts of shearing strain in the development of simple bending deformations. This phenomenon of excessive stiffness is called shear locking and is explained in [62,121]. Early remedies to this problem were reduced or selective integration [149-153] where the shear term (selective) or all terms (reduced) were integrated using low order numerical quadrature. This, sometimes, lead to matrices that are rank deficient and possess spurious (or zero energy) modes called hourglass modes. Stabilization matrices were used to remove the spurious modes [154]. Some investigators used discrete Kirchhoff constraints which enforce the Kirchhoff assumption at discrete Gaussian points. Among the recent remedies, the approach proposed by Dvorkin and Bathe [4,5], which is referred to as the Assumed Natural Strain (ANS) method, seems to be presently the best formulation for Reissner-Mindlin based plate and shell elements [17]. It has been used almost exclusively in recent finite rotation shell models [12-15,17,19,20,23,25,32,66,95]. In this procedure, a mixed interpolation of the various strain tensor components is used: the bending and membrane strain components are calculated as usual from the displacement interpolations, while the

transverse shear strain components are interpolated differently. In this study, the constant part of the transverse shear strain (i.e. $\overset{(o)}{E}_{13}$ and $\overset{(o)}{E}_{23}$) will be interpolated using the assumed strain method of Dvorkin and Bathe[4,5]. However, the quadratic part of the transverse shear strain (i.e. $\overset{(2)}{E}_{13}$ and $\overset{(2)}{E}_{23}$) will be treated in the same way as the bending and membrane strains, i.e. calculated as usual from the displacement interpolations.

Figure 4.2 shows the four-noded shell element with the midside points A,B,C and D. The interpolations of the shear strains $\overset{(o)}{E}_{13}$ and $\overset{(o)}{E}_{23}$ are given by

$$\overset{(o)}{E}_{13} = \frac{1}{2} (1-\eta) \overset{(o)}{E}_{13}^B + \frac{1}{2} (1+\eta) \overset{(o)}{E}_{13}^D \quad (4.79)$$

$$\overset{(o)}{E}_{23} = \frac{1}{2} (1-\xi) \overset{(o)}{E}_{23}^A + \frac{1}{2} (1+\xi) \overset{(o)}{E}_{23}^C \quad (4.80)$$

where $\overset{(o)}{E}_{13}^B$, $\overset{(o)}{E}_{13}^D$, $\overset{(o)}{E}_{23}^A$ and $\overset{(o)}{E}_{23}^C$ are the strain components at points B, D, A and C, directly evaluated from the displacement interpolations using Equations (3.52a). The natural coordinates (ξ, η) of these points are (see Fig. 4.2): A(-1,0), B(0,-1), C(1,0) and D(0,1). Taking the variation of Equations (4.79) and (4.80) we get

$$\overset{(o)}{\delta E}_{13} = \frac{1}{2} (1-\eta) \overset{(o)}{\delta E}_{13}^B + \frac{1}{2} (1+\eta) \overset{(o)}{\delta E}_{13}^D \quad (4.81)$$

$$\overset{(o)}{\delta E}_{23} = \frac{1}{2} (1-\xi) \overset{(o)}{\delta E}_{23}^A + \frac{1}{2} (1+\xi) \overset{(o)}{\delta E}_{23}^C \quad (4.82)$$

where $\overset{(o)}{\delta E}_{13}^B$, $\overset{(o)}{\delta E}_{13}^D$, $\overset{(o)}{\delta E}_{23}^A$ and $\overset{(o)}{\delta E}_{23}^C$ will be evaluated using Equations (4.23), using appropriate coordinates ξ and η for each point as defined above.

The matrix formulation of the internal virtual work presented in section (4.1.5) used the

variables in their continuum form, i.e. prior, to their discretization using the finite element method. The matrix formulation in its discretized form will be presented in the next section.

4.3.5. Matrix Formulation of the Discretized Internal Virtual Work

After applying the finite element discretization, described in previous sections, to the kinematic variables and the constant part of the transverse shear strain, we get the discrete form of the strain displacement operators $\left[B_p^{(i)} \right]$ ($i = 0,1,2,3$) and $\left[B_s^{(j)} \right]$ ($j = 0,2$).

$$\begin{aligned} \left\{ \delta \varepsilon^{(\bullet)} \right\} &= \begin{Bmatrix} \delta E_{11}^{(\bullet)} \\ \delta E_{22}^{(\bullet)} \\ 2\delta E_{12}^{(\bullet)} \end{Bmatrix} = \begin{Bmatrix} \varphi_{,1} \cdot \delta \varphi_{,1} \\ \varphi_{,2} \cdot \delta \varphi_{,2} \\ \varphi_{,2} \cdot \delta \varphi_{,1} + \varphi_{,1} \cdot \delta \varphi_{,2} \end{Bmatrix} = \begin{Bmatrix} \sum_{I=1}^4 N_{,1}^I \varphi_{,1}^T \delta u_I \\ \sum_{I=1}^4 N_{,2}^I \varphi_{,2}^T \delta u_I \\ \sum_{I=1}^4 (N_{,1}^I \varphi_{,2}^T + N_{,2}^I \varphi_{,1}^T) \delta u_I \end{Bmatrix} \\ &= \sum_{I=1}^4 \left[B_p^{(\bullet)} \right]_I \{ \delta \phi \}_I \end{aligned} \quad (4.83)$$

$$\text{where} \quad \left[B_p^{(\bullet)} \right]_I = \begin{bmatrix} N_{,1}^I \varphi_{,1}^T & 0_{b \times 2} & 0_{b \times 2} \\ N_{,2}^I \varphi_{,2}^T & 0_{b \times 2} & 0_{b \times 2} \\ N_{,1}^I \varphi_{,2}^T + N_{,2}^I \varphi_{,1}^T & 0_{b \times 2} & 0_{b \times 2} \end{bmatrix} \quad (4.84)$$

In the same way, we obtain the other strain-displacement matrices

$$\left[B_p^{(1)} \right]_I = \begin{bmatrix} N_{,1}^I d_{1,1}^T & N_{,1}^I \varphi_{,1}^T \bar{R}_I & 0_{b \times 2} \\ N_{,2}^I d_{1,2}^T & N_{,2}^I \varphi_{,2}^T \bar{R}_I & 0_{b \times 2} \\ N_{,1}^I d_{1,2}^T + N_{,2}^I d_{1,1}^T & (N_{,1}^I \varphi_{,2}^T + N_{,2}^I \varphi_{,1}^T) \bar{R}_I & 0_{b \times 2} \end{bmatrix} \quad (4.85)$$

$$\begin{bmatrix} {}^{(2)} \\ \mathbf{B}_p \end{bmatrix}_I = \begin{bmatrix} 0_{\text{bc3}} & N_{,1}^I \mathbf{d}_{1,1}^T \bar{\mathbf{R}}_I & 0_{\text{bc2}} \\ 0_{\text{bc3}} & N_{,2}^I \mathbf{d}_{1,2}^T \bar{\mathbf{R}}_I & 0_{\text{bc2}} \\ 0_{\text{bc3}} & (N_{,1}^I \mathbf{d}_{1,2}^T + N_{,2}^I \mathbf{d}_{1,1}^T) \bar{\mathbf{R}}_I & 0_{\text{bc2}} \end{bmatrix} \quad (4.86)$$

$$\begin{bmatrix} {}^{(3)} \\ \mathbf{B}_p \end{bmatrix}_I = \begin{bmatrix} N_{,1}^I \mathbf{d}_{3,1}^T & -N_{,1}^I \boldsymbol{\varphi}_1^T (\mathbf{d}_{\text{y}(I)} \otimes \mathbf{d}_{\text{z}(I)}) \bar{\mathbf{R}}_I & N_{,1}^I \boldsymbol{\varphi}_1^T \bar{\mathbf{R}}_I \\ N_{,2}^I \mathbf{d}_{3,2}^T & -N_{,2}^I \boldsymbol{\varphi}_2^T (\mathbf{d}_{\text{y}(I)} \otimes \mathbf{d}_{\text{z}(I)}) \bar{\mathbf{R}}_I & N_{,2}^I \boldsymbol{\varphi}_2^T \bar{\mathbf{R}}_I \\ N_{,1}^I \mathbf{d}_{3,2}^T + N_{,2}^I \mathbf{d}_{3,1}^T & -(N_{,1}^I \boldsymbol{\varphi}_2^T + N_{,2}^I \boldsymbol{\varphi}_1^T) (\mathbf{d}_{\text{y}(I)} \otimes \mathbf{d}_{\text{z}(I)}) \bar{\mathbf{R}}_I & (N_{,1}^I \boldsymbol{\varphi}_2^T + N_{,2}^I \boldsymbol{\varphi}_1^T) \bar{\mathbf{R}}_I \end{bmatrix} \quad (4.87)$$

For the transverse shear strain variations $\left\{ \delta \boldsymbol{\gamma}^{(\circ)} \right\}$, the use of the assumed strain method

yields

$$\left\{ \delta \boldsymbol{\gamma}^{(\circ)} \right\} = \begin{bmatrix} 2\delta \bar{\mathbf{E}}_{13}^{(\circ)} \\ 2\delta \bar{\mathbf{E}}_{23}^{(\circ)} \end{bmatrix} = \sum_{I=1}^4 \begin{bmatrix} {}^{(\circ)} \\ \mathbf{B}_s \end{bmatrix}_I \left\{ \delta \boldsymbol{\phi} \right\}_I \quad (4.88)$$

where $\delta \bar{\mathbf{E}}_{13}^{(\circ)}$ and $\delta \bar{\mathbf{E}}_{23}^{(\circ)}$ are given respectively by Equations (4.81) and (4.82). After going

through the computations, the following expressions for the matrices $\begin{bmatrix} {}^{(I)} \\ \mathbf{B}_s \end{bmatrix}_I$ ($I=1,2,3,4$)

are obtained.

$$\begin{bmatrix} {}^{(1)} \\ \mathbf{B}_s \end{bmatrix}_1 = \frac{1}{4} \begin{bmatrix} -(1-\eta)(\mathbf{d}_1^B)^T & (1-\eta)(\boldsymbol{\varphi}_1^B)^T \bar{\mathbf{R}}_1 & 0_{\text{bc2}} \\ -(1-\xi)(\mathbf{d}_1^A)^T & (1-\xi)(\boldsymbol{\varphi}_2^A)^T \bar{\mathbf{R}}_1 & 0_{\text{bc2}} \end{bmatrix} \quad (4.89a)$$

$$\begin{bmatrix} {}^{(2)} \\ \mathbf{B}_s \end{bmatrix}_2 = \frac{1}{4} \begin{bmatrix} (1-\eta)(\mathbf{d}_1^B)^T & (1-\eta)(\boldsymbol{\varphi}_1^B)^T \bar{\mathbf{R}}_2 & 0_{\text{bc2}} \\ -(1+\xi)(\mathbf{d}_1^C)^T & (1+\xi)(\boldsymbol{\varphi}_2^C)^T \bar{\mathbf{R}}_2 & 0_{\text{bc2}} \end{bmatrix} \quad (4.89b)$$

$$\begin{bmatrix} \delta^{(e)} \\ B_s \end{bmatrix}_3 = \frac{1}{4} \begin{bmatrix} (1+\eta)(d_1^D)^T & (1+\eta)(\varphi_{,1}^D)^T \bar{R}_3 & 0_{1 \times 2} \\ (1+\xi)(d_1^C)^T & (1+\xi)(\varphi_{,2}^C)^T \bar{R}_3 & 0_{1 \times 2} \end{bmatrix} \quad (4.89c)$$

$$\begin{bmatrix} \delta^{(e)} \\ B_s \end{bmatrix}_4 = \frac{1}{4} \begin{bmatrix} -(1+\eta)(d_1^D)^T & (1+\eta)(\varphi_{,1}^D)^T \bar{R}_4 & 0_{1 \times 2} \\ (1-\xi)(d_1^A)^T & (1-\xi)(\varphi_{,2}^A)^T \bar{R}_4 & 0_{1 \times 2} \end{bmatrix} \quad (4.89d)$$

$$\left\{ \delta^{(2)} \gamma \right\} = \begin{Bmatrix} 2\delta^{(2)} E_{13} \\ 2\delta^{(2)} E_{23} \end{Bmatrix} = 3 \left\{ \begin{matrix} d_3 \cdot \delta\varphi_{,1} + \varphi_{,1} \cdot \delta d_3 \\ d_3 \cdot \delta\varphi_{,2} + \varphi_{,2} \cdot \delta d_3 \end{matrix} \right\} = \sum_{I=1}^4 \left[E_s \right]_I \left\{ \delta\phi \right\}_I \quad (4.90)$$

where

$$\left[E_s \right]_I = 3 \begin{bmatrix} N_{,1}^I d_3^T & -N^I \varphi_{,1}^T (d_{1(I)} \otimes d_{3(I)}) \bar{R}_I & N^I \varphi_{,1}^T \bar{R}_I \\ N_{,2}^I d_3^T & -N^I \varphi_{,2}^T (d_{1(I)} \otimes d_{3(I)}) \bar{R}_I & N^I \varphi_{,2}^T \bar{R}_I \end{bmatrix} \quad (4.91)$$

4.4 Linearization and Tangent Operators

After the discretization of Equation (4.7), we find a system of highly nonlinear equations. Solving this problem by Newton-Raphson method requires a linearization of the virtual work. We assume here that the external loads are conservative. The linearization of the internal virtual work can be obtained by the directional derivative of δW_I in the direction of $\{\Delta\phi\} = [\Delta u \ \Delta D_1 \ \Delta D_3]^T$

First, we rewrite the discretized internal virtual work expression using matrix notation

$$\delta W_I = \sum_{N=1}^{NEL} \int_{\Omega_N^0} \left(\sum_{n=0}^3 \left\{ \delta \varepsilon^{(n)} \right\}^T \left\{ m^{(n)} \right\} + \sum_{k=0,2} \left\{ \delta \gamma^{(k)} \right\}^T \left\{ Q^{(k)} \right\} \right) d\Omega^0 \quad (4.92)$$

where the domain Ω^0 has been divided into sub-domains Ω_N^0 ($N=1, NEL$) representing

the area of the finite element N . NEL represents the total number of finite elements in the domain. The other quantities in Equation (4.92) have already been defined previously.

Now, taking the derivative of δW_I in the direction of $\{\Delta\phi\} = [\Delta u \ \Delta D_1 \ \Delta D_3]^T$, we get

$$\begin{aligned}
 D[\delta W_I] \cdot \{\Delta\phi\} &= \sum_{N=1}^{NEL} \int_{\Omega_N^o} \left(\sum_{n=0}^3 D\{\delta \varepsilon^{(n)}\}^T \cdot \{\Delta\phi\} \{m^{(n)}\} + \sum_{k=0,2} D\{\delta \gamma^{(k)}\}^T \cdot \{\Delta\phi\} \{Q^{(k)}\} \right) d\Omega^o \\
 &+ \sum_{N=1}^{NEL} \int_{\Omega_N^o} \left(\sum_{n=0}^3 \{\delta \varepsilon^{(n)}\}^T D\{m^{(n)}\} \cdot \{\Delta\phi\} + \sum_{k=0,2} \{\delta \gamma^{(k)}\} D\{Q^{(k)}\} \cdot \{\Delta\phi\} \right) d\Omega^o \quad (4.93)
 \end{aligned}$$

where the first two terms, which result from the variation of the geometry while holding the material part constant, will yield the geometric tangent stiffness matrix. The last two terms which are obtained from the linearization of the constitutive equations while keeping the geometry constant will produce the material tangent stiffness matrix. We notice from the first part of Equation (4.93) that the second variation of strain the measures, thus the second variation of the kinematic variables are necessary, in order to carry out the linearization of that term and this will be considered next.

4.4.1 Second Variation of Kinematic Variables

The second variations of d_1 and d_3 are obtained by applying the operator Δ to Equations (4.26) and (4.28), respectively. Thus $\Delta\delta d_1$ and $\Delta\delta d_3$ are given by

$$\Delta\delta d_1 = \Delta R(\delta\psi \times E_3) + R(\Delta\delta\psi \times E_3) = R[\Delta\psi \times (\delta\psi \times E_3) + \Delta\delta\psi \times E_3] \quad (4.94)$$

$$\Delta\delta d_3 = \Delta R(\delta\psi \times D_3 + \delta D_3) + R(\Delta\delta\psi \times D_3 + \delta\psi \times \Delta D_3)$$

$$= \mathbf{R} [\Delta\boldsymbol{\psi} \times (\delta\boldsymbol{\psi} \times \mathbf{D}_3) + \Delta\boldsymbol{\psi} \times \delta\mathbf{D}_3 + \delta\boldsymbol{\psi} \times \Delta\mathbf{D}_3 + \Delta\delta\boldsymbol{\psi} \times \mathbf{D}_3] \quad (4.95)$$

Our goal now is to find the relation between $\Delta\delta\boldsymbol{\psi}$ and $\Delta\boldsymbol{\theta}$ and $\delta\boldsymbol{\theta}$. We mention here that $\Delta\delta\boldsymbol{\theta} = 0$ because $\boldsymbol{\theta}$ is the primary variable in the explicit representation of the rotation matrix \mathbf{R} .

Taking the variation of Equation (4.30) we obtain

$$\begin{aligned} \Delta\delta\boldsymbol{\psi} &= \Delta\mathbf{T}(\boldsymbol{\theta})\delta\boldsymbol{\theta} = \left(\frac{\|\boldsymbol{\theta}\| \cos(\|\boldsymbol{\theta}\|) - \sin(\|\boldsymbol{\theta}\|)}{\|\boldsymbol{\theta}\|^2} \right) (\Delta\boldsymbol{\theta} \cdot \mathbf{e}) \delta\boldsymbol{\theta} \\ &+ \left(\frac{2 - 2 \cos(\|\boldsymbol{\theta}\|) - \|\boldsymbol{\theta}\| \sin(\|\boldsymbol{\theta}\|)}{\|\boldsymbol{\theta}\|^2} \right) (\Delta\boldsymbol{\theta} \cdot \mathbf{e}) (\mathbf{e} \times \delta\boldsymbol{\theta}) - \left(\frac{1 - \cos(\|\boldsymbol{\theta}\|)}{\|\boldsymbol{\theta}\|^2} \right) \Delta\boldsymbol{\theta} \times \delta\boldsymbol{\theta} \\ &+ \left(\frac{3 \sin(\|\boldsymbol{\theta}\|) - 2\|\boldsymbol{\theta}\| - \|\boldsymbol{\theta}\| \cos(\|\boldsymbol{\theta}\|)}{\|\boldsymbol{\theta}\|^2} \right) (\Delta\boldsymbol{\theta} \cdot \mathbf{e}) (\delta\boldsymbol{\theta} \cdot \mathbf{e}) \mathbf{e} \\ &+ \left(\frac{\|\boldsymbol{\theta}\| - \sin(\|\boldsymbol{\theta}\|)}{\|\boldsymbol{\theta}\|^2} \right) ((\delta\boldsymbol{\theta} \cdot \Delta\boldsymbol{\theta}) \mathbf{e} + (\delta\boldsymbol{\theta} \cdot \mathbf{e}) \Delta\boldsymbol{\theta}) \end{aligned} \quad (4.96)$$

As $\|\boldsymbol{\theta}\| \rightarrow 0$, Equation (4.96) reduces to a very simple expression

$$\Delta\delta\boldsymbol{\psi} = \frac{1}{2} \delta\boldsymbol{\theta} \times \Delta\boldsymbol{\theta} \quad (4.97)$$

A similar finding is reported in reference [22]. Using this result and that of Equation (4.31) we obtain

$$\Delta\delta\mathbf{d}_1 = \mathbf{R} \left[\frac{1}{2} ((\Delta\boldsymbol{\theta} \cdot \mathbf{E}_3) \delta\boldsymbol{\theta} + (\delta\boldsymbol{\theta} \cdot \mathbf{E}_3) \Delta\boldsymbol{\theta}) - (\Delta\boldsymbol{\theta} \cdot \delta\boldsymbol{\theta}) \mathbf{E}_3 \right] \quad (4.98)$$

$$\Delta\delta\mathbf{d}_3 = \mathbf{R} \left[\frac{1}{2} ((\Delta\boldsymbol{\theta} \cdot \mathbf{D}_3) \delta\boldsymbol{\theta} + (\delta\boldsymbol{\theta} \cdot \mathbf{D}_3) \Delta\boldsymbol{\theta}) + \Delta\boldsymbol{\theta} \times \delta\mathbf{D}_3 + \delta\boldsymbol{\theta} \times \Delta\mathbf{D}_3 - (\Delta\boldsymbol{\theta} \cdot \delta\boldsymbol{\theta}) \mathbf{D}_3 \right] \quad (4.99)$$

It can be noticed that these two equations show symmetry with respect to the differential operators δ and Δ ; thus this leads to the symmetry of the geometric stiffness matrix, which depends on the second variations of \mathbf{d}_1 and \mathbf{d}_3 . Equations (4.98) and (4.99) are general, i.e. they are valid in the presence of drilling rotations. Since in this study $\delta\theta$ and $\Delta\theta$ are normal to \mathbf{E}_3 , the first two terms of Equation (4.98) will vanish. Making use of Equation (4.36) into Equations (4.99) and after some manipulations we get

$$\Delta\delta\mathbf{d}_1 = -(\delta\mathbf{d}_1 \cdot \Delta\mathbf{d}_1)\mathbf{d}_1 \quad (4.100)$$

$$\Delta\delta\mathbf{d}_3 = -\frac{1}{2}[(\delta\mathbf{d}_1 \cdot \mathbf{d}_3)\Delta\mathbf{d}_1 + (\Delta\mathbf{d}_1 \cdot \mathbf{d}_3)\delta\mathbf{d}_1] - (\delta\mathbf{d}_3 \cdot \Delta\mathbf{d}_1)\mathbf{d}_1 - (\Delta\mathbf{d}_3 \cdot \delta\mathbf{d}_1)\mathbf{d}_1 \quad (4.101)$$

The interpolation of the second variations of \mathbf{d}_1 and \mathbf{d}_3 are based on Equations (4.50) where the operator Δ is substituted by $\Delta\delta$. This yields

$$\Delta\delta\mathbf{d}_1 = \sum_{I=1}^4 N^I(\xi, \eta) \Delta\delta\mathbf{d}_1^I \quad \Delta\delta\mathbf{d}_3 = \sum_{I=1}^4 N^I(\xi, \eta) \Delta\delta\mathbf{d}_3^I \quad (4.102)$$

The interpolation of the derivatives of $\Delta\delta\mathbf{d}_1$ and $\Delta\delta\mathbf{d}_3$ with respect to ξ and η are given by

$$\Delta\delta\mathbf{d}_{1,\alpha} = \sum_{I=1}^4 N_{,\alpha}^I(\xi, \eta) \Delta\delta\mathbf{d}_1^I \quad \Delta\delta\mathbf{d}_{3,\alpha} = \sum_{I=1}^4 N_{,\alpha}^I(\xi, \eta) \Delta\delta\mathbf{d}_3^I \quad (4.103)$$

where

$$\Delta\delta\mathbf{d}_{1(I)} = -(\delta\mathbf{d}_{1(I)} \cdot \Delta\mathbf{d}_{1(I)})\mathbf{d}_{1(I)} \quad (4.104)$$

$$\Delta\delta\mathbf{d}_{3(I)} = -\frac{1}{2}[(\delta\mathbf{d}_{1(I)} \cdot \mathbf{d}_{3(I)})\Delta\mathbf{d}_{1(I)} + (\Delta\mathbf{d}_{1(I)} \cdot \mathbf{d}_{3(I)})\delta\mathbf{d}_{1(I)}]$$

$$- (\delta d_{3(I)} \cdot \Delta d_{1(I)}) d_{1(I)} - (\Delta d_{3(I)} \cdot \delta d_{1(I)}) d_{1(I)} \quad (4.105)$$

are obtained from Equations (4.100) and (4.101) applied at node I. This ends the treatment of $\Delta \delta d_1$, $\Delta \delta d_3$ and their derivatives with respect to ξ and η which will be used for the construction of the geometric stiffness matrix.

4.4.2 Material stiffness Operator

The material stiffness operator is given, as indicated above, by the first two terms of Equation (4.93)

$$D_M [\delta w_I] \cdot \{\Delta \phi\} = \sum_{N=1}^{NEL} \int_{\Omega_N^e} \left(\sum_{n=0}^3 \left\{ \delta \varepsilon^{(n)} \right\}^T D \left\{ m^{(n)} \right\} \cdot \{\Delta \phi\} + \sum_{k=0,2} \left\{ \delta \gamma^{(k)} \right\}^T D \left\{ Q^{(k)} \right\} \cdot \{\Delta \phi\} \right) d\Omega^e \quad (4.106)$$

where

$$D \left\{ m^{(n)} \right\} \cdot \{\Delta \phi\} = \sum_{i=0}^3 \left[C_p^{n+i} \right] \left\{ \Delta \varepsilon^{(i)} \right\} = \sum_{i=0}^3 \left[C_p^{n+i} \right] \left[B_p^{(i)} \right] \{\Delta \phi\} \quad (4.107)$$

$$D \left\{ Q^{(k)} \right\} \cdot \{\Delta \phi\} = \sum_{j=0,2} \left[C_s^{k+j} \right] \left\{ \Delta \gamma^{(j)} \right\} = \sum_{j=0,2} \left[C_s^{k+j} \right] \left[B_s^{(j)} \right] \{\Delta \phi\} \quad (4.108)$$

The strain displacement operators $\left[B_p^{(i)} \right]$ and $\left[B_s^{(j)} \right]$ are detailed in section (4.2.5).

Using Equations (4.107) and (4.108), Equation (4.106) becomes

$$D_M [\delta w_I] \cdot \{\Delta \phi\} = \sum_{N=1}^{NEL} \{\Delta \phi\}_N^T [KM]^N \{\Delta \phi\}_N \quad (4.109)$$

where

$$[KM]^N = \int_{\Omega_N^0} \left(\sum_{n=0}^3 \sum_{i=0}^3 [B_p^{(n)}]^T [C_p^{n+i}] [B_p^{(i)}] + \sum_{k=0,2} \sum_{j=0,2} [B_s^{(k)}]^T [C_s^{k+j}] [B_s^{(j)}] \right) d\Omega^0 \quad (4.110)$$

represents the material tangent stiffness matrix of element N . Using Gauss-Quadrature method to numerically integrate Equation (4.110) over the domain Ω_N^0 and using the discretized strain displacement operators, Equation (4.109) becomes

$$D_M [\delta W_I] \cdot \{\Delta \phi\} = \sum_{N=1}^{NEL} \sum_{I=1}^4 \sum_{J=1}^4 \{\Delta \phi\}_{N(I)}^T [KM]_{IJ}^N \{\Delta \phi\}_{N(J)} \quad (4.111)$$

where $[KM]_{IJ}^N$ is a 7x7 submatrix of the total 28x28 element matrix $[KM]^N$ given by

$$[KM]_{IJ}^N = \sum_{G=1}^{NG\text{-pts}} \left(\sum_{n=0}^3 \sum_{i=0}^3 [B_p^{(n)}]_I^T [C_p^{n+i}] [B_p^{(i)}]_J + \sum_{k=0,2} \sum_{j=0,2} [B_s^{(k)}]_I^T [C_s^{k+j}] [B_s^{(j)}]_J \right) \sqrt{A_G} W_G \quad (4.112)$$

where NG-pts represents the total number of sampling Gauss points taken over the domain Ω_N^0 , W_G is an appropriate weight and A_G is the determinant of the metric tensor $A_{\alpha\beta}$ evaluated at the sampling Gauss point G

4.4.3 Geometric Stiffness Operator

The two terms contributing to the geometric tangent stiffness operator are given by

$$D_G [\delta w_I] \cdot \{\Delta \phi\} = \sum_{N=1}^{NEL} \int_{\Omega_N^0} \left(\sum_{n=0}^3 D \left\{ \delta \varepsilon \right\}^T \cdot \{\Delta \phi\} \left\{ m \right\} + \sum_{k=0,2} D \left\{ \delta \gamma \right\}^T \cdot \{\Delta \phi\} \left\{ Q \right\} \right) d\Omega^0 \quad (4.113)$$

Here for convenience, we rewrite Equation (4.113) using the indicial notation for strains and stress resultants.

$$D_G[\delta w_I] \cdot \{\Delta \phi\} = \sum_{N=1}^{NEL} \int_{\Omega_N^*} \left(\sum_{n=0}^j m^{\alpha\beta} \Delta \delta E_{\alpha\beta}^{(n)} + 2 \sum_{k=0,2}^{(k)} Q^\alpha \Delta \delta E_{\alpha 3}^{(k)} \right) d\Omega^o \quad (4.114)$$

where

$$m^{\alpha\beta} \Delta \delta E_{\alpha\beta}^{(0)} = m^{\alpha\beta} \delta \varphi_{,\alpha} \cdot \Delta \varphi_{,\beta} \quad (4.115-a)$$

$$m^{\alpha\beta} \Delta \delta E_{\alpha\beta}^{(1)} = m^{\alpha\beta} \delta \varphi_{,\alpha} \cdot \Delta d_{1,\beta} + m^{\alpha\beta} \delta d_{1,\alpha} \cdot \Delta \varphi_{,\beta} + m^{\alpha\beta} \Delta \delta d_{1,\alpha} \cdot \varphi_{,\beta} \quad (4.115-b)$$

$$m^{\alpha\beta} \Delta \delta E_{\alpha\beta}^{(2)} = m^{\alpha\beta} \delta d_{1,\alpha} \cdot \Delta d_{1,\beta} + m^{\alpha\beta} \Delta \delta d_{1,\alpha} \cdot d_{1,\beta} \quad (4.115-c)$$

$$m^{\alpha\beta} \Delta \delta E_{\alpha\beta}^{(3)} = m^{\alpha\beta} \delta \varphi_{,\alpha} \cdot \Delta d_{3,\beta} + m^{\alpha\beta} \delta d_{3,\alpha} \cdot \Delta \varphi_{,\beta} + m^{\alpha\beta} \Delta \delta d_{3,\alpha} \cdot \varphi_{,\beta} \quad (4.115-d)$$

$$2 Q^\alpha \Delta \delta E_{\alpha 3}^{(2)} = 3 Q^\alpha \left(\delta \varphi_{,\alpha} \cdot \Delta d_3 + \delta d_3 \cdot \Delta \varphi_{,\alpha} + \Delta \delta d_3 \cdot \varphi_{,\alpha} \right) \quad (4.115-e)$$

The terms $\Delta \delta E_{\alpha 3}^{(0)}$ will be computed using the assumed strain method i.e.

$$\begin{cases} \Delta \delta E_{13}^{(0)} = \frac{1}{2}(1-\eta) \Delta \delta E_{13}^B + \frac{1}{2}(1+\eta) \Delta \delta E_{13}^D \\ \Delta \delta E_{23}^{(0)} = \frac{1}{2}(1-\xi) \Delta \delta E_{23}^A + \frac{1}{2}(1+\xi) \Delta \delta E_{23}^C \end{cases} \quad (4.116)$$

$\Delta \delta E_{13}^B$, $\Delta \delta E_{13}^D$, $\Delta \delta E_{23}^A$ and $\Delta \delta E_{23}^C$ will be computed by applying the operator Δ to

Equations (4.22) and (4.23) to obtain

$$\Delta\delta E_{\alpha\beta}^{(o)} = \frac{1}{2} (\delta\varphi_{,\alpha} \cdot \Delta d_{,\beta} + \delta d_{,\beta} \cdot \Delta\varphi_{,\alpha} + \Delta\delta d_{,\beta} \cdot \varphi_{,\alpha}) \quad (4.117)$$

and then, the appropriate values of coordinates (ξ, η) corresponding to each point are used. In a similar way, Equation (4.114) can be put in the following form

$$D_G [\delta W_I] \cdot \{\Delta\phi\} = \sum_{N=1}^{NEL} \{\Delta\phi\}_N^T [KG]^N \{\Delta\phi\}_N \quad (4.118)$$

where $[KG]^N$ is the geometric tangent stiffness matrix. Introducing numerical integration and discrete strain displacement operator as done for the material tangent stiffness matrix, Equation (4.118) becomes

$$D_G [\delta W_I] \cdot \{\Delta\phi\} = \sum_{N=1}^{NEL} \sum_{I=1}^4 \sum_{J=1}^4 \{\Delta\phi\}_{N(I)}^T [KG]_{IJ}^N \{\Delta\phi\}_{N(J)} \quad (4.119)$$

Further details concerning the construction of submatrices $[KG]_{IJ}^N$ are found in Appendix I

CHAPTER 5

STATIC SOLUTION PROCEDURE

5.1. Introduction

As mentioned in the previous chapter, the Newton Raphson method will be used for the solution of the system of equations obtained through the discretization of the weak form of the equilibrium equations. This method will be introduced, first in its general form, then its algorithmic counterpart will be considered. Due to the presence of buckling problems in shells and the inability of the standard Newton Raphson method to deal with such situations, an adaptive strategy, the cylindrical arc-length method which is capable of tracing very complex equilibrium paths, is presented along with its algorithmic implementation. The last and important part of this chapter concerns the description of the implementation process based on the formulation derived in the two previous chapters. The essential tasks involved in the solution procedure are defined and explained along with the subroutines designed to perform them, then the flowchart of the designed computer program for the static analysis, with different levels of nesting between the subroutines, is presented including the cylindrical arc-length method.

5.2. Basic Newton-Raphson Method

The basic goal in a general nonlinear analysis is to find the state of equilibrium of a body corresponding to some applied loads or prescribed displacements. The first step in achieving this goal numerically is the introduction of the finite element discretization, which replaces the actual body by a system of finite elements. The equilibrium conditions corresponding to this system can be expressed as

$$\mathbf{F}_t^{\text{ext}} - \mathbf{F}_t^{\text{int}} = \mathbf{0} \quad (5.1)$$

where $\mathbf{F}_t^{\text{ext}}$ represents the vector of nodal external forces corresponding to configuration at time t and $\mathbf{F}_t^{\text{int}}$ contains the equivalent nodal forces corresponding to the element stresses in this configuration.

Equation (5.1) must be satisfied at each time t . In static case, t is only a convenient variable, which denotes different levels of load applications and correspondingly different configurations. The basic approach in solving Equation (5.1) is to start from the initial configuration and then proceed incrementally. Assuming that the solution is known for time t , then the equilibrium conditions are required for $t + \Delta t$ i.e.[8]

$$g(\hat{\Phi}) = \mathbf{F}_{t+\Delta t}^{\text{ext}}(\hat{\Phi}) - \mathbf{F}_{t+\Delta t}^{\text{int}}(\hat{\Phi}) = \mathbf{0} \quad (5.2)$$

where Δt is a suitably chosen increment and $\hat{\Phi}$ represents the, yet unknown configuration of the body at time $t + \Delta t$. Equation (5.2) will be solved iteratively. Assuming that the configuration at iteration $(i-1)$, $\Phi_{t+\Delta t}^{(i-1)}$, has been evaluated, then a truncated Taylor series expansion (linearization) of $g(\hat{\Phi})$ at $\Phi_{t+\Delta t}^{(i-1)}$ gives

$$g(\hat{\Phi}) = g(\Phi_{t+\Delta t}^{(i-1)}) + \left[\frac{\partial g}{\partial \Phi} \right]_{\Phi_{t+\Delta t}^{(i-1)}} \Delta \Phi^{(i)} \quad (5.3)$$

where $\Delta \Phi^{(i)}$ represents the iterative configuration change. Assuming that there is equilibrium at $\hat{\Phi}$, which means that Equation (5.2) is satisfied, we get

$$\left[\frac{\partial g}{\partial \Phi} \right]_{\Phi_{t+\Delta t}^{(i-1)}} \Delta \Phi^{(i)} = -g(\Phi_{t+\Delta t}^{(i-1)}) \quad (5.4)$$

Since this study is limited to external forces that are configuration independent, Equation (5.4) becomes

$$\left[\frac{\partial F^{int}}{\partial \Phi} \right]_{\Phi_{t+\Delta t}^{(i-1)}} \Delta \Phi^{(i)} = F_{t+\Delta t}^{ext} - F_{t+\Delta t}^{int}(\Phi_{t+\Delta t}^{(i-1)}) \quad (5.5)$$

We recognize here that

$$\left[\frac{\partial F^{int}}{\partial \Phi} \right]_{\Phi_{t+\Delta t}^{(i-1)}} = [K]_{t+\Delta t}^{(i-1)} \quad (5.6)$$

represents the total tangent stiffness matrix based on the configuration obtained at iteration (i-1) of time step $t + \Delta t$. Equation (5.5) can be written as

$$[K]_{t+\Delta t}^{(i-1)} \Delta \Phi^{(i)} = F_{t+\Delta t}^{ext} - F_{t+\Delta t}^{int}(\Phi_{t+\Delta t}^{(i-1)}) = F_{t+\Delta t}^{res(i-1)} \quad (5.7)$$

where $F_{t+\Delta t}^{res(i-1)}$ represents the residual (out of balance) force vector at iteration (i-1). Equations (5.6) and (5.7) constitute the Newton-Raphson solution of Equation (5.2). The initial conditions for starting this iterative scheme are as follow,

$$[K]_{t+\Delta t}^0 = [K] \quad ; \quad F_{t+\Delta t}^{int(0)} = F_t^{int} \quad ; \quad \Phi_{t+\Delta t}^{(0)} = \Phi_t \quad (5.8)$$

Iterations are repeated within this time step until appropriate convergence criterion is met. At each iteration, the iterative configuration changes $\Delta\Phi^{(i)}$ are used to update the structure configuration. This can be represented symbolically by

$$\Phi_{t+\Delta t}^{(i)} = \Phi_{t+\Delta t}^{(i-1)} + \Delta\Phi^{(i)} \quad (5.9)$$

Furthermore the external loading is often expressed in the proportional manner as

$$F_{t+\Delta t}^{ext} = \lambda_{t+\Delta t} F_0^{ext} \quad (5.10)$$

where F_0^{ext} is a base load vector and $\lambda_{t+\Delta t}$ is the current load factor. The total load is then applied in steps by specifying λ_{min} , λ_{max} , a load factor increment $\Delta\lambda$ and advancing the solution ($\lambda_{t+\Delta t} = \lambda_t + \Delta\lambda$) upon achieving convergence at each time step.

The basic Newton-Raphson algorithm is not adequate for situations where the equilibrium path contains limit (load or displacement) and bifurcation points, which are characteristics of shell buckling analysis. For such situations, various adaptive strategies have emerged [167]. Such strategies enable the analyst to proceed beyond critical points without worrying about the associated near singularity or negative definite stiffness matrices that have troubled earlier methods such as load controlled or displacement controlled methods. The arc length methods, which is one of the adaptive strategies, is discussed next.

5.3. Arc-Length Method

The arc-length method was originally introduced, with respect to structural analysis, by Riks [155,156] and Wempner [157] independently. It was modified later by Crisfield

[158,159] and others [160-166]. The arc-length ('cylindrical arc-length') method adopted in this study is based on Crisfield implementation [167]. Figure 5.1 shows four possible load/deflection curves involving limit points with both 'snap through' (5.1(a)) and 'snap back' (5.1(b)). These situations show the need for arc-length methods and similar techniques. Figures 5.1(a), 5.1(c) and 5.1(d) may be obtained by displacement controlled procedure. There are, however, occasions where this is difficult or impossible to apply [167]. The true response in Figures 5.1(a) and 5.1(b) involves dynamic effects. Under load control, the dynamic response in Figure 5.1(a) would follow the dashed line followed by possibly some oscillations around point C. In contrast, the solid static curve from A to C would maintain equilibrium but be unstable under load control but stable under displacement control. Under displacement control, the dynamic response in Figure 5.1(b) would follow the dashed line.

The starting point for arc-length method is to rewrite the equilibrium equation in the following form

$$g(\Phi, \lambda) = \lambda \mathbf{F}_0^{\text{ext}} - \mathbf{F}^{\text{int}}(\Phi) \quad (5.11)$$

where a proportional loading is assumed. The main essence of the arc-length method is that the load parameter λ becomes a variable, and will be computed via the quadratic constraint scalar equation

$$a = \Delta\Phi \cdot \Delta\Phi + \Delta\lambda^2 \psi^2 \mathbf{F}_0^{\text{ext}} \cdot \mathbf{F}_0^{\text{ext}} - \Delta l^2 = 0 \quad (5.12)$$

where

Δl is an approximation of the incremental arc-length.

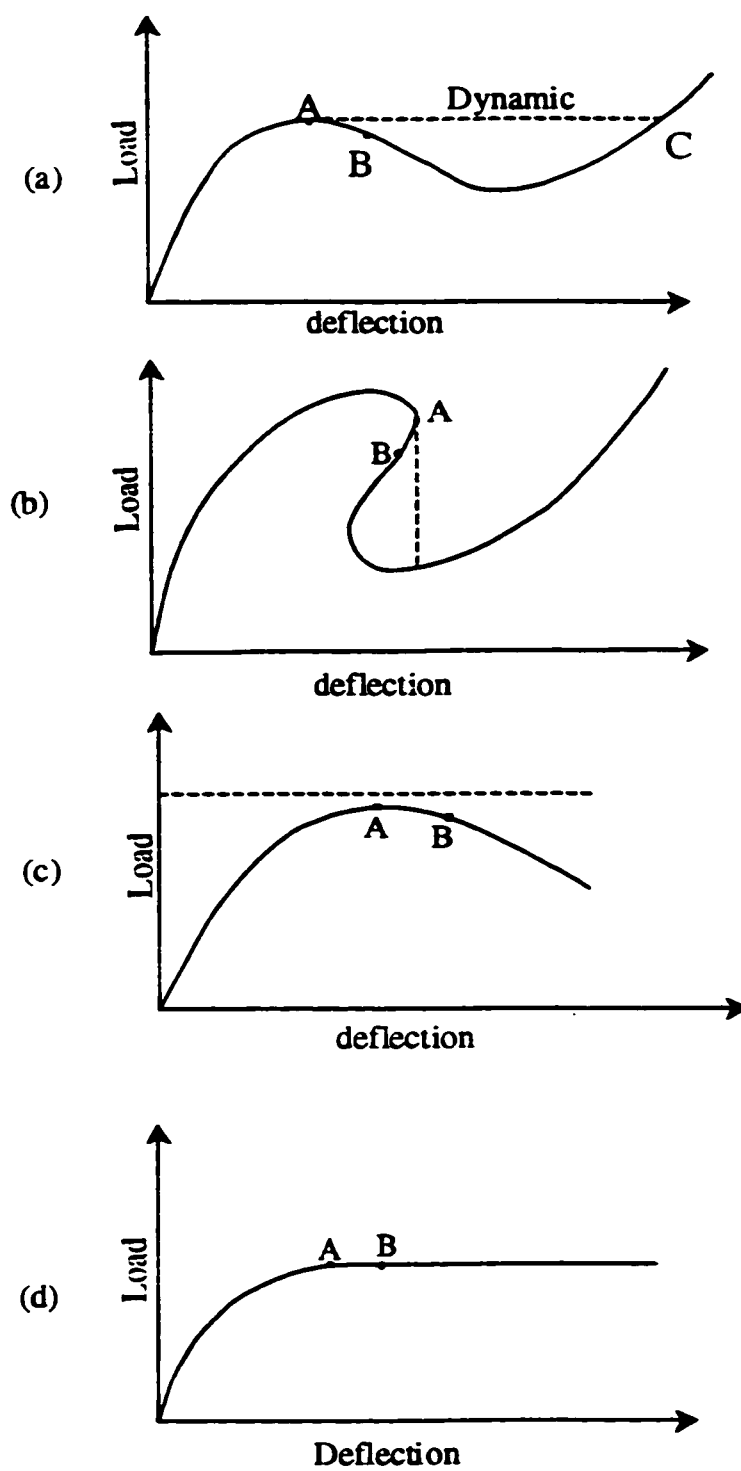


Figure 5.1 Various load/deflection curves : (a) snap through ; (b) snap back ; (c) 'brittle' collapse; (d) 'ductile' collapse

ψ is a scaling parameter, it is required because the load contribution depends on the adopted scaling between the load and displacement terms.

The vector $\Delta\Phi$ and the scalar $\Delta\lambda$ are incremental (not iterative) quantities and relate back to the last converged equilibrium state (see Figure 5.2).

Equation (5.12) imposes a constraint on the arc-length (along a curve in multi-dimensional load/deflection space) that may be traversed within a given load step. Hence, rather than specifying the load factor increment $\Delta\lambda$, the analyst specifies the arc length parameter Δl , and the algorithm increments (or decrements) the load accordingly.

Linearizing g at g_0 , we get

$$g_n = g_o + \left[\frac{\partial g}{\partial \Phi} \right] \delta\Phi + \left[\frac{\partial g}{\partial \lambda} \right] \delta\lambda = g_o - [K]_o \delta\Phi + \delta\lambda F_o^{ext} = 0 \quad (5.13)$$

where the subscripts 'n' and 'o' stand, respectively, for new and old. $\delta\Phi$ is the iterative correction in the current configuration, which can be obtained from Equation (5.13) as follows

$$\delta\Phi = [K]_o^{-1} g_o + \delta\lambda [K]_o^{-1} F_o^{ext} = \delta\bar{\Phi} + \delta\lambda \delta\hat{\Phi} \quad (5.14)$$

where $\delta\bar{\Phi}$ is the iterative change in the configuration produced by the standard load-controlled Newton-Raphson method (at a fixed load level λ_0). $\delta\hat{\Phi}$ is the change in the configuration produced by the fixed load vector F_o^{ext} . $\delta\lambda$ is still unknown in Equation (5.14) and can be obtained from Equation (5.12) by substituting $\Delta\Phi_n$ for $\Delta\Phi$ where

$$\Delta\Phi_n = \Delta\Phi_o + \delta\Phi = \Delta\Phi_o + \delta\bar{\Phi} + \delta\lambda \delta\hat{\Phi} \quad (5.15)$$

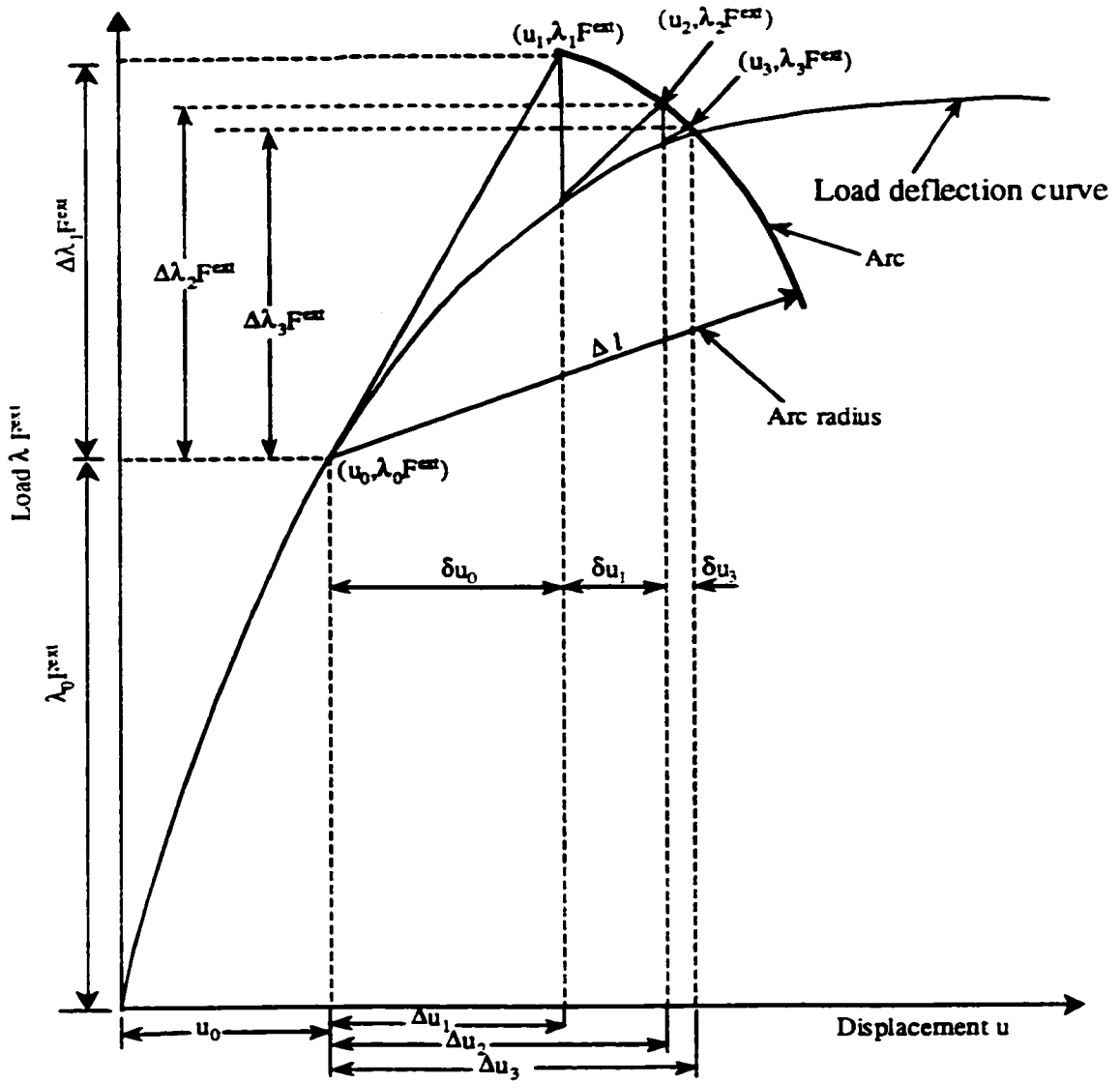


Figure 5.2 Arc-length procedure and notation for one degree of freedom system (with $\psi=1$)

and using $\psi = 0$. This last condition was arrived at by Crisfield [158] and Ramm [160,161] independently; they concluded that for practical problems involving a realistic number of variables, 'the loading terms' (i.e. those involving ψ) had little effect. Equation (5.12) becomes

$$\Delta\Phi_n \cdot \Delta\Phi_n - \Delta l^2 = a_1 \delta\lambda^2 + a_2 \delta\lambda + a_3 = 0 \quad (5.16)$$

where

$$a_1 = \delta\hat{\Phi} \cdot \delta\hat{\Phi} \quad (5.17a)$$

$$a_2 = 2\delta\hat{\Phi} \cdot (\Delta\Phi_o + \delta\bar{\Phi}) \quad (5.17b)$$

$$a_3 = (\Delta\Phi_o + \delta\bar{\Phi}) \cdot (\Delta\Phi_o + \delta\bar{\Phi}) - \Delta l^2 \quad (5.17c)$$

which can be solved for $\delta\lambda$ so that, from Equation (5.15), the complete change $\Delta\Phi_n$ is defined. Equation (5.16) yields two solutions ($\delta\lambda_1$ and $\delta\lambda_2$), thus two new configuration increments

$$\Delta\Phi_{n1} = \Delta\Phi_o + \delta\bar{\Phi} + \delta\lambda_1 \delta\hat{\Phi} \quad (5.18a)$$

$$\Delta\Phi_{n2} = \Delta\Phi_o + \delta\bar{\Phi} + \delta\lambda_2 \delta\hat{\Phi} \quad (5.18b)$$

The new incremental configuration ($\Delta\Phi_{n1}$ or $\Delta\Phi_{n2}$), whose direction lies the closest to the old incremental direction, i.e., that of $\Delta\Phi_o$, will be retained. This should prevent the solution from 'doubling back' on its track [167]. This can be implemented by finding the solution with minimum angle $\Delta\Phi_o$ and $\Delta\Phi_n$, thus the maximum cosine of the angle,

which is given by

$$\cos \theta = \frac{\Delta \Phi_o \cdot \Delta \Phi_o}{\Delta l^2} = \frac{a_4 + a_5 \delta \lambda}{\Delta l^2} \quad (5.19)$$

where

$$a_4 = \Delta \Phi_o \cdot \delta \bar{\Phi} + \Delta \Phi_o \cdot \Delta \Phi_o \quad (5.20a)$$

and

$$a_5 = \Delta \Phi_o \cdot \delta \hat{\Phi} \quad (5.20b)$$

Considering the 'predictor' solution, i.e., the solution obtained before starting the iterations, it is given by

$$\Delta \Phi_{i+\Delta t}^{(0)} = [K_{\tau}]^{-1} (F_{i+\Delta t}^{ext(0)} - F_{i+\Delta t}^{int(0)}) = [K_{\tau}]^{-1} (F_{i+\Delta t}^{ext(0)} - F_i^{ext}) = \Delta \lambda^{(0)} [K_{\tau}]^{-1} F_0^{ext} = \Delta \lambda^{(0)} \delta \hat{\Phi}_{i+\Delta t}^{(0)} \quad (5.21)$$

Substituting Equation (5.21) in the constraint Equation (5.16) yields

$$\Delta \lambda^{(0)} = \pm \frac{\Delta l}{\sqrt{\delta \hat{\Phi}_{i+\Delta t}^{(0)} \cdot \delta \hat{\Phi}_{i+\Delta t}^{(0)}}} = \text{sign} \frac{\Delta l}{\sqrt{\delta \hat{\Phi}_{i+\Delta t}^{(0)} \cdot \delta \hat{\Phi}_{i+\Delta t}^{(0)}}} \quad (5.22)$$

Equation (5.22) shows two possible choices because of the sign. This sign is taken as (+1) when $[K_{\tau}]$ (at the beginning of the increment is positive definite), i.e., when all terms in D , the diagonal matrix of LDL^T factorization of $[K_{\tau}]$, are positive. When one of these terms becomes negative, this means that we have overcome a limit point then the sign of 'sign' is set to (-1). After obtaining the predictor solution ($\Delta \Phi_{i+\Delta t}^{(0)}$ and $\Delta \lambda^{(0)}$), the updated configuration is obtained by

$$\Phi_{i+\Delta t}^{(0)} = \Phi_i + \Delta \Phi_{i+\Delta t}^{(0)} \quad ; \quad \lambda_{i+\Delta t}^{(0)} = \lambda_i + \Delta \lambda^{(0)} \quad (5.23)$$

Then, the iterative procedure is applied as follows:

$$\delta\hat{\Phi}_{t+\Delta t}^{(i)} = [K_T^{-1}]_{t+\Delta t}^{(i-1)} F_0^{ext} \quad (5.24)$$

$$\delta\bar{\Phi}_{t+\Delta t}^{(i)} = [K_T^{-1}]_{t+\Delta t}^{(i-1)} (\lambda_{t+\Delta t}^{(i-1)} F_0^{ext} - F_{t+\Delta t}^{int(i-1)}) \quad (5.25)$$

$$a_1 = \delta\hat{\Phi}_{t+\Delta t}^{(i)} \cdot \delta\hat{\Phi}_{t+\Delta t}^{(i)} \quad (5.26a)$$

$$a_2 = 2\delta\hat{\Phi}_{t+\Delta t}^{(i)} \cdot (\Delta\Phi_{t+\Delta t}^{(i-1)} + \delta\bar{\Phi}_{t+\Delta t}^{(i)}) \quad (5.26b)$$

$$a_3 = (\Delta\Phi_{t+\Delta t}^{(i-1)} + \delta\bar{\Phi}_{t+\Delta t}^{(i)}) \cdot (\Delta\Phi_{t+\Delta t}^{(i-1)} + \delta\bar{\Phi}_{t+\Delta t}^{(i)}) - \Delta t^2 \quad (5.26c)$$

$$a_4 = \Delta\Phi_{t+\Delta t}^{(i-1)} \cdot \delta\bar{\Phi}_{t+\Delta t}^{(i)} + \Delta\Phi_{t+\Delta t}^{(i-1)} \cdot \Delta\Phi_{t+\Delta t}^{(i-1)} \quad (5.26d)$$

$$a_5 = \Delta\Phi_{t+\Delta t}^{(i-1)} \cdot \delta\hat{\Phi}_{t+\Delta t}^{(i)} \quad (5.26e)$$

From the above expressions for a_i ($i = 1$ to 5), solve for $\delta\lambda^{(i)}$ using Equations (5.16) and

(5.19). Once $\delta\lambda^{(i)}$ is obtained, the incremental configuration change at iteration i is given by

$$\Delta\Phi_{t+\Delta t}^{(i)} = \Delta\Phi_{t+\Delta t}^{(i-1)} + \delta\bar{\Phi}_{t+\Delta t}^{(i)} + \delta\lambda^{(i)} \delta\hat{\Phi}_{t+\Delta t}^{(i)} \quad (5.27)$$

$$\Phi_{t+\Delta t}^{(i)} = \Phi_{t+\Delta t}^{(i-1)} + \delta\bar{\Phi}_{t+\Delta t}^{(i)} + \delta\lambda^{(i)} \delta\hat{\Phi}_{t+\Delta t}^{(i)} \quad (5.28)$$

The configuration update shown in Equation (5.28) is valid for translational degrees of freedom only. For the update of directors d_1 and d_3 , the expressions outlined in section 4.3.3. are used. Next, the internal forces are computed, based on the updated configurations. Then Equation (5.11) is check whether it is satisfied within a certain prescribed tolerance or not. If yes, we go to the next load step; otherwise, we go back to Equation (5.24) and keep iterating until the convergence criteria are satisfied.

5.4. Implementation

A computer program called **STLSHEL7** (**S**Tatic analysis of **L**aminated **S**HELLs having 7 degrees of freedom per node) is developed to implement the previously discussed shell model within the finite element method. This computer program is used to simulate the static response of general isotropic or laminated shell type structures with smooth surface subjected to external loads. The necessary steps concerning the global solution procedure of a nonlinear finite element problem including the arc-length method were discussed in the previous sections. Those concerning the laminated shell model, developed in this study, were outlined in the previous chapter. In this section, the implementation steps of the proposed shell model are enumerated. This flowchart-like account will be presented in three sections. The first one concerns the initial computations to be performed at the initial configuration, and the second one is aimed at the updates and stiffness calculations to be performed at the current configuration. The last part is devoted to the nesting of all the discussed steps in a global procedure. The entire program is written explicitly for this study; no parts of other programs are utilized unless otherwise stated.

5.4.1. Reference Configuration

5.4.1.1 Construction of Nodal Normals

After introducing the necessary data concerning the geometry, loading and boundary conditions of the problem, the first thing to be done in the reference configuration is the computation of the nodal normals $d_{i(I)}^0$, where I is the node number. In this case, the

program leaves the option of supplying none, some or all nodal normals and leaving the rest of them to be computed internally within a subroutine called **NORMALS**. This is done by looping over all elements and within each element, the four nodal normals are defined. It is worthy to mention here that the four-node quadrilateral elements don't have to be flat. Thus, the same element may have different nodal normals. Elements meeting at the same node are not required to be coplanar and this will result in different nodal normals for the same node. The remedy to this is to compute average normals (pseudo-normals) at each node as stated in Reference [23].

5.4.1.2 Identification of Nodal Reference Directions (Axes)

In the case of laminated fiber reinforced materials, the layers are designated by a laminate orientation code, which has evolved, through the years, in the composites literature [147,168]. This code is intended to adequately describe many possible combinations of ply orientations and stacking sequences in laminates. The identification of a laminate can be achieved through the use of the following orientation code:

1. Each layer is designated by a number indicating the value in degrees between its fiber direction and the direction of the reference axis
2. Successive layers are separated by a “/,” if their angles are different
3. Successive layers with the same orientation are denoted by a numerical index.
4. The layers are successively designated going from one face to the other. Brackets (or parentheses) indicate the beginning and end of the code. The designation depends on the system of axes chosen

The convention for positive and negative angles depends on the system of axes

chosen. The angle is measured from the reference axis to the fiber direction (less than or equal to 90 degrees). Assuming that x is the reference axis, Figure 5.3 shows positive and negative angles designating the fiber directions.

A laminate is symmetric if its geometric midplane is the plane of symmetry. It can be described, in this case, by listing only the ply angles of half of the laminate and using the subscript "s" outside the brackets. If a laminate has an even number of layers, its designation starts from a face and finishes at the plane of symmetry. If the symmetric laminate has an odd number of layers, its designation is similar to the previous one except that the center ply angle is denoted by an overbar. The sets of ply angles which are repeated in the laminate are identified by enclosing the set of angles in parentheses followed by an index indicating the number of times the set is successively repeated. Figure 5.4 shows examples of laminates and the corresponding laminate orientation code.

The reference axis discussed above is fixed in the case of laminated plates; however, it is not the case for laminated general shells. In this study, it is assumed that the stacking sequence remains the same, but with respect to a local reference axis tangent to the shell midsurface and whose spatial direction may change from point to point. The program user is asked to input the information concerning the different reference directions, and then identify the nodes with these directions so that each node is linked to a reference direction. This task is carried out in a subroutine called **DIRSEQ**

5.4.1.3 Construction of the Initial Nodal Rotation Matrices

It was mentioned in Chapter three that R_0 , which represents the initial value of the rotation matrix R , can be constructed based on the normals to the midsurface of the

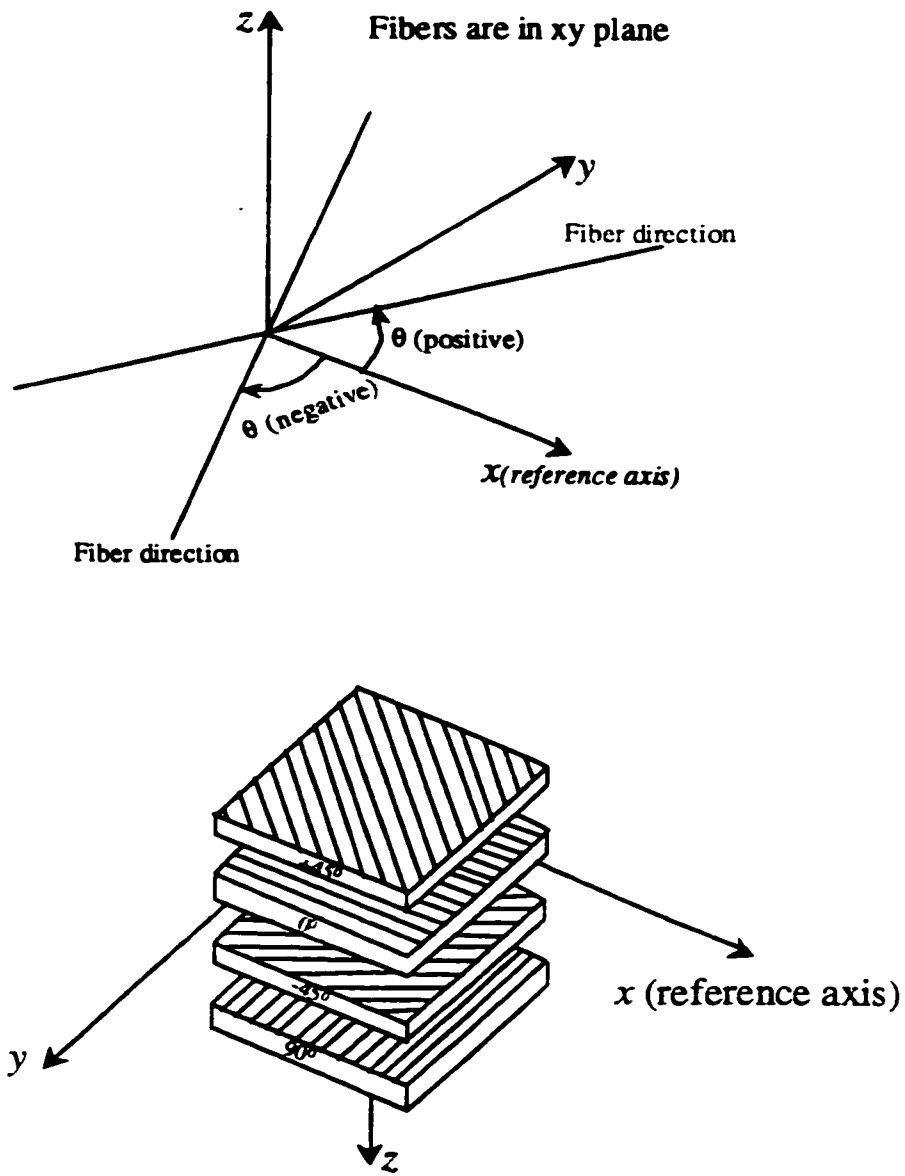


Figure 5.3 Sign convention for the stacking sequence in a laminate

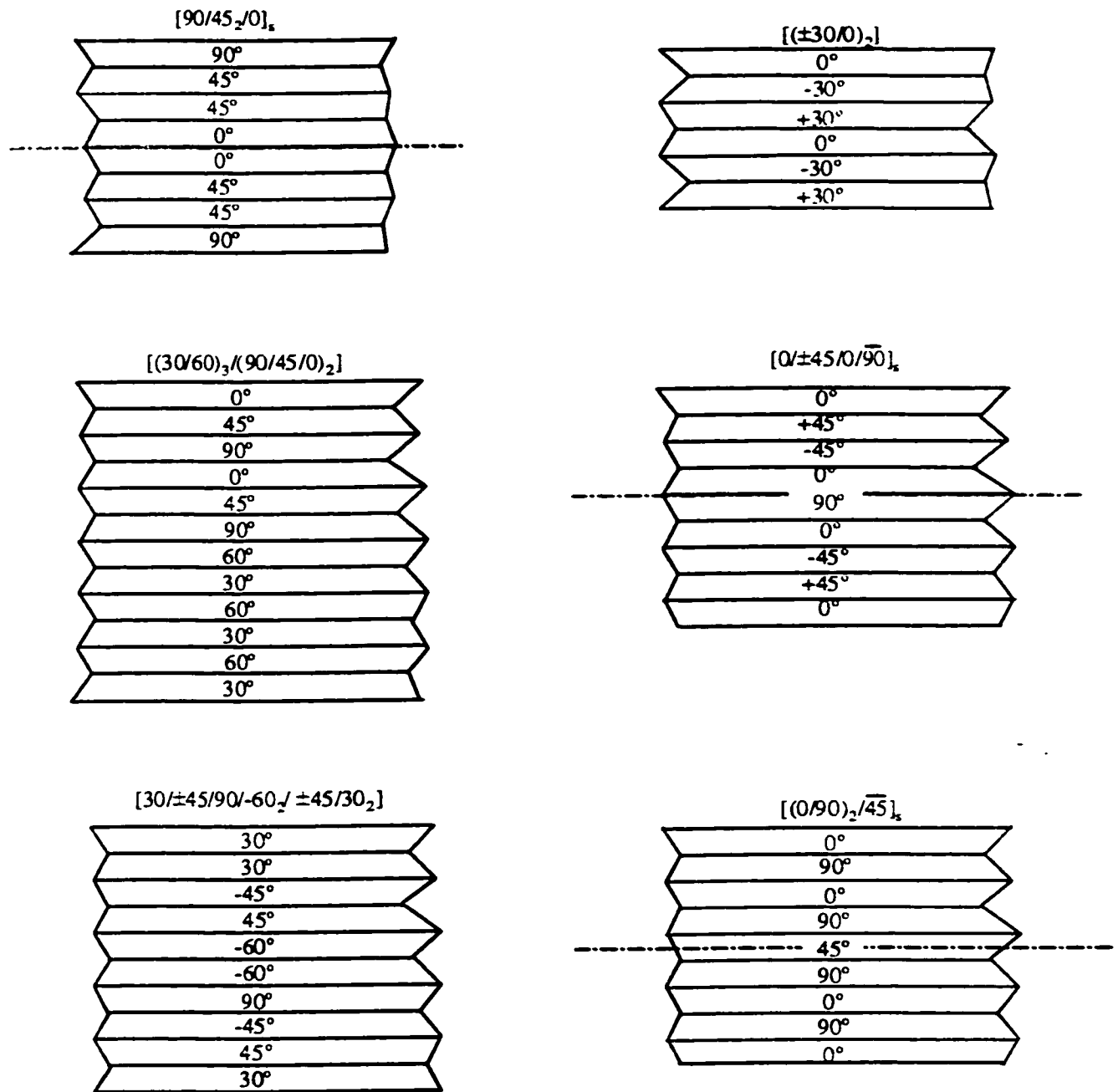


Figure 5.4 Examples of laminate stacking sequences and the corresponding laminate orientation code

shell body in the reference configuration. The three columns of the rotation matrix $\mathbf{R}_{(0)I}$ represent, respectively, the components of the vectors $(\mathbf{t}_{1(I)}^0, \mathbf{t}_{2(I)}^0, \mathbf{d}_{1(I)}^0)$ which form a basis at node I. Thus, $\mathbf{R}_{(0)I}$ maps the fixed reference basis $(\mathbf{E}_1, \mathbf{E}_2, \mathbf{E}_3)$ into the nodal basis $(\mathbf{t}_{1(I)}^0, \mathbf{t}_{2(I)}^0, \mathbf{d}_{1(I)}^0)$. It is expressed symbolically as follows

$$\mathbf{R}_{(0)I} [\mathbf{E}_1, \mathbf{E}_2, \mathbf{E}_3] = [\mathbf{t}_{1(I)}^0, \mathbf{t}_{2(I)}^0, \mathbf{d}_{1(I)}^0] \quad (5.29)$$

The expression of the initial nodal rotation matrix $\mathbf{R}_{(0)I}$ is given by [64]

$$\mathbf{R}_{(0)I} = (\mathbf{E}_3 \cdot \mathbf{d}_{1(I)}^0) I_3 + \overbrace{[\mathbf{E}_3 \times \mathbf{d}_{1(I)}^0]} + \frac{1}{1 + \mathbf{E}_3 \cdot \mathbf{d}_{1(I)}^0} (\mathbf{E}_3 \times \mathbf{d}_{1(I)}^0) \otimes (\mathbf{E}_3 \times \mathbf{d}_{1(I)}^0) \quad (5.30)$$

where $\overbrace{[\mathbf{E}_3 \times \mathbf{d}_{1(I)}^0]}$ represents the skew symmetric matrix associated with the axial vector $(\mathbf{E}_3 \times \mathbf{d}_{1(I)}^0)$. It can be noticed from Equation (5.30) that when $\mathbf{d}_{1(I)}^0 = -\mathbf{E}_3$, the denominator of the third term becomes zero, thus inducing a singularity. In this case $\mathbf{R}_{(0)I}$ is given by (see Figure 5.5(a))

$$\mathbf{R}_{(0)I} = \begin{bmatrix} 1 & 0 & 0 \\ 0 & -1 & 0 \\ 0 & 0 & -1 \end{bmatrix} \quad (5.31)$$

Equation (5.31) is based on the rotation of \mathbf{E}_3 about \mathbf{E}_1 with an angle equal to π .

Nodes located on the boundary of the shell structure may have some restraining along some of their degrees of freedom (translation or rotation). In the presence of skew boundary conditions, a new reference frame $(\mathbf{E}_1', \mathbf{E}_2', \mathbf{E}_3')$ is defined for each of these

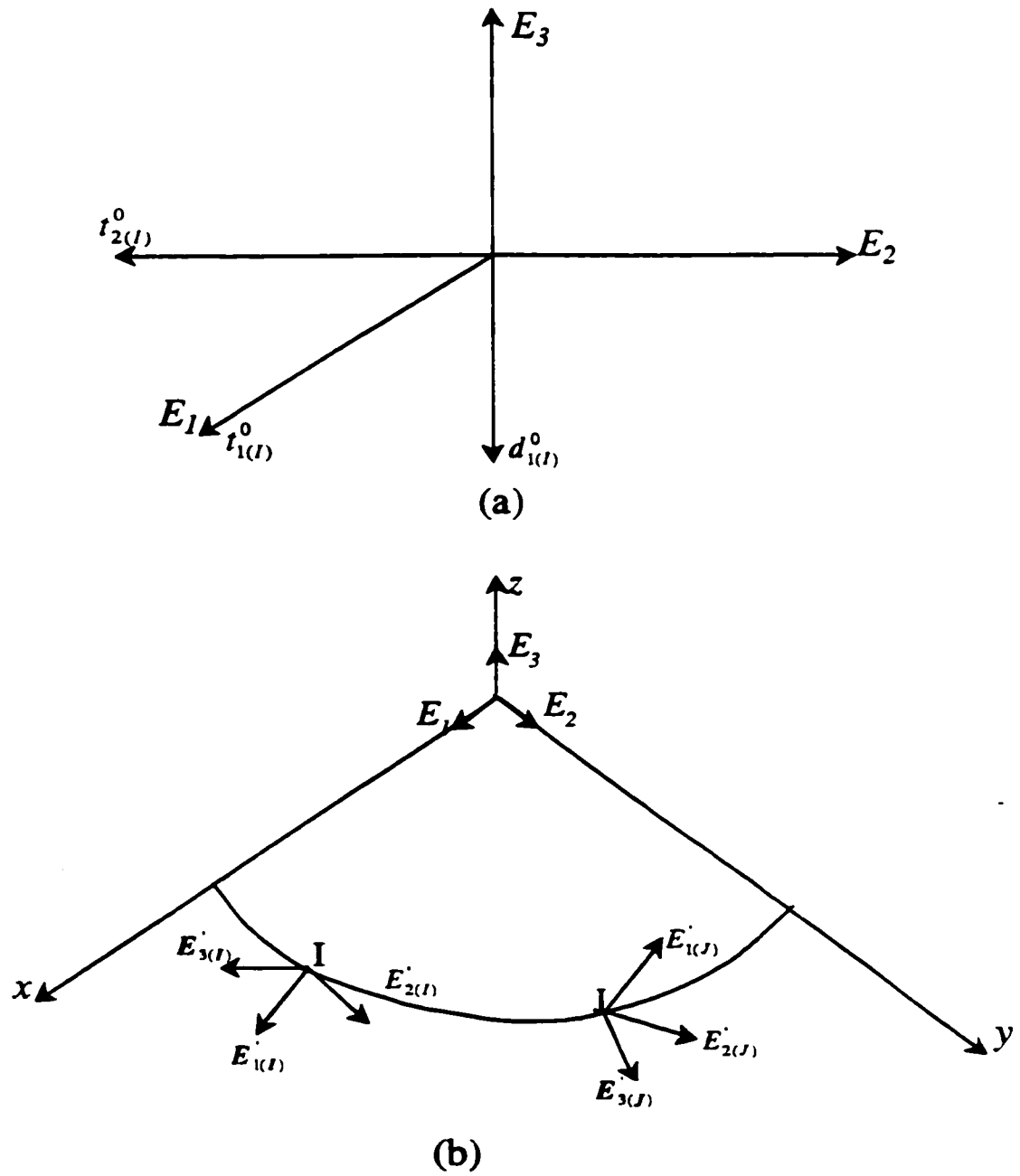


Figure 5.5 (a) Nodal bases in case $d_{1(l)}^0 = -E_3$
 (b) Local frames for skewed boundary conditions

nodes (see Figure 5.5(b)). Thus, the boundary conditions concerning these nodes are specified in these new reference frames.

5.4.1.4 Construction of Cartesian Reference Frames at Integration Points for Composite Materials

In case of composite materials, it is necessary to erect local cartesian frames at Gauss points (sampling points used during the numerical integration) where one of the axes tangent to the shell surface should be in the direction of the reference axis. This reference axis is furnished for nodal points; thus, we need to use interpolation functions to find the reference directions at Gauss points. Suppose that the unit vector in the reference direction, at a Gauss point, is denoted by $e_{1\text{ ref}(G)}$; it is given by

$$e_{1\text{ ref}(G)} = \frac{\sum_{I=1}^4 N^I(\xi_G, \eta_G) e_{1\text{ ref}(I)}}{\left| \sum_{I=1}^4 N^I(\xi_G, \eta_G) e_{1\text{ ref}(I)} \right|} \quad (5.32)$$

where $e_{1\text{ ref}(I)}$ represents the reference direction at node I.

The normal at Gauss point G is $d_{1(G)}^0$; it is given by Equation (4.48) with ξ and η taking, respectively, the values ξ_G and η_G . The base for the reference cartesian frame at Gauss point G is $(e_{1\text{ ref}(G)}, e_{2\text{ ref}(G)}, d_{1(G)}^0)$, where $e_{2\text{ ref}(G)}$ is the second tangent to the shell surface and normal to $e_{1\text{ ref}(G)}$; it is given by

$$e_{2\text{ ref}(G)} = \frac{d_{1(G)}^0 \times e_{1\text{ ref}(G)}}{\left| d_{1(G)}^0 \times e_{1\text{ ref}(G)} \right|} = \frac{(\varphi_{,1(G)} \times \varphi_{,2(G)}) \times e_{1\text{ ref}(G)}}{\left| (\varphi_{,1(G)} \times \varphi_{,2(G)}) \times e_{1\text{ ref}(G)} \right|} \quad (5.33)$$

Once the reference basis $(e_{1\text{ref}(G)}, e_{2\text{ref}(G)})$ is established, the angles of the stacking sequence will be used to find the principal bases (e_1, e_2) corresponding to each layer.

5.4.1.5 Computation of Metric Tensor Coefficients at Integration Points

In the implementation of the shell model, case 1 of section 4.2.1 was considered where the metric G of the laminate is approximated by that of the reference surface Ω^0 , i.e., A . Thus,

$$G_\alpha = A_\alpha \quad ; \quad G^\beta = A^\beta \quad ; \quad \mu = 1 \quad (5.34a,b,c)$$

The coefficients $A^{\alpha\beta}$ are needed in isotropic constitutive equations, whereas the reciprocal bases A^β are used in computing the coefficients $C_{\alpha\beta}$ of Equation (3.108) which are needed in transforming the constitutive equations from local principal directions to laminate coordinates in the case of composite material. From A_α , which are computed using Equations (3.21), A^β can be obtained using

$$A^\beta = A^{\beta\alpha} A_\alpha \quad (5.35)$$

where

$$A^{\beta\alpha} A_{\alpha\lambda} = \delta_\lambda^\alpha \quad (5.36)$$

Equation (5.36) shows that $A^{\beta\alpha}$ is the inverse of $A_{\alpha\lambda}$. Using matrix notation, we get

$$[A^{\beta\alpha}] = [A_{\alpha\lambda}]^{-1} = \begin{bmatrix} A_{11} & A_{12} \\ A_{12} & A_{22} \end{bmatrix}^{-1} = \frac{1}{A} \begin{bmatrix} A_{22} & -A_{12} \\ -A_{12} & A_{11} \end{bmatrix} \quad (5.37)$$

where

$$A = A_{11}A_{22} - A_{12}^2. \quad (5.38)$$

Equation (5.37) implies the following expressions

$$A^{11} = \frac{A_{22}}{A} \quad ; \quad A^{12} = A^{21} = -\frac{A_{12}}{A} \quad ; \quad A^{22} = \frac{A_{11}}{A} \quad (5.39)$$

Applying Equation (5.35) and (5.39), we obtain

$$A^1 = A^{11}A_1 + A^{12}A_2 = \frac{1}{A}(A_{22}A_1 - A_{12}A_2) \quad (5.40)$$

$$A^2 = A^{21}A_1 + A^{22}A_2 = \frac{1}{A}(-A_{12}A_1 + A_{11}A_2) \quad (5.41)$$

The above three tasks (construction of nodal rotation matrices, construction of cartesian reference frames and computation of A^α and $A^{\alpha\beta}$) are performed within a subroutine called **REFCONFIG**.

5.4.1.6 Construction of Stiffness Coefficient Matrices

In the case of isotropic material, there is no need to construct a local cartesian frame at each Gauss point because the constitutive equations are directly given with respect to laminate coordinates and the quantities needed are the coefficients $A^{\beta\alpha}$, given by Equation (5.39), and used in Equations (3.80) and (3.81). For composite laminates, Equations (3.103) are used to compute the layer stiffness coefficients C_L^{ijkl} followed by Equations (4.15) and (4.16) to evaluate the laminate stiffness coefficient matrices $\overset{i}{C}_P$ ($i = 0, 1, \dots, 6$) and $\overset{j}{C}_S$ ($j = 0, 2, 4$). At each Gauss point, a subroutine called **CONSTMAT** is called by **REFCONFIG** to loop over all layers and generate the laminate stiffness coefficient matrices and then store them internally so that they can be retrieved by other subroutines to compute the tangent stiffness matrix and internal forces.

5.4.2 Current Configuration

we are concerned here about the tasks performed repeatedly based on the current configuration. They comprise:

- the update of the structure configuration
- the computation of Green strains and the internal stress resultants at Gauss points
- the update of the discrete strain displacement operators
- the computation of the element internal force vectors and their contribution to the structure (global) internal force vector
- the computation of the element material and geometric tangent stiffness matrices and the assembly into the structure tangent stiffness matrix.

The update of the structure configuration was detailed in section 4.3.3. It starts by updating the nodal quantities $\varphi_{(I)}$, $d_{1(I)}$, $d_{3(I)}$ and $\bar{R}_{(I)}$. This task is carried out in a subroutine called **UPDATE**. The subroutine **RSPSHEL7**, which is also concerned with the structure update besides other computations, starts by localizing nodal quantities to the element level. Afterwards, it updates the director d_1 at assumed strain points A,B,C, and D followed by the update of d_1 and d_3 at the Gauss points along with the derivatives $\varphi_{,\alpha}$, $d_{1,\alpha}$ and $d_{3,\alpha}$.

The computation of Green strains ($E_{\alpha\beta}^{(n)}$, ($n=0,1,2,3$), $E_{\alpha 3}^{(k)}$ ($k=0,2$)), internal stress resultants ($m^{\alpha\beta}$, Q^α) and the update of the discrete strain displacement operators

($[B_p]_I$, $[B_s]_I$, $I=1,4$) at each Gauss point are treated in a subroutine called **RSPSHEL7**. The contribution of the internal stress resultants at each Gauss point to the

element internal force vector is as follows:

Considering the discretized internal virtual work expression (4.92)

$$\delta W_I = \sum_{N=1}^{NEL} \int_{\Omega_N^e} \left(\sum_{n=0}^3 \left\{ \delta \boldsymbol{\varepsilon}^{(n)} \right\}^T \left\{ \boldsymbol{m}^{(n)} \right\} + \sum_{k=0,2} \left\{ \delta \boldsymbol{\gamma}^{(k)} \right\}^T \left\{ \boldsymbol{Q}^{(k)} \right\} \right) d\Omega^e \quad (5.42)$$

and substituting the discretized strain displacement operators $[\boldsymbol{B}_P]^{(n)}$ and $[\boldsymbol{B}_S]^{(k)}$ given, respectively, by their expressions in Equations (4.83)-(4.91), Equation (5.42) becomes

$$\delta W_I = \sum_{N=1}^{NEL} \int_{\Omega_N^e} \left(\sum_{n=0}^3 \sum_{I=1}^4 \left\{ \delta \boldsymbol{\Phi}^{(n)} \right\}_I^T [\boldsymbol{B}_P]_I^{(n)} \left\{ \boldsymbol{m}^{(n)} \right\} + \sum_{k=0,2} \sum_{I=1}^4 \left\{ \delta \boldsymbol{\Phi}^{(n)} \right\}_I^T [\boldsymbol{B}_S]_I^{(k)} \left\{ \boldsymbol{Q}^{(k)} \right\} \right) d\Omega^e \quad (5.43)$$

Introducing Gauss quadrature (numerical integration), Equation (5.43) becomes

$$\begin{aligned} \delta W_I &= \sum_{N=1}^{NEL} \sum_{G=1}^{NG-ps} \sum_{I=1}^4 \left\{ \delta \boldsymbol{\Phi}^{(n)} \right\}_I^T \left(\sum_{n=0}^3 [\boldsymbol{B}_P]_I^{(n)} \left\{ \boldsymbol{m}^{(n)} \right\} \sqrt{A_G} W_G + \sum_{k=0,2} [\boldsymbol{B}_S]_I^{(k)} \left\{ \boldsymbol{Q}^{(k)} \right\} \sqrt{A_G} W_G \right) \\ &= \sum_{N=1}^{NEL} \sum_{G=1}^{NG-ps} \sum_{I=1}^4 \left\{ \delta \boldsymbol{\Phi} \right\}_I^T \left(\left\{ \boldsymbol{F}_P \right\}_{G(I)} + \left\{ \boldsymbol{F}_S \right\}_{G(I)} \right) \end{aligned} \quad (5.44)$$

$$\text{where} \quad \left\{ \boldsymbol{F}_P \right\}_{G(I)} = \sum_{n=0}^3 [\boldsymbol{B}_P]_I^{(n)} \left\{ \boldsymbol{m}^{(n)} \right\} \sqrt{A_G} W_G \quad (5.45)$$

$$\text{and} \quad \left\{ \boldsymbol{F}_S \right\}_{G(I)} = \sum_{k=0,2} [\boldsymbol{B}_S]_I^{(k)} \left\{ \boldsymbol{Q}^{(k)} \right\} \sqrt{A_G} W_G \quad (5.46)$$

are the contributions of, respectively, inplane (membrane and bending) and transverse stress resultants at Gauss point G to the internal force vector along the degrees of freedom of node I of element N. These vectors are added appropriately to the global internal force vector. **RSPSHEL7** makes a call to a subroutine called **BMAT** to compute the matrices $[\boldsymbol{B}_P]_I^{(n)}$ and $[\boldsymbol{B}_S]_I^{(k)}$.

The computation of the material and geometric tangent stiffness matrices is done in subroutine **STFSHEL7**. This subroutine loops over the elements of the structure and within each element it starts, as in **RSPSHEL7**, by localizing some global arrays to element level. Then, it starts constructing the element tangent and geometric stiffness matrices. The element material tangent stiffness matrix is based on Equation (4.112) which gives the expression for 7×7 submatrices composing the 28×28 element matrix. The element stiffness coefficient matrices $[C^p]$ and $[C^s]$ are retrieved from the internal files where they are stored. In contrast to the element material tangent stiffness matrix, which is somehow straightforward and simple, the construction of the element geometric tangent stiffness matrix is very tedious and lengthy. Its constituent submatrices are given in detail in appendix I. The subroutine **MATSTFIJ** is called by **STFSHEL7** to compute the element material tangent stiffness submatrices $[KM]_{ij}$ and the subroutines **GESTFBIJ** and **GESTFSIJ** are called by **STFSHEL7** to evaluate the contribution to the element geometric stiffness submatrices from respectively inplane and transverse stress resultants.

5.4.3. Description of the Program **STLSHEL7**

The main features of the finite element computer program **STLSHEL7** are outlined in the previous sections. The global structure of this program including the implementation of the arc-length method is discussed in this section. Figure 5.6 shows the primary

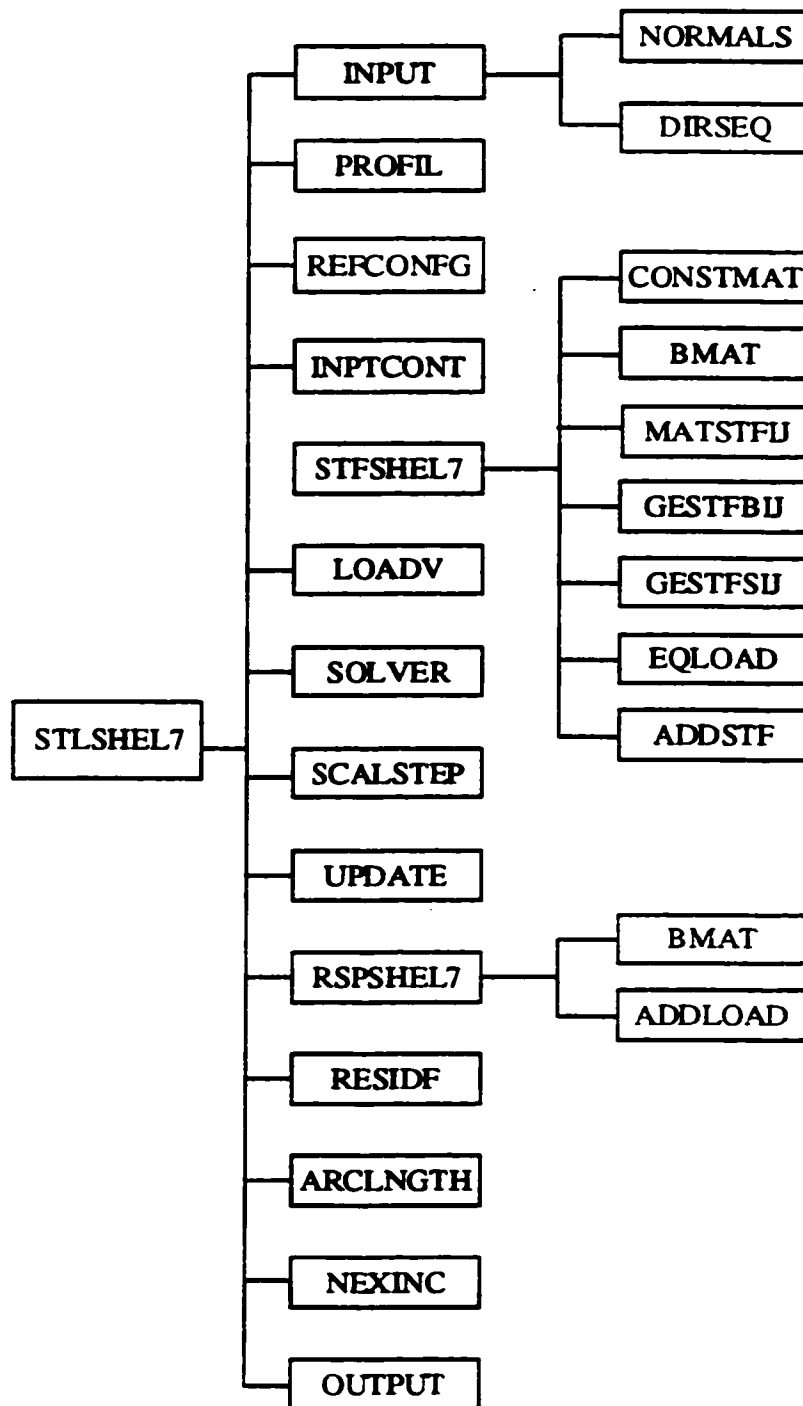


Figure 5.6 Structure of STL7 program containing primary and some secondary subroutines

subroutines called from the main program **STLSHEL7** with some secondary ones called within these primary subroutines. Most of the subroutines have already been mentioned while describing the different tasks. Thus, there is no need to describe them again here. These subroutines are **DIRSEC**, **NORMALS**, **REFCONFIG**, **CONSTMAT**, **STFSHEL7**, **BMAT**, **MATSTFIJ**, **GESTFBIJ**, **GESTFSIJ**, **UPDATE** and **RSPSHEL7**. Some primary subroutines such as **INPUT**, **PROFIL** and **SOLVER**, which are very "standard", are adopted from Reference [169] with the inclusion of **DIRSEC** and **NORMALS** in **INPUT**. Among the secondary "standard" subroutines which are also adopted from Reference [169] are **EQLOAD**, **ADDSTF** and **ADDLOAD**. These subroutines along with the other ones shown in Figure 5.6, but not discussed previously, are briefly described below:

INPUT: It reads the different commands from the input data file and directs the pointer to the appropriate secondary subroutines to read the data concerning the geometry, boundary conditions and loading conditions of the problem. The secondary subroutines **DIRSEC** and **NORMALS** are added inside **INPUT** to, respectively, construct arrays containing the nodal reference directions, in case of composites, and the nodal normals.

PROFIL: It computes the profile of the global structural stiffness matrix

INPTCONT: This subroutine reads the incremental/iterative control parameters. Among these parameters is **IAUTO** which, when it is equal to unity, allows for automatic increment sizes to be computed based on the desired number of iterations to be performed in each step before convergence is satisfied. Such

automatic increments must be used with the arc length method. When it is set to zero, equal increments are adopted. The other controlling parameter is MAXITR, which sets the maximum number of iterations within each increment. If the convergence is not satisfied after MAXITR number of iterations, the program will restore the previously converged configuration, decrease the load step and then resume iterating.

LOADV: It assembles the global fixed load vector F_0^{ext} as discussed in the section concerning the arc-length method.

SOLVER: It solves the system of equations (structural equilibrium equations by Gaussian elimination and takes into account the stiffness matrix being symmetric and banded (Crout reduction method).

SCALSTEP: It finds the current incremental load factor in the predictor phase whose sign (increment or decrement) depends on the number of negative pivots along the diagonal D of the factorized structure stiffness matrix.

RESIDF: It computes the residual force vector and checks the convergence criterion.

ARCLNGTH: It computes the correction to be applied to the load factor in the iteration due to the application of the arc-length method.

NEXINC: This subroutine is called when IAUTO is equal to unity in order to compute the parameters for the next increment.

EQLOAD: It computes the equivalent element nodal force, in case of prescribed displacement, and assemble them into the global force vector.

ADDSTF: It assembles the element stiffness matrices into the global (structure) stiffness

matrix

ADDLOAD: It assembles the element internal force vector into the structure internal force vector

Other secondary subroutines concerning reading nodal data, element data, material data, boundary conditions, loading data and computation of shape functions are not mentioned here. They are adopted from Reference [169] after undergoing some necessary modifications to suit the type and number of degrees of freedom of the shell element developed in this study.

The flowchart shown in Figure 5.7 elucidates the general structure of the program **STLSHEL7** and shows the different tasks carried out inside this program.

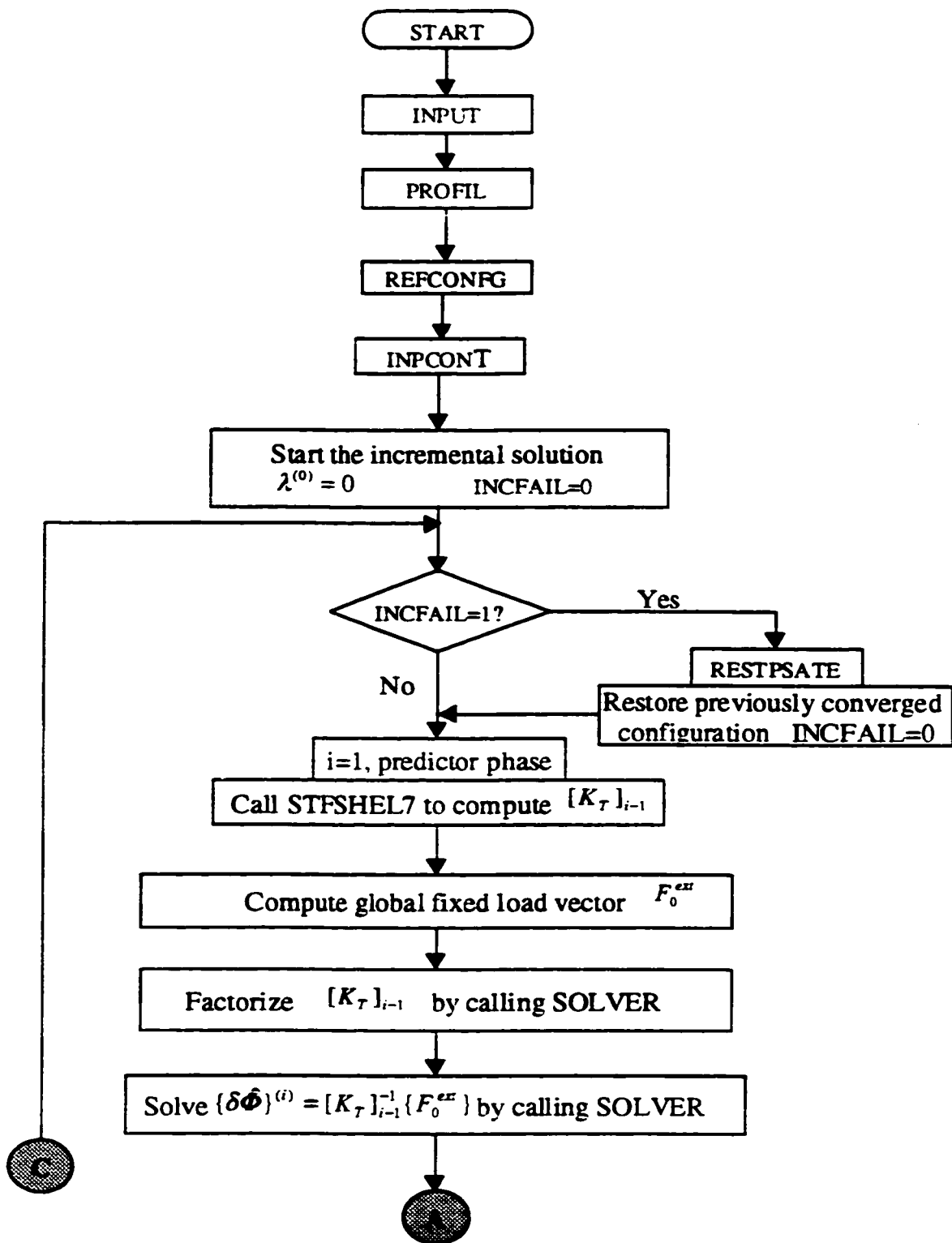


Figure 5.7 Flowchart for the computer program STLSHEL7

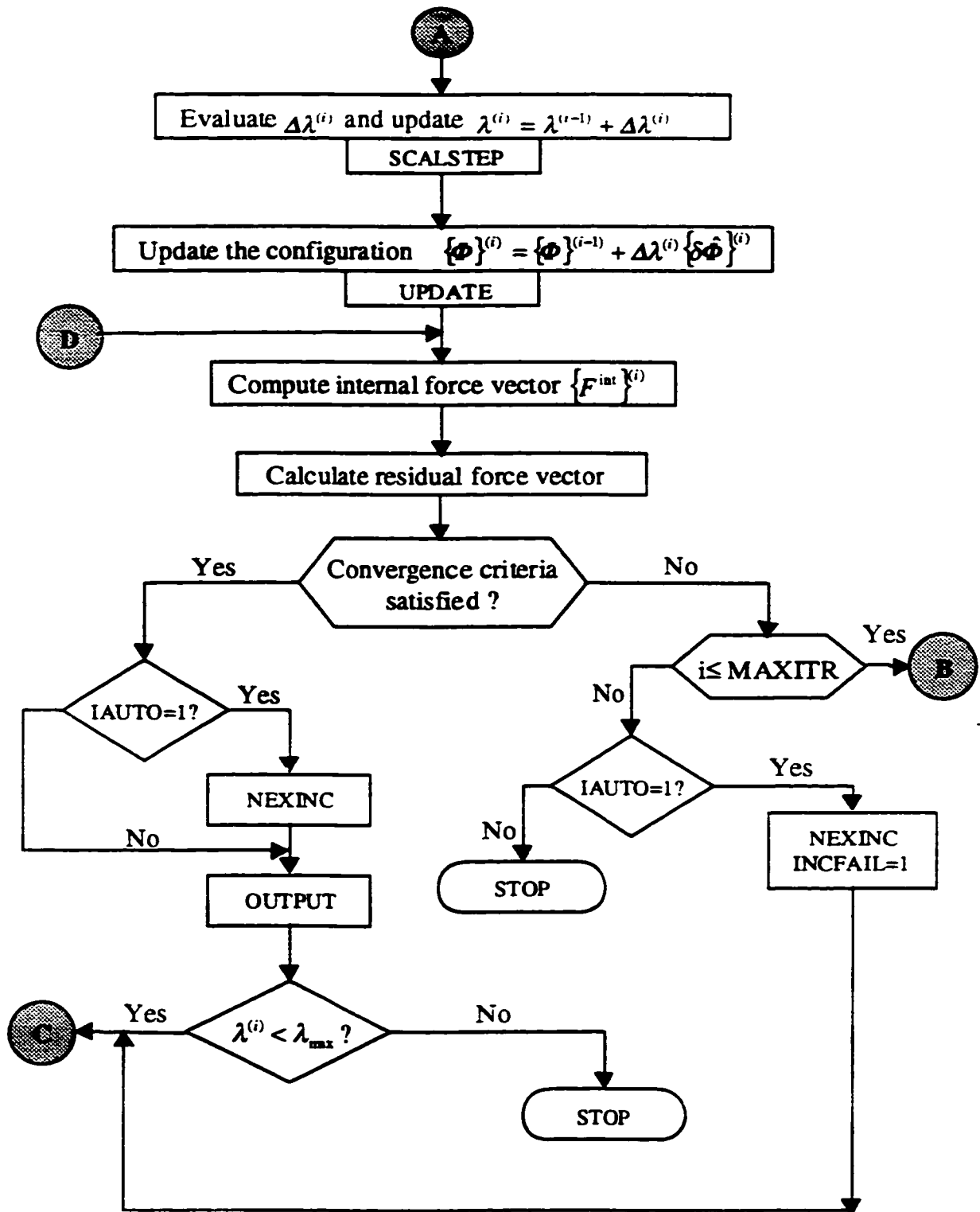


Figure 5.7 (continued)

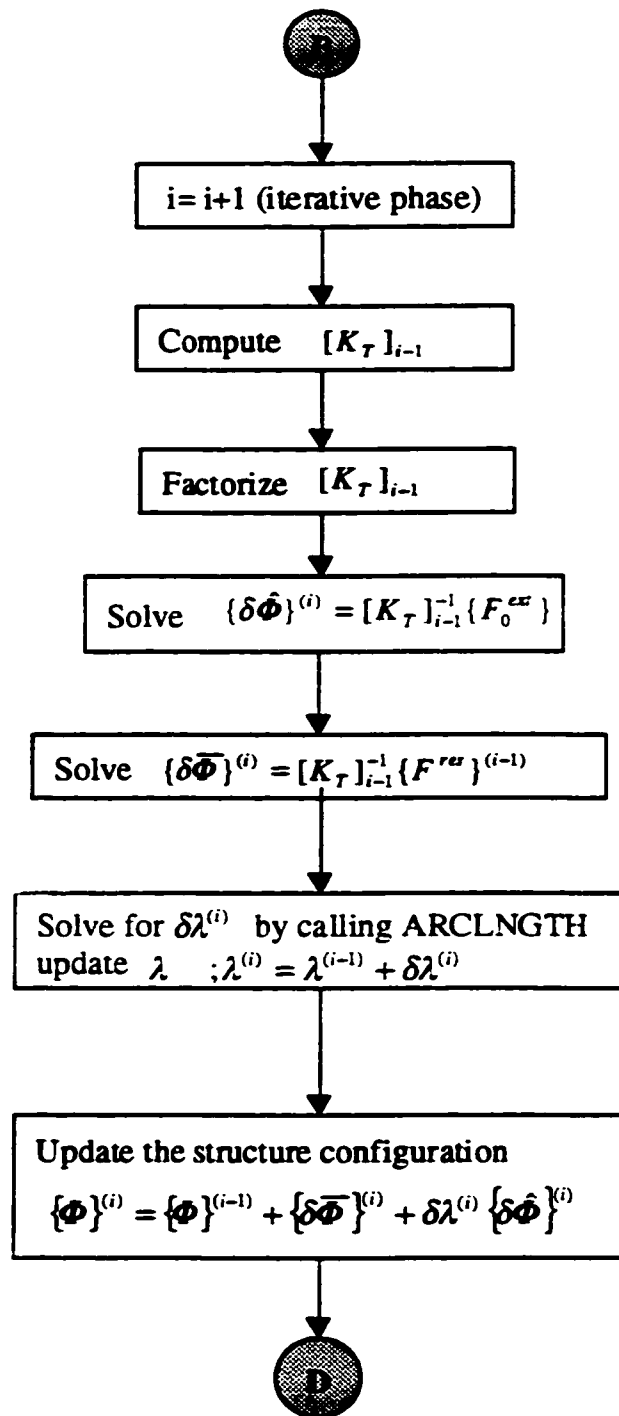


Figure 5.7 (continued)

CHAPTER 6

DYNAMIC FORMULATION

6.1 Introduction

In the previous two chapters, a finite element formulation and a solution procedure were developed for the static analysis of laminated shell type structures subjected to conservative forces and undergoing large deformation accompanied by finite rotations. This formulation is based on the shell theory exposed in chapter three. This chapter is concerned with a dynamical formulation using the same shell theory. The end goal is to design an energy-momentum conserving time stepping algorithm which can be used for the dynamic analysis of laminated shells undergoing large rigid body motion, large deformations, within small strains limits, and large rotations. This algorithm is based on a general methodology for the design of exact energy-momentum conserving algorithms proposed recently by Simo and Tarnow [6]. It is second order accurate, unconditionally stable and preserves exactly, by design, the fundamental constants of the shell motion such as the total linear momentum, the total angular momentum, and the total energy.

The main motivation behind the design of this class of algorithm, as mentioned in

Reference [6], is the widespread belief that conserved quantities such as momentum and energy capture key qualitative features of the long term dynamics and should therefore be preserved. Since only FOSDT, as reported in the literature survey, was considered in the design of previous energy-momentum conserving algorithms applied to shell structures, this study will contribute to this class of algorithms by extending them to TOSDT.

This chapter starts by defining and deriving the shell total linear and angular momenta followed by the kinetic and potential energies. Afterwards the weak form of the equations of motion is established in its continuum form. Then the conservation laws of the shell motion, which are the conservation of total energy, in case the system is Hamiltonian, and the conservation of linear and angular momenta, in case the external forces are self-equilibrated, are stated and their analytical expression derived. The time discretization is introduced with the intent to achieve exact energy-momentum conservation; it is followed by the spatial finite element discretization to yield a fully discretized initial boundary value problem. A particular attention is devoted here, as it was in the static case, for the consistent linearization of the resulting discretized initial boundary value problem in order to achieve quadratic rate of convergence typical for the Newton-Raphson solution. The resulting tangent mass matrix is derived in the same way as the tangent stiffness matrix, i.e. no lumping of masses is adopted in this study.

6.2. Continuum Form of the Equation of Motion

Before formulating the equations governing the dynamic response of the shell model, we need to determine the following quantities.

6.2.1 Total Linear and Angular Momenta

The total linear momentum of the shell structure is defined by

$$L = \int_{V^0} dm \cdot \dot{\mathbf{x}} \quad (6.1)$$

where

dm represents the mass of a volume element dV^0 as described in section 4.1.2.

$\dot{\mathbf{x}}$ represents the velocity of a material point $p(\xi, \eta, \zeta)$, which is obtained by differentiating the position vector \mathbf{x} with respect to time.

$$\dot{\mathbf{x}} = \dot{\phi} + \zeta \dot{d}_1 + \zeta^3 \dot{d}_3 \quad (6.2)$$

Using Equations (4.3) and (4.21), dm becomes

$$dm = \rho^0 \sqrt{G} d\xi d\eta d\zeta \quad (6.3)$$

By substituting dm back in Equation (6.1) and using Equation (4.5), L becomes

$$L = \int_{\Omega^0} \left\{ \frac{1}{\sqrt{A}} \int_{-h/2}^{h/2} \rho^0 \sqrt{G} \dot{\mathbf{x}} d\zeta \right\} d\Omega^0 \quad (6.4)$$

where A and G represent, respectively, the determinants of the metric tensors $A_{\alpha\beta}$ and $G_{\alpha\beta}$ which are defined by Equations (3.21) and (3.23).

From Equation (6.4), we define the midsurface linear momentum \mathbf{P} as

$$\mathbf{P} = \frac{1}{\sqrt{A}} \int_{-h/2}^{h/2} \rho^0 \sqrt{G} \dot{\mathbf{x}} d\zeta = A_{,\rho^0} \dot{\phi} \quad (6.5)$$

where

$$A_{\rho^{\circ}} = \frac{1}{\sqrt{A}} \int_{-h/2}^{h/2} \rho^{\circ} \sqrt{G} d\zeta \quad (6.6)$$

is the surface mass density in the reference configuration.. Finally, the total linear momentum becomes

$$L = \int_{\Omega^{\circ}} P d\Omega^{\circ} \quad (6.7)$$

The total angular momentum of the shell body, which is also a vectorial quantity, with respect to the origin, is

$$J = \int_{V^{\circ}} \mathbf{x} \times \dot{\mathbf{x}} dm \quad (6.8)$$

where 'x' represents the cross product. Substituting the position vector \mathbf{x} and dm by their expressions, yields

$$J = \int_{V^{\circ}} (\boldsymbol{\phi} + \zeta \mathbf{d}_1 + \zeta^3 \mathbf{d}_3) \times \dot{\mathbf{x}} \rho^{\circ} \sqrt{G} d\xi d\eta d\zeta \quad (6.9)$$

Using Equation (6.8) and substituting $\dot{\mathbf{x}}$ by its expression, we define the directors momenta $\boldsymbol{\pi}_1$ and $\boldsymbol{\pi}_3$ as

$$\boldsymbol{\pi}_1 = \frac{1}{\sqrt{A}} \int_{-h/2}^{h/2} \rho^{\circ} \sqrt{G} \zeta (\boldsymbol{\phi} + \zeta \dot{\mathbf{d}}_1 + \zeta^3 \dot{\mathbf{d}}_3) = I_2 \dot{\mathbf{d}}_1 + I_4 \dot{\mathbf{d}}_3 \quad (6.10)$$

$$\boldsymbol{\pi}_3 = \frac{1}{\sqrt{A}} \int_{-h/2}^{h/2} \rho^{\circ} \sqrt{G} \zeta^3 (\boldsymbol{\phi} + \zeta \dot{\mathbf{d}}_1 + \zeta^3 \dot{\mathbf{d}}_3) = I_4 \dot{\mathbf{d}}_1 + I_6 \dot{\mathbf{d}}_3 \quad (6.11)$$

where

$$I_k = \frac{1}{\sqrt{A}} \int_{-h/2}^{h/2} \rho^{\circ} \sqrt{G} \zeta^k d\zeta \quad , \quad k = 2, 4, 6 \quad (6.12)$$

is the surface k^{th} rotational inertia in the reference configuration.

With the use of Equations (6.5), (6.10) and (6.11), the expansion of Equation (6.9) yields the following expression for the total angular momentum.

$$J = \int_{\Omega^0} (\boldsymbol{\varphi} \times \mathbf{P} + \mathbf{d}_1 \times \boldsymbol{\pi}_1 + \mathbf{d}_3 \times \boldsymbol{\pi}_3) d\Omega^0 \quad (6.13)$$

Equations (6.5), (6.10) and (6.11) transform the velocities $\dot{\boldsymbol{\varphi}}$, $\dot{\mathbf{d}}_1$ and $\dot{\mathbf{d}}_3$ to momenta \mathbf{P} , $\boldsymbol{\pi}_1$ and $\boldsymbol{\pi}_3$. The collection of all possible configurations of the shell forms the configuration space $\Phi = (\boldsymbol{\varphi}, \mathbf{d}_1, \mathbf{d}_3)$. This configuration space and the momenta $\boldsymbol{\pi} = (\mathbf{P}, \boldsymbol{\pi}_1, \boldsymbol{\pi}_3)$ form the phase space $Z = (\Phi, \boldsymbol{\pi})$ of the shell body.

6.2.2 Kinetic and Potential Energies

The total kinetic energy of the shell structure is defined as

$$K = \frac{1}{2} \int_{V^0} dm \dot{\mathbf{x}} \cdot \dot{\mathbf{x}} = \frac{1}{2} \int_{\Omega^0} (\mathbf{P} \cdot \dot{\boldsymbol{\varphi}} + \boldsymbol{\pi}_1 \cdot \dot{\mathbf{d}}_1 + \boldsymbol{\pi}_3 \cdot \dot{\mathbf{d}}_3) d\Omega^0 \quad (6.14)$$

Equations (6.5), (6.10) and (6.11) can be solved to express the velocities $\dot{\boldsymbol{\varphi}}$, $\dot{\mathbf{d}}_1$ and $\dot{\mathbf{d}}_3$ in terms of momenta \mathbf{P} , $\boldsymbol{\pi}_1$ and $\boldsymbol{\pi}_3$.

$$\dot{\boldsymbol{\varphi}} = \mathbf{P} / A_\rho \quad (6.15a)$$

$$\dot{\mathbf{d}}_1 = (I_6 \boldsymbol{\pi}_1 - I_4 \boldsymbol{\pi}_3) / \text{Det} \quad (6.15b)$$

$$\dot{\mathbf{d}}_3 = (-I_4 \boldsymbol{\pi}_1 + I_2 \boldsymbol{\pi}_3) / \text{Det} \quad (6.15a)$$

$$\text{where } Det = I_2 I_6 - I_4^2. \quad (6.16)$$

Substituting $\dot{\phi}$, \dot{d}_1 and \dot{d}_3 by their respective expressions in Equation (6.14) yields

$$K(\boldsymbol{\pi}) = \frac{1}{2} \int_{\Omega^o} \left(\frac{1}{A_{\rho^o}} \mathbf{P} \cdot \mathbf{P} + \frac{I_6}{Det} \boldsymbol{\pi}_1 \cdot \boldsymbol{\pi}_1 + \frac{I_2}{Det} \boldsymbol{\pi}_3 \cdot \boldsymbol{\pi}_3 - \frac{2I_4}{Det} \boldsymbol{\pi}_1 \cdot \boldsymbol{\pi}_3 \right) d\Omega^o \quad (6.17)$$

The total potential energy of the shell structure is defined as

$$V(\boldsymbol{\Phi}) = V_{int}(\boldsymbol{\Phi}) + V_{ext}(\boldsymbol{\Phi}) \quad (6.18)$$

where $V_{ext}(\boldsymbol{\Phi})$ is the potential energy of the external forces which are assumed to be conservative.

$V_{int}(\boldsymbol{\Phi})$ is the total stored elastic energy of the structure. It is given by

$$V_{int}(\boldsymbol{\Phi}) = \frac{1}{2} \int_{V^o} S^{ij} E_{ij} dV^o \quad (6.19)$$

where

$$S^{ij} = \frac{\partial V_{int}(\boldsymbol{\Phi})}{\partial E_{ij}} = C^{ijkl} E_{kl} \quad (6.20)$$

Note here that the variation of $V_{int}(\boldsymbol{\Phi})$, i.e., $\delta V_{int}(\boldsymbol{\Phi})$ is equivalent to the virtual work of the external forces δw_f used in chapter four.

The introduction of the assumed displacement field in the expressions of Green-Lagrange strains E_{ij} and the pre-integration along the thickness through orthotropic layers leads to a two dimensional expression for $V_{int}(\boldsymbol{\Phi})$ analogous of that of Equation (4.7) for the virtual work.

$$V_{int}(\Phi) = \frac{1}{2} \int_{\Omega^o} \left(\sum_{n=0}^3 m^{(n)\alpha\beta} E_{\alpha\beta}^{(n)} + 2 \sum_{k=0,2} Q^{(k)\alpha} E_{\alpha 3}^{(k)} \right) d\Omega^o \quad (6.21)$$

The stress resultants $m^{(n)\alpha\beta}$ and $Q^{(k)\alpha}$ have already been detailed in chapter four.

6.2.3 Formulation of the Weak Form of the Equations of Motion

The Hamiltonian (total energy) of the shell body is defined as

$$H(\mathbf{Z}) = K(\boldsymbol{\pi}) + V(\Phi) \quad (6.22)$$

The equations governing the motion of the shell body can be expressed using either a Lagrangian or Hamiltonian formulation. In the Lagrangian formulation a system with N degrees of freedom possesses N equations of motion of the form

$$\frac{d}{dt} \left(\frac{\partial L}{\partial \dot{q}_i} \right) - \frac{\partial L}{\partial q_i} = 0 \quad (6.23)$$

where L is the Lagrangian given by

$$L = K - V \quad (6.24)$$

q_i ($i=1, \dots, N$) represent N generalized coordinates. Here the state of the system is described by N -dimensional configuration space whose coordinates are the N generalized coordinates q_i . The differential equations are of second order with respect to time.

The Hamiltonian formulation is based on a fundamentally different picture. The motion is described in terms of first order differential equations. Thus the number of differential equations will be $2N$ and the motion is described in $2N$ -dimensional phase

space. \dot{q}_i are considered as independent of q_i . The $2N$ variables used are the N generalized coordinates q_i and N generalized momenta p_i given by

$$p_i = \frac{\partial L}{\partial \dot{q}_i} \quad (6.25)$$

The quantities (q_i, p_i) are known as the canonical variables [102].

The transformation of the equations of motion from Lagrangian formulation to Hamiltonian formulation is carried out through Legendre transformation and the resulting equations of motion are [102]

$$\dot{p}_i + \frac{\partial H}{\partial q_i} = 0 \quad , \quad \dot{q}_i - \frac{\partial H}{\partial p_i} = 0 \quad (6.26a,b)$$

where H is the Hamiltonian and it represents the total energy in this situation as given by Equation (6.22)

To relate this review to this study, $\Phi = (\varphi, d_1, d_3)$ represents the generalized coordinates and $\pi = (P, \pi_1, \pi_3)$ represents the generalized momenta. Equations (6.26) can be written in the weak form as[170]

$$\int_{\Omega^o} \dot{\pi} \cdot \delta\Phi \, d\Omega^o + \frac{\partial H(z)}{\partial \Phi} \cdot \delta\Phi = 0 \quad , \quad \int_{\Omega^o} \dot{\Phi} \cdot \delta\pi \, d\Omega^o - \frac{\partial H(z)}{\partial \pi} \cdot \delta\pi = 0 \quad (6.27a,b)$$

The weak form is obtained by multiplying the "strong" equations of motions by a test function and then carrying the integration over the whole reference area of the shell body so that the equations of motion are satisfied in an average way.

Equation (6.27a) yields the weak form of the momentum equations

$$G_{dyn}(\dot{\boldsymbol{\pi}}, \boldsymbol{\Phi}, \delta\boldsymbol{\Phi}) = G_{inert}(\dot{\boldsymbol{\pi}}, \delta\boldsymbol{\Phi}) + G_{stat}(\boldsymbol{\Phi}, \delta\boldsymbol{\Phi}) - G_{ext}(\delta\boldsymbol{\Phi}) = 0 \quad (6.28)$$

where

$$G_{inert}(\dot{\boldsymbol{\pi}}, \delta\boldsymbol{\Phi}) = \int_{\Omega^o} (\dot{\mathbf{P}} \cdot \delta\boldsymbol{\varphi} + \dot{\boldsymbol{\pi}}_1 \cdot \delta\mathbf{d}_1 + \dot{\boldsymbol{\pi}}_3 \cdot \delta\mathbf{d}_3) d\Omega^o \quad (6.29)$$

$$G_{stat}(\boldsymbol{\Phi}, \delta\boldsymbol{\Phi}) = \int_{V^o} S^{ij} \delta E_{ij} dV^o = \int_{\Omega^o} \left(\sum_{\alpha=0}^3 m^{\alpha\beta} \delta E_{\alpha\beta} + 2 \sum_{k=0,2} Q^\alpha \delta E_{\alpha 3} \right) d\Omega^o \quad (6.30)$$

$\dot{\mathbf{P}}, \dot{\boldsymbol{\pi}}_1$ and $\dot{\boldsymbol{\pi}}_3$ are time derivatives of momenta.

The resulting Equations (6.29) and (6.30) are obtained by using Equations (6.17) and (6.21) to express the Hamiltonian in terms of $\boldsymbol{\Phi} = (\boldsymbol{\varphi}, \mathbf{d}_1, \mathbf{d}_3)$ and $\boldsymbol{\pi} = (\mathbf{P}, \boldsymbol{\pi}_1, \boldsymbol{\pi}_3)$, and then carrying out the differentiation present in Equations (6.27a) and (6.27b).

The contribution of the external loads to the weak form of the momentum equations is contained in $G_{ext}(\delta\boldsymbol{\Phi}) = -V_{ext}(\delta\boldsymbol{\Phi})$. The strong form of Equation (6.27b) produces Equations (6.15a,b,c).

The initial boundary value problem (IBVP) of nonlinear shells can be stated as:

Find the configuration and momenta $\mathbf{Z}(t) = (\boldsymbol{\Phi}(t), \boldsymbol{\pi}(t))$ for time $t \in [0, T]$ such that

$G_{dyn}(\mathbf{Z}(t), \delta\boldsymbol{\Phi}) = 0$ for all test functions $\delta\boldsymbol{\Phi} = (\delta\boldsymbol{\varphi}, \delta\mathbf{d}_1, \delta\mathbf{d}_3)$. This IBVP is subjected

to the initial conditions

$$(\boldsymbol{\varphi}, \mathbf{d}_1, \mathbf{d}_3)|_{t=0} = (\boldsymbol{\varphi}^{(o)}, \mathbf{d}_1^{(o)}, \mathbf{d}_3^{(o)}) \quad \text{and} \quad (\mathbf{P}, \boldsymbol{\pi}_1, \boldsymbol{\pi}_3)|_{t=0} = (\mathbf{P}^{(o)}, \boldsymbol{\pi}_1^{(o)}, \boldsymbol{\pi}_3^{(o)})$$

6.3 Conservation Laws of the Shell Motion

The objective of this section is to go through the conservation laws in their continuum

form, i.e., before the introduction of any discretization scheme either temporal or spatial.

6.3.1 Conservation of the Total Energy

The conservation law of the total energy $\frac{dH(z)}{dt} = 0$ may be obtained by using, as test functions the velocity field in Equations (6.28) and (6.29), i.e., $\delta\Phi = (\dot{\phi}, \dot{d}_1, \dot{d}_3)$.

Based on these test functions, Equation (6.29) becomes

$$G_{\text{iner}}(\dot{\pi}, \dot{\Phi}) = \int_{\Omega^o} (\dot{P} \cdot \dot{\phi} + \dot{\pi}_1 \cdot \dot{d}_1 + \dot{\pi}_3 \cdot \dot{d}_3) d\Omega^o \quad (6.31)$$

and the integrand of Equation (6.30) becomes

$$S^{ij} \delta E_{ij} = S^{ij} \delta x_{,i} \cdot x_{,j} = S^{ij} \dot{x}_{,i} \cdot x_{,j} = S^{ij} \dot{E}_{ij} \quad (6.32)$$

which leads to the following expression of Equation (6.30)

$$G_{\text{stat}}(\Phi, \dot{\Phi}) = \int_{\Omega^o} S^{ij} \dot{E}_{ij} dV^o \quad (6.33)$$

By differentiating Equations (6.17), representing K , and (6.19), representing V_{int} , with respect to time, we find respectively $G_{\text{iner}}(\dot{\pi}, \dot{\Phi})$ and $G_{\text{stat}}(\Phi, \dot{\Phi})$.

When the two conditions $G_{\text{ext}}(\delta\Phi) = 0$ and $\frac{dV_{\text{ext}}}{dt} = 0$ are satisfied, it can be observed

that

$$\frac{dH(z)}{dt} = \frac{dK(\pi)}{dt} + \frac{dV}{dt} = G_{\text{dyn}}(\Phi, \dot{\Phi}) = 0 \quad (6.34)$$

which means that the total energy is conserved.

6.3.2 Conservation of the Total Linear and Angular Momenta

It is assumed that the external loads applied to the shell structure are of a traction type and are equilibrated in the sense that balance of moments and balance of forces hold. We suppose that the shell motion is not restricted by any prescribed displacement/rotation on any part of the shell boundary. In this case, the total linear and angular momenta of the shell are conserved, i.e., $\frac{dL}{dt} = 0$, $\frac{dJ}{dt} = 0$.

The above two conservation laws are associated with the invariance of the Hamiltonian under spatial translations and rotations [6]. This can be checked by choosing $(\mathbf{v}, 0, 0)$ and $(\mathbf{v} \times \boldsymbol{\varphi}, \mathbf{v} \times \mathbf{d}_1, \mathbf{v} \times \mathbf{d}_3)$, where $\mathbf{v} \in \mathfrak{R}^3$ is arbitrary and independent of the surface coordinates, as test functions for the weak form given by Equation (6.28). Based on the adopted test functions and the assumption concerning external loads, $G_{ext}(\delta\Phi)$ is equal to zero.

Using $\delta\Phi = (\mathbf{v}, 0, 0)$ we get

$$G_{dyn} = G_{inert} + G_{nat} = \int_{\Omega^o} \dot{\mathbf{P}} \cdot \mathbf{v} d\Omega^o = \mathbf{v} \cdot \frac{dL}{dt} = 0 \quad (6.35)$$

For $\delta\Phi = (\mathbf{v} \times \boldsymbol{\varphi}, \mathbf{v} \times \mathbf{d}_1, \mathbf{v} \times \mathbf{d}_3)$, the integrand of Equation (6.30) becomes

$$S^{ij} \delta E_{ij} = S^{ij} (\mathbf{v} \times \mathbf{x}_j) \cdot \mathbf{x}_j = \mathbf{v} \cdot (S^{ij} \mathbf{x}_j \times \mathbf{x}_j) \quad (6.36)$$

Exploiting the symmetry condition of the tensor S^{ij} in Equation (6.36) yields

$$S^{ij} \mathbf{x}_j \times \mathbf{x}_j = 0 \quad (6.37)$$

which leads to

$$G_{stat}(\Phi, (\mathbf{v} \times \boldsymbol{\varphi}, \mathbf{v} \times \mathbf{d}_1, \mathbf{v} \times \mathbf{d}_3)) = 0 \quad (6.38)$$

$G_{inert}(\dot{\boldsymbol{\pi}}, (\mathbf{v} \times \boldsymbol{\varphi}, \mathbf{v} \times \mathbf{d}_1, \mathbf{v} \times \mathbf{d}_3))$ is given by

$$G_{inert}(\dot{\boldsymbol{\pi}}, (\mathbf{v} \times \boldsymbol{\varphi}, \mathbf{v} \times \mathbf{d}_1, \mathbf{v} \times \mathbf{d}_3)) = \int_{\Omega^*} (\dot{\mathbf{P}} \cdot \mathbf{v} \times \boldsymbol{\varphi} + \dot{\boldsymbol{\pi}}_1 \cdot \mathbf{v} \times \mathbf{d}_1 + \dot{\boldsymbol{\pi}}_3 \cdot \mathbf{v} \times \mathbf{d}_3) d\Omega^* \quad (6.39)$$

After some manipulations, Equation (6.39) yields

$$G_{inert}(\dot{\boldsymbol{\pi}}, (\mathbf{v} \times \boldsymbol{\varphi}, \mathbf{v} \times \mathbf{d}_1, \mathbf{v} \times \mathbf{d}_3)) = \mathbf{v} \cdot \frac{d\mathbf{J}}{dt} = 0 \quad (6.40)$$

Equations (6.38) and (6.40) imply

$$G_{dyn}(\mathbf{Z}, (\mathbf{v} \times \boldsymbol{\varphi}, \mathbf{v} \times \mathbf{d}_1, \mathbf{v} \times \mathbf{d}_3)) = \mathbf{v} \cdot \frac{d\mathbf{J}}{dt} = 0 \quad (6.41)$$

Since $\mathbf{v} \in \mathfrak{R}^3$ is arbitrary, it follows from Equations (6.35) and (6.41) that $\frac{d\mathbf{L}}{dt} = 0$ and

$$\frac{dJ}{dt} = 0.$$

6.4 Time Discretization: Energy-Momentum Conserving Algorithm

The general methodology for the design of an exact energy-momentum conserving algorithm presented in Reference [3] is closely followed in this section. First, an algorithm with momentum conservation is selected. In the second step, an algorithmic approximation of the constitutive equations is constructed in such a way that the total energy is conserved for Hamiltonian systems.

6.4.1 Approximation of Configuration and Momenta

Let $[t_n, t_{n+1}]$ be a subinterval of the time interval of interest $[0, T]$. The initial conditions (configuration and momenta) at t_n are given. In order to construct a time discretization of the weak form, Equation (6.28), which is evaluated at time $t_{n+1/2} = \frac{1}{2}(t_n + t_{n+1})$, some quantities need to be approximated at $t_{n+1/2}$. The configuration $\Phi_{n+1/2}$ and the momenta $\pi_{n+1/2}$ are taken as the average of their initial and final counterparts.

$$(\Phi_{n+1/2}, \mathbf{d}_{1(n+1/2)}, \mathbf{d}_{3(n+1/2)}) = \frac{1}{2}(\Phi_{n+1}, \mathbf{d}_{1(n+1)}, \mathbf{d}_{3(n+1)}) + \frac{1}{2}(\Phi_n, \mathbf{d}_{1(n)}, \mathbf{d}_{3(n)}) \quad (6.42a)$$

$$(\mathbf{P}_{n+1/2}, \boldsymbol{\pi}_{1(n+1/2)}, \boldsymbol{\pi}_{3(n+1/2)}) = \frac{1}{2}(\mathbf{P}_{n+1}, \boldsymbol{\pi}_{1(n+1)}, \boldsymbol{\pi}_{3(n+1)}) + \frac{1}{2}(\mathbf{P}_n, \boldsymbol{\pi}_{1(n)}, \boldsymbol{\pi}_{3(n)}) \quad (6.42b)$$

The differential Equations (6.5), (6.10) and (6.11) are approximated at $t_{n+1/2}$ by

$$\mathbf{P}_{n+1/2} = A_{\rho^*} (\Phi_{n+1} - \Phi_n) / \Delta t \quad (6.43a)$$

$$\boldsymbol{\pi}_{1(n+1/2)} = (I_2 (\mathbf{d}_{1(n+1)} - \mathbf{d}_{1(n)}) + I_4 (\mathbf{d}_{3(n+1)} - \mathbf{d}_{3(n)})) / \Delta t \quad (6.43b)$$

$$\boldsymbol{\pi}_{3(n+1/2)} = (I_4 (\mathbf{d}_{1(n+1)} - \mathbf{d}_{1(n)}) + I_6 (\mathbf{d}_{3(n+1)} - \mathbf{d}_{3(n)})) / \Delta t \quad (6.43c)$$

where $\Delta t = t_{n+1} - t_n$.

Using Equations (6.42) and (6.43a,b,c) we get

$$\mathbf{P}_{n+1} = 2A_{\rho^*} (\Phi_{n+1} - \Phi_n) / \Delta t - \mathbf{P}_n \quad (6.44a)$$

$$\boldsymbol{\pi}_{1(n+1)} = 2(I_2 (\mathbf{d}_{1(n+1)} - \mathbf{d}_{1(n)}) + I_4 (\mathbf{d}_{3(n+1)} - \mathbf{d}_{3(n)})) / \Delta t - \boldsymbol{\pi}_{1(n)} \quad (6.44b)$$

$$\boldsymbol{\pi}_{3(n+1)} = 2(I_4 (\mathbf{d}_{1(n+1)} - \mathbf{d}_{1(n)}) + I_6 (\mathbf{d}_{3(n+1)} - \mathbf{d}_{3(n)})) / \Delta t - \boldsymbol{\pi}_{3(n)} \quad (6.44c)$$

Equations (6.44a,b,c) can be solved to find the configuration difference

$$\varphi_{n+1} - \varphi_n = \Delta t (P_{n+1} + P_n) / (2A_p) \quad (6.45a)$$

$$d_{1(n+1)} - d_{1(n)} = \Delta t (I_6 (\pi_{1(n+1)} + \pi_{1(n)}) - I_4 (\pi_{3(n+1)} + \pi_{3(n)})) / (2Der) \quad (6.45b)$$

$$d_{3(n+1)} - d_{3(n)} = \Delta t (-I_4 (\pi_{1(n+1)} + \pi_{1(n)}) + I_2 (\pi_{3(n+1)} + \pi_{3(n)})) / (2Der) \quad (6.45c)$$

The quantities $\dot{P}_{n+1/2}$, $\dot{\pi}_{1(n+1/2)}$ and $\dot{\pi}_{3(n+1/2)}$ are approximated by

$$\dot{P}_{n+1/2} = (P_{n+1} - P_n) / \Delta t, \quad (6.46a)$$

$$\dot{\pi}_{1(n+1/2)} = (\pi_{1(n+1)} - \pi_{1(n)}) / \Delta t \quad (6.46b)$$

$$\dot{\pi}_{3(n+1/2)} = (\pi_{3(n+1)} - \pi_{3(n)}) / \Delta t \quad (6.46c)$$

6.4.2 Time Discretization of the Weak Form

Once the vectorial quantities describing the shell configuration and momenta have been discretized, the substitution of their expressions in the weak form of the equations of motion will temporally discretize these equations. The inertia part (6.29) of the weak form (6.28) is discretized using Equations (6.46a,b,c).

$$G_{inert}(\pi_{n+1}, \pi_n, \delta\Phi) = \frac{1}{\Delta t} \int_{\Omega^0} ((P_{n+1} - P_n) \cdot \delta\varphi + (\pi_{1(n+1)} - \pi_{1(n)}) \cdot \delta d_1 + (\pi_{3(n+1)} - \pi_{3(n)}) \cdot \delta d_3) d\Omega^0 \quad (6.47)$$

Introducing a midpoint evaluation of $G_{inert}(\Phi, \delta\Phi)$ as

$$G_{inert}(\Phi, \delta\Phi) = \int_{V^0} S_{(n+1/2)}^{ij} \delta E_{ij(n+1/2)} dV^0 \quad (6.48)$$

The strain variations $\delta E_{ij(n+1/2)}$ at configuration $\Phi_{(n+1/2)}$ are given by

$$\delta E_{ij(n+1/2)} = \frac{1}{2} (\delta \mathbf{x}_j \cdot \mathbf{x}_{(n+1/2),j} + \mathbf{x}_{(n+1/2),j} \cdot \delta \mathbf{x}_j) \quad (6.49)$$

6.4.3 Momenta Conservation of the Algorithm

The algorithmic approximation considered so far enables us to exactly conserve the total linear and angular momenta in case the applied loads are self-equilibrated. Conservation of linear momentum follows from the discretized form of Equation (6.28) by choosing a test function $\delta \Phi = (\mathbf{v}, 0, 0)$ with $\mathbf{v} \in \mathcal{R}^3$ as arbitrary. With this choice, $\delta E_{ij(n+1/2)} = 0$, thus $G_{stat}(\Phi, \delta \Phi) = 0$. Then

$$G_{dyn}(\mathbf{Z}_n, \mathbf{Z}_{n+1}, \delta \Phi) = \frac{1}{\Delta t} \mathbf{v} \cdot (\mathbf{L}_{n+1} - \mathbf{L}_n) = 0 \quad (6.50)$$

Equation (6.50) implies that $\mathbf{L}_{n+1} = \mathbf{L}_n$ since \mathbf{v} is arbitrary. The conservation of the total angular momentum is proven by choosing an infinitesimal rotation $\delta \Phi = (\mathbf{v} \times \boldsymbol{\varphi}_{n+1/2}, \mathbf{v} \times \mathbf{d}_{1(n+1/2)}, \mathbf{v} \times \mathbf{d}_{3(n+1/2)})$ as a test function. With this choice, $\delta E_{ij(n+1/2)} = 0$ and $G_{stat}(\Phi, \delta \Phi) = 0$ are directly obtained.

The discretized weak form, Equation (6.28), becomes

$$\begin{aligned} G_{dyn}(\mathbf{Z}_n, \mathbf{Z}_{n+1}, \delta \Phi) = & \frac{1}{\Delta t} \mathbf{v} \cdot \int_{\Omega^*} \left(\boldsymbol{\varphi}_{n+1/2} \times (\mathbf{P}_{n+1} - \mathbf{P}_n) + \mathbf{d}_{1(n+1/2)} \times (\boldsymbol{\pi}_{1(n+1)} - \boldsymbol{\pi}_{1(n)}) \right. \\ & \left. + \mathbf{d}_{3(n+1/2)} \times (\boldsymbol{\pi}_{3(n+1)} - \boldsymbol{\pi}_{3(n)}) \right) d\Omega^* = 0 \end{aligned} \quad (6.51)$$

After straight manipulations, we get

$$\begin{aligned}
G_{dyn}(\mathbf{Z}_n, \mathbf{Z}_{n+1}, \delta\Phi) = & -\frac{1}{\Delta t} \mathbf{v} \cdot \int_{\Omega^*} ((\boldsymbol{\varphi}_{n+1} - \boldsymbol{\varphi}_n) \times \mathbf{P}_{n+1/2} + (\mathbf{d}_{1(n+1)} - \mathbf{d}_{1(n)}) \times \boldsymbol{\pi}_{1(n+1/2)} \\
& + (\mathbf{d}_{3(n+1)} - \mathbf{d}_{3(n)}) \times \boldsymbol{\pi}_{3(n+1/2)}) d\Omega^* + \frac{1}{\Delta t} \mathbf{v} \cdot (\mathbf{J}(\mathbf{z}_{n+1}) - \mathbf{J}(\mathbf{z}_n)) = 0 \quad (6.52)
\end{aligned}$$

By using Equations (6.43a,b,c), the first part of Equation (6.52) vanishes, leaving the last term which states that $\mathbf{J}(\mathbf{z}_{n+1}) = \mathbf{J}(\mathbf{z}_n)$ since \mathbf{v} is arbitrary.

6.4.4 Exact Moment-Energy Conserving Scheme

It has been shown in the previous sub-section how this algorithm conserves the total linear and angular momenta in case the external forces are self equilibrated, as stated by the physical laws. The target now is to seek the conservation of the total energy. In the absence of external loads, the conservation of the total energy ($H(\mathbf{z})$) of the Hamiltonian system is achieved only when $S_{(n+1/2)}^{ij}$ is given by

$$S_{(n+1/2)}^{ij} = \frac{1}{2} C^{ijkl} [E_{kl(n+1)} + E_{kl(n)}] \quad (6.53)$$

The algorithmic representation of the constitutive equations shown in Equation (6.53) states that the Green strains $E_{kl(n+1/2)}$ are defined as the average of the strains of configurations Φ_n and Φ_{n+1} and not as the strains of configuration $\Phi_{(n+1/2)}$. The proof concerning the conservation of energy, in case the constitutive equation is given by Equation (6.53), is obtained by choosing as test function $\delta\Phi = (\boldsymbol{\varphi}_{n+1} - \boldsymbol{\varphi}_n, \mathbf{d}_{1(n+1)} - \mathbf{d}_{1(n)}, \mathbf{d}_{3(n+1)} - \mathbf{d}_{3(n)})$ in the algorithmic weak form. After using Equations (6.45a,b,c) in the weak form, Equation (6.28), the following expression is obtained

$$G_{dyn}(\mathbf{Z}_{n+1}, \mathbf{Z}_n, \delta\Phi) = H_{(n+1)} - H_{(n)} = 0 \quad (6.54)$$

which implies the conservation of the total energy. $G_{stat}(\Phi_n, \Phi_{n+1}, \delta\Phi)$ can be rewritten in the following form

$$\begin{aligned} G_{stat}(\Phi_n, \Phi_{n+1}, \delta\Phi) &= \int_{\Omega^o} S_{n+1/2}^{ij} \delta E_{ij(n+1/2)} dV^o \\ &= \int_{\Omega^o} \left(\sum_{i=0}^3 m_{n+1/2}^{(i)\alpha\beta} \delta E_{\alpha\beta(n+1/2)} + 2 \sum_{k=0,2} Q_{n+1/2}^{(k)\alpha} \delta E_{\alpha 3(n+1/2)} \right) d\Omega^o \end{aligned} \quad (6.55)$$

where

$$m_{n+1/2}^{(i)\alpha\beta} = \frac{1}{2} \left(m_{n+1}^{(i)\alpha\beta} + m_n^{(i)\alpha\beta} \right) \quad i = 0,1,2,3 \quad (6.56a)$$

$$Q_{n+1/2}^{(k)\alpha} = \frac{1}{2} \left(Q_{n+1}^{(k)\alpha} + Q_n^{(k)\alpha} \right) \quad k = 0,2 \quad (6.56b)$$

Equations (6.56a,b) show that the algorithmic representation of the constitutive equations adopted leads to the stress resultants of configuration $\Phi_{(n+1/2)}$, defined as the average of their counterpart configurations Φ_n and Φ_{n+1} .

Finally, the time discretized weak form becomes

$$\begin{aligned} G_{dyn}(\mathbf{Z}_n, \mathbf{Z}_{n+1}, \delta\Phi) &= \frac{1}{\Delta t} \int_{\Omega^o} \left((\mathbf{P}_{n+1} - \mathbf{P}_n) \cdot \delta\boldsymbol{\varphi} + (\boldsymbol{\pi}_{1(n+1)} - \boldsymbol{\pi}_{1(n)}) \cdot \delta\mathbf{d}_1 + (\boldsymbol{\pi}_{3(n+1)} - \boldsymbol{\pi}_{3(n)}) \cdot \delta\mathbf{d}_3 \right) d\Omega^o \\ &+ \int_{\Omega^o} \left(\sum_{i=0}^3 m_{n+1/2}^{(i)\alpha\beta} \delta E_{\alpha\beta(n+1/2)} + 2 \sum_{k=0,2} Q_{n+1/2}^{(k)\alpha} \delta E_{\alpha 3(n+1/2)} \right) d\Omega^o \end{aligned} \quad (6.57)$$

6.5 Spatial Finite Element Discretization

The finite element discretization is based, as in the static part, on an isoparametric four-noded quadrilateral laminated shell element.

6.5.1 Interpolation of the Kinematic and Momenta Fields

The interpolation of the directors \mathbf{d}_1 and \mathbf{d}_3 , adopted in this section, is different from that of the static part. Here, the unit norm of \mathbf{d}_1 and the orthogonality condition between \mathbf{d}_1 and \mathbf{d}_3 , which represent the kinematic constraints stated in Equation (3.29), have been relaxed away from nodal points. The interpolation adopted in the static part does not preserve, as reported by Simo et al.[124], the conserving properties of the continuum and time discretized equations of motion. This interpolation, in contrast to the one adopted in the static part, results in much simpler expressions.

The spatial discretization of the phase space is defined by

$$\boldsymbol{\varphi}(\xi, \eta) = \sum_{I=1}^4 N^I(\xi, \eta) \boldsymbol{\varphi}_I \quad , \quad \mathbf{P}(\xi, \eta) = \sum_{I=1}^4 N^I(\xi, \eta) \mathbf{P}_I \quad (6.58a)$$

$$\mathbf{d}_1(\xi, \eta) = \sum_{I=1}^4 N^I(\xi, \eta) \mathbf{d}_{1(I)} \quad , \quad \boldsymbol{\pi}_1(\xi, \eta) = \sum_{I=1}^4 N^I(\xi, \eta) \boldsymbol{\pi}_{1(I)} \quad (6.58b)$$

$$\mathbf{d}_3(\xi, \eta) = \sum_{I=1}^4 N^I(\xi, \eta) \mathbf{d}_{3(I)} \quad , \quad \boldsymbol{\pi}_3(\xi, \eta) = \sum_{I=1}^4 N^I(\xi, \eta) \boldsymbol{\pi}_{3(I)} \quad (6.58c)$$

where $N^I(\xi, \eta)$ are standard bilinear shape functions defined in chapter four.

The interpolation of the quantities involved in the strain variations $\delta \mathbf{E}_{\alpha\beta(n+1/2)}^{(i)}$ ($i =$

0,1,2,3) and $\delta \mathbf{E}_{\alpha 3(n+1/2)}^{(k)}$ ($k = 0,2$) can be obtained from Equations (6.58) as follows

$$\delta \boldsymbol{\varphi} = \delta \mathbf{u} = \sum_{I=1}^4 N^I \delta \mathbf{u}_I \quad , \quad \delta \boldsymbol{\varphi}_{,\alpha} = \sum_{I=1}^4 N^I_{,\alpha} \delta \mathbf{u}_I \quad (6.59a)$$

$$\delta \mathbf{d}_1 = \sum_{I=1}^4 N^I \delta \mathbf{d}_{1(I)} \quad , \quad \delta \mathbf{d}_{1,\alpha} = \sum_{I=1}^4 N^I_{,\alpha} \delta \mathbf{d}_{1(I)} \quad (6.59b)$$

$$\delta \mathbf{d}_3 = \sum_{l=1}^4 N^l \delta \mathbf{d}_{3(l)} \quad , \quad \delta \mathbf{d}_{3,\alpha} = \sum_{l=1}^4 N^l_{,\alpha} \delta \mathbf{d}_{3(l)} \quad (6.59c)$$

which are similar to the interpolations used in the static part. Thus, the difference between the two interpolations resides in the way to interpolate the field directors \mathbf{d}_1 , \mathbf{d}_3 and their respective derivatives with respect to ξ and η .

The constant part of the transverse shear strain field, i.e., $\bar{E}_{\alpha\beta}^{(0)}$ will be interpolated following the static part, i.e., using the assumed strain concept of Dvorkin and Bathe [4,5]

6.5.2 Admissible Test Functions

The test function $\delta \mathbf{d}_1$ needs to satisfy the condition $\delta \mathbf{d}_1 \cdot \tilde{\mathbf{d}}_{1(n+1/2)} = 0$, which is an algorithmic approximation of the linearized constraint of $|\mathbf{d}_1| = 1$.

where

$$\tilde{\mathbf{d}}_{1(n+1/2)} = \frac{\mathbf{d}_{1(n+1/2)}}{|\mathbf{d}_{1(n+1/2)}|} \quad , \quad \mathbf{d}_{1(n+1/2)} = (\mathbf{d}_{1(n)} + \mathbf{d}_{1(n+1)})/2 \quad (6.60)$$

$\tilde{\mathbf{d}}_{1(n+1/2)}$ is a unit vector obtained from $\mathbf{E}_3 = [0,0,1]^T$ by the rotation matrix $\mathbf{R}_{n+1/2}$; thus

$$\tilde{\mathbf{d}}_{1(n+1/2)} = \mathbf{R}_{n+1/2} \mathbf{E}_3 \quad (6.61)$$

The explicit construction of $\mathbf{R}_{n+1/2}$ is obtained by equating Equations (6.60) and (6.61)

which leads to

$$\mathbf{R}_{n+1/2} = (\mathbf{R}_n + \mathbf{R}_{n+1}) / |\mathbf{d}_{1(n)} + \mathbf{d}_{1(n+1)}| \quad (6.62)$$

where \mathbf{R}_n and \mathbf{R}_{n+1} are the rotation matrices mapping \mathbf{E}_3 into respectively $\mathbf{d}_{1(n)}$ and

$\mathbf{d}_{1(n+1)}$. Finally the test function $\delta \mathbf{d}_1$ is given by

$$\delta d_1 = \delta \tilde{d}_{1(n+1/2)} = \delta R_{n+1/2} E_3 = R_{n+1/2} (\delta \psi \times E_3) = R_{n+1/2} \delta D_1 \quad (6.63)$$

where

$$\delta D_1 = \delta D_1^1 E_1 + \delta D_1^2 E_2 \quad (6.64)$$

is normal to the unit vector E_3 , i.e. lying in the plane (E_1, E_2) .

The test function δd_3 is obtained from the variation of

$$\tilde{d}_{3(n+1/2)} = R_{n+1/2} D_{3(n+1/2)} \quad , \quad D_{3(n+1/2)} = (D_{3(n)} + D_{3(n+1)})/2 \quad (6.65)$$

$$\begin{aligned} \delta d_3 &= \delta R_{n+1/2} D_{3(n+1/2)} + R_{n+1/2} \delta D_3 = -(\delta D_1 \cdot D_{3(n+1/2)}) R_{n+1/2} E_3 + R_{n+1/2} \delta D_3 \\ &= -(\tilde{d}_{1(n+1/2)} \otimes D_{3(n+1/2)}) \delta D_1 + R_{n+1/2} \delta D_3 \end{aligned} \quad (6.66)$$

6.5.3 Strain Variations

The strain variations $(\delta E_{\alpha\beta(n+1/2)}^{(i)}, i=0,1,2,3)$ and $(\delta E_{\alpha 3(n+1/2)}^{(k)}, k=0,2)$ given in the time discretized weak form (6.57) need to be discretized. Following the method used in the static part but bearing in mind that we are at configuration $\Phi_{(n+1/2)}$. Based on Equations (4.22) and (4.23), we get

$$\delta E_{\alpha\beta(n+1/2)}^{(*)} = \frac{1}{2} (\delta \varphi_{,\alpha} \cdot \varphi_{,\beta(n+1/2)} + \varphi_{,\alpha(n+1/2)} \cdot \delta \varphi_{,\beta}) \quad (6.67a)$$

$$\delta E_{\alpha\beta(n+1/2)}^{(1)} = \frac{1}{2} (\delta \varphi_{,\alpha} \cdot d_{1,\beta(n+1/2)} + \varphi_{,\alpha(n+1/2)} \cdot \delta d_{1,\beta} + \delta \varphi_{,\beta} \cdot d_{1,\alpha(n+1/2)} + \varphi_{,\beta(n+1/2)} \cdot \delta d_{1,\alpha}) \quad (6.67b)$$

$$\delta E_{\alpha\beta(n+1/2)}^{(2)} = \frac{1}{2} (\delta d_{1,\alpha} \cdot d_{1,\beta(n+1/2)} + d_{1,\alpha(n+1/2)} \cdot \delta d_{1,\beta}) \quad (6.67c)$$

$$\delta \tilde{E}_{\alpha\beta}^{(3)} = \frac{1}{2} \left(\delta\varphi_{,\alpha} \cdot \mathbf{d}_{3,\beta(n+1/2)} + \varphi_{\alpha(n+1/2)} \cdot \delta\mathbf{d}_{3,\beta} + \delta\varphi_{,\beta} \cdot \mathbf{d}_{3,\alpha(n+1/2)} + \varphi_{\beta(n+1/2)} \cdot \delta\mathbf{d}_{3,\alpha} \right) \quad (6.67d)$$

$$\delta \tilde{E}_{\alpha 3}^{(\varphi)} = \frac{1}{2} \left(\delta\varphi_{,\alpha} \cdot \mathbf{d}_{(n+1/2)1} + \varphi_{\alpha(n+1/2)} \cdot \delta\mathbf{d}_1 \right) \quad (6.68a)$$

$$\delta \tilde{E}_{\alpha 3}^{(2)} = \frac{3}{2} \left(\delta\varphi_{,\alpha} \cdot \mathbf{d}_{3(n+1/2)} + \varphi_{\alpha(n+1/2)} \cdot \delta\mathbf{d}_3 \right) \quad (6.68)$$

From the strain variations given above and the admissible test functions and after applying the FEM discretization, the following strain-displacement operators

$$\left[\begin{matrix} (i) \\ B_p \end{matrix} \right]_{I(n+1/2)} \quad (i = 0,1,2,3) \text{ and } \left[\begin{matrix} (j) \\ B_s \end{matrix} \right]_{I(n+1/2)} \quad (j = 0,2). \quad (\text{I stands for node number}) \text{ are}$$

obtained. The operators $\left[\begin{matrix} (i) \\ B_p \end{matrix} \right]_{I(n+1/2)}$ ($i = 0,1,2$) and $\left[\begin{matrix} (0) \\ B_s \end{matrix} \right]_{I(n+1/2)}$ are similar to those of

the static part except that the quantities involved are evaluated at configuration $\Phi_{(n+1/2)}$.

The position vector φ and the directors \mathbf{d}_1 and \mathbf{d}_3 are based on Equations (6.42a). The

rotation matrix $\mathbf{R}_{n+1/2}$ is based on Equation (6.62). The interpolations are applied to φ ,

\mathbf{d}_1 , \mathbf{d}_3 and their derivatives but the rotations are evaluated at the nodal points only.

$\left[\begin{matrix} (3) \\ B_p \end{matrix} \right]_{I(n+1/2)}$ and $\left[\begin{matrix} (2) \\ B_s \end{matrix} \right]_{I(n+1/2)}$ are different from their static counterparts, thus they will be

given below

$$\begin{aligned}
\left[\mathbf{B}_r \right]_{I(n+1/2)}^{(3)} &= \begin{bmatrix} N_{,1}^I \mathbf{d}_{3,1(n+1/2)}^T & -N_{,1}^I \boldsymbol{\varphi}_{,1(n+1/2)}^T \left(\tilde{\mathbf{d}}_{1(I)} \otimes \mathbf{D}_{3(I)} \right)_{(n+1/2)} \\ N_{,2}^I \mathbf{d}_{3,2(n+1/2)}^T & -N_{,2}^I \boldsymbol{\varphi}_{,2(n+1/2)}^T \left(\tilde{\mathbf{d}}_{1(I)} \otimes \mathbf{D}_{3(I)} \right)_{(n+1/2)} \\ (N_{,1}^I \mathbf{d}_{3,2}^T + N_{,2}^I \mathbf{d}_{3,1}^T)_{(n+1/2)} & - (N_{,1}^I \boldsymbol{\varphi}_{,2}^T + N_{,2}^I \boldsymbol{\varphi}_{,1}^T)_{(n+1/2)} \left(\tilde{\mathbf{d}}_{1(I)} \otimes \mathbf{D}_{3(I)} \right)_{(n+1/2)} \end{bmatrix} \\
&\left[\begin{array}{l} N_{,1}^I \boldsymbol{\varphi}_{,1(n+1/2)}^T \bar{\mathbf{R}}_{I(n+1/2)} \\ N_{,2}^I \boldsymbol{\varphi}_{,2(n+1/2)}^T \bar{\mathbf{R}}_{I(n+1/2)} \\ (N_{,1}^I \boldsymbol{\varphi}_{,2}^T + N_{,2}^I \boldsymbol{\varphi}_{,1}^T)_{(n+1/2)} \bar{\mathbf{R}}_{I(n+1/2)} \end{array} \right] \quad (6.69)
\end{aligned}$$

$$\left[\mathbf{B}_r \right]_{I(n+1/2)}^{(2)} = 3 \left[\begin{array}{lll} N_{,1}^I \mathbf{d}_{3(n+1/2)}^T & -N^I \boldsymbol{\varphi}_{,1(n+1/2)}^T \left(\tilde{\mathbf{d}}_{1(I)} \otimes \mathbf{D}_{3(I)} \right)_{(n+1/2)} & N^I \boldsymbol{\varphi}_{,1(n+1/2)}^T \bar{\mathbf{R}}_{I(n+1/2)} \\ N_{,2}^I \mathbf{d}_{3(n+1/2)}^T & -N^I \boldsymbol{\varphi}_{,2(n+1/2)}^T \left(\tilde{\mathbf{d}}_{1(I)} \otimes \mathbf{D}_{3(I)} \right)_{(n+1/2)} & N^I \boldsymbol{\varphi}_{,2(n+1/2)}^T \bar{\mathbf{R}}_{I(n+1/2)} \end{array} \right] \quad (6.70)$$

It should be mentioned here that the strain variations $(\Delta \mathbf{E}_{\alpha\beta(n+1)}^{(i)}, i=0,1,2,3)$ and $(\Delta \mathbf{E}_{\alpha 3(n+1)}^{(k)}, k=0,2)$ will be needed during the linearization procedure. Their evaluation is exactly similar to the static case except that all the quantities involved are based on the configuration $\Phi_{(n+1)}$.

This ends the discretization of the strain variations at configuration $\Phi_{(n+1/2)}$.

6.6 Linearization

After full discretization (time and spatial) of the weak form of the equations of motion of the shell model given by Equation (6.57), a system of highly nonlinear equations is obtained. Solving this problem by Newton-Raphson method requires a linearization of the discrete form which may be obtained using the directional derivative of the test functions $\delta \mathbf{u}$, $\delta \mathbf{d}_1$ and $\delta \mathbf{d}_3$ in the direction of $\{\Delta \Phi\}_{n+1} = [\Delta \mathbf{u} \ \Delta \mathbf{d}_1 \ \Delta \mathbf{d}_3]_{n+1}^T$. It

should be mentioned here that the linearization is done at configuration Φ_{n+1} corresponding to time t_{n+1} . The linearization of G_{dyn} can be split into three parts

$$\begin{aligned} D[G_{dyn}(Z_n, \Phi_{n+1}, \delta\Phi)] \cdot \{\Delta\Phi\}_{n+1} &= D_{inert}[G_{dyn}(Z_n, \Phi_{n+1}, \delta\Phi)] \cdot \{\Delta\Phi\}_{n+1} \\ &+ D_M[G_{dyn}(Z_n, \Phi_{n+1}, \delta\Phi)] \cdot \{\Delta\Phi\}_{n+1} + D_G[G_{dyn}(Z_n, \Phi_{n+1}, \delta\Phi)] \cdot \{\Delta\Phi\}_{n+1} \end{aligned} \quad (6.71)$$

which represent, respectively, the inertia part, the material part and the geometric part of the tangent stiffness operator. The evaluation of the terms involved in Equation (6.71) requires the directional derivative of the test functions δu , δd_1 and δd_3 in the direction of $\{\Delta\Phi\}_{n+1} = [\Delta u \ \Delta d_1 \ \Delta d_3]^T_{n+1}$ which will be considered next.

6.6.1 Second Variation of the Kinematic Variables

The directional derivative of test functions δu , δd_1 and δd_3 in the direction of $\{\Delta\Phi\}_{n+1}$ can be written as $\Delta\delta u$, $\Delta\delta d_1$ and $\Delta\delta d_3$. Contrary to $\Delta\delta u$ which can be shown to be zero, $\Delta\delta d_1$ and $\Delta\delta d_3$ are different from zero. Their expressions are obtained from the variation of Equations (6.63) and (6.66) which, after some manipulations, yield

$$\Delta\delta d_1 = -\frac{1}{NRMD} \left((\delta D_1 \cdot \Delta D_1) d_{1(n+1)} + (R_{n+1} \Delta D_1 \cdot \bar{d}_{1(n+1/2)}) R_{n+1/2} \delta D_1 \right) \quad (6.72)$$

where

$$NRMD = |d_{1(n)} + d_{1(n+1)}| \quad (6.73)$$

is the norm of the resultant vector of $d_{1(n)}$ and $d_{1(n+1)}$, and

$$\begin{aligned}
\Delta \delta d_3 &= -\frac{1}{2}(\delta D_1 \cdot D_{3(n+1/2)}) R_{n+1/2} \Delta D_1 - \frac{1}{2}(\Delta D_1 \cdot D_{3(n+1/2)}) R_{n+1/2} \delta D_1 \\
&+ \frac{1}{NRMD}(\delta D_1 \cdot D_{3(n+1/2)}) R_n \Delta D_1 + \frac{1}{NRMD}(R_{n+1} \Delta D_1 \cdot \bar{d}_{1(n+1/2)})(\delta D_1 \cdot D_{3(n+1/2)}) \bar{d}_{1(n+1/2)} \\
&- \frac{1}{2}(\delta D_1 \cdot \Delta D_3) \bar{d}_{1(n+1/2)} - \frac{1}{NRMD}(\delta D_3 \cdot \Delta D_1) d_{1(n+1)} - \frac{1}{NRMD}(R_{n+1} \Delta D_1 \cdot \bar{d}_{1(n+1/2)}) R_{n+1/2} \delta D_3
\end{aligned} \tag{6.74}$$

6.6.2 Inertia Part of the Tangent Stiffness Operator

The inertia contribution to the tangent stiffness matrix is given by

$$\begin{aligned}
D_{inert} [G_{dyn}] \cdot \{\Delta \Phi\}_{n+1} &= \sum_{N=1}^{NEL} \frac{1}{\Delta t} \int_{\Omega_N^*} (\Delta P_{n+1} \cdot \delta \varphi + \Delta \pi_{1(n+1)} \cdot \delta d_1 + (\pi_{1(n+1)} - \pi_{1(n)}) \cdot \Delta \delta d_1 \\
&+ \Delta \pi_{3(n+1)} \cdot \delta d_3 + (\pi_{3(n+1)} - \pi_{3(n)}) \cdot \Delta \delta d_3) d\Omega^o
\end{aligned} \tag{6.75}$$

ΔP_{n+1} , $\Delta \pi_{1(n+1)}$ and $\Delta \pi_{3(n+1)}$ are obtained by taking the variation of Equations (6.44a,b,c)

$$\Delta P_{n+1} = \frac{2A_p}{\Delta t} \Delta \varphi_{n+1} \tag{6.76a}$$

$$\Delta \pi_{1(n+1)} = \frac{2I_2}{\Delta t} \Delta d_{1(n+1)} + \frac{2I_4}{\Delta t} \Delta d_{3(n+1)} \tag{6.76b}$$

$$\Delta \pi_{3(n+1)} = \frac{2I_5}{\Delta t} \Delta d_{1(n+1)} + \frac{2I_6}{\Delta t} \Delta d_{3(n+1)} \tag{6.76c}$$

6.6.3 Material Part of the Tangent Stiffness Operator

The material part of the tangent stiffness operator is obtained from the linearization of the constitutive equations while keeping the geometry of the shell structure as constant.

By using matrix notation for G_{mat} , the material contribution to the tangent operator is

given by

$$D_M [G_{dyn}] \cdot \{\Delta\Phi\}_{n+1} = \sum_{N=1}^{NEL} \int_{\Omega_N^o} \left(\sum_{i=0}^3 \left\{ \delta \epsilon \right\}_{n+1/2}^{(i)T} D \left\{ m \right\}_{n+1/2}^{(i)} \cdot \{\Delta\Phi\}_{n+1} \right. \\ \left. + \sum_{k=0,2} \left\{ \delta \gamma \right\}_{n+1/2}^{(k)T} D \left\{ Q \right\}_{n+1/2}^{(k)} \cdot \{\Delta\Phi\}_{n+1} \right) d\Omega^o \quad (6.77)$$

where

$$D \left\{ m \right\}_{n+1/2}^{(i)} \cdot \{\Delta\Phi\}_{n+1} = \frac{1}{2} \sum_{j=0}^3 \left[C_P \right] \left\{ \Delta \epsilon \right\}_{n+1}^{(j)} \quad (6.78a)$$

and

$$D \left\{ Q \right\}_{n+1/2}^{(k)} \cdot \{\Delta\Phi\}_{n+1} = \frac{1}{2} \sum_{j=0,2} \left[C_S \right] \left\{ \Delta \gamma \right\}_{n+1}^{(j)} \quad (6.78b)$$

6.6.4 Geometric Part of the Tangent Stiffness Operator

The geometric part of the tangent operator is obtained from the variation of geometry while holding the material part constant. Here, for convenience, G_{star} is written using indicial rotation

$$D_G [G_{dyn}] \cdot \{\Delta\Phi\}_{n+1} = \sum_{N=1}^{NEL} \int_{\Omega_N^o} \left(\sum_{i=0}^3 m_{n+1/2}^{(i)\alpha\beta} \Delta\delta E_{\alpha\beta(n+1/2)}^{(i)} + 2 \sum_{k=0,2} Q_{n+1/2}^{(k)\alpha} \Delta\delta E_{\alpha 3(n+1/2)}^{(k)} \right) d\Omega^o \quad (6.79)$$

Since the second variation of the kinematic variables is shown in section 6.6.1, the computation of $\Delta\delta E_{\alpha\beta(n+1/2)}^{(i)}$ and $\Delta\delta E_{\alpha 3(n+1/2)}^{(k)}$ is straightforward.

The construction of the element tangent matrices, i.e., mass and stiffness (material and geometric) follows the same procedure used in the static part except that here a careful attention is paid to the operators δ and Δ . The former one operates at configuration

$\Phi_{(n+1/2)}$ and the latter one at configuration $\Phi_{(n+1)}$. This has resulted in different strain-displacement operators, as shown in section 6.5.3 concerning strain variations. Therefore, in contrast to the static part, the element and global stiffness matrices resulting from the dynamic formulation will be unsymmetrical.

6.7 Implementation Notes

The implementation of the dynamic formulation is based on the standard Newton-Raphson method. The problem can be stated as follows. Given the configuration $(\varphi_n, \mathbf{d}_{1(n)}, \mathbf{d}_{3(n)})$ and momenta $(\mathbf{p}_n, \boldsymbol{\pi}_{1(n)}, \boldsymbol{\pi}_{3(n)})$ at time t_n , find the configuration at time t_{n+1} such that $G_{dyn}(\mathbf{Z}_n, \phi_{n+1}, \delta\phi) = 0$ for any test functions $\delta\phi$ related to the intermediate configuration $\Phi_{(n+1/2)}$. The use of Newton Raphson method requires a linearization of $G_{dyn}(\mathbf{Z}_n, \phi_{n+1}, \delta\phi) = 0$ which was carried out in the previous section. The element tangent matrices obtained from the linearization process are much more involved than their counterparts of the static formulation.

The dynamic predictors are used to start the Newton Raphson method. Their purpose is to estimate the configuration and momenta at time t_{n+1} during the first iteration. Many alternative schemes exist for these predictors and the difference between them resides in how fast each of them will reach the converged solution[]. In this study a constant velocity (zero acceleration) predictor was attempted but the problem of enforcing the constraint $|\mathcal{I}_{1(n+1)}^{(0)}| = 1$ and finding $\mathbf{R}_{n+1}^{(0)}$ led to the adoption of a predictor based on a constant deformation between t_n , and t_{n+1} at iteration 0. This lead to the following

equations

$$\begin{aligned}
 \varphi_{(n+1)}^{(0)} &= \varphi_n \\
 \mathbf{d}_{1(n+1)}^{(0)} &= \mathbf{d}_{1(n)} \\
 \mathbf{d}_{3(n+1)}^{(0)} &= \mathbf{d}_{3(n)}
 \end{aligned} \tag{6.80}$$

and based on these conditions and Equations (6.44a,b,c), the expressions of momenta are given by

$$\begin{aligned}
 \mathbf{P}_{(n+1)}^{(0)} &= -\mathbf{P}_n \\
 \boldsymbol{\pi}_{1(n+1)}^{(0)} &= -\boldsymbol{\pi}_{1(n)} \\
 \boldsymbol{\pi}_{3(n+1)}^{(0)} &= -\boldsymbol{\pi}_{3(n)}
 \end{aligned} \tag{6.81}$$

Another important thing to be mentioned here is the update procedure of the configuration which is carried out at each iteration. Since the interpolation adopted in the dynamic part is different and simpler than that of the static part, the configuration update will be also simpler than that of the static formulation. The field Equations from (6.63) to (6.75), used to update the directors \mathbf{d}_1 and \mathbf{d}_3 and their derivatives at Gauss points, are not needed in the dynamic formulation. The simpler Equations (6.58), used to interpolate \mathbf{d}_1 and \mathbf{d}_3 , will be used to update these directors at Gauss points based on the updated nodal directors which are computed as in the static case.

Once the nodal directors are updated at a specified iteration, Equations (6.44a,b,c) are used to update the nodal momenta.

CHAPTER 7

NUMERICAL SIMULATIONS

7.1 Introduction

This chapter concerns the assessment of the performance of the proposed finite rotation laminated shell element using a TOSDT. The response predicting capability of this model in static and dynamic situations is investigated through test problems available in the recent literature. The results obtained from these simulations are compared with those available from other researchers.

The first three static problems deal with linear cases. The results of the linear analysis are obtained from this formulation by performing the linearization at the reference configuration and taking the predicted solution without going into further iterations. The remaining static test problems are nonlinear and involve finite rotations and large changes in the geometric shape of the structures treated.

The dynamic test problems, considered in this study, involve large rotations, snap-through and large rigid body motion. The first four dynamic test problems, which have been reported recently in the literature, deal with thin shells, while last example deals

with thick shells. The last example is designed to show the difference in prediction between the first and third order shear deformation theories in case of a sandwich cylindrical panel with a soft core.

7.2 Static Simulations

7.2.1 Linear Problems

7.2.1.1 Pinched Isotropic Cylinder with End Diaphragms.

This example considers a short isotropic cylinder subjected to two pinching vertical forces at the middle section and two rigid diaphragms at the end. It should be mentioned that for isotropic cases, no significant difference exists between FOSDT and TOSDT models. The purpose of including such examples is the assessment of the viability of the present model.

The data describing the problem are: The length of the cylinder is $L = 600$, the radius $R = 300$, and the thickness $t = 3$. The Young's modulus is $E = 3 \times 10^6$ and the Poisson's ratio is $\nu = 0.3$.

By exploiting the symmetry, present in this case, the cylinder is modeled using one octant. Figure 7.1 shows an 8X8 mesh of this octant of a cylinder along with the appropriate boundary conditions of geometry and loading. To test the convergence to the exact solution of this model, a mesh refinement is adopted starting with a 4X4 mesh and ending by a 32x32 mesh.

The numerical results found, concerning the displacement at the location of the punching force, are presented in Table 7.1 and normalized against the analytical solution

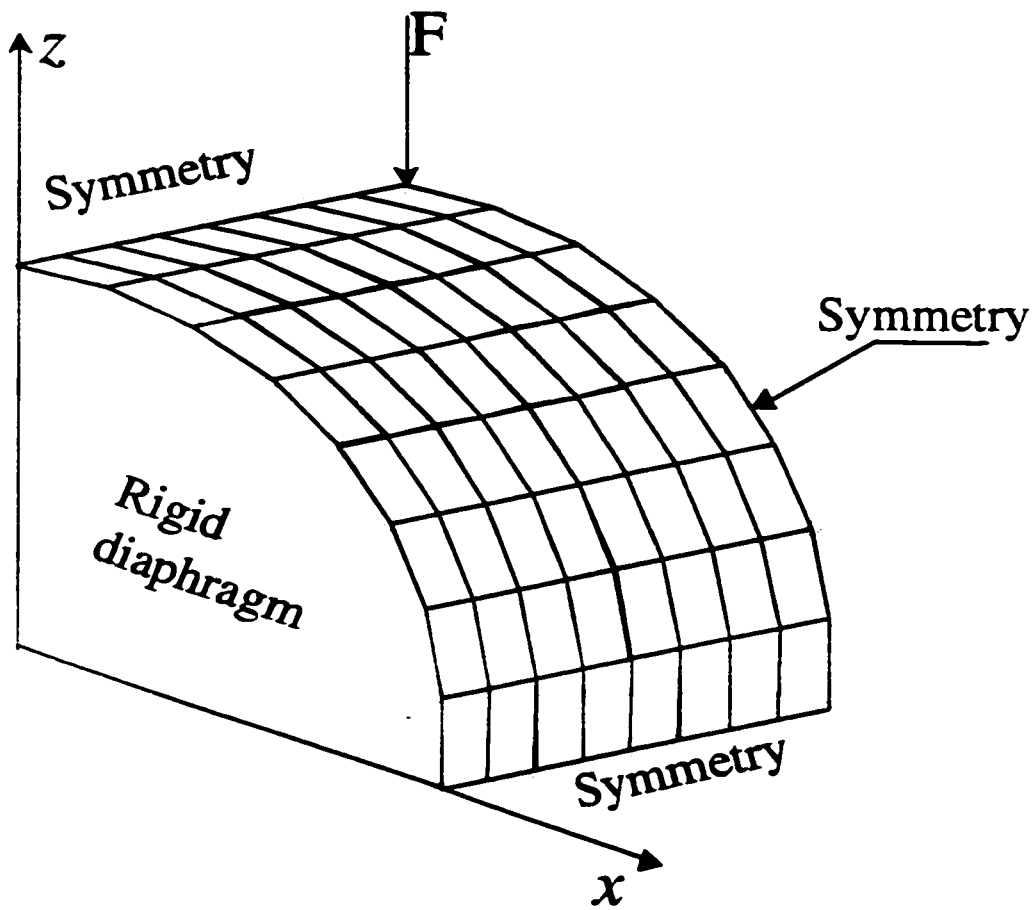


Figure 7.1 Pinched cylinder with end diaphragms
Geometry and loading condition

Table 7.1 Displacement results of the pinched cylinder with diaphragms

Mesh size	Displacement x 10 ⁻⁵		% of analytical solution		
	Present	[23]	Present	[23]	[65]
4x4	0.6756	0.6774	37.0	37.1	37.5
8x8	1.3569	1.3566	74.3	74.3	75.6
16x16	1.6958	1.6957	92.9	92.9	92.7
32x32	1.8062	1.8098	99.0	99.2	

of 1.82488×10^{-5} [65]. The results reported in References [23,65] are also given for comparison. The results of Simo et al. [65] are those of the displacement-based formulation and not the mixed one. For a better visualization of the convergence versus refinement, the results of Table 7.1 are plotted in Figure 7.2. It was stated in Reference [65] that this problem is a severe test of the inextensional bending and complex membrane states of stress. Furthermore, most four-noded shell elements do not converge efficiently in this problem, except the discrete Kirchhoff formulations. The results shown in Table 7.1 or Figure 7.2 indicate clearly that this element has passed satisfactorily this test and its performance is similar to that of Simo et al [65] and Parisch [23]

The maximum stresses occur at the load location except for the inplane shear stresses. As mentioned before, there is no significant difference between FOSDT and TOSDT models. Table 7.2 shows the maximum stresses with mesh refinement. The directions 1 and 2 stand, respectively, for axial and circumferential. For the normal stresses, both the maximum tensile (+) and maximum compressive (-) stresses are shown. By comparing Tables 7.1 and 7.2, it can be noticed that the rate of convergence of stresses is slower than that of deflections.

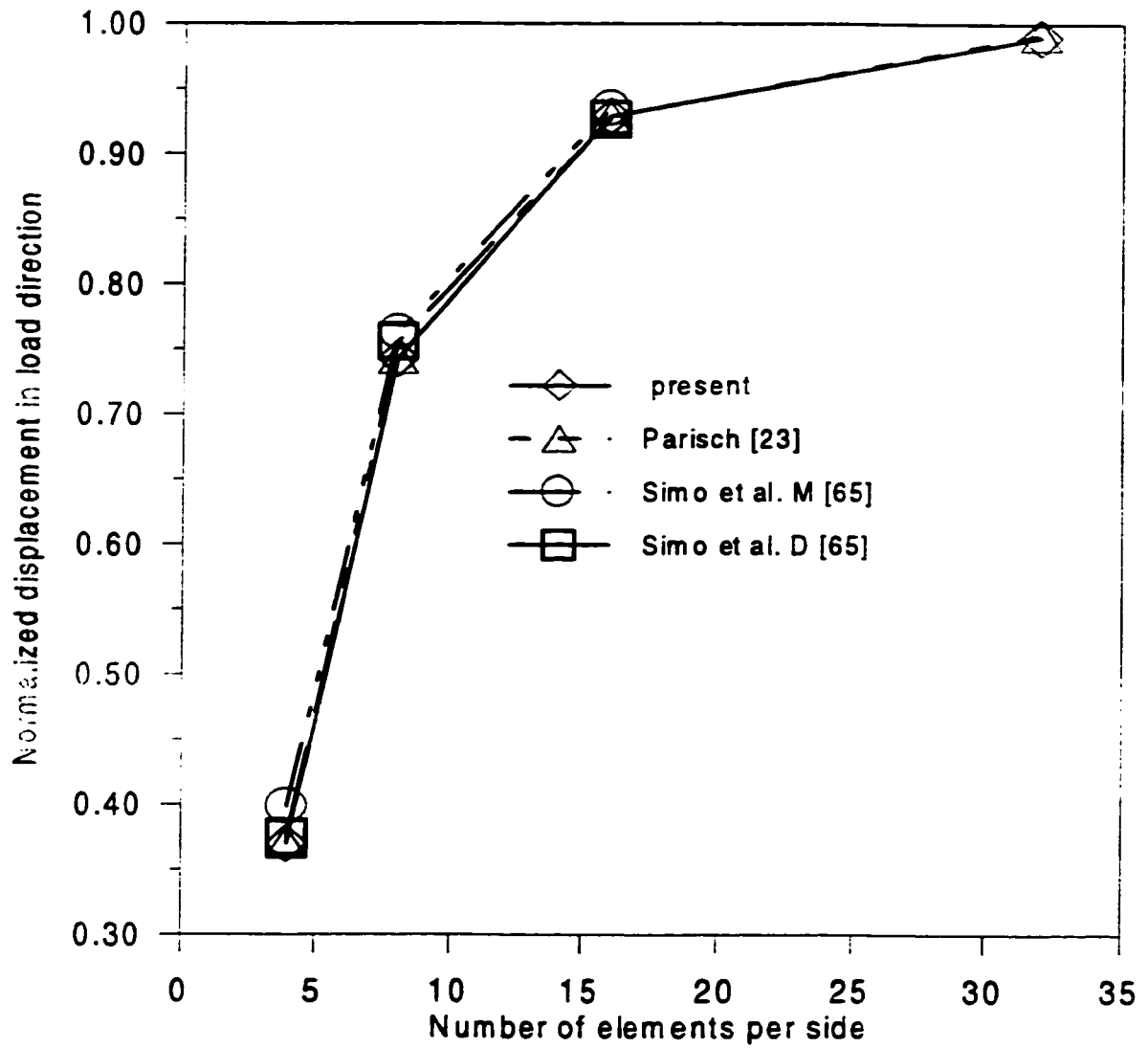


Figure 7.2 Pinched cylinder: Normalized displacement in load direction

Table 7.2 Pinched cylinder with end diaphragms: Maximum stresses with mesh refinement

Maximum Stresses	Mesh size			
	4x4	8x8	16x16	32x32
$\sigma_{11}(+)$	0.07493E-1	0.1251E-1	0.3775E-1	0.8203E-1
$\sigma_{11}(-)$	-0.1156E-1	-0.3504E-1	-0.7417E-1	-1.204E-1
$\sigma_{22}(+)$	0.09127E-1	0.2069E-1	0.4912E-1	0.9234E-1
$\sigma_{22}(-)$	-0.1126E-1	-0.4047E-1	-0.8610E-1	-1.356E-1
τ_{12}	0.03918E-1	0.08838E-1	0.1846E-1	0.2152E-1
τ_{13}	0.02000E-2	0.1192E-2	0.3968E-2	0.9040E-2
τ_{23}	0.05010E-2	0.1501E-2	0.4226E-2	0.9020E-2

7.2.1.2 Pinched Isotropic Hemisphere.

The second application concerns a pinched hemispherical isotropic shell with two inward and two outward forces 90° apart. This hemisphere is closed, i.e., there is no hole at its pole. The shell is fixed at the pole and loaded at the free edge. Figure 7.3 shows one quadrant of the hemispherical shell with the geometry of the mesh adopted in this example. It shows also the boundary conditions and the loads to be applied with their directions and intensities. The mesh adopted is highly skewed for coarse mesh situations. The geometric and material properties are given by the shell radius $R = 10$, thickness $t = 0.04$, Young's modulus $E = 6.825 \times 10^7$ and Poisson's ratio $\nu = 0.3$.

The analytical solution yields a displacement of 0.0924 [65] in the direction of the applied forces. Here also a mesh refinement is adopted to assess the convergence of the present element. Three meshes are considered, four, eight and sixteen elements per each of the three sides of the shell. The rest of the elements inside the domain are designed as

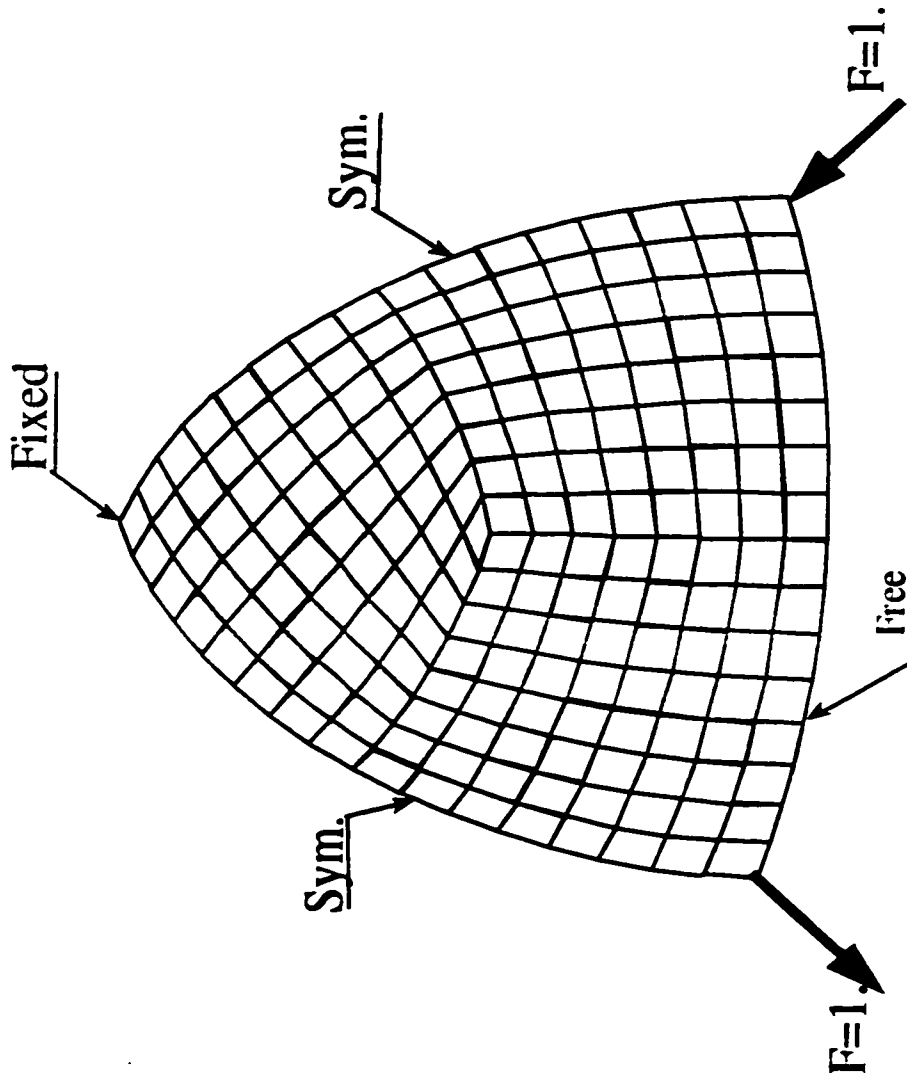


Figure 7.3 Pinched hemispherical shell: Geometry and loading

shown in Figure 7.3. The displacement results of this simulation are shown in Table 7.3. In this example, as can be seen from Figure 7.4 which shows convergence versus refinement, the present element clearly exhibits a better performance than those of Parisch [23] and Simo et al.[65], especially in the case of coarse meshes.

Table 7.3 Pinched hemisphere: Displacement along the applied load

Elements per side	Displacement Present	% of analytical solution		
		Present	[65]	[23]
4	0.065367	70.7	46.8	31.1
8	0.089208	96.6	93.3	87.9
16	0.091809	99.4	98.8	98.5

The maximum stresses versus mesh refinement are reported in Table 7.4. The same remark, as before, can be made about the convergence of stresses in the case of the pinched isotropic hemisphere. The directions 1 and 2 correspond to the curvilinear coordinates defined at the element level, i.e., direction 1 is along sides 1-2 and 4-3 and direction 2 is along sides 1-4 and 2-3 (see Figure 4.2). Because of the mesh adopted in this problem, these directions are not orthogonal.

Table 7.4 Pinched hemisphere : Maximum stresses with mesh refinement

Maximum Stresses	Elements per side		
	4	8	16
$\sigma_{11}(+)$	0.2176E4	0.3532E4	0.5447E4
$\sigma_{11}(-)$	-0.1725E4	-0.3540E4	-0.5455E4
$\sigma_{22}(+)$	0.1939E4	0.3008E4	0.4012E4
$\sigma_{22}(-)$	-0.2175E4	-0.3028E4	-0.4047E4
τ_{12}	0.1757E4	0.2237E4	0.2338E4
τ_{13}	0.1717E2	0.5050E2	0.7709E2
τ_{23}	0.08425E2	0.3464E2	0.6340E2

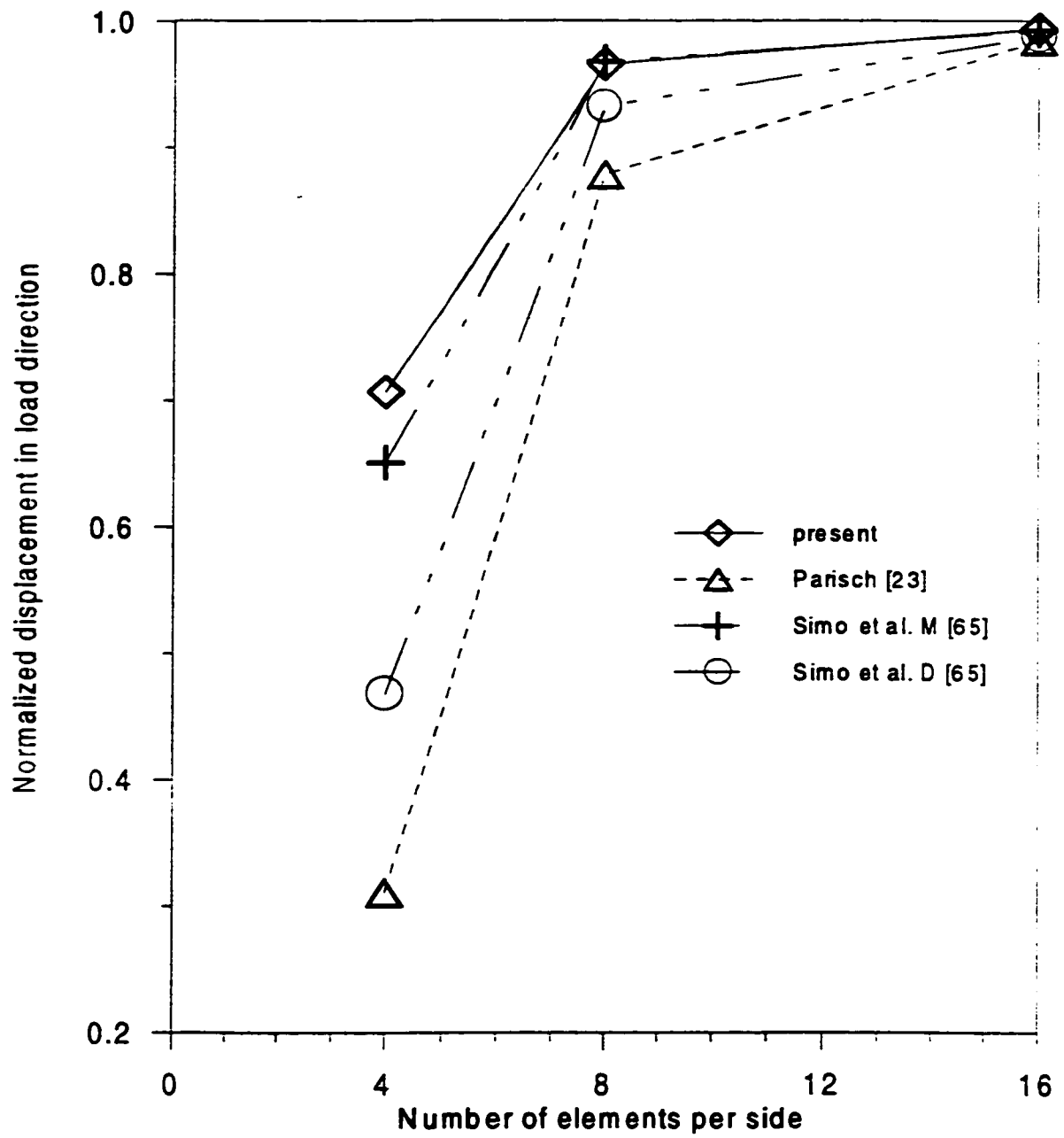


Figure 7.4 Pinched hemisphere : convergence versus mesh refinement

7.2.1.3 Sandwich Plate under Sinusoidal Transverse Loads.

This example consists of a square sandwich plate simply supported along all four edges. It is composed of three layers placed symmetrically with respect to the middle surface. Figure 7.5 shows the form of the plate with the dimensions of its face sheets and core and the sinusoidal loading on top of it. This problem was analyzed by Pandya and Kant [69] and Basar et al.[19] for different values of the plate width-to-thickness ratios. The results reported by those authors concern the deflection at the center of the plate and stresses at different locations. These locations will be defined through the coordinate system (x,y,z) shown also in Figure 7.5. The deflection and stresses, reported by these authors, were presented in a nondimensional form using the following multipliers:

$$m_1 = \frac{100h^3 E_2}{Pa^4} ; \quad m_2 = \frac{h^2}{Pa^2} ; \quad m_3 = \frac{h}{Pa} \quad (7.1)$$

where P is the intensity of the sinusoidal load whose equation is shown in Figure 7.5. h represents the total thickness of the plate and a is its side length. E_2 is Young's modulus in the direction 2 which is defined here by the y axis. Thus, the x axis defines the direction 1. The geometric and material properties of the sandwich plate are as follows.

$$a=1.0 \qquad h_1=h_3=0.1h \qquad h_2=0.8h \qquad P=1$$

Core material

$$E_1=E_2=0.4 \times 10^5 \qquad G_{12}=0.16 \times 10^5 \qquad G_{13}=G_{23}=0.6 \times 10^5 \qquad \nu_{12}=0.25$$

Face sheet material

$$E_1=25 \times 10^6 \qquad E_2=10^6 \qquad G_{12}=G_{13}=0.5 \times 10^6 \qquad G_{23}=0.2 \times 10^6 \qquad \nu_{12}=0.25$$

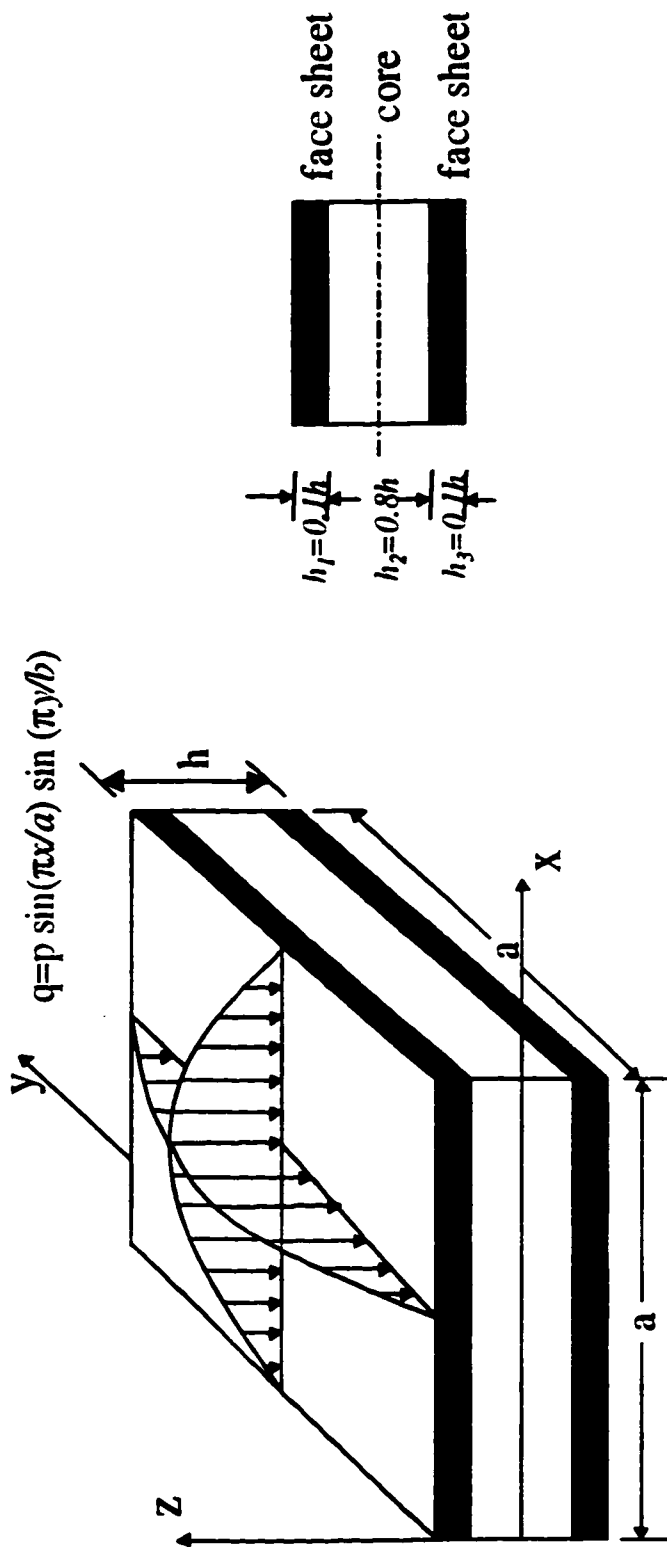


Figure 7.5 Simply supported sandwich plate under sinusoidal loading

where h_1 , h_2 and h_3 are visualized in Figure 7.5. The rest of the coefficients have already been explained in chapter three.

The symmetry is exploited in this case too, by considering only one quarter of the plate with the appropriate boundary conditions. The results of the analysis are obtained using a 16×16 mesh. The plate is analyzed for the following values of the width to thickness ratios; $\frac{a}{h} = 100, 25, 10$ and 4 . These ratios cover the whole range of plates from thin to thick. The quantities compared in this study are the maximum transverse deflection and maximum normal and shear stresses. It is noteworthy to mention here that in the linear case there is no difference between the different stress and strain measures. The results obtained from the simulation of this problem are reported in Tables 7.5, 7.6 and 7.7 with those available in the literature, which are obtained either from the exact or other finite element formulations.

Pandya and Kant [69] considered, in their analysis, two HOSDT models: the first one uses five parameters and satisfies the free transverse shear stress conditions on top and bottom free surfaces and the second one uses seven parameters but does not satisfy the above mentioned condition. The second one had a superior agreement with the exact solution compared to the first one. Thus, only the second model is reported here and it is referred to by HOSDT2. The results of the FOSDT are also reported by Pandya and Kant [69]. The results of the TOSDT of Basar et al.[19], referred to as RT7, along with those of their layerwise theory (LWT) are also reported here. The exact solution to this problem was derived by Pagano [171], and since then it has been used by many researchers as a reference to assess their numerical models.

Tables 7.5, 7.6 and 7.7 show the predictions of the different quantities by the different theories. The normal stresses σ_{11} and σ_{22} are evaluated at the center of the plate at the top (or bottom due to symmetry) where their maximum value occurs. The membrane shear stress σ_{12} is evaluated at the corner ($x=0, y=0$) with $z=0$ (middle of the core material). The transverse shear stresses σ_{13} and σ_{23} are evaluated at the middle of their respective sides. It can be seen from the results reported in these tables that all theories shown agree well with each other in the case of thin plates ($a/h = 100$) especially concerning the deflection and the in-plane stresses. For moderately thick plates ($a/h = 10$) to thick plates ($a/h = 4$), the results of the FOSDT are in gross error and should not be used for response prediction in this range. However, HOSDT of the present formulation and that of Reference [69] still yield good to satisfactory results compared to the exact solution. The results of Reference [69] are slightly better than those of the present study.

Table 7.5 Simply supported square sandwich plate: Maximum stresses and deflection for ($a/h=100$)

Model	$M2*\sigma_{11}$ ($a/2, a/2,$ $h/2$)	$m2*\sigma_{22}$ ($a/2, a/2,$ $h/2$)	$m2*\tau_{12}$ ($0, 0, h/2$)	$m3*\tau_{13}$ ($0, a/2, 0$)	$m3*\tau_{23}$ ($a/2, 0, 0$)	$m1*W0$ ($a/2, a/2, 0$)
Present	1.0958	0.0548	-0.0436	0.3741	0.03419	0.8903
RT7 [19]	1.0931	0.0547	-0.0435	-----	-----	0.8903
LWT [19]	1.0931	0.0547	-0.0435	-----	-----	0.8917
FOSDT [69]	1.104	0.0546	-0.0435	0.1152	0.01767	0.883
HOSDT2 [69]	1.109	0.0554	-0.0440	0.3627	0.03322	0.891
EXACT [171]	1.098	0.0550	-0.0437	0.324	0.0297	0.892

Table 7.6 Simply supported square sandwich plate: Maximum stresses and deflection for (a/h=10)

Model	$m2*\sigma_{11}$ (a/2,a/2, h/2)	$M2*\sigma_{22}$ (a/2,a/2, h/2)	$m2*\tau_{12}$ (0,0,h/2)	$m3*\tau_{13}$ (0,a/2,0)	$m3*\tau_{23}$ (a/2,0,0)	$m1*W0$ (a/2,a/2,0)
Present	1.147	0.1040	-0.0687	0.3489	0.05780	2.083
FOSDT [69]	1.062	0.08057	-0.05532	0.1112	0.02384	1.557
HOSDT2 [69]	1.166	0.1052	-0.0692	0.3400	0.05642	2.087
EXACT [171]	1.153	0.1104	-0.0707	0.3000	0.05270	2.200

Table 7.7 Simply supported square sandwich plate: Maximum stresses and deflection for (a/h=4)

Model	$M2*\sigma_{11}$ (a/2,a/2, h/2)	$m2*\sigma_{22}$ (a/2,a/2, h/2)	$m2*\tau_{12}$ (0,0,h/2)	$m3*\tau_{13}$ (0,a/2,0)	$m3*\tau_{23}$ (a/2,0,0)	$m1*W0$ (a/2,a/2,0)
Present	1.4994	0.2386	-0.1406	0.2822	0.1166	7.147
FOSDT [69]	0.9056	0.1578	-0.0912	0.0995	0.0436	4.755
HOSDT2 [69]	1.5230	0.2414	-0.1419	0.2750	0.1137	7.160
EXACT [171]	1.556	0.2595	-0.1437	0.2390	0.1072	7.596

7.2.1.4 Laminated Rectangular Plate under sinusoidal Transverse Loads

A laminated rectangular plate with boundary conditions and loading similar to those of the previous example is considered. The plate has five layers constructed in the sequence (0°/90°/0°/90°/0°) The following lamina properties are used [172]:

$$E_1=25E_2 \quad , \quad E_3=E_2 \quad , \quad G_{12}=G_{13}=0.5E_2 \quad , \quad G_{23}=0.2E_2 \quad , \quad \nu_{12}=\nu_{13}=\nu_{23}=0.25$$

The plate is simply supported in such a manner that the edges are fixed against tangential

displacements but free to translate in the normal direction. The sides of the plate are a and b with $a/b=3$. Its thickness h is varied in order to have side-to-thickness ratios (a/h) of 5 and 10. In addition to the multipliers m_1 , m_2 and m_3 used for the sandwich plate, another multiplier m_4 is added in this example. It is given by

$$m_4 = \frac{100h^2 E_2}{pa^3} \quad (7.2)$$

The quantities compared in this example are the maximum transverse deflection, the inplane displacements at midsides and the maximum normal and shear stresses. Various numbers (N) of layers have been considered in the analysis. Two different meshes are first considered for the case $a/h=10$ and $N=5$ layers; they are 8×8 and 16×24 for one fourth of the plate where symmetry conditions are exploited. The results obtained using these two meshes are shown in Table 7.8. The quantities reported are made dimensionless as follows:

$$\begin{aligned} \bar{w} &= m_1 w(a/2, b/2, 0) & , \bar{u} &= m_4 u(0, b/2, z) & , \bar{v} &= m_4 v(a/2, 0, z) \\ \bar{\sigma}_{xx} &= m_2 \sigma_{xx}(a/2, b/2, z) & , \bar{\sigma}_{yy} &= m_2 \sigma_{yy}(a/2, b/2, z) & , \bar{\sigma}_{xy} &= m_2 \sigma_{xy}(0, 0, z) \\ \bar{\sigma}_{xz} &= m_3 \sigma_{xz}(0, b/2, z) & , \bar{\sigma}_{yz} &= m_3 \sigma_{yz}(a/2, 0, 0) \end{aligned} \quad (7.3a,b,c)$$

It can be noticed from Table 7.8 that there is no significant variation in the results between the two meshes. For the sake of comparison, the second mesh, i.e., 16×24 is used in the remaining simulations using $a/h=5, 10$ and $N=2, 3, 4, 5$ and 10. The results concerning inplane displacements, inplane and transverse stresses with those of Reference [171] are reported in Tables 7.9-7.11 and the normalized center deflections,

with respect to the elastic solution, are shown in Figures 7.6 and 7.7.

Table 7.8 Laminated plate with $a/h=10$ and $N=5$ layers: Nondimensional results with mesh refinement

Model Mesh	\bar{w}	\bar{u} -	\bar{v} -	$\bar{\sigma}_{xx}$ +	$\bar{\sigma}_{yy} * 10$ *	$\bar{\sigma}_{xy} * 10$ -	$\bar{\sigma}_{xz}$	$\bar{\sigma}_{yz} * 10$
FOSDT 8x8	0.8633	0.945	0.4345	0.7369	-0.7209	0.1164	0.4105	0.0758
TSODT 8x8	0.9207	1.004	0.4660	0.7840	-0.7555	0.1245	0.6366	0.1154
FOSDT 16x24	0.8638	0.945	0.4335	0.7429	-0.7257	0.1173	0.4123	0.0762
TOSDT 16x24	0.9213	1.005	0.4650	0.7904	-0.7606	0.1254	0.6416	0.1162

+ values are calculated at $z=h/2$

- values are calculated at $z=-h/2$

* values are calculated at the lower face of the second layer (from the bottom)

Table 7.9 Laminated plate: Nondimensional inplane displacements \bar{u} and \bar{v}

a/h	Model	\bar{u}			\bar{v}		
		N=3	N=4	N=5	N=3	N=4	N=5
5	FOSDT	0.780 -	-2.065 +	-0.9360 +	0.708 -	1.164 -	0.7359 -
	TOSDT	1.189 -	-2.541 +	-1.164 +	0.9136 -	1.311 -	0.8644 -
	HOSDT[172]	1.130 -	-2.524 +	-1.195 +	0.9202 -	1.310 -	0.8554 -
	ELAST.[172]	1.222 -	-3.663 +	-1.252 +	1.003 -	1.624 -	0.9942 -
10	FOSDT	0.7900 -	-2.088 +	0.9450 -	0.3815 -	0.8413 -	0.4335 -
	TOSDT	0.9038 -	-2.215 +	1.005 -	0.4417 -	0.8845 -	0.4650 -
	HOSDT[172]	0.8779 -	-2.206 +	1.011 -	0.4401 -	0.8843 -	0.4638 -
	ELAST.[172]	0.9197 -	-2.536 +	1.029 -	0.4746 -	0.9879 -	0.5069 -

+ values are calculated at $z=h/2$

- values are calculated at $z=-h/2$

Table 7.10 Laminated plate under sinusoidal loading: Nondimensional
inplane stresses $\bar{\sigma}_x$, $\bar{\sigma}_y$ and $\bar{\sigma}_{xy}$

a/h	Mode	$\bar{\sigma}_x$			$\bar{\sigma}_y * 10$			$\bar{\sigma}_{xy} * 10$		
		N=3 +	N=4 -	N=5 +	N=3 *	N=4 +	N=5 *	N=3 -	N=4 -	N=5 -
5	FOSDT	0.6159	-1.015	0.7359	-0.6390	2.094	-1.216	0.1519	0.2496	0.1657
	TOSDT	0.9376	-1.280	0.9153	-0.7905	2.377	-1.318	0.2055	0.2905	0.1963
	HOSDT[172]	0.8924	-1.275	0.9430	-0.7843	2.378	-1.320	0.1969	0.2903	0.1969
	ELAST.[172]	0.9835	-1.325	1.000	-0.9023	2.809	-1.528	0.2214	0.3429	0.2214
10	FOSDT	0.6202	-1.026	0.7429	-0.3537	1.498	-0.7257	0.1010	0.2001	0.1173
	TOSDT	0.7103	-1.097	0.7904	-0.4002	1.579	-0.7606	0.1164	0.2115	0.1254
	HOSDT[172]	0.6924	-1.094	0.7969	-0.3981	1.581	-0.7621	0.1151	0.2115	0.1258
	ELAST.[172]	0.7260	-1.116	0.8120	-0.4349	1.740	-0.8297	1.227	0.2292	0.1335

+ Values are calculated at $z=h/2$

- Values are calculated at $z=-h/2$

* values are calculated on the lower face (from the bottom)

Table 7.11 Laminated plate under sinusoidal loading: Nondimensional
transverse shear stresses $\bar{\sigma}_x$ and $\bar{\sigma}_{yz}$

a/h	Model	$\bar{\sigma}_x$			$\bar{\sigma}_{yz} * 10$		
		N=3	N=4 *	N=5	N=3	N=4 ~	N=5
5	FOSDT	0.3924	0.4379	0.4102	0.0765	0.4826	0.1134
	TOSDT	0.7221	0.6640	0.6254	0.1036	0.7821	0.1801
	HOSDT[172]	0.4022	0.5321	0.3833	0.1210	0.2949	0.3429
	ELAST.[172]	0.3755	0.4837	0.4094	0.1324	0.3450	0.3892
10	FOSDT	0.1576	0.4417	0.4128	0.1282	0.3693	0.0762
	TOSDT	0.3058	0.6850	0.6416	0.1582	0.5824	0.1162
	HOSDT[172]	0.4299	0.5480	0.4027	0.1447	0.4407	0.2213
	ELAST.[172]	0.4201	0.5333	0.4093	0.1524	0.4801	0.2375

* values are calculated at the lower face of the third layer (from the bottom)

~ values are calculated at the upper face of the second layer (from the bottom)

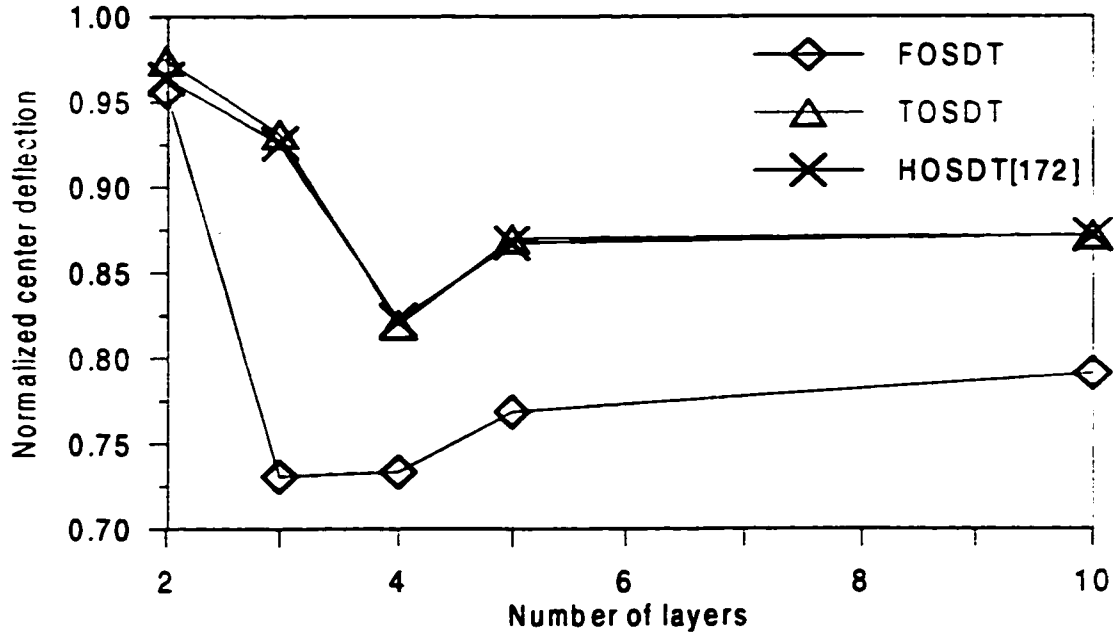


Figure 7.6 laminated plate under sinusoidal loading ($a/h=5$)
Nondimensional center deflection

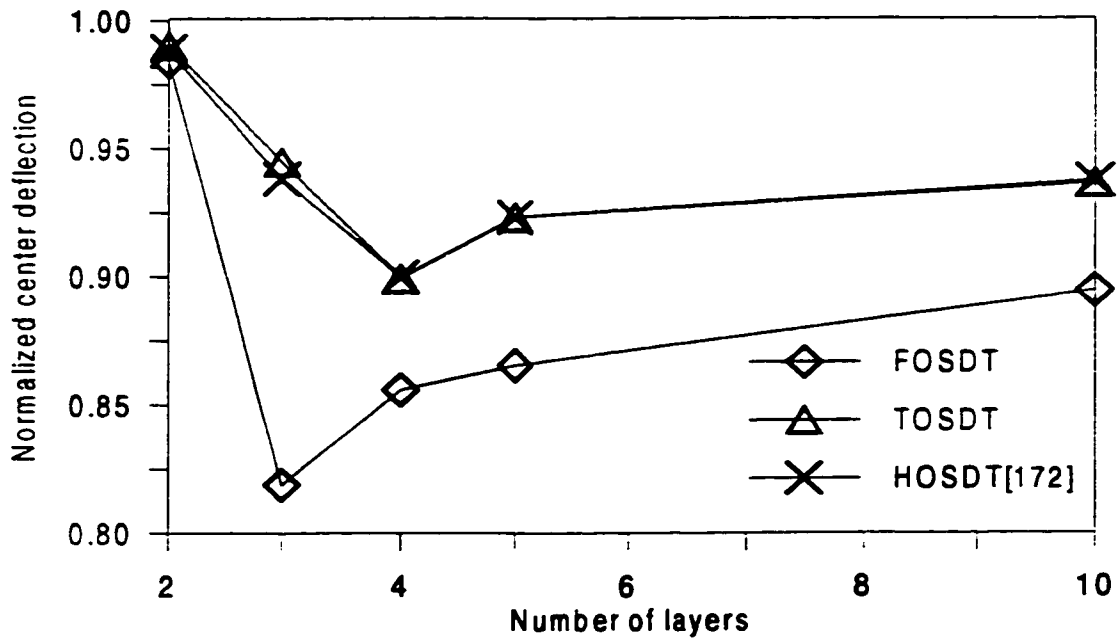


Figure 7.7 laminated plate under sinusoidal loading ($a/h=10$)
Nondimensional center deflection

The model HOSDT of Reference [172] represents the analytical solution using a third order shear deformation theory and enforcing the zero transverse shear stress condition at the bounding surfaces but does not use a shear correction factor. It can be seen from the results shown that the predictions of the present TOSDT model are in excellent agreement with those of the analytical solution using HOSDT except for the transverse shear stresses where the prediction of the present model are poor. This is mainly due to the non-enforcement of the zero transverse shear stress condition at the bounding surface. As expected, the predictions of the TOSDT model are better than those of the FOSDT model but the gap between the predictions of the two models decreases as the ratio a/h increases from 5 to 10, i.e., as the plate gets thinner. In terms of the number of layers, the worst prediction of the FOSDT model is for $N=3$ but it improves as N increases.

7.2.1.5 Laminated Cylindrical Panel under Sinusoidal Transverse Loads

This example is similar to the previous one except that now the side a is a circular arc with a radius R . The ratio a/b is maintained at 3. The cases studied are for $R/a=1$ and 4 and $a/h=5,10$ and 50. The mesh adopted here is 16×16 for one fourth of the cylinder. The loading is normal to the surface of the cylinder. The center deflections are normalized, as in the previous example, with respect to the elastic solution. The results are shown in Figures 7.8-7.11 for the nondimensional central deflections and in Tables 7.12 and 7.13 for the inplane and transverse stresses respectively. The model indicated by SHAL in the results refers to the analytical solution based on shallow shell theory using the third order shear deformation theory without shear correction factor. It can be noticed from the results that there is a good agreement between the present TOSDT

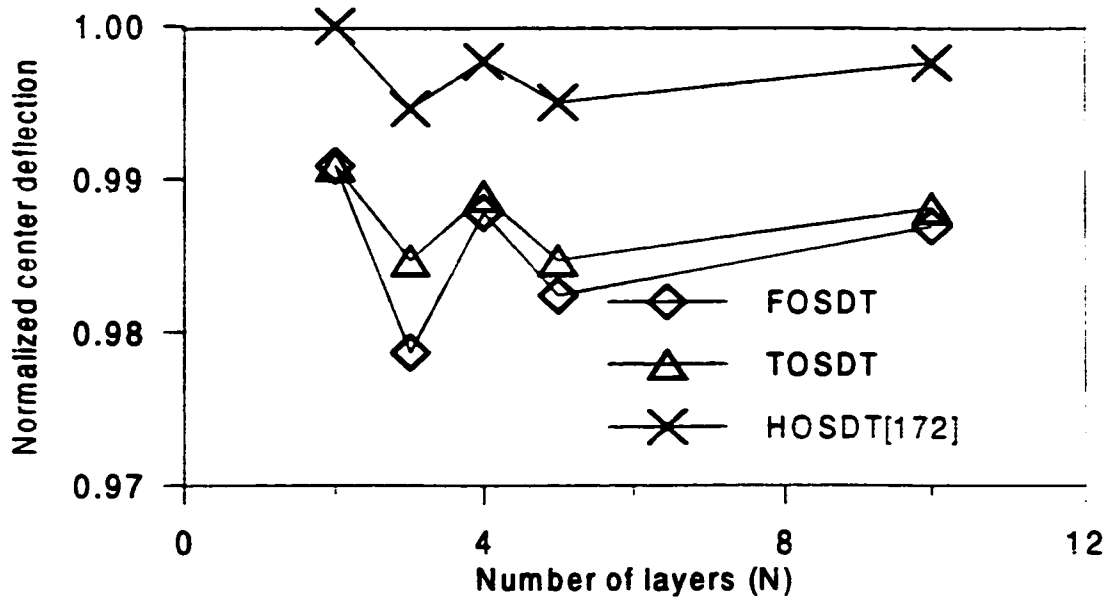


Figure 7.8 laminated cylindrical panel under sinusoidal loading ($R/a=1$, $a/h=50$) Nondimensional center deflection

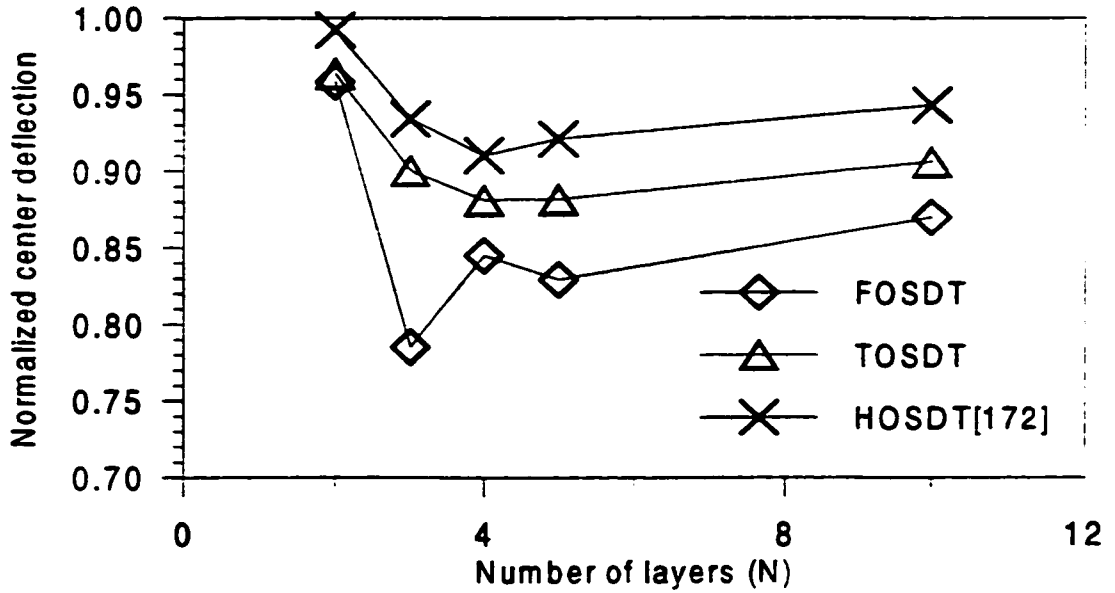


Figure 7.9 Laminated cylindrical panel under sinusoidal loading ($R/a=1$, $a/h=10$) Nondimensional center deflection

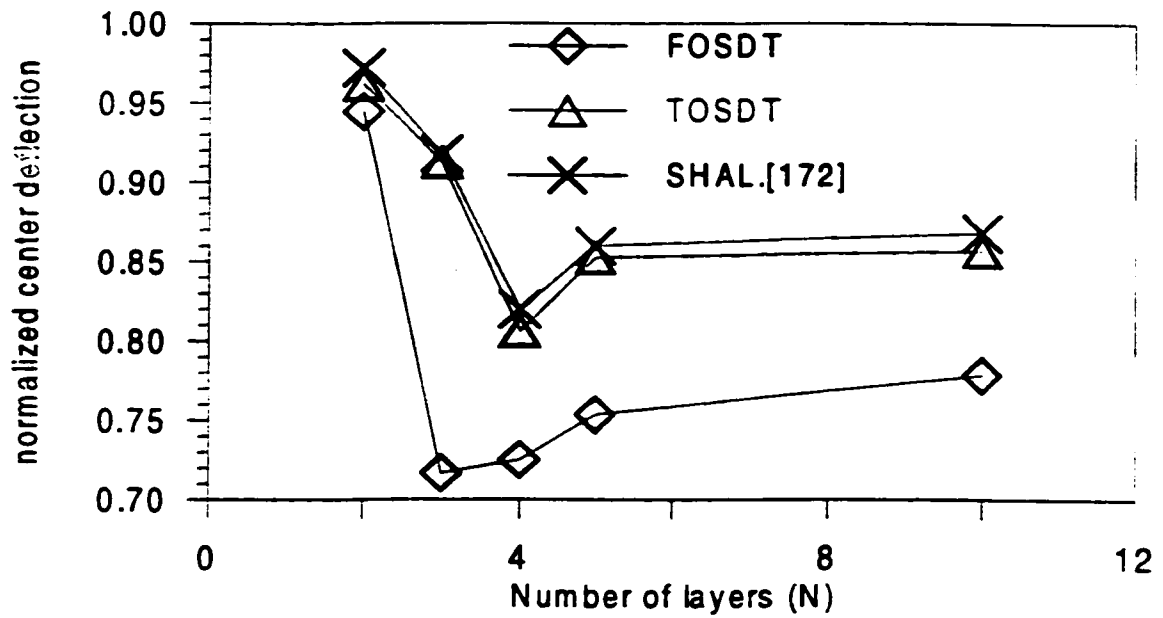


Figure 7.10 Laminated cylindrical panel under sinusoidal loading ($R/a=4$, $a/h=5$) Nondimensional center deflection

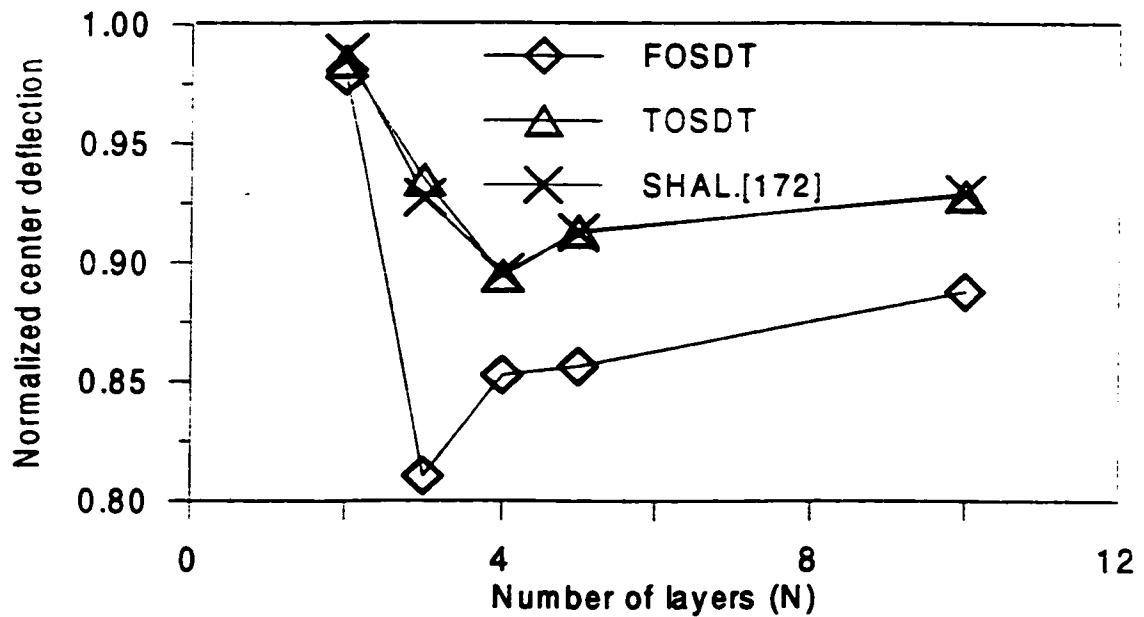


Figure 7.11 Laminated cylindrical panel under sinusoidal loading ($R/a=4$, $a/h=10$) Nondimensional center deflection

Table 7.12 Laminated cylindrical panel under sinusoidal loading

Nondimensional inplane stresses $\bar{\sigma}_x$, $\bar{\sigma}_y$ and $\bar{\sigma}_r$

R/a	a/h	Model	$\bar{\sigma}_x$			$\bar{\sigma}_y * 10$			$\bar{\sigma}_r * 10$		
			N=3 -	N=4 -	N=5 -	N=3 *	N=4 +	N=5 *	N=3 -	N=4 -	N=5 -
1	10	FOSDT	-0.6750	-1.060	-0.7987	1.275	2.830	1.727	0.2089	0.3996	0.2450
		TOSDT	-0.7731	-1.132	-0.8499	1.450	2.957	1.820	0.2397	0.4183	0.2611
		HOSDT[172]	-0.7876	-1.176	-0.9000	1.498	3.049	1.895	0.2581	0.4478	0.2839
		ELAST.[172]	-0.8534	-1.222	-0.9436	1.602	3.314	2.044	0.2725	0.4883	0.3030
4	5	FOSDT	-0.6251	-1.024	-0.7444	0.8297	2.305	1.410	0.1737	0.2834	0.1907
		TOSDT	-0.9549	-1.289	-0.9302	1.030	2.601	1.535	0.2338	0.3272	0.2250
		SHAL.[172]	-0.9125	-1.301	-0.9641	1.028	2.640	1.547	0.2356	0.3342	0.2293
		ELAST.[172]	-1.022	-1.388	-1.040	1.116	3.117	1.763	0.2588	0.4006	0.2626
	10	FOSDT	-0.6253	-1.029	-0.7475	0.5370	1.754	0.9172	0.1225	0.2424	0.1432
		TOSDT	-0.7165	-1.100	-0.7957	0.6108	1.845	0.9643	0.1413	0.2558	0.1530
		SHAL.[172]	-0.6985	-1.100	-0.8037	0.6037	1.846	0.9623	0.1405	0.2573	0.1543
		ELAST.[172]	-0.7463	-1.137	-0.8340	0.6468	2.045	1.047	0.1510	0.2822	0.1660

+ values are calculated at $z=h/2$ - Values are calculated at $z=-h/2$

* Values are calculated on the upper face of the second layer (from the top)

Table 7.13 Laminated cylindrical panel under sinusoidal loading

Nondimensional transverse shear stresses $\bar{\sigma}_z$ and $\bar{\sigma}_{yz}$

R/a	a/h	Model	$\bar{\sigma}_z$			$\bar{\sigma}_{yz} * 10$		
			N=3	N=4 *	N=5	N=3	N=4 ~	N=5
1	10	FOSDT	0.1693	0.4528	0.4400	0.4193	0.5044	0.0852
		TOSDT	0.3265	0.6908	0.6814	0.1739	0.7534	0.1307
		HOSDT[172]	0.4821	0.5781	0.4491	0.1746	0.5028	0.2679
		ELAST.[172]	0.4697	0.5597	0.4544	0.1848	0.5567	0.2904
4	5	FOSDT	0.1578	0.4391	0.4122	0.1927	0.5028	0.1144
		TOSDT	0.2902	0.6611	0.6283	0.2608	0.8046	0.1817
		SHAL.[172]	0.4118	0.5443	0.3922	0.2479	0.5995	0.3511
		ELAST.[172]	0.3867	0.4924	0.4260	0.2729	0.7049	0.4016
	10	FOSDT	0.1583	0.4418	0.4144	0.1289	0.3930	0.077
		TOSDT	0.3070	0.6829	0.6440	0.1591	0.6108	0.1170
		SHAL.[172]	0.4344	0.5525	0.4068	0.1462	0.4400	0.2235
		ELAST.[172]	0.4271	0.5379	0.4160	0.1555	0.4869	0.2425

* values are calculated at the lower face of the second layer (from the top)

~ values are calculated at the upper face of the third layer (from the top)

model and HOSDT or SHAL models of Reference [172] with respect to the center deflection and inplane stresses. The only significant difference is shown for the case of a deep moderately thick panel ($R/a=1$, $a/h=10$). The transverse shear stresses predicted by the TOSDT model are poor. The worst prediction of the FOSDT model is also for $N=3$ as was the case for the laminated plate. For the case of a deep very thin panel ($R/a=1$, $a/h=50$), the center deflection predicted by all the models is very close to the elasticity solution.

7.2.1.6 Laminated Spherical Panel under Sinusoidal Transverse Loads

The last example in the linear analysis concerns a doubly curved simply supported laminated spherical shell ($R_x = R_y = R$) with its curved sides a and b equal ($a=b$). The boundary conditions are defined as before, i.e., the edges are fixed against tangential displacements but free to translate in the direction normal to the edge and tangent to the shell surface. A mesh of 16×16 is used for one fourth of the spherical panel. The sinusoidal loading is normal to the shell surface. The results concerning the normalized center deflection for different values of R/a , a/h and N are shown in Figures 7.12 and 7.13. A good agreement between the TOSDT model and the analytical solutions HOSDT or SHAL except for a slight difference for the case of a thick moderately shallow shell ($R/a=5$, $a/h=5$). The largest difference in prediction between the TOSDT and FOSDT models is shown for the case ($R/a=5$, $a/h=5$, $N=3$) which reaches about 17% of the elasticity solution.

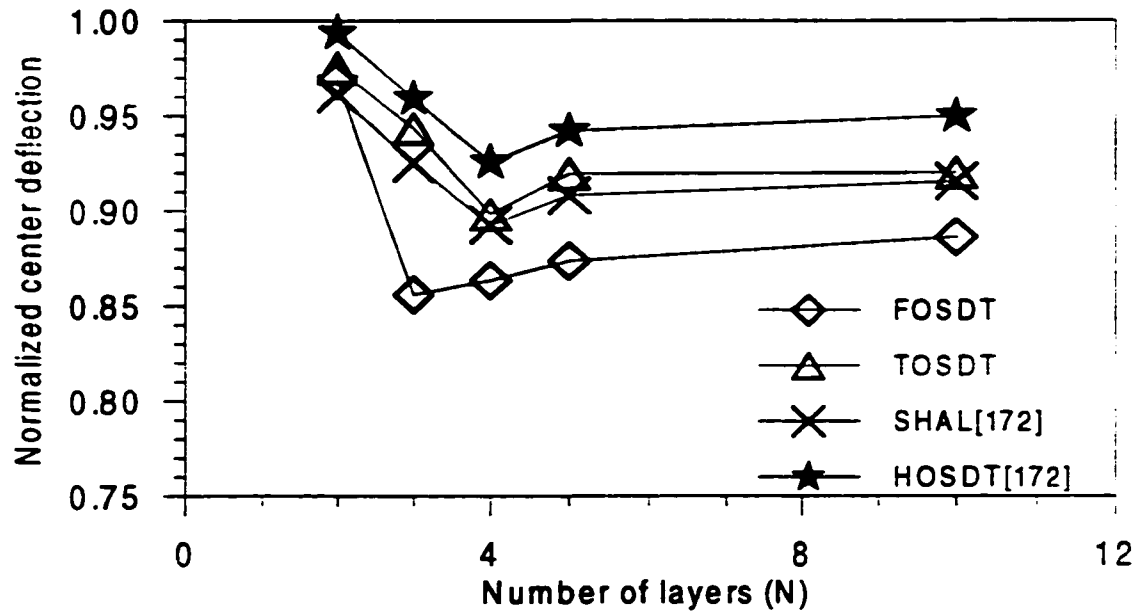


Figure 7.12 Laminated spherical panel under sinusoidal loading ($R/a=2$, $a/h=10$) Nondimensional center deflection

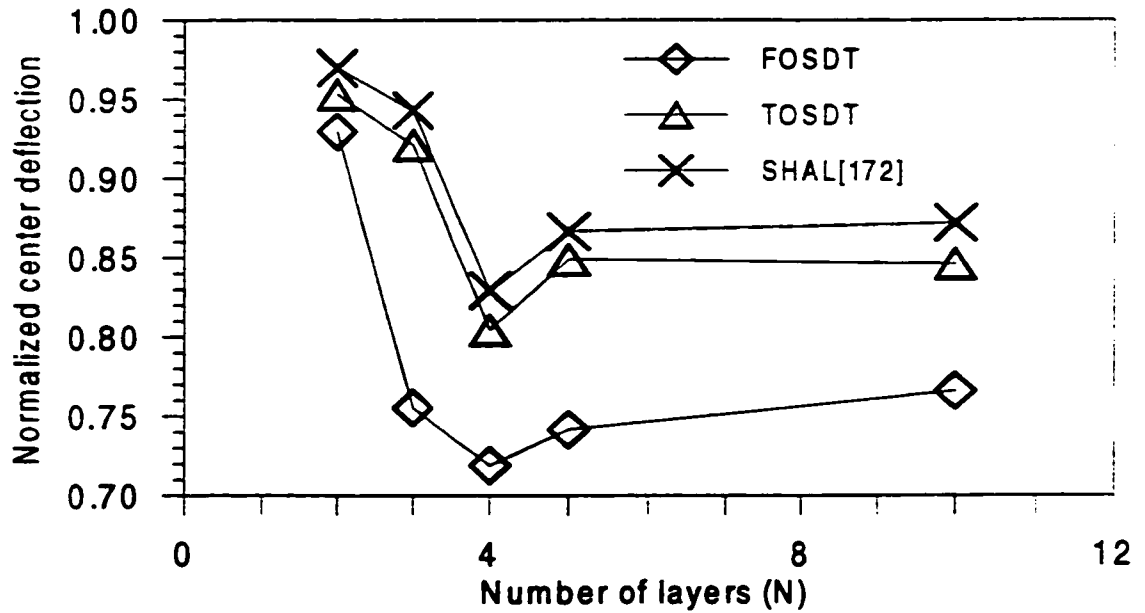


Figure 7.13 Laminated spherical panel under sinusoidal loading ($R/a=5$, $a/h=5$) Nondimensional center deflection

7.2.2 Nonlinear Problems

7.2.2.1 Pinching of a Clamped Isotropic Cylinder

The structure consists of a short isotropic cylindrical shell, fully clamped at one end and free at the other end where it is subjected to two pinching forces acting in opposite directions. Figure 7.14 shows one quarter of a cylinder where symmetry has been exploited again in this problem. The geometric and material properties describing the cylinder are its length $L = 3.048$, thickness $t = 0.03$, radius $R = 1.016$, Young's modulus $E = 2.0685 \times 10^7$ and Poisson's ratio $\nu = 0.3$.

This problem was investigated by Stander et al.[25] and Parisch [23]. The quarter of the cylinder is modeled using a regular mesh of 16×16 elements along with the appropriate boundary conditions.

The loading applied to the quarter of the cylinder is increased up to $F = 800$ in twenty equal increments. The response sought here is the deflection at the pinching force point along the direction of the force and maximum second Piola-Kirchhoff stresses and Green strains. The displacement variation along the applied load obtained from this simulation is plotted in Figure 7.15. To have an idea about the large deformation meant in this study, the ratio of maximum displacement found, which is around 1.6, to the radius $R=1.016$ gives a value of about 1.58. From the physical point of view, the deflection cannot exceed R . Since the structure studied is just one fourth of the cylinder, the deflection of $1.58R$ can be attained. Besides the results of this study, those of Stander et

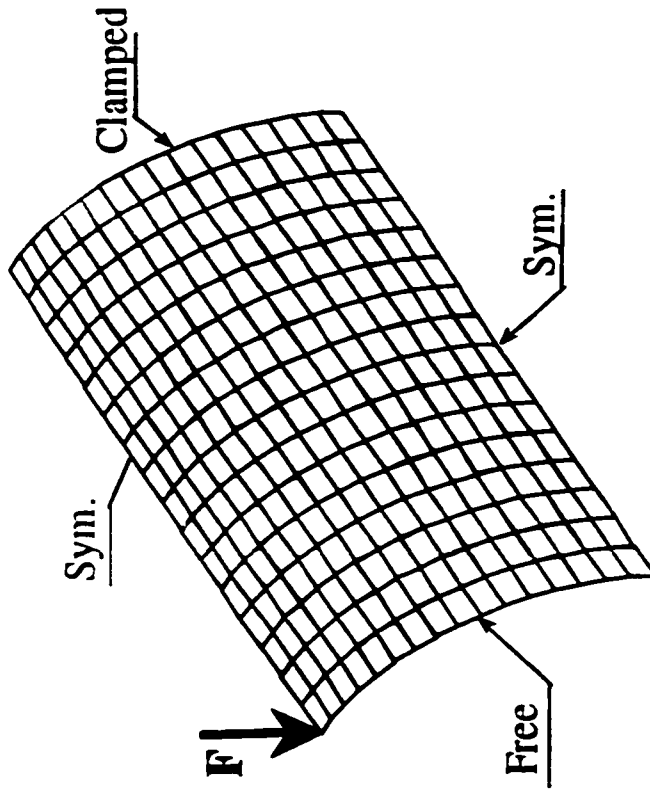


Figure 7.14 Pinching of a clamped cylinder: Geometry and loading

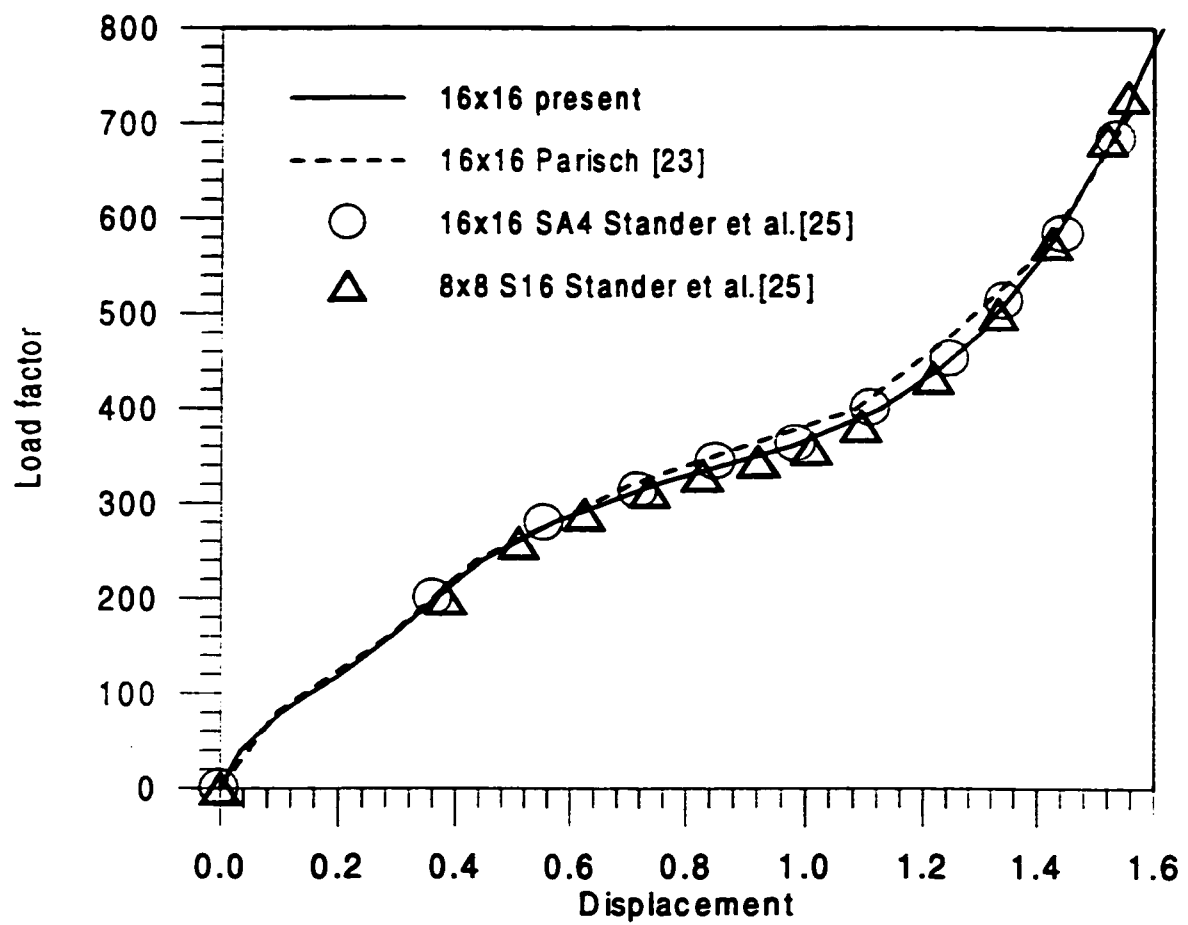


Figure 7.15 Pinching of a clamped cylinder
Displacement at the load location

al [25] and Parisch [23] are reported. A good agreement can be observed between the present element and that Reference [25]. Parisch's element[23] is slightly stiffer between load levels of 300 and 500.

Gauss points where the maximum second Piola-Kirchhoff stresses are obtained for most of the increments are considered. The stresses and strains obtained at these points are plotted versus the load factor and sometimes versus the displacement along the applied load. 1 and 2 represent the axial and circumferential directions respectively. The stresses sought are the maximum positive (P), the maximum negative (N) normal stresses, and the absolute maximum inplane and transverse shear stresses. Their corresponding Green strains are also recorded and plotted. The results are shown in Figures 7.16-7.20. It can be seen from Figure 7.20 that up to a vertical displacement of 0.75, which represents around 75% of the radius, all the strains are less than 1%. Thus, this region represents well the large deformation but small strain assumption. Beyond this, the strains increase sharply with the displacement which may violate the constitutive equations assumed in this study.

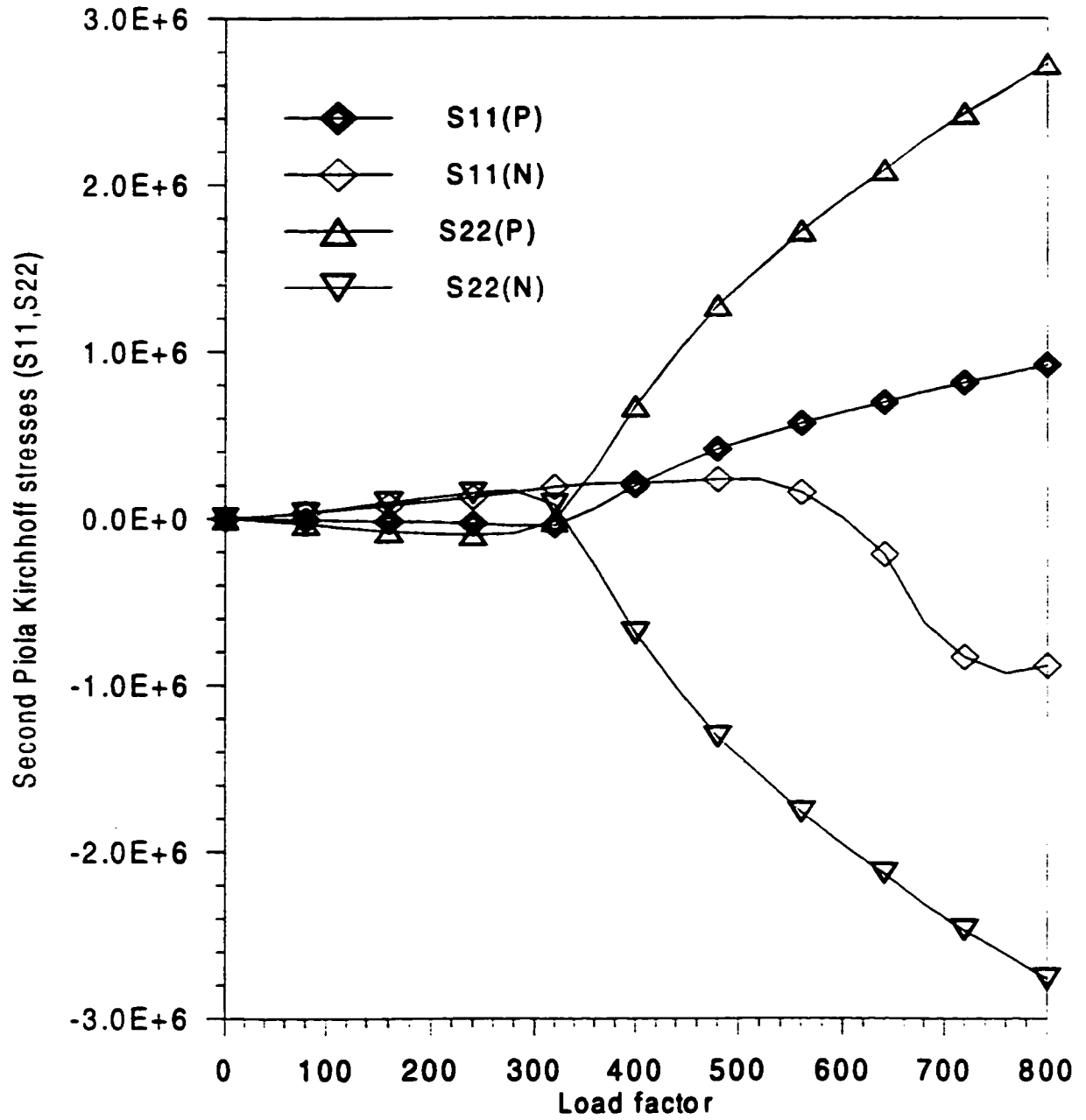


Figure 7.16 pinching of a clamped cylinder
Maximum normal stresses

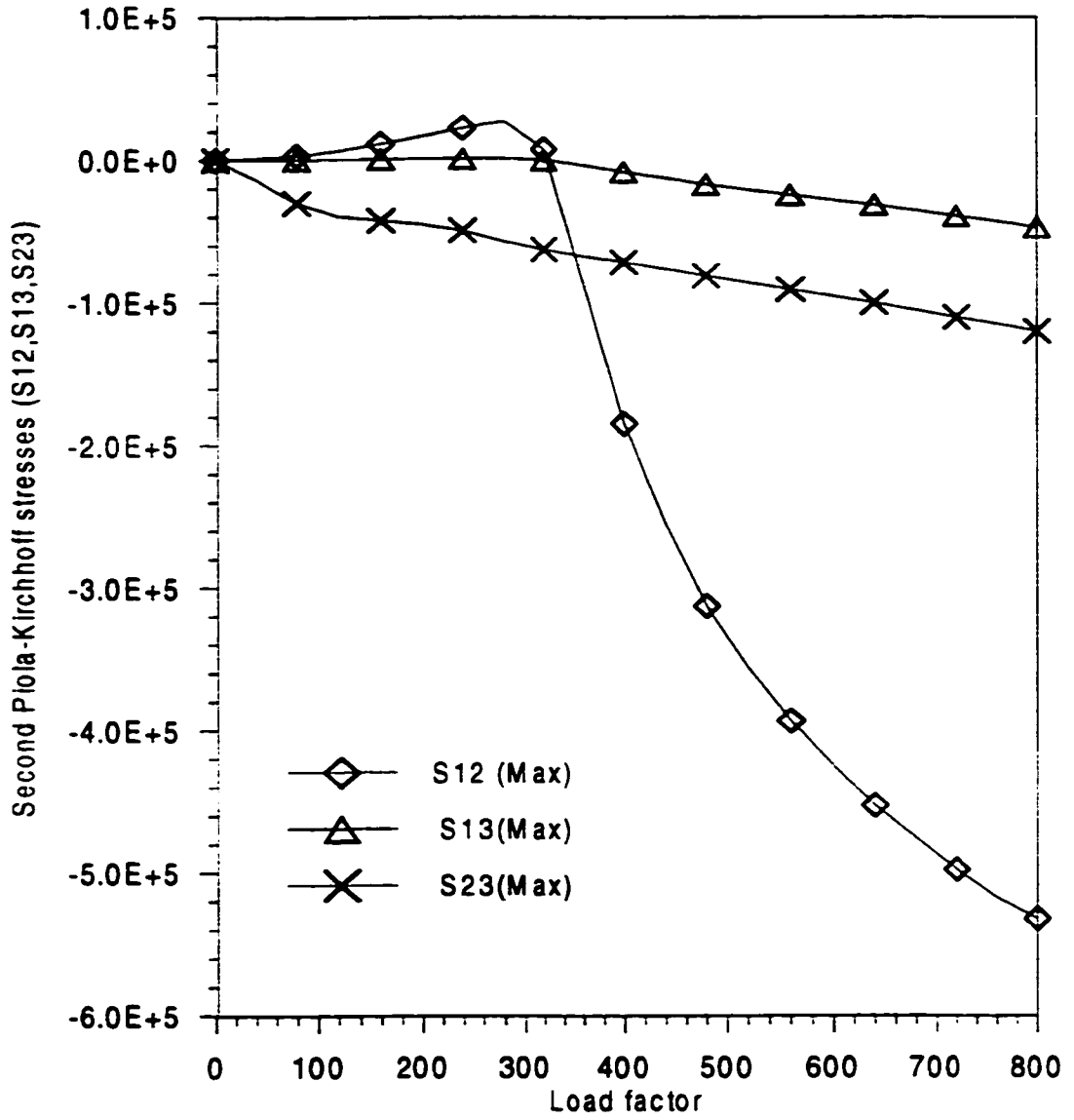


Figure 7.17 Pinching of a clamped cylinder
maximum shear stresses

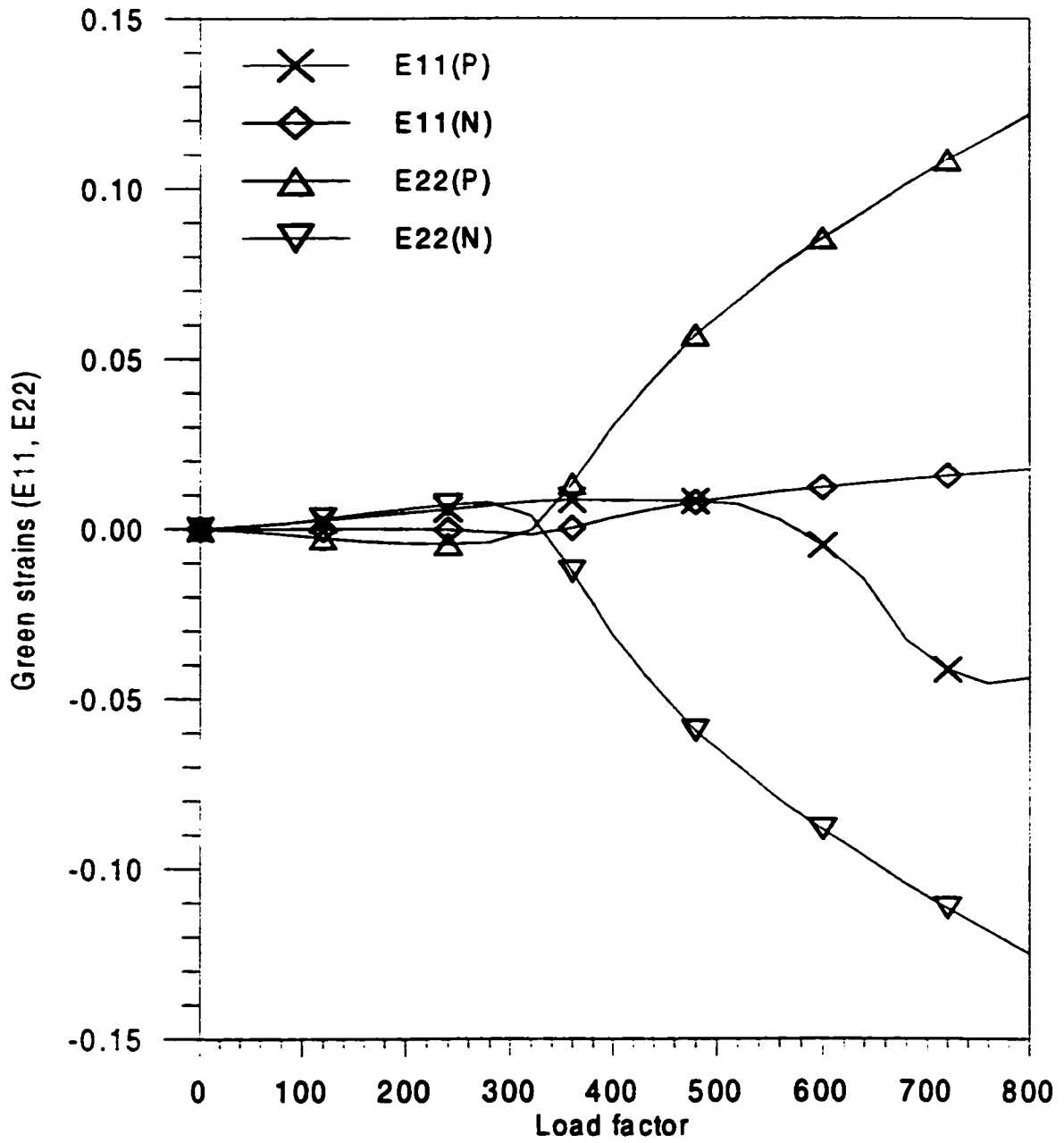


Figure 7.18 Pinching of a clamped cylinder
Maximum normal Green strains

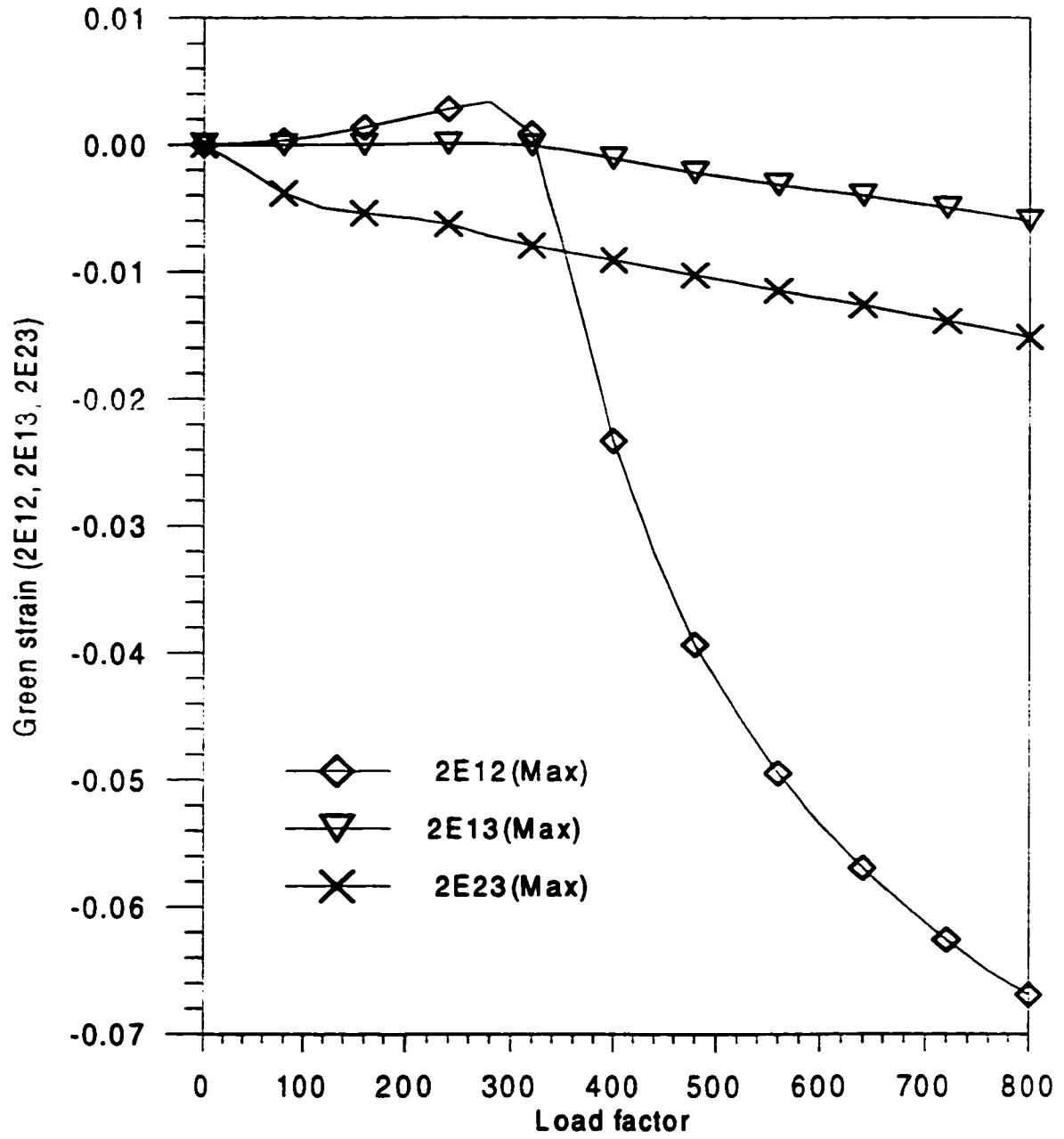


Figure 7.19 Pinching of a clamped cylinder
Maximum shear strains

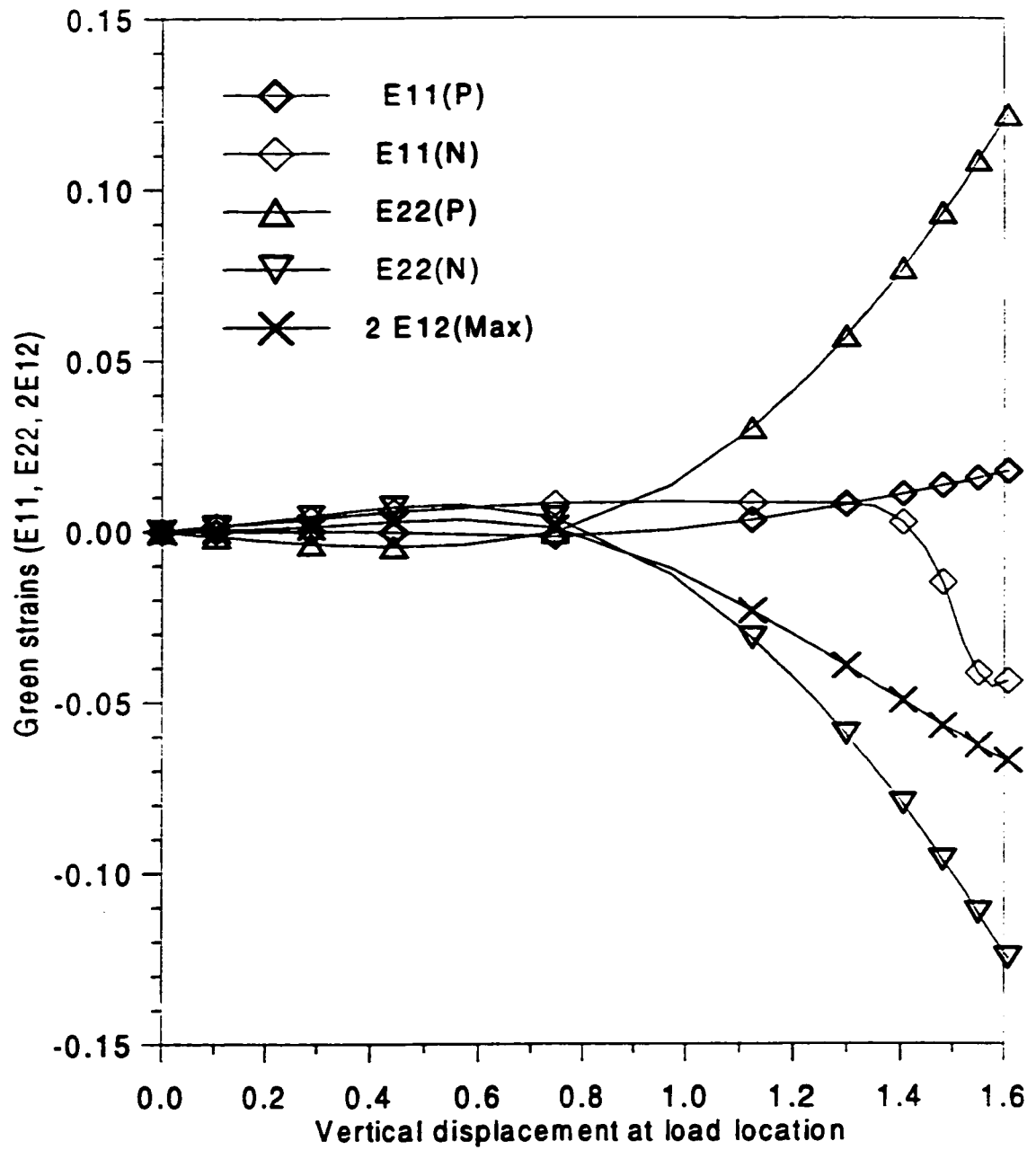


Figure 7.20 Pinching of a clamped cylinder: vertical displacement at load location versus Green strains

7.2.2.2 Pinching of a Hemispherical Shell with a Hole.

A hemispherical shell, with an 18° hole at the top, is subjected to the action of two inward and two outward forces 90° apart. Figure 7.21 shows the geometry and loading of one quadrant of this hemisphere which represents the only part to be modeled using symmetry conditions.

The sphere radius is $R = 10$, its thickness $t = 0.04$, the material properties are $E = 6.825 \times 10^7$ and $\nu = 0.3$.

This problem was investigated by Simo et al.[66]. It is reanalyzed here for the following mesh configurations: 8×8 , 16×16 and 32×32 elements for one quarter of the hemisphere. The numerical results showing the pinching loads versus deflection for these mesh configurations are plotted in Figure 7.22 along with those of Reference [66]. It can be noticed that the inward and outward deflections are not the same in the case of large deformations in contrast to the linear case. The maximum deflection obtained is around 60% the radius value. The present element shows good convergence properties with mesh refinement and the results of the 32×32 mesh agree very well with those of the 16×16 mesh of Reference.[66]. It is believed that the results reported in Reference [66] are those of the mixed formulation which is known to be superior to the displacement based FEM.

The variations of the maximum stresses and their corresponding strains with the load factor and the variations of these strains with the X displacement of point A are plotted in Figures 7.23-7.25. According to the mesh adopted in this example, the direction 1 refers to the meridian and 2 to the parallel circle. The maximum normal stresses in the

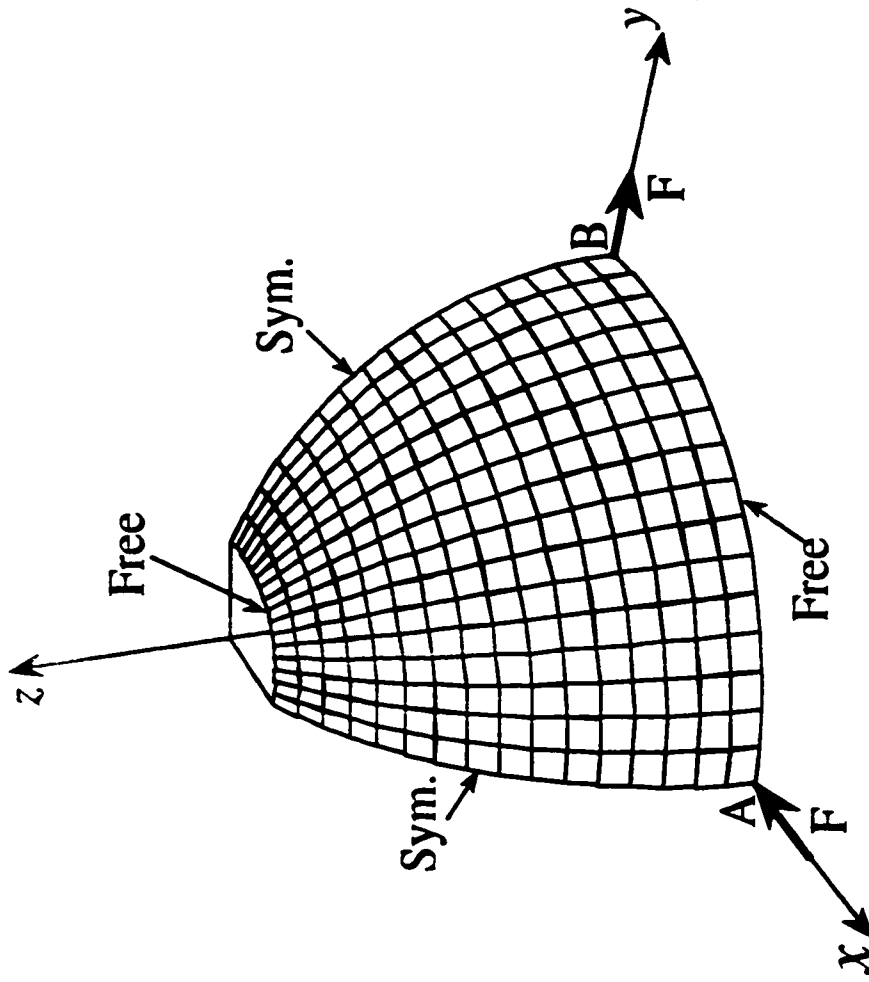


Figure 7.21 Pinching of a hemispherical shell with a hole: Geometry and loading

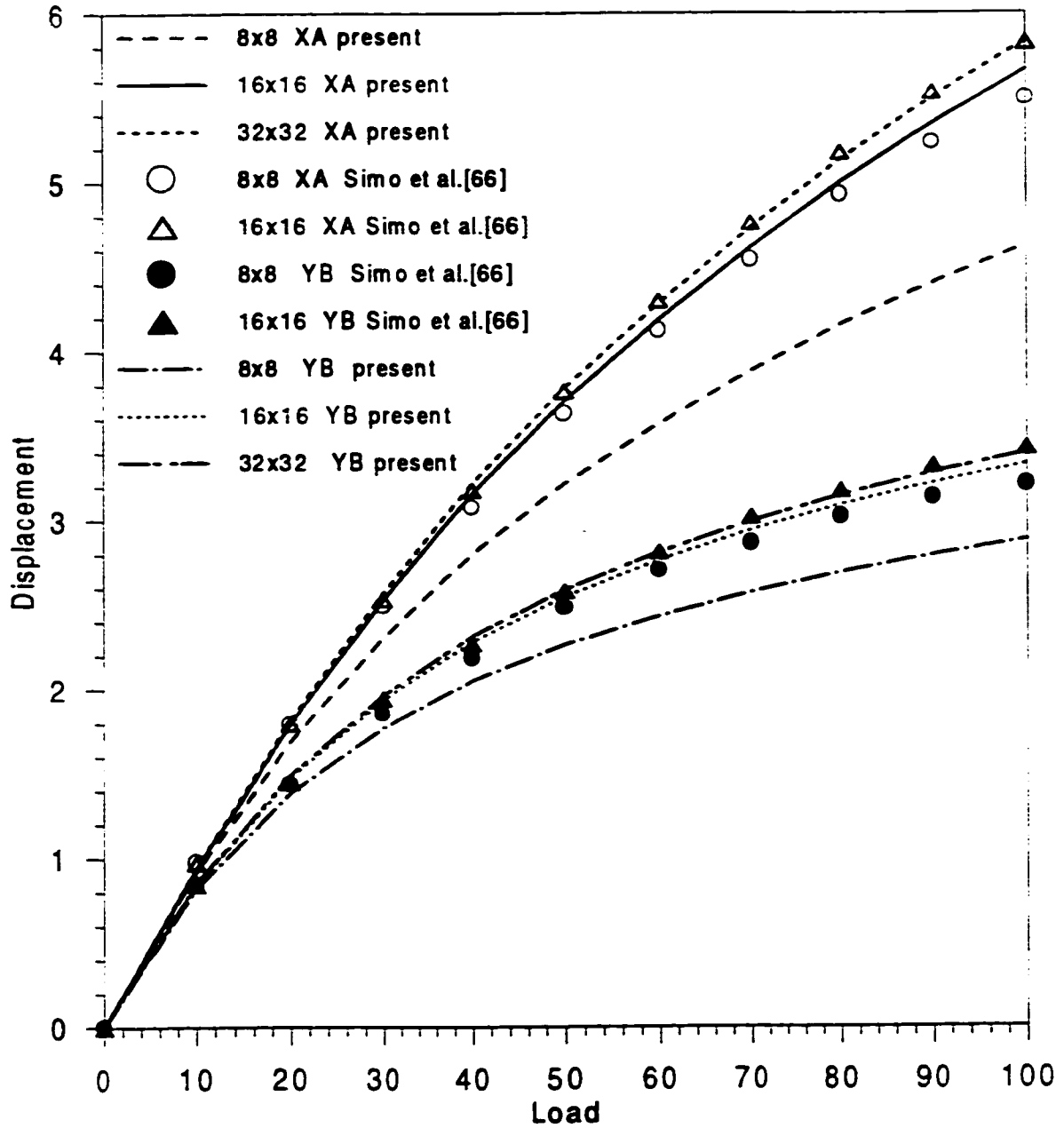


Figure 7.22 Pinching of a hemispherical shell with a hole
Deflection-load plots

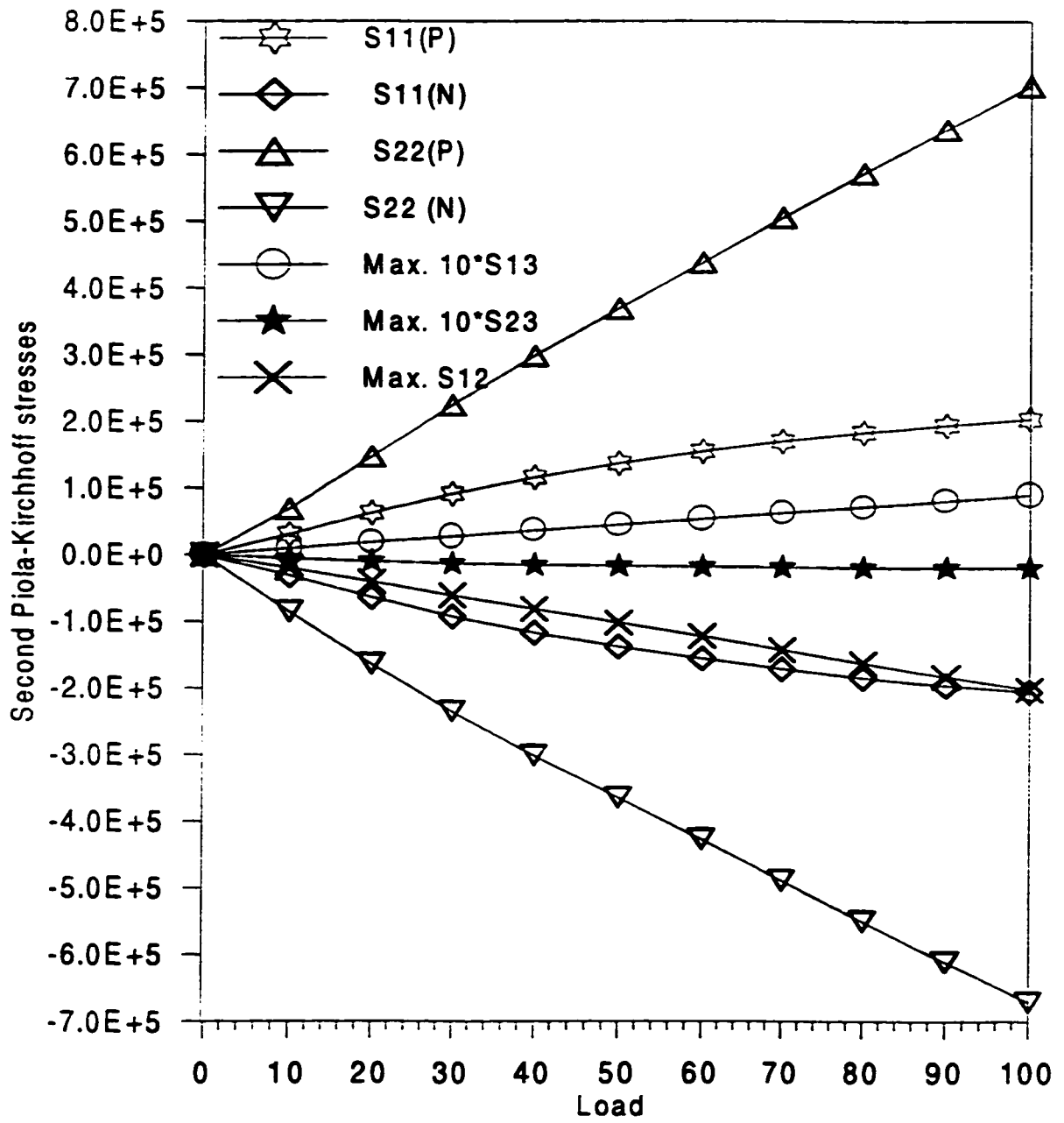


Figure 7.23 Pinching of a hemispherical shell with a hole
Maximum stresses-load plot

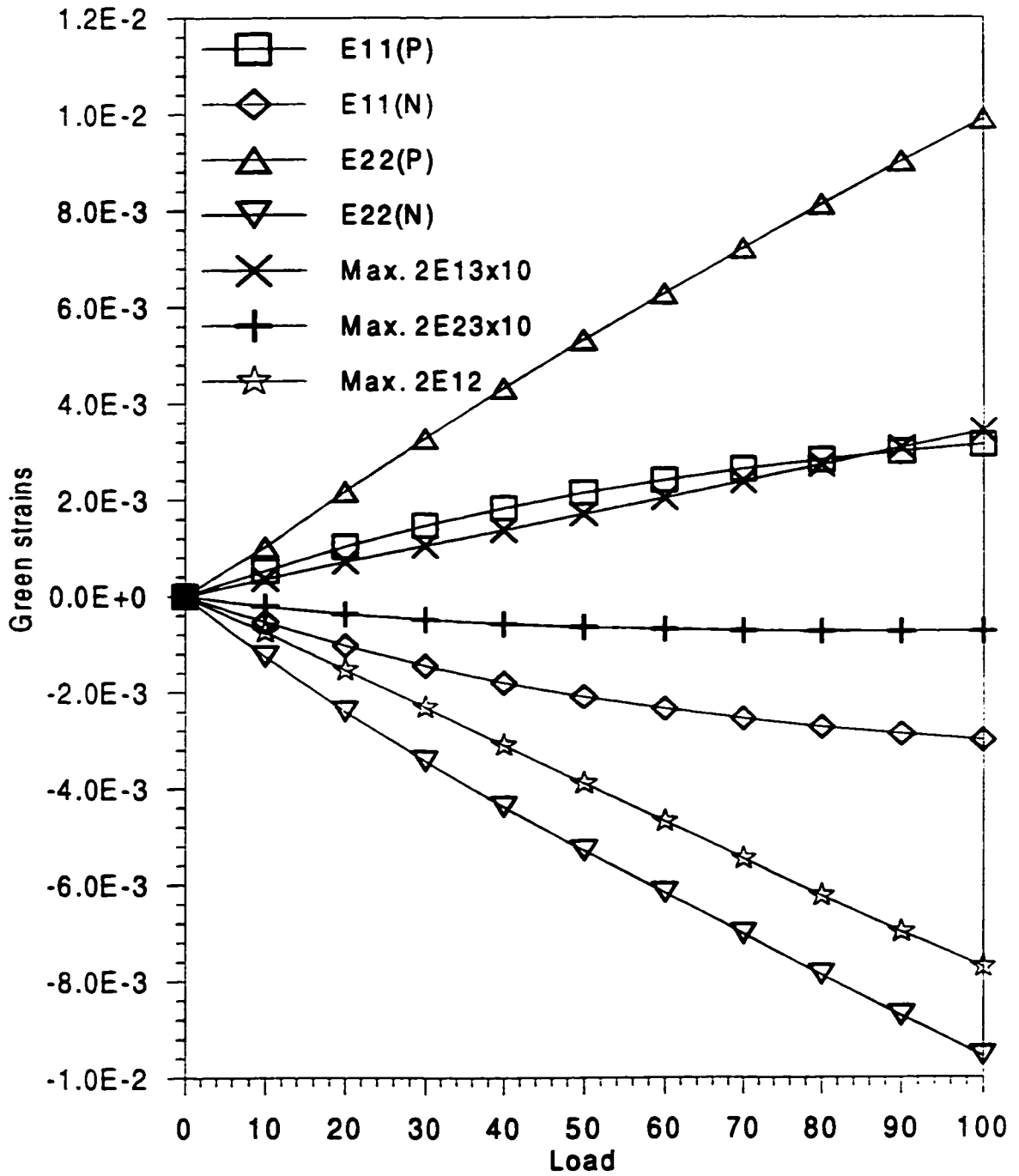


Figure 7.24 Pinching of a hemispherical shell with a hole
Green strains-Load plot

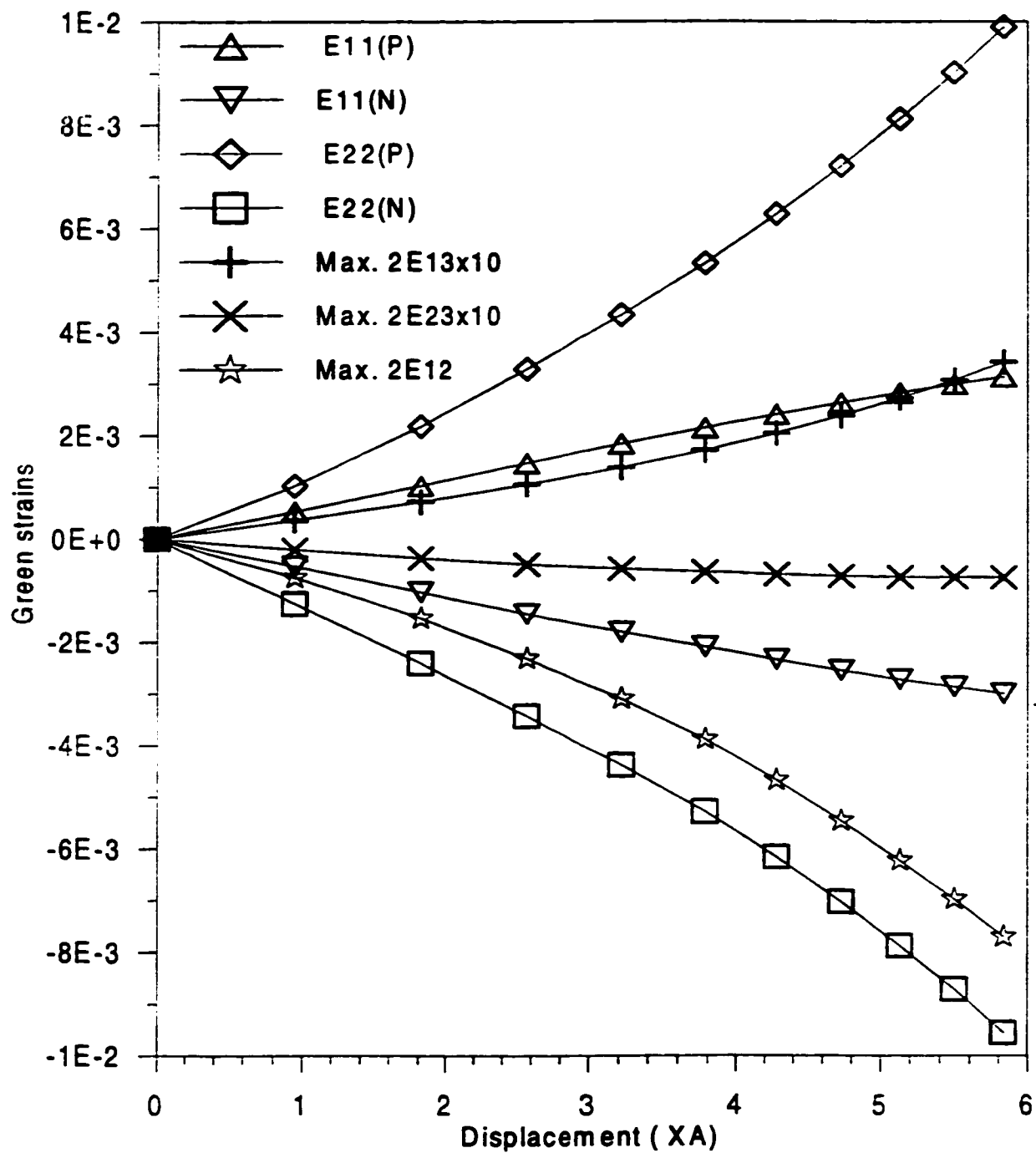


Figure 7.25 Pinching of a hemispherical shell with a hole
Green strains versus X-displacement of point A

meridional direction are on the meridional line containing point A with an angle of approximately 10 degrees between the radial line through this point and the X axis. The maximum stresses in the circumferential direction are at point B where the load is applied in the positive Y direction. Figure 7.25 shows that the maximum strain (E_{22}) obtained when the displacement of point A reaches its maximum, i.e., about 60% of the radius is just 1%.

7.2.2.3 Composite Shallow Cylindrical Shell with a Central Point Load.

This problem was investigated by Laschet and Jeusette [173] and Brank et al.[15]. The shallow shell is simply supported along its straight edges and free along the curved edges. It is subjected to a concentrated vertical downward force at its center. The problem data are:

$$L = 508 \text{ mm} \quad R = 2540 \text{ mm} \quad \theta = 0.2 \text{ rad (curved edge)}$$

Figure 7.26 shows the geometry and loading conditions and the geometry of the mesh used. Two thicknesses were considered, $t_A = 12.6 \text{ mm}$ and $t_B = 6.3 \text{ mm}$. The panel is built up by a lay-up of 12 plies with ply thickness $t_p = t_A/12 = 1.05 \text{ mm}$ in Case A and $t_p = t_B/12 = 0.525 \text{ mm}$ in Case B. To investigate the effects of lay-up on the performance, two stacking sequences are chosen for each case. They are

(i) $[90_4^{\circ}/0_4^{\circ}/90_4^{\circ}]$

(ii) $[0_4^{\circ}/90_4^{\circ}/0_4^{\circ}]$

Here 0° means that the fiber orientation is in the circumferential direction.

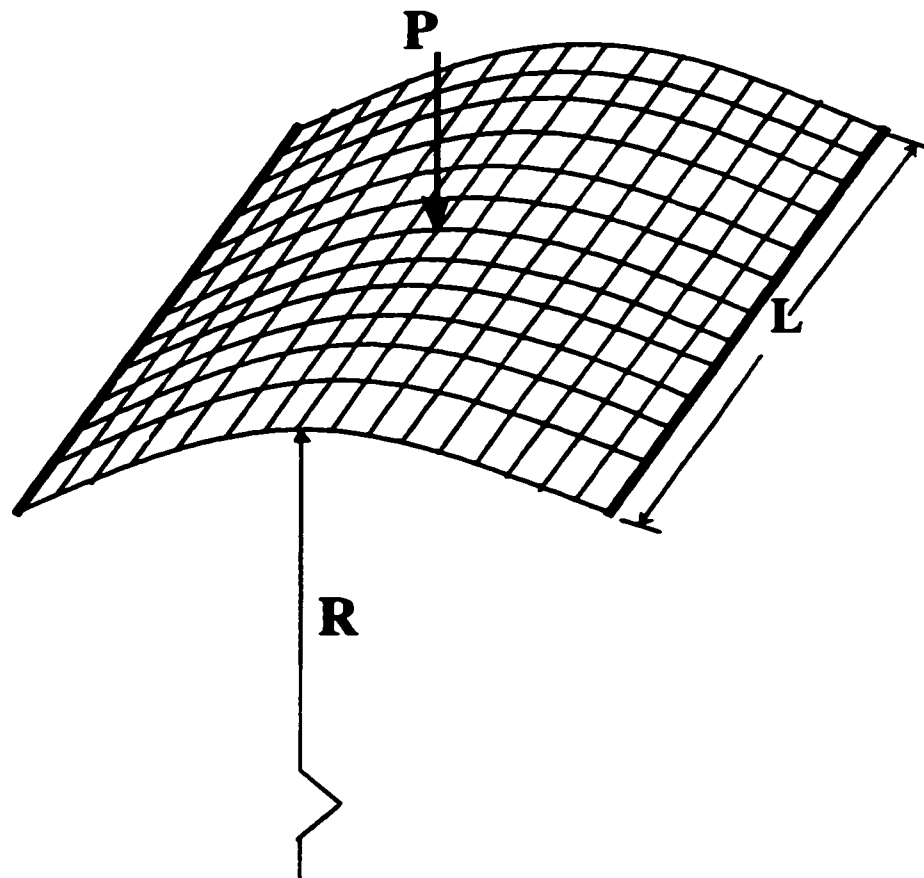


Figure 7.26 Composite shallow cylindrical shell with a central point load

The material properties of the carbon-epoxy layers are:

$$E_1 = 3.3 \text{ kN/mm}^2 \quad , \quad E_2 = E_3 = 1.1 \text{ kN/mm}^2$$

$$G_{12} = 0.66 \text{ kN/mm}^2 \quad , \quad G_{13} = G_{23} = 0.66 \text{ kN/mm}^2 \quad , \quad \nu_{12} = 0.25$$

The two thicknesses considered lead to a thin panel. Thus, there is no significant difference between the predictions of the FOSDT and TOSDT models in this situation; therefore the objective of this example is to assess the response prediction of the present shell model.

Due to the symmetry of the problem, only one quarter of the panel is modeled with appropriate boundary conditions imposed. A 16×16 mesh is used in the present analysis for all cases. The authors of Reference [15] used 32×32 elements, but no information is available about the mesh used in Reference [173]. The numerical results concerning the deflection at the central point load location are drawn in Figures 7.27 and 7.28 with those of References [15,173]. Both figures show a very good agreement between the results of the present element and those of References [15,173]. The thicker panel of Case A exhibits standard limit points, whereas the thin panel of Case B shows a complex path of equilibrium configurations with snap-through and snapback limit points. The arc-length method was used all along to follow the path of equilibrium configurations. As expected, the second lay-up shows a significantly stiffer response to the prescribed loading conditions. This is due to the fact that in the second lay-up (ii) the four top and four bottom layers have their fibers in the circumferential direction which has end supports whereas in the first lay-up they are in longitudinal direction which has free ends. The weaker lay-up of the thinner panel exhibits a very complex path of equilibrium with

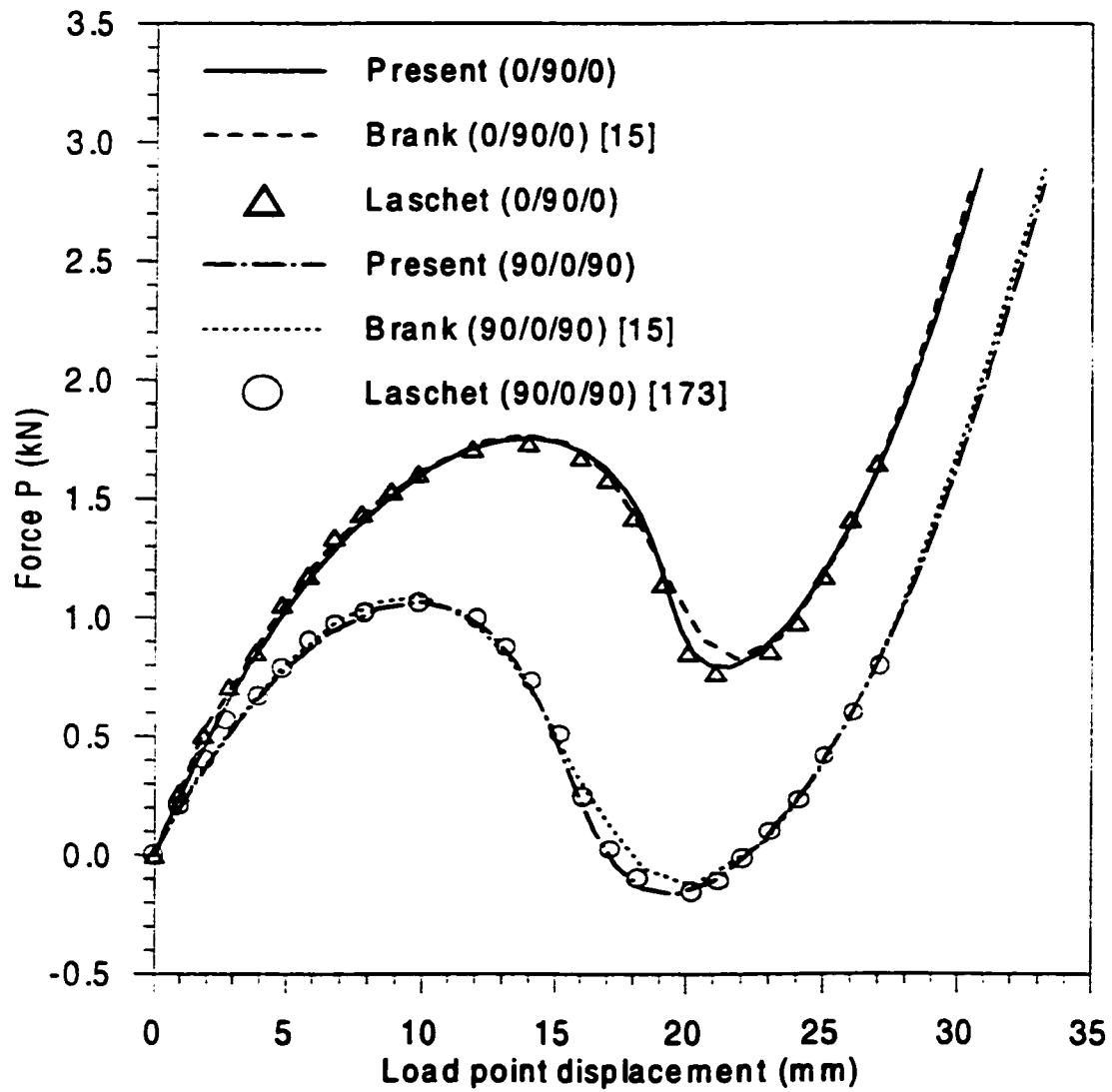


Figure 7.27 Composite cylindrical shell, $t=12.6$ mm
Load-displacement variation

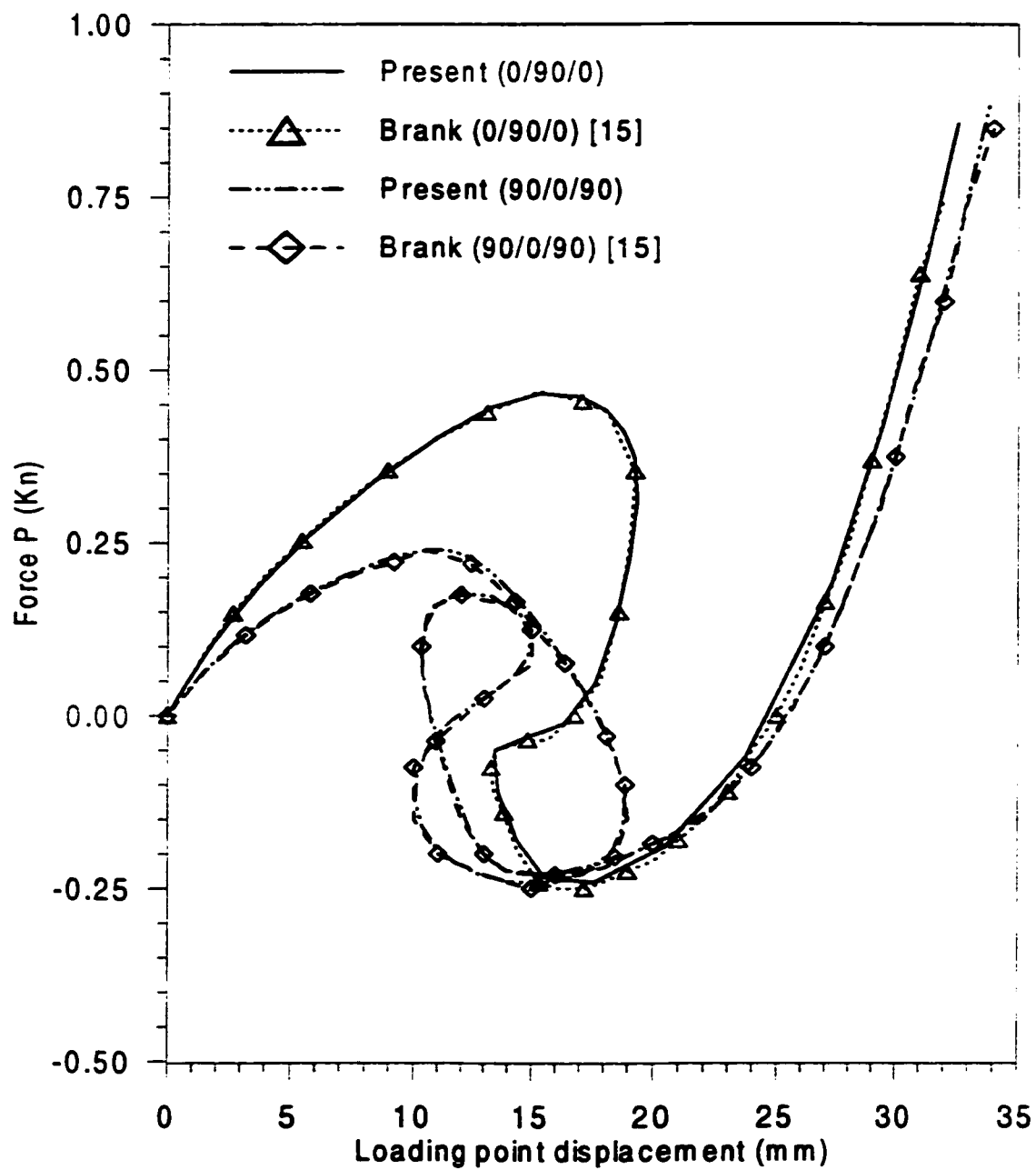


Figure 7.28 Composite cylindrical shell , $t=6.3$ mm
load-displacement variation

several limit points before it reaches its stiffer equilibrium branch. The stiff region on the right side of Figures 7.27 and 7.28 occurs after the snap-through where the panel deformation is mainly dominated by tensile action.

The variation of the maximum stresses and their corresponding strains with the load are plotted for case A with lay-up (i) and they are shown in Figures 7.29 and 7.30 respectively. The direction 1 stands for circumferential and 2 for axial. The variations of the Green strains corresponding to the maximum stresses with the vertical displacement at the load location are plotted for all four cases in Figures 7.31-7.34. In case A, Green strains vary approximately from -1.7% for both lay-ups to 1% for lay-up (ii) and 1.5% for lay-up (i). For case B, it is from -1% for both lay-ups to 0.6% for lay-up (ii) and 1.3 % for lay-up (i). The maximum stresses are acting in the circumferential direction. The maximum stresses in both directions are located at the center of the panel where the load is applied. The maximum values are -45 Mpa and 60 Mpa.

7.2.2.4 Composite Hyperboloidal Shell under two Pairs of Opposite Loads.

This problem was designed by Basar et al[19] to test the performance of shell elements in the case of very large rotations. The same example was later considered by Wagner and Gruttmann.[17]. The problem data are:

$$\begin{array}{lll}
 E_1 = 40 \times 10^6 & E_2 = 1 \times 10^6 & \nu_{12} = 0.25 \\
 G_{12} = 0.6 \times 10^6 & G_{13} = 0.6 \times 10^6 & G_{23} = 0.6 \times 10^6 \\
 h = 0.04 & R_1 = 7.5 & R_2 = 15.0 \\
 H = 20.0 & P = 5 &
 \end{array}$$

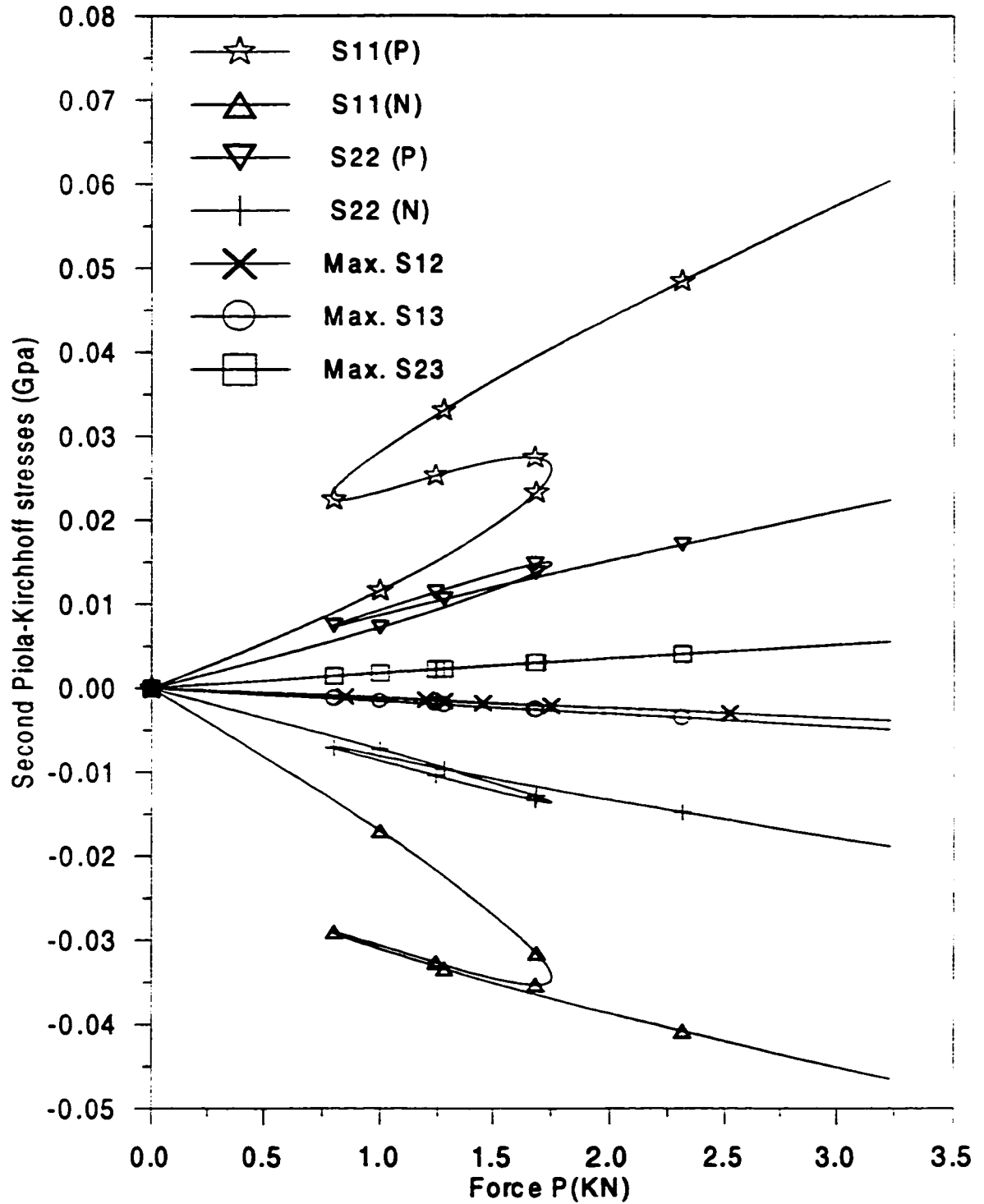


Figure 7.29 Composite shallow cylindrical shell ,(0/90/0), $t=12.6\text{mm}$
Stresses-Load variation

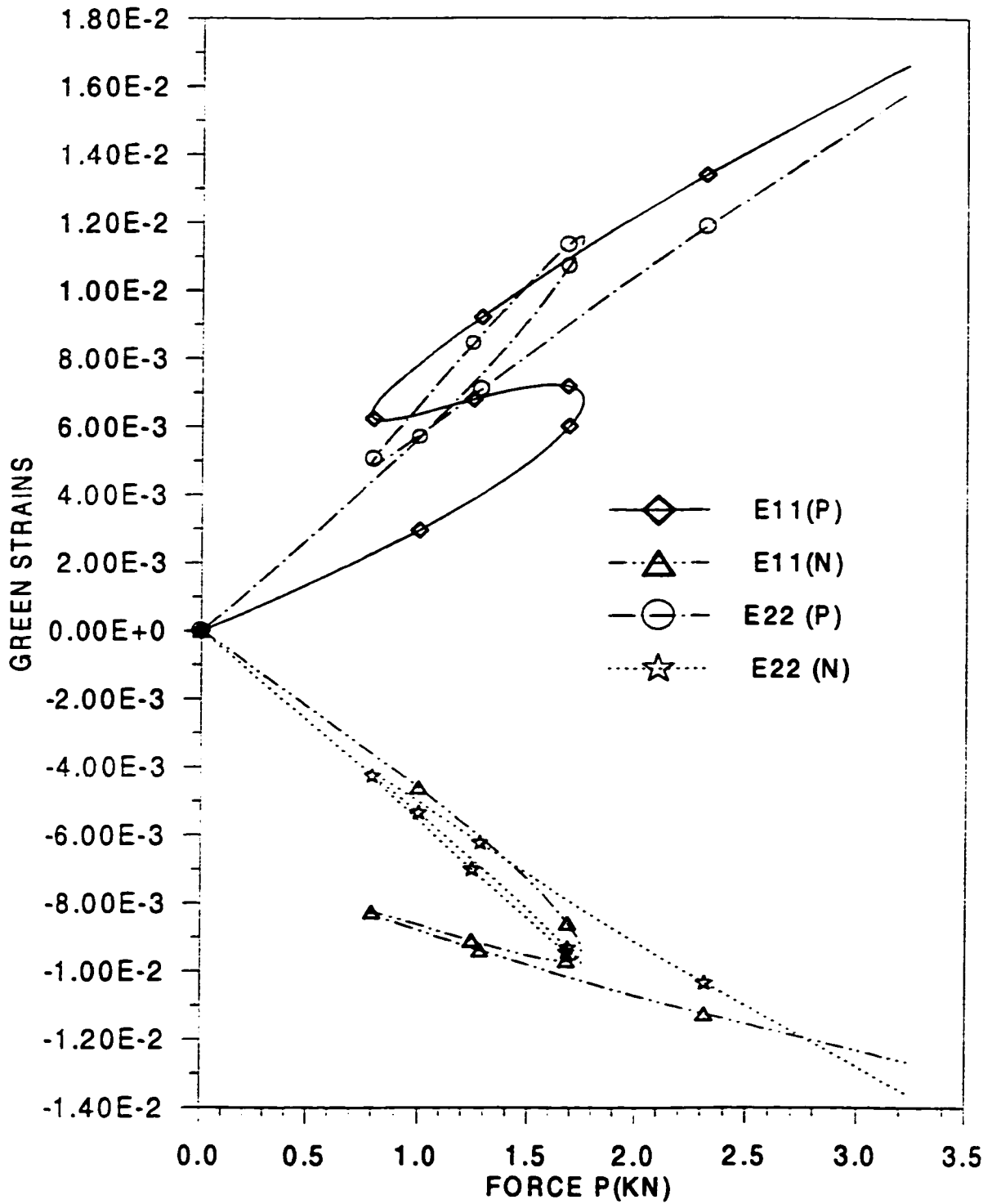


Figure 7.30 Composite shallow cylindrical shell, (0/90/0), t=12.6mm
Normal Green strains-Load variation

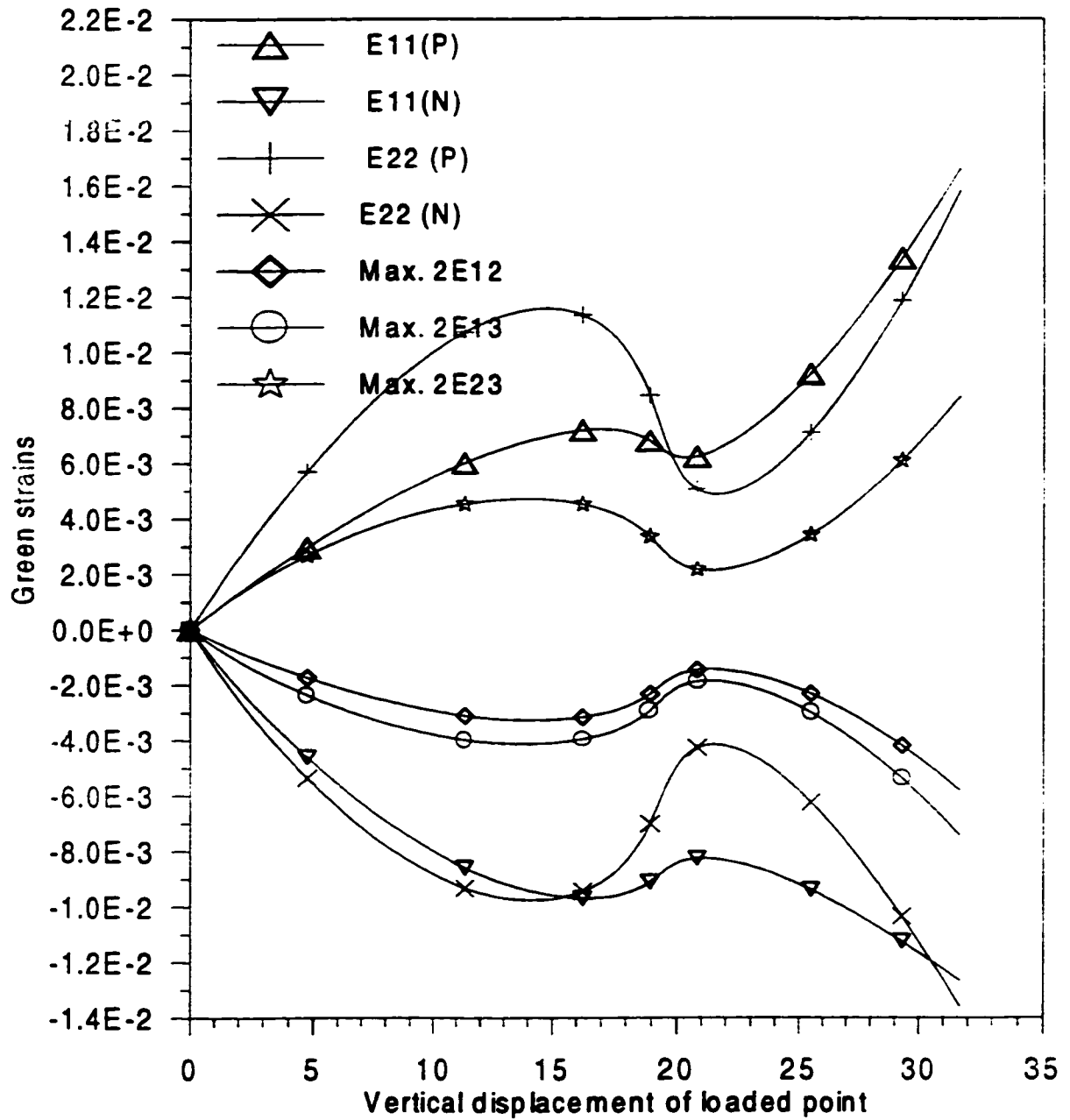


Figure 7.31 Composite shallow cylinder, (0/90/0), $t=12.6\text{ mm}$
Green strains-displacement variation

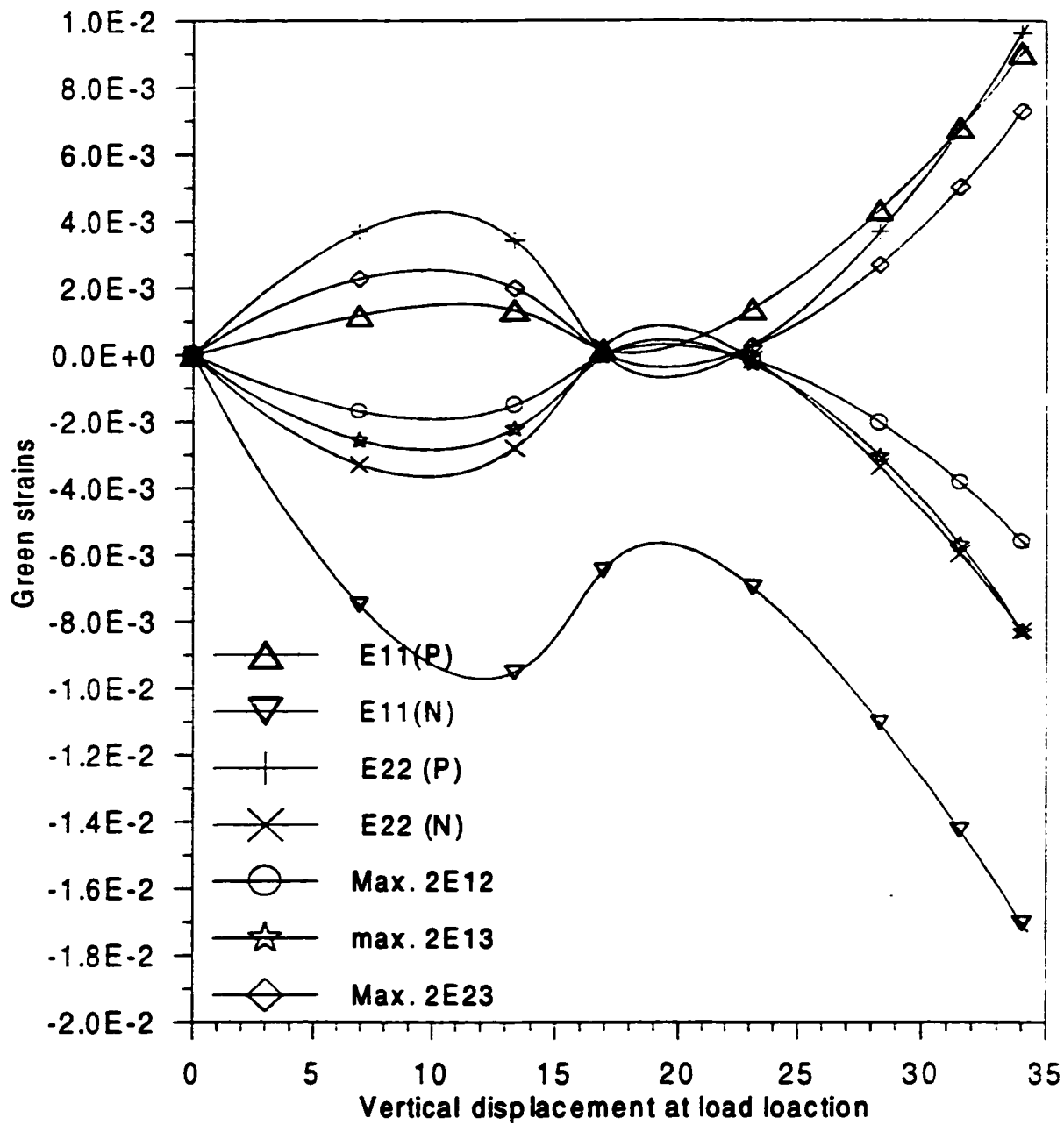


Figure 7.32 Composite shallow cylinder, (90/0/90), $t=12.6\text{ mm}$
Green strains-displacement variation

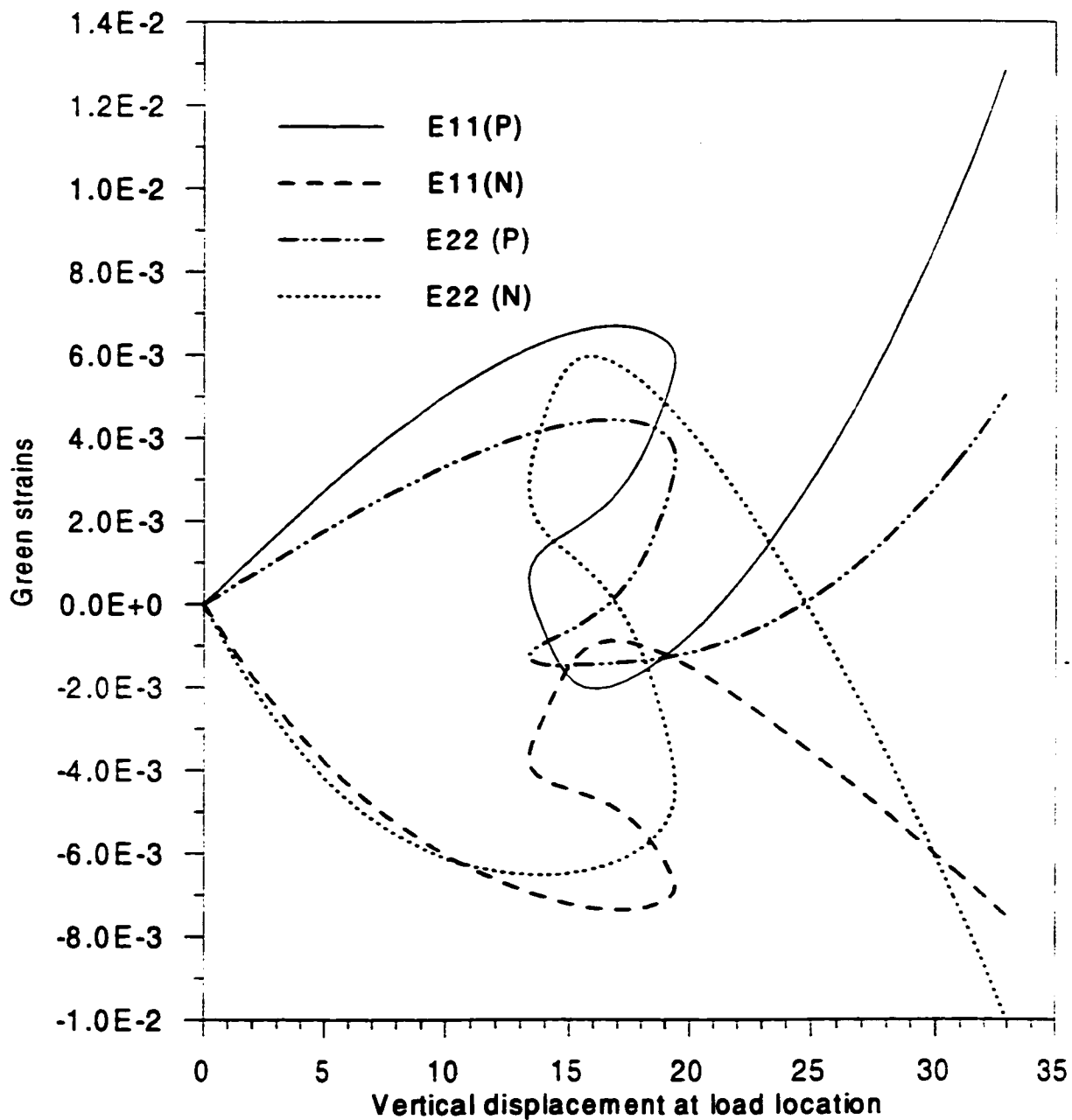


Figure 7.33 Composite shallow cylinder, (0/90/0), $t=6.3\text{mm}$
Green strains-displacement variation

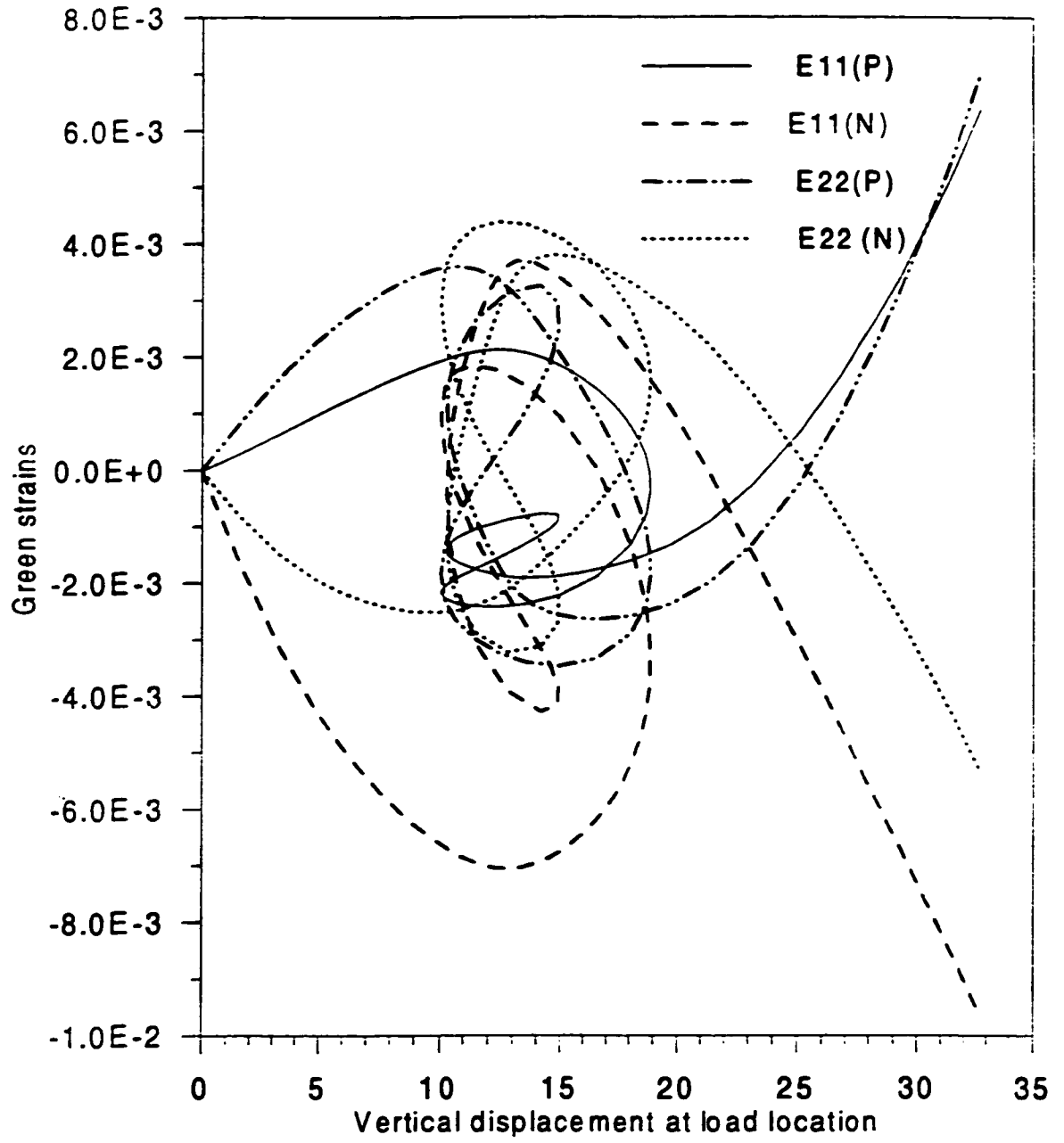


Figure 7.34 Composite shallow cylinder, (90/0/90), $t=6.3\text{mm}$
Green strains-displacement variation

The radius of the hyperboloidal shell is described by the following equation:

$$R(x_3) = \frac{R_1}{C} \sqrt{C^2 + (x_3)^2} \quad \text{with} \quad C = \frac{20}{\sqrt{3}} \quad (7.4)$$

Due to symmetry conditions, only one eighth of the hyperboloidal shell needs to be modeled as shown in Figure 7.35. The laminate is made of three equal layers. The shell is analyzed for two stacking sequences, $[0^\circ, 90^\circ, 0^\circ]$ and $[90^\circ, 0^\circ, 90^\circ]$. Here also 0° means that the fiber orientation is in the circumferential direction.

The numerical results concerning the variations of the displacements of points A, B, C and D are shown in Figures 7.36-7.39. Very large displacements and rotations are observed in this example especially for the stacking sequence $[90^\circ, 0^\circ, 90^\circ]$ which is the weaker of the two sequences considered. The laminate scheme $[0^\circ, 90^\circ, 0^\circ]$ was analyzed using a 16×16 mesh but in the second one a 28×28 mesh was used as in Reference [19]. From these figures, a very good match between the results of the present study and those of Basar et al.[19] can be observed.

To have an idea about the change of the geometric shape involved in this problem, the initial dimensions of the hyperboloidal shell, which are shown in Figure 7.35, are as follows. $R_1=7.5$ (radius at the middle of the shell), $R_2=15$ (radius at the top) and $H=20$ (height of half of the hyperboloidal shell). The maximum displacements obtained for points A, B, C and D, range from around 2.75 to 4.2, for the stacking sequence $[0^\circ, 90^\circ, 0^\circ]$, and from around 2 to 8, for the stacking sequence $[90^\circ, 0^\circ, 90^\circ]$.

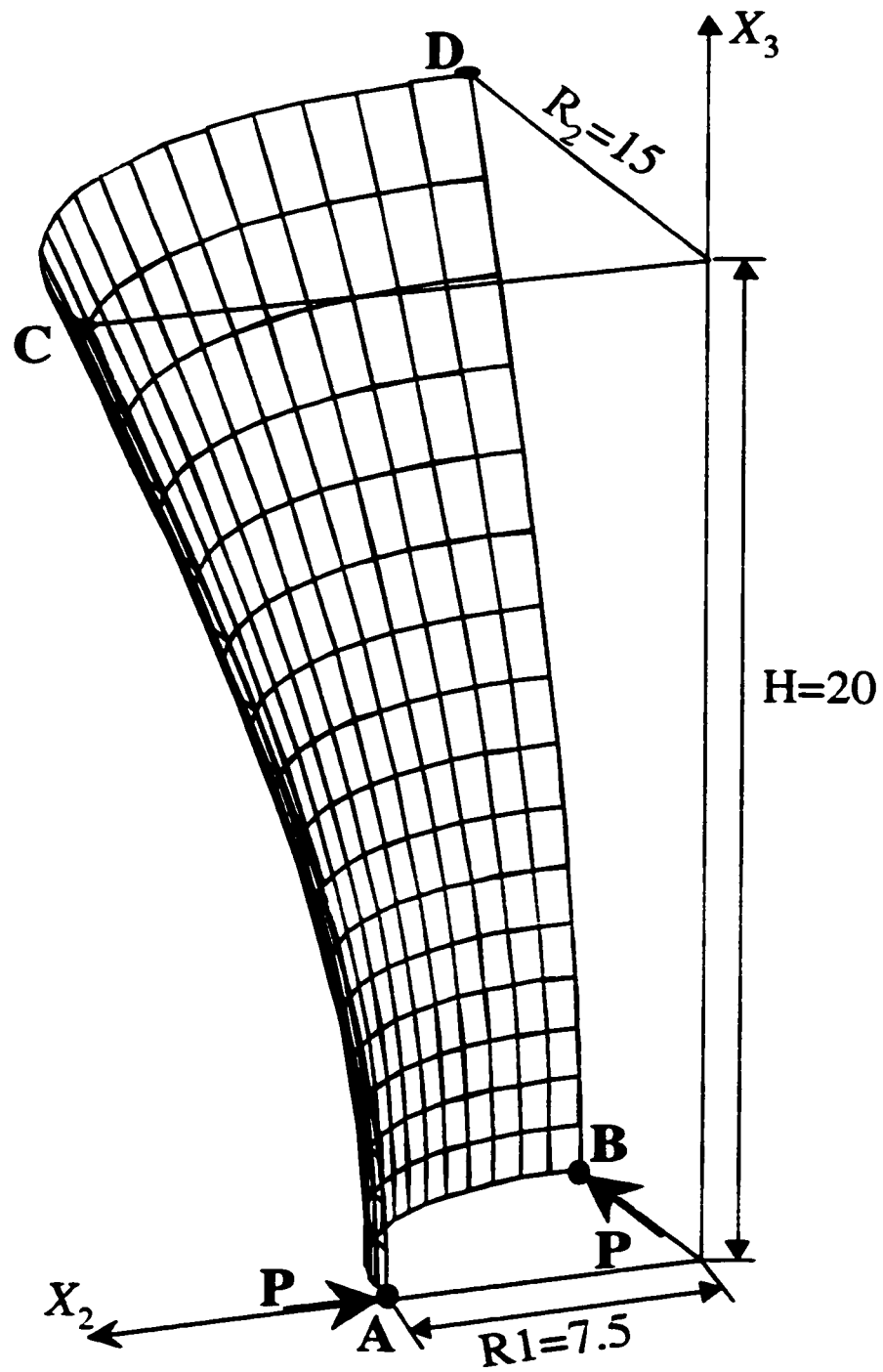


Figure 7.35 Composite hyperboloidal shell :
Geometry and loading conditions

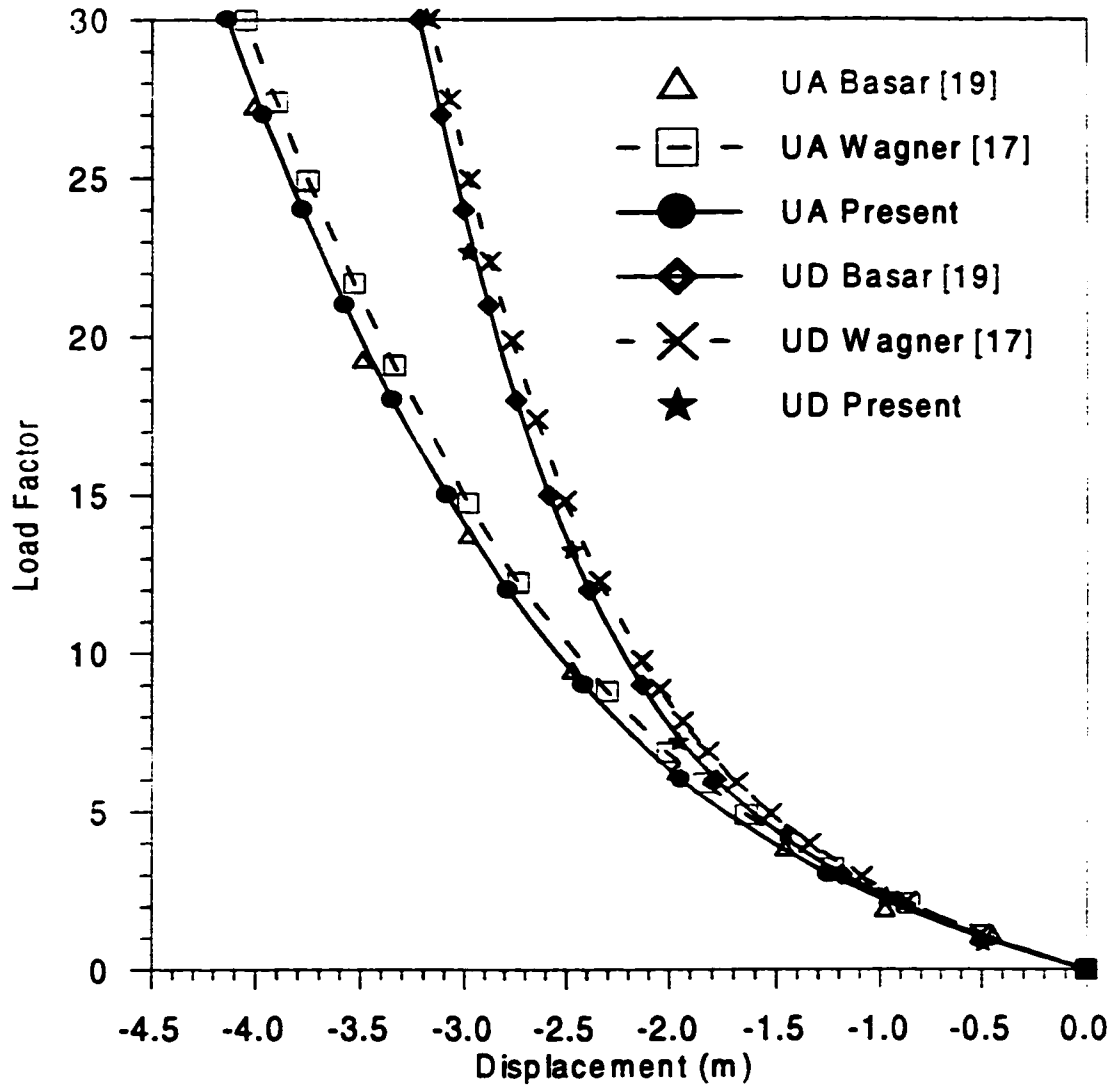


Figure 7.36 Composite hyperboloidal shell,[0/90/0],
Displacements of A and D

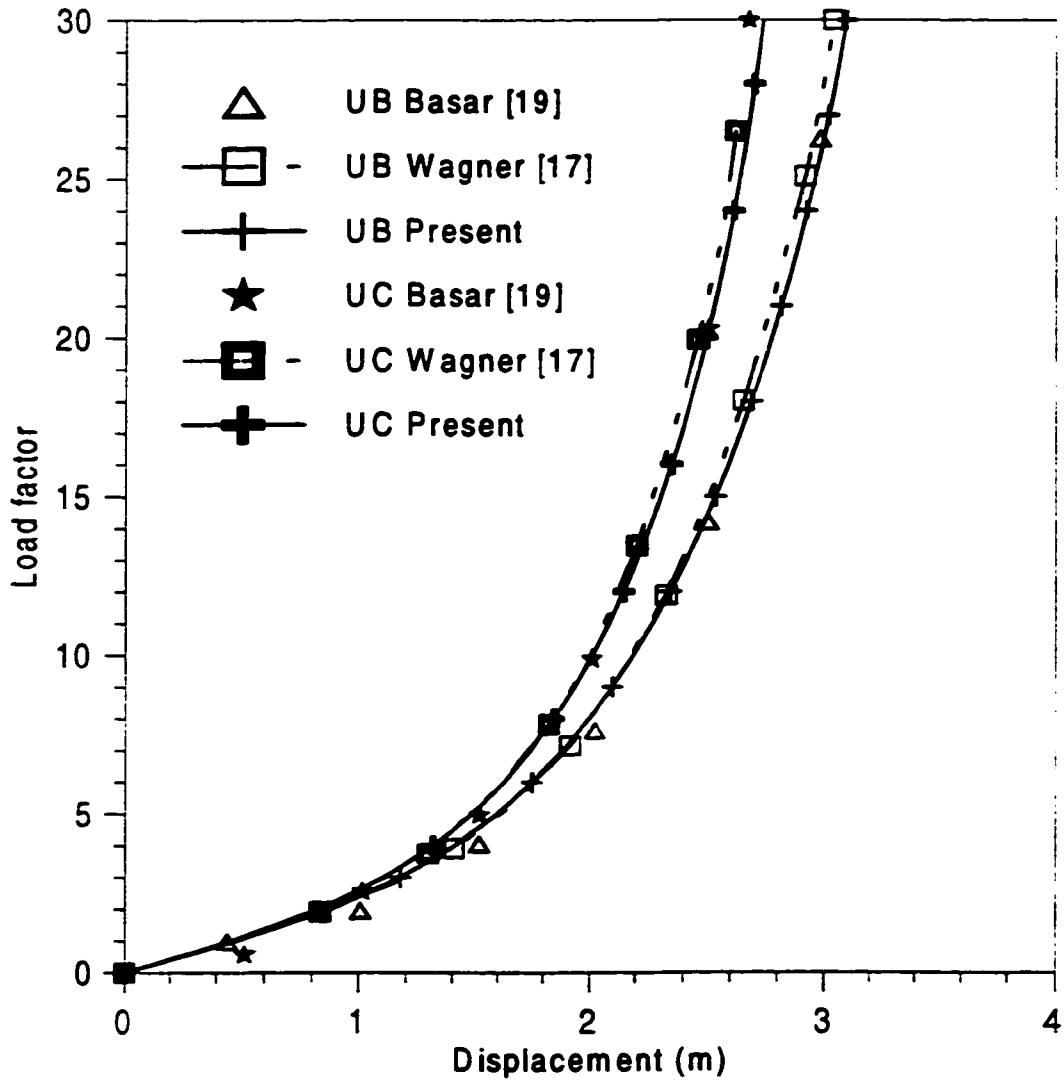


Figure 7.37 Composite hyperboloidal shell $[0/90/0]$, Displacements of B and C

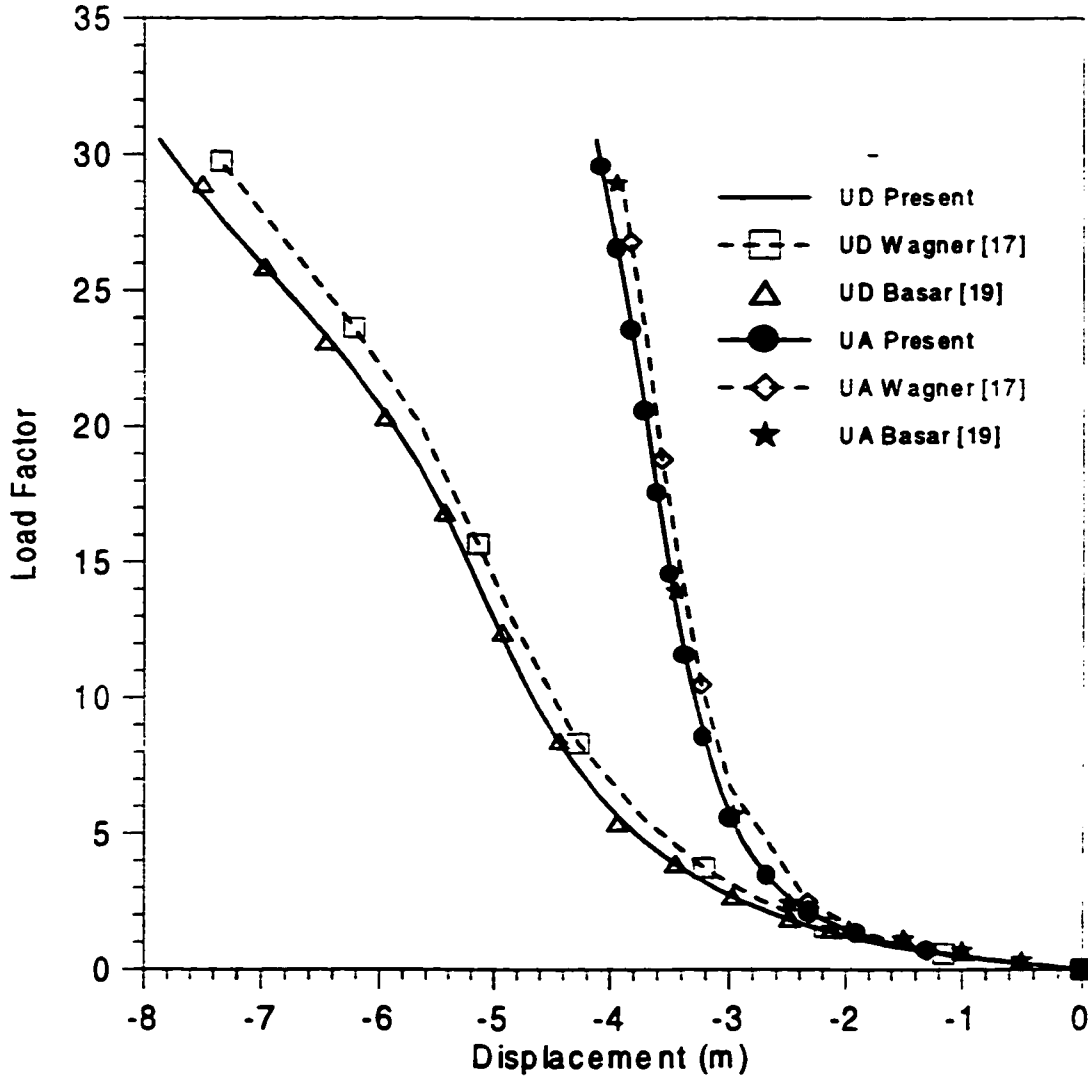


Figure 7.38 Composite hyperboloidal shell,[90/0/90],
Displacements of A and D

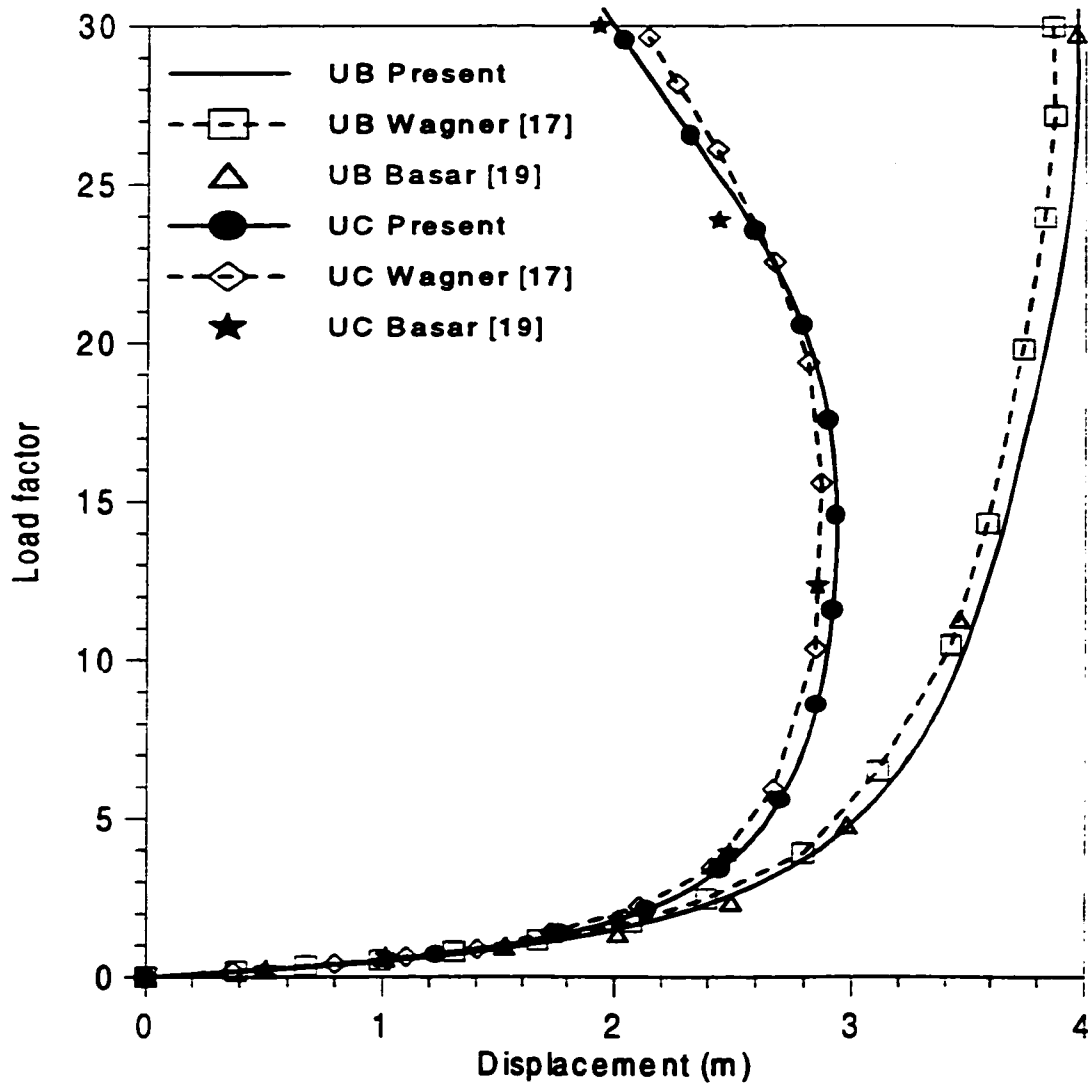


Figure 7.39 Composite hyperboloidal shell, [90/0/90],
Displacements of B and C

The variation of the maximum stresses and their corresponding strains with the displacement in Y direction of point A (UA) are shown in Figures 7.40-7.43 for both stacking sequences. The directions 1 and 2 are defined for this example as circumferential and axial respectively. For the stacking sequence $[0^\circ.90^\circ.0^\circ]$, i.e., the stronger one, the maximum positive and negative strains reached the value of 1.3% at UA=4. It can be noticed from Figure 7.42 which represents this stacking sequence the presence of high inplane shear strain. Figure 7.43 shows the strain variations corresponding to the weaker sequence where the maximum positive and negative strains reached a value of approximately 0.7% at UA=4. After that there is a sharp increase in the inplane shear maximum shear strain reaching a value of 5.5% at UA=8. It can be noticed also that the circumferential normal strains, which stayed the largest in the first stacking sequence, become smaller than the axial strains in the second sequence after UA=5.5. The strains and stresses obtained in this example are high, but there is no mention about stresses or yielding in the published literature containing this example. Thus, it is believed that the purpose of such examples is to show how the capability of the finite rotation shell elements in modeling structures with large change in geometry.

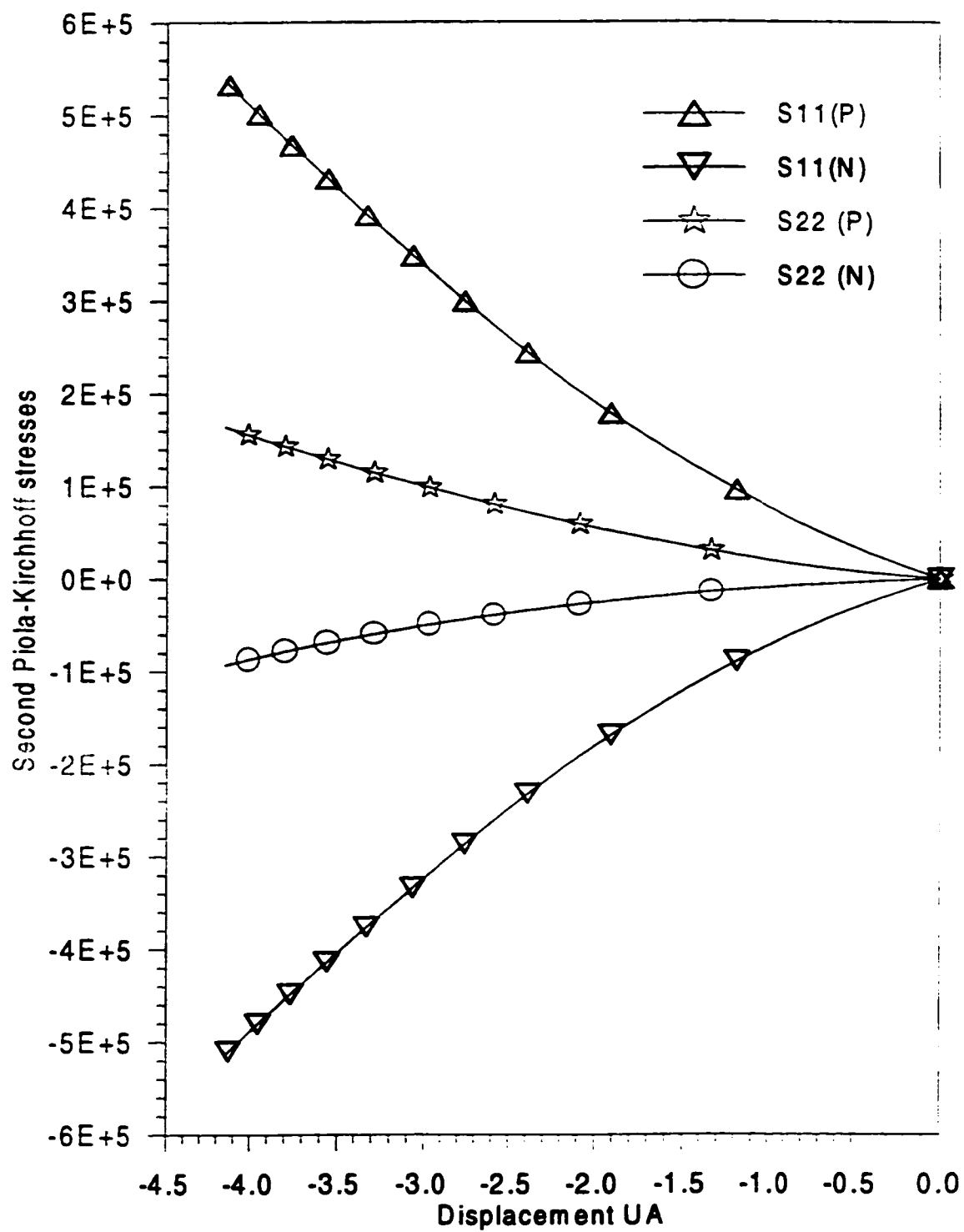


Figure 7.40 Composite hyperboloidal shell, [0/90/0]
Stresses-Displacement UA variations

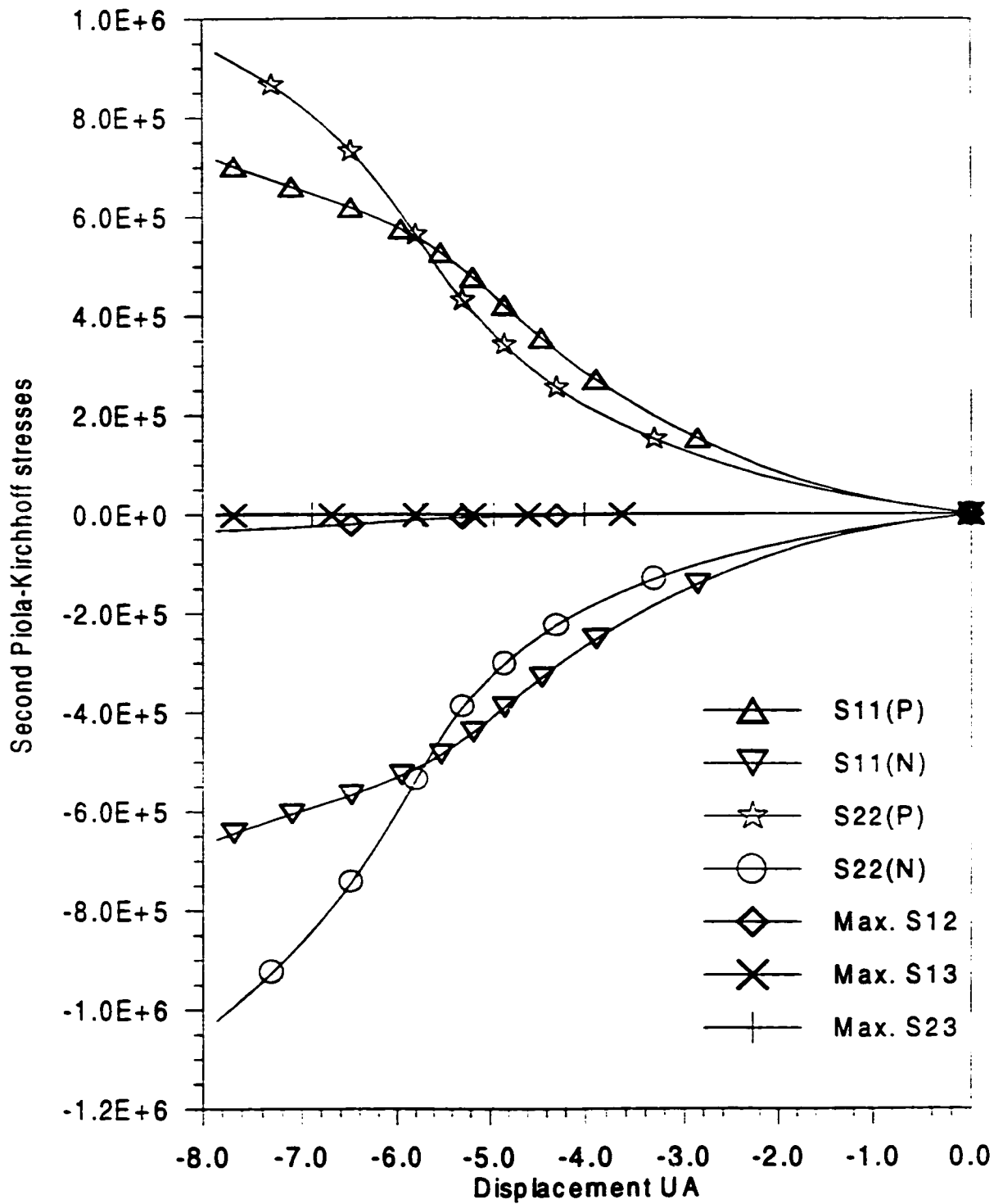


Figure 7.41 Composite hyperboloidal shell, [90/0/90]
Stresses-displacement UA variations

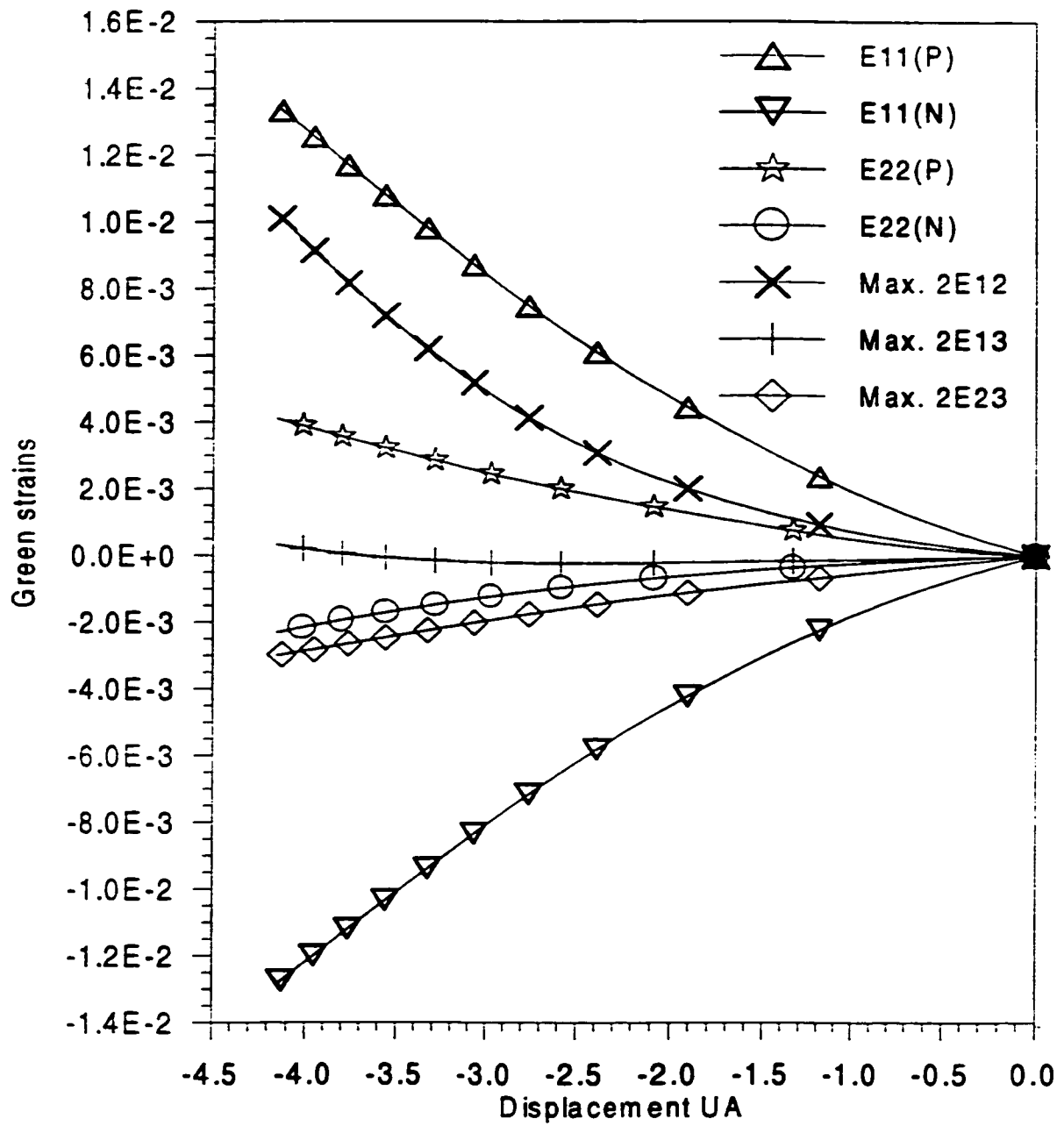


Figure 7.42 Composite hyperboloidal shell, [0/90/0]
Strains-Displacement UA variations

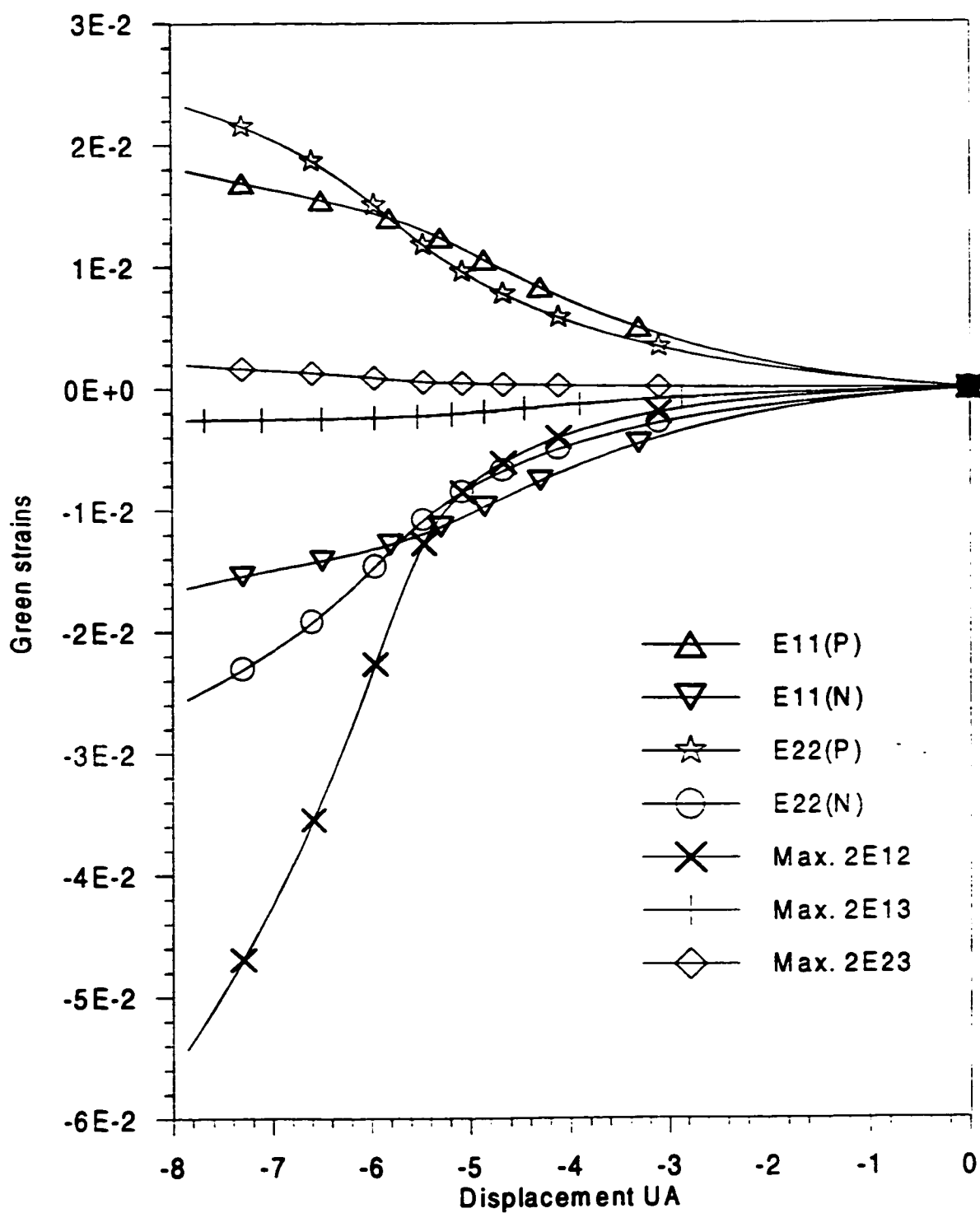


Figure 7.43 Composite hyperboloidal shell, [90/0/90]
Strains-Displacement UA variations

7.2.2.5 Cylindrical Bending of an Asymmetric Cross-Plied Laminate under Uniformly Distributed Transverse Load

This example concerns an antisymmetric cross-plyed ($90^{\circ}/0^{\circ}$) plate strip under uniformly distributed transverse load. The geometry, finite element mesh and the boundary conditions for the pinned and hinged cases are shown in Figure 7.44. The material properties and geometry are:

$$\begin{array}{llll}
 E_1 = 2.0 \times 10^7 \text{ lb/in}^2 & E_2 = 1.4 \times 10^6 \text{ lb/in}^2 & G_{12} = G_{23} = G_{13} = 0.7 \times 10^7 \text{ lb/in}^2 \\
 \nu_{12} = 0.3 & q = 0.005 \text{ lb/in}^2 & a = 9 \text{ in} & b = 1.5 \text{ in} & h = 0.04 \text{ in}
 \end{array}$$

This example was treated by Reddy [2] where nonlinearities were not considered exactly, then it was reanalyzed by Basar et al. [19] using a finite rotation shell model. A mesh of 32×1 elements applied to one fourth of the plate strip is considered as in Reference [19]. The cases considered are positive and negative loading for the pinned case and positive loading for the hinged case. In the latter case there is no significant difference between the positive and negative loading because the plate is essentially in pure bending. The results shown in Figures 7.45 and 7.46 show an excellent agreement between the present results and those of the two other references for the pinned case and between these results and those of Basar et al. [19] for the hinged case. The discrepancies between the results in the hinged case show the importance of considering finite rotation models for a reliable treatment of highly nonlinear problems. It should be mentioned here that there were no significant differences between the prediction of the FOSDT and TOSDT models due to the thinness of the plate strip.

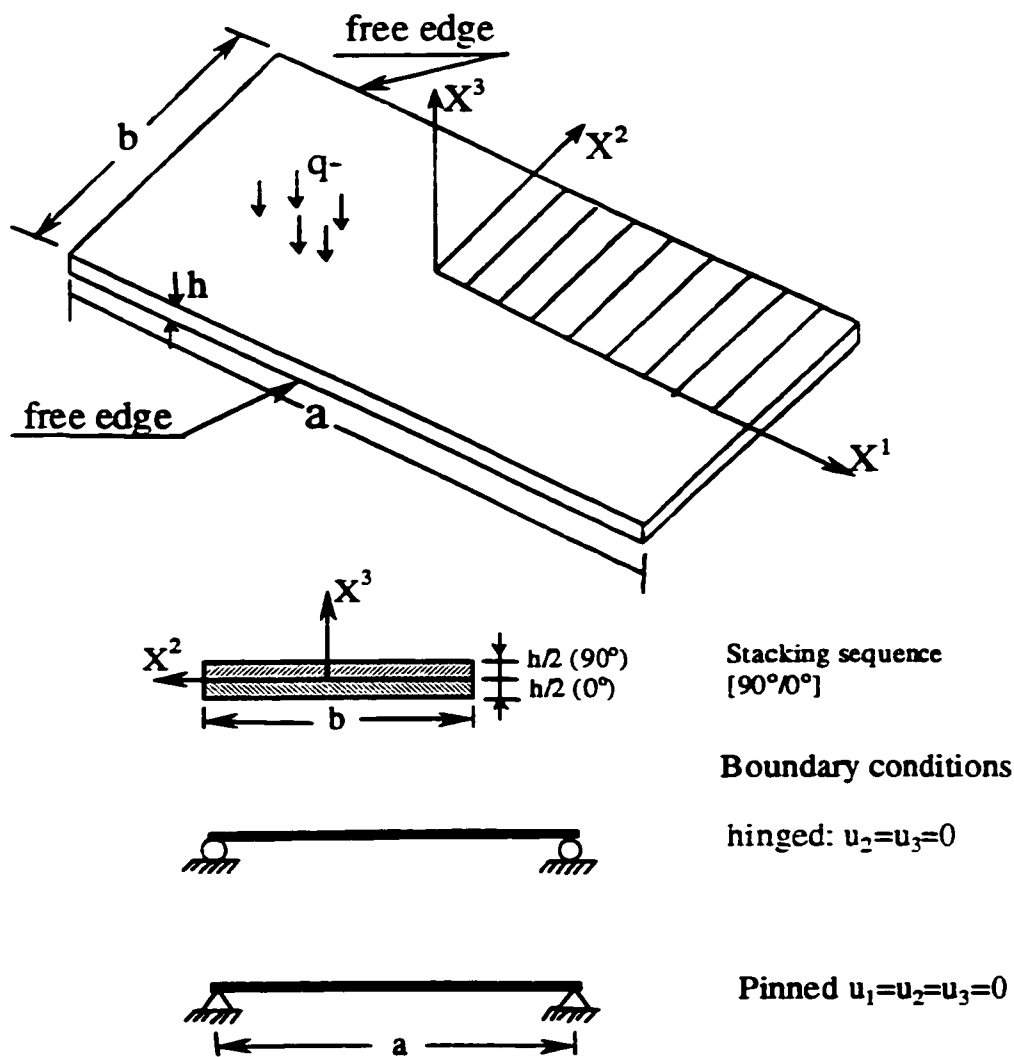


Figure 7.44 Asymmetric cross-ply laminate under uniform transverse load: Geometry and loading

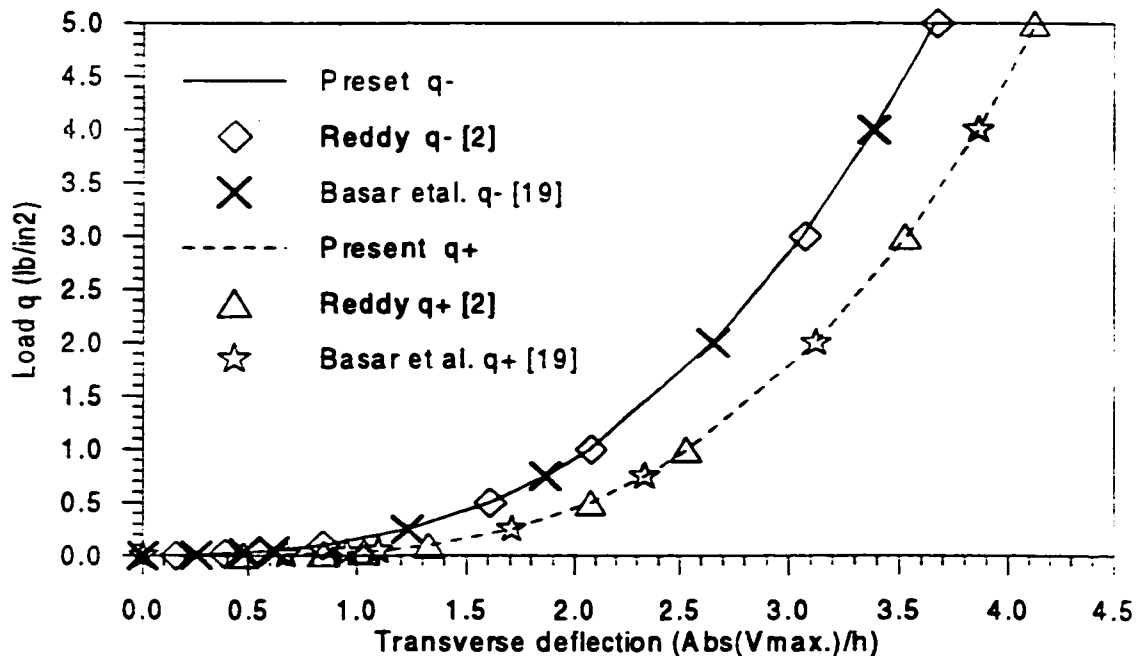


Figure 7.46 Asymmetric cross-ply laminate under uniform loading
Pinned case: Load-displacement plot

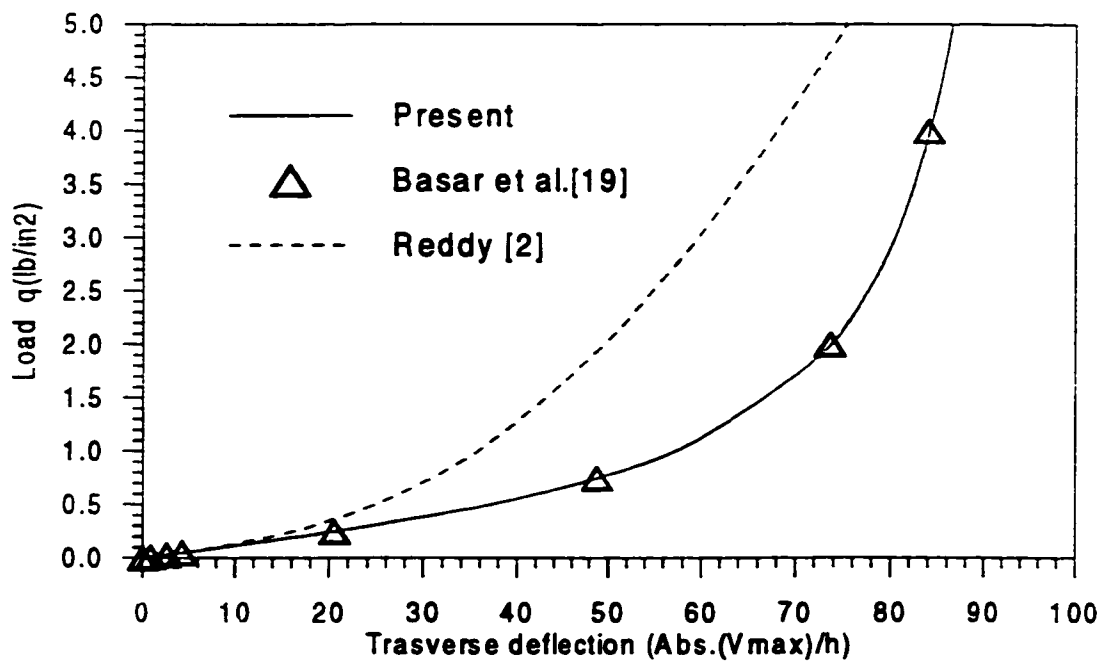


Figure 7.45 Asymmetric cross-ply laminate under uniform loading
Hinged case: Load-displacement plot

7.2.2.6 Bending of a Nine Layer Cross-Ply [0°/90°/0°/...] Simply Supported Spherical Shell Subjected to a Uniformly Distributed Load

This problem is concerned with a spherical cross-ply panel under external uniform pressure load. The following geometrical data are used in the analysis:

$$R=1000 \text{ in} \quad a=b=100 \text{ in} \quad h=1 \text{ in}$$

Individual layers are assumed to be of equal thickness ($h_i=h/9$). This example was analyzed by Reddy and Chandrashekhara [174] using 2x2 nine noded shell elements for one quarter of the panel. Figure 7.47 shows the spherical panel with a mesh of 4x4 four noded shell elements used for the same quarter of the panel. The following boundary conditions are used:

$$v = w = \phi_1 = 0 \quad \text{at } \eta = b/2 \quad u = w = \phi_2 = 0 \quad \text{at } \xi = a/2 \quad (7.5)$$

where u, v and w denote the displacements along the curvilinear coordinates ξ and η and the normal to the shell surface, respectively. ϕ_1 and ϕ_2 denote the rotations of the transverse normals about η and ξ axes, respectively. The following material properties are used:

Material 1:

$$\begin{aligned} E_1 &= 25 \times 10^6 \text{ psi} & E_2 &= 10^6 \text{ psi} & G_{12} &= G_{13} = 0.5 \times 10^6 \text{ psi} \\ G_{23} &= 0.2 \times 10^6 \text{ psi} & \nu_{12} &= 0.25 \end{aligned}$$

Material 2:

$$\begin{aligned} E_1 &= 40 \times 10^6 \text{ psi} & E_2 &= 10^6 \text{ psi} & G_{12} &= G_{13} = 0.6 \times 10^6 \text{ psi} \\ G_{23} &= 0.5 \times 10^6 \text{ psi} & \nu_{12} &= 0.25 \end{aligned}$$

The nondimensional loading pressure is given by

$$\bar{p} = \frac{qR^2}{E_2 h^2} \quad (7.6)$$

The results of this simulations which represent the center deflection are shown in Figure 7.48 with those of Reference [174]. From Figure 7.48, it can be seen the FOSDT and TOSDT models predicted the same results for both materials because of the ratio a/h which is 100 in this case (thin panel). A good agreement is shown between the present results and those of Reddy and Chandrashekhara, but in their case they did not go beyond the load limit point.

7.3 Dynamic Simulations

The numerical examples found in the open literature, concerning the energy-conserving algorithms, are all based on isotropic shell models which are formulated using Reissner-Mindlin theory.i.e., FOSDT.

7.3.1 Dynamics of a Short Cylinder under Impulsive Loading

This example was studied by Simo and Tarnow [6] where they compared the performance of the exact energy-momentum conserving scheme with the midpoint and trapezoidal rules. It was reanalyzed by Brank et al.[32] within the context of energy-momentum conserving scheme. The cylindrical shell is shown in Figure 7.49. The material properties of this shell and the loading description are as follows.

R	= 7.5	Height = 3.0	Thickness = 0.02
Young's modulus	=2.E8	Poisson's ratio = 0.5	Density =1.0

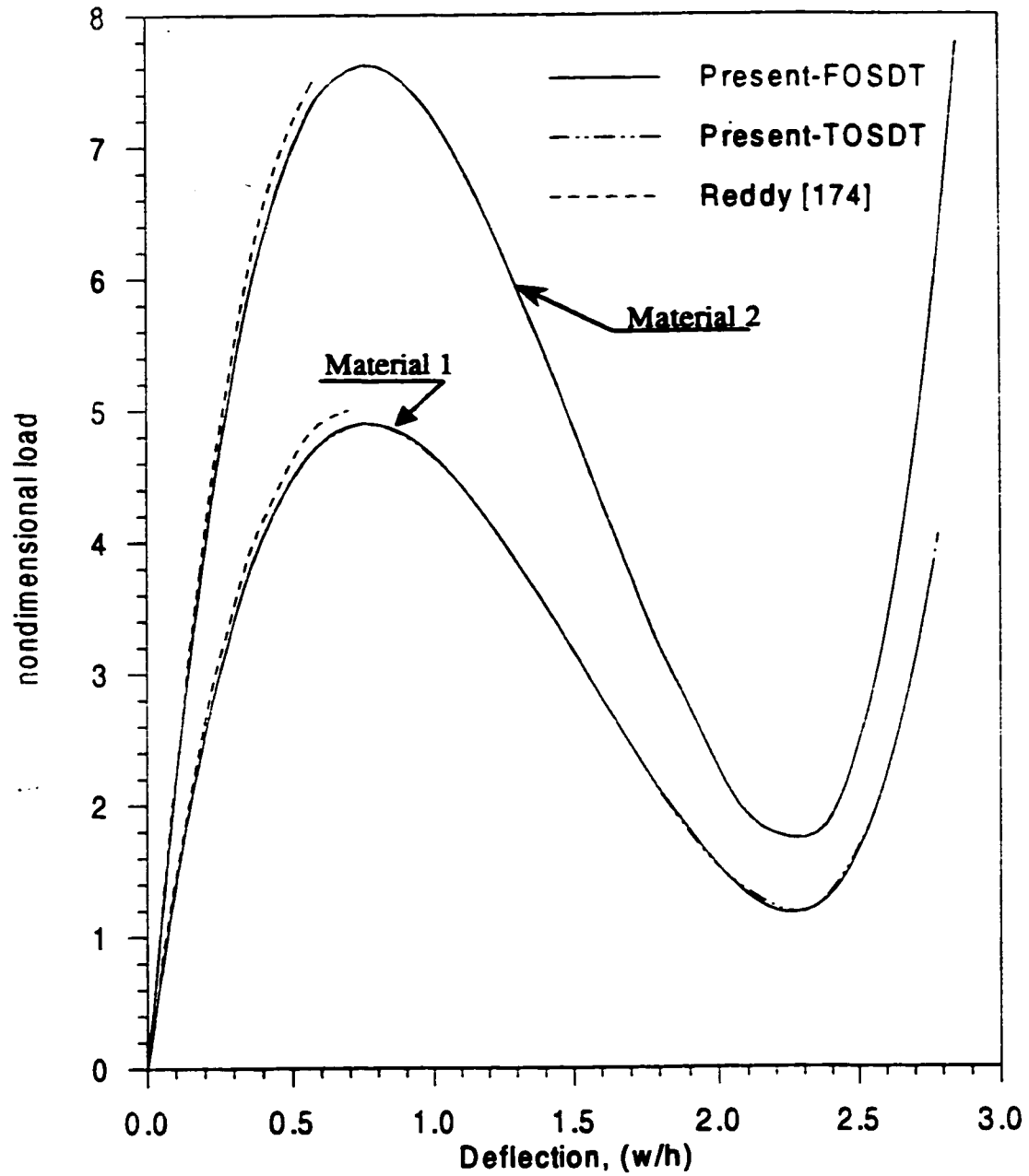


Figure 7.48 Nine layer cross-ply simply supported spherical shell under uniform load: load-deflection variation

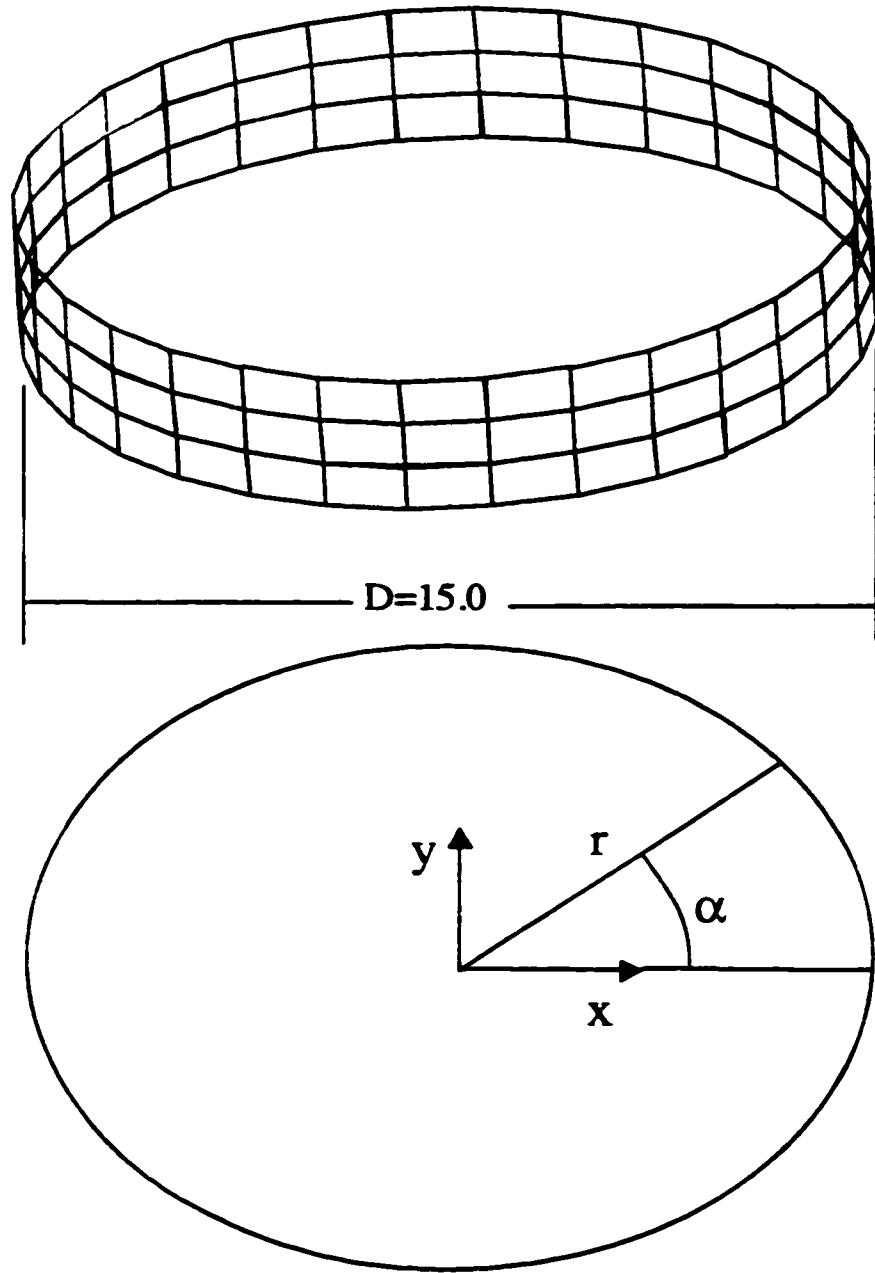


Figure 7.49 Short cylinder : Geometry description

The angle α , as shown in Figure 7.49, defines the location of nodal points where the loads are applied. At each position α , there are four nodal points with different z coordinates, as shown in the mesh. The same concentrated force is applied at each of these four nodal points. The force intensity is the same for all nodal points: i.e., for all values of α ; it is given by the following expression

$$p(t) = \begin{cases} 10t & \text{for } t \leq 0.5 \\ 10 - 10t & \text{for } 0.5 \leq t \leq 1. \\ 0 & \text{for } t \geq 1.0 \end{cases} \quad (7.7)$$

At each value of α , the applied concentrated force at each of the four nodes is given by its three components along x , y and z coordinates as shown in Table 7.14

Table 7.14 Short cylinder under impulsive loading: Nodal loads

Angle α	0	$\pi/2$	π	$3\pi/2$
Nodal loads	$[0,-1,-1]^T p(t)$	$[1,1,1]^T p(t)$	$[1,1,1]^T p(t)$	$[0,-1,-1]^T p(t)$

Starting from rest, the cylinder is subjected to an impulsive loading, represented by the nodal loads shown above, during one second, after which it is left in free motion where the total energy, the total linear momentum and the total angular momentum are exactly conserved. The cylinder is spatially discretized using a mesh of 3×32 elements. Its motion is studied during 25 seconds using a time step $\Delta t = 0.02$ s, equal to that of Reference [32], thus leading to 1250 time steps. The time histories of the total linear momentum, total angular momentum and the various energies, i.e., kinetic, internal and total are shown, respectively, in Figures 7.50, 7.51 and 7.52. An excellent agreement can be observed between the results reported here and those of References [6,32] concerning

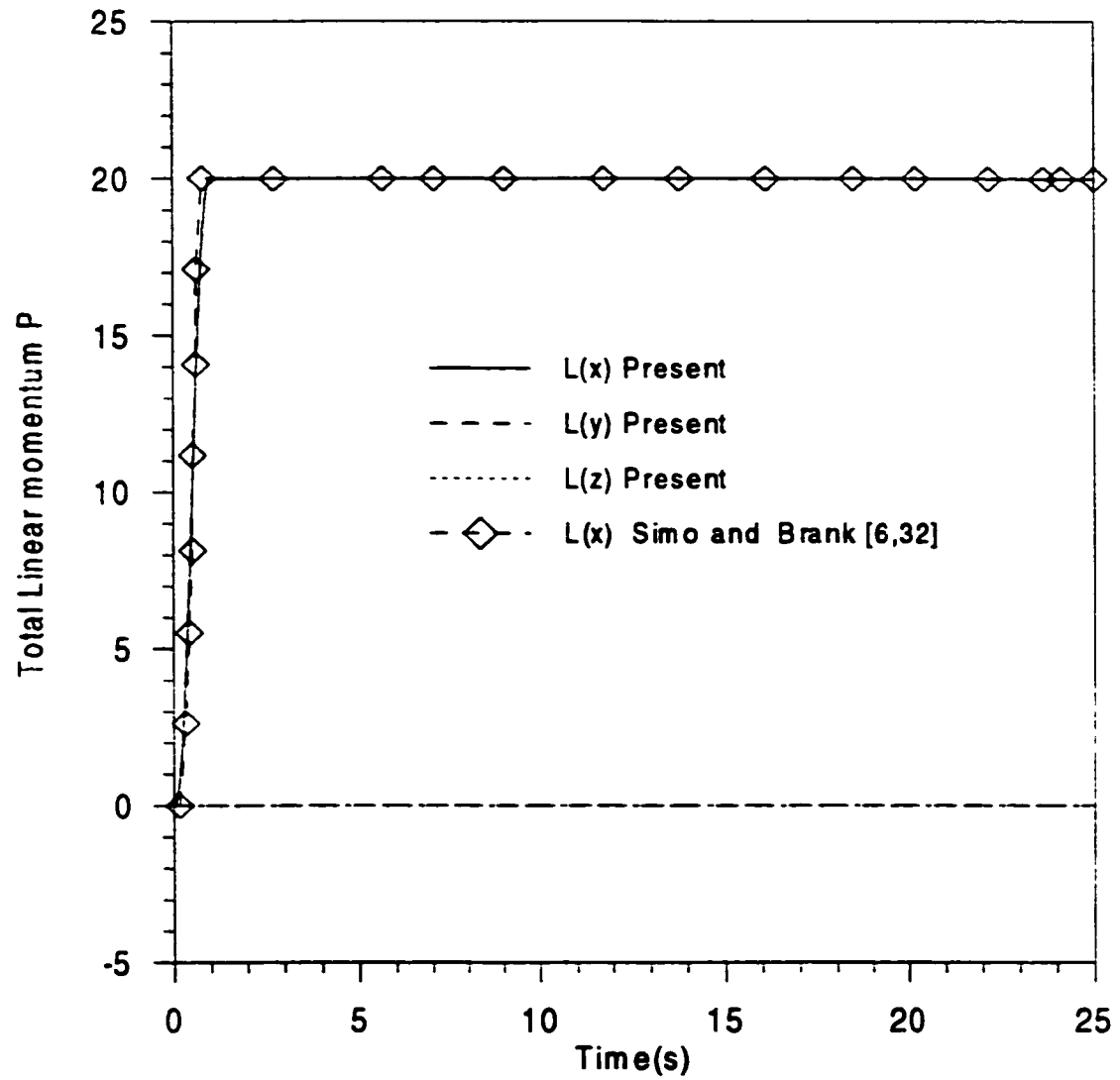


Figure 7.50 Short cylinder: Time history of the total linear momentum

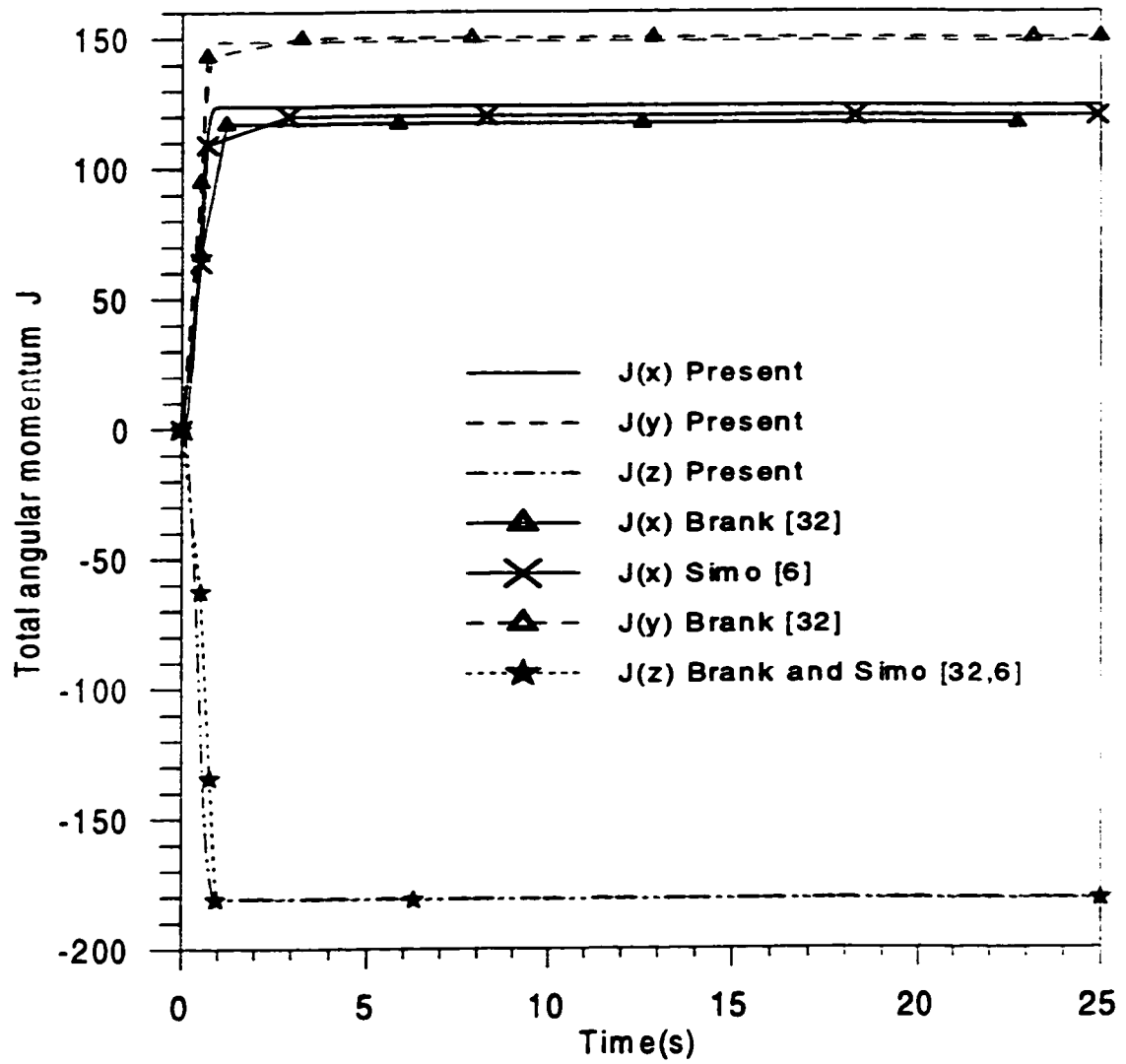


Figure 7.51 Short cylinder: Time history of the total angular momentum

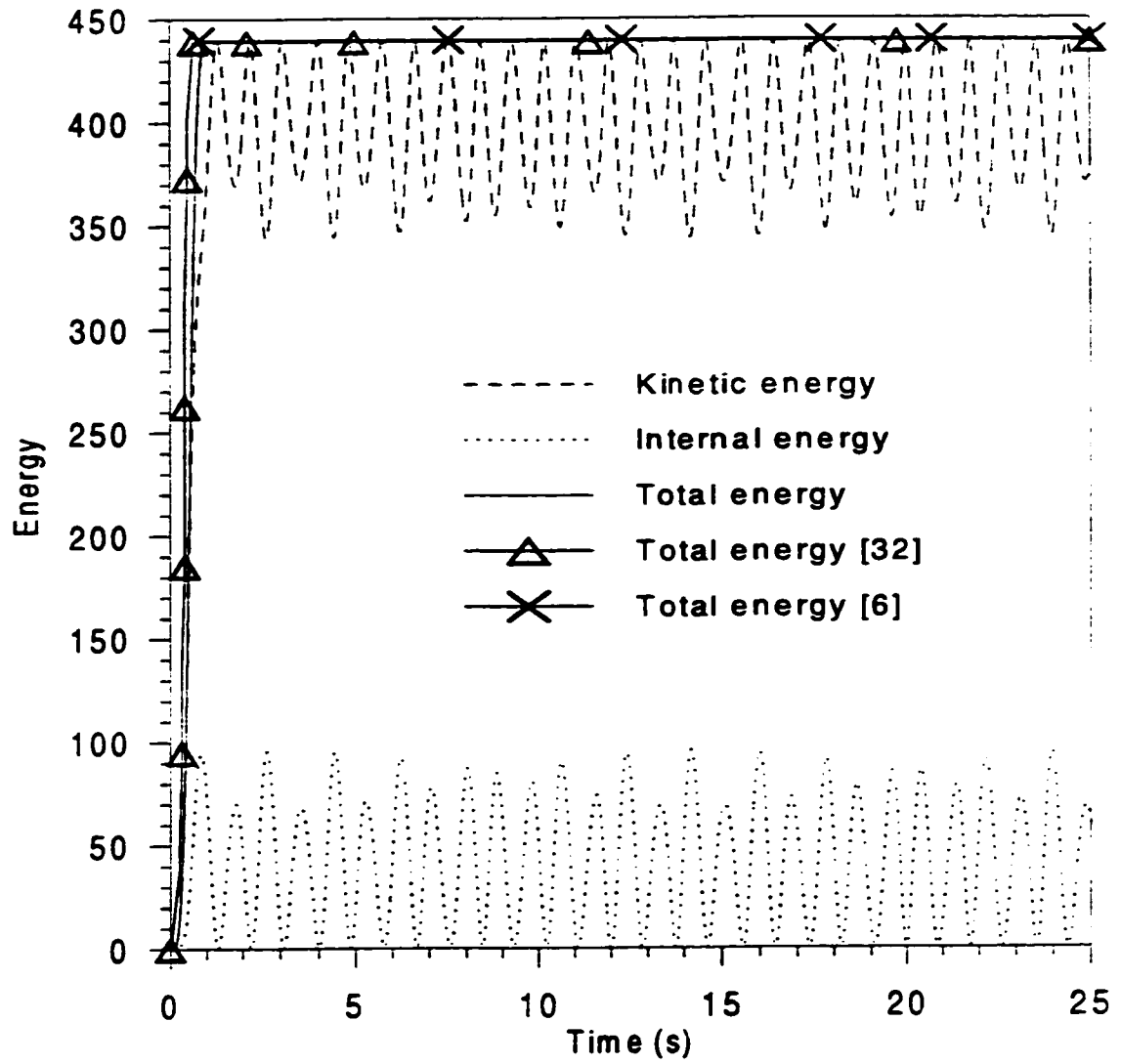


Figure 7.52 Short cylinder: Time history of the energy

the linear momentum, the angular momentum component $J(z)$ and the total energy. The values of $J(y)$ are matching those of Reference [32], but slightly higher than those obtained by Simo and Tarnow [6]. A very slight difference exists also between $J(x)$ found in all these three studies. It can be seen clearly from these figures how these quantities are exactly conserved during the free three-dimensional rigid body motion and large deformation of the short cylinder. The deformed shape of the cylinder during motion is not shown in this study, but the reader can consult the cited references where a sequence of deformed finite element meshes are depicted and shown from different perspectives.

7.3.2 Free Large Motion of a Cylindrical Panel

The second example treated here was considered by Sansour et al.[175] who presented a time integration scheme different from that of Simo and Tarnow[6]. Their scheme conserves momenta and total energy. The cylindrical panel with its geometry, mesh shape with 6x6 elements, as in Reference [173], and loading forces and their directions are shown in Figure 7.53. The geometric and material properties defining the panel are

$$\begin{array}{llll}
 R=150 & L=15 & h=1 & \theta=0.1 \text{ radians} \\
 E=31027.5 & \nu=0.3 & \text{Density} =1E-8 &
 \end{array}$$

where h represents the thickness of the panel.

The two concentrated forces applied at the corner of the shell have the same intensity $P(t)$ and act respectively in the x and z directions. The time variation of the amplitude

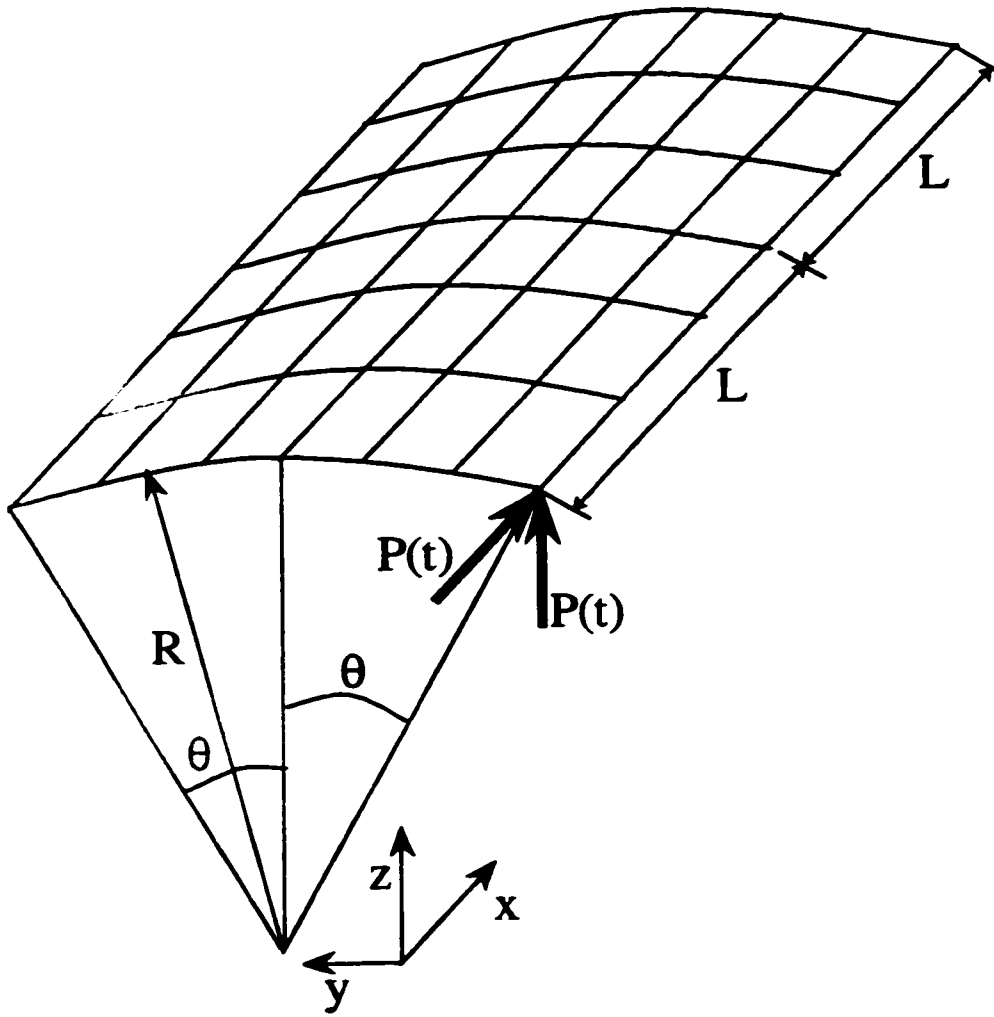


Figure 7.53 Free cylindrical panel: Geometry and loading

$P(t)$ of these two forces is given by

$$p(t) = \begin{cases} 200000t & \text{for } t \leq 0.005 \\ 2000(1 - 100t) & \text{for } 0.005 \leq t \leq 0.01 \\ 0 & \text{for } t \geq 0.01 \end{cases} \quad (7.8)$$

After 0.01 s of impulsive loading, as described by Equation (7.8), the cylindrical panel is left in complex free motion. The simulation of this problem is performed for a total time of one second, using a time step $\Delta t=1E-5$. Thus, resulting in $1E5$ time steps to simulate one second of motion! The plots of Figures 7.54, 7.55 and 7.56 show the time history, respectively, of the total linear momentum, the total angular momentum and the different types of energies. From these figures, we see that the results of this study are matching exactly those of Reference [175]. Although the panel is highly deforming while undergoing large rigid body motion, its internal energy is negligible compared to its kinetic energy and this is due to the high flexibility of the panel itself. The angular momentum components $J(x)$ and $J(z)$ along with the linear momentum $L(y)$ are nil.

7.3.3 Dynamic Snap Through of a Pseudo-Spherical Cap under Impulsive Ring Loading

This example was designed by Brank et al.[32] in such a way that the dynamic snap-through occurs. The parameters describing the geometry of this pseudo-spherical cap are

$$R = 10 \qquad R_{hole} = 3.88 \qquad \text{height} = 4.60 \qquad \text{thickness} = 0.4$$

The material properties are described by

$$E = 1000 \qquad \nu = 0.3 \qquad \text{density} = 0.0001$$

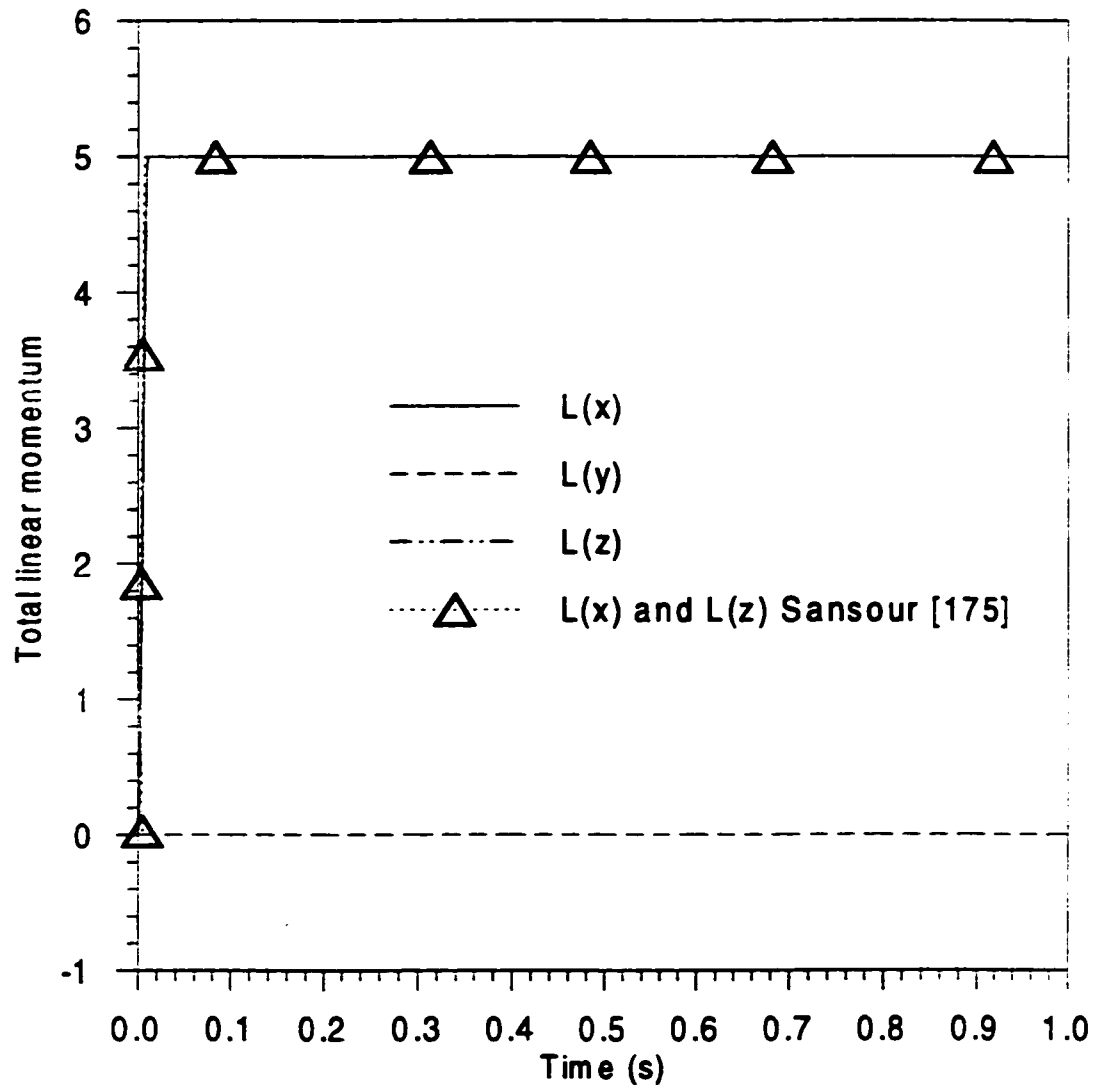


Figure 7.54 Free cylindrical panel: Time history of the total linear momentum

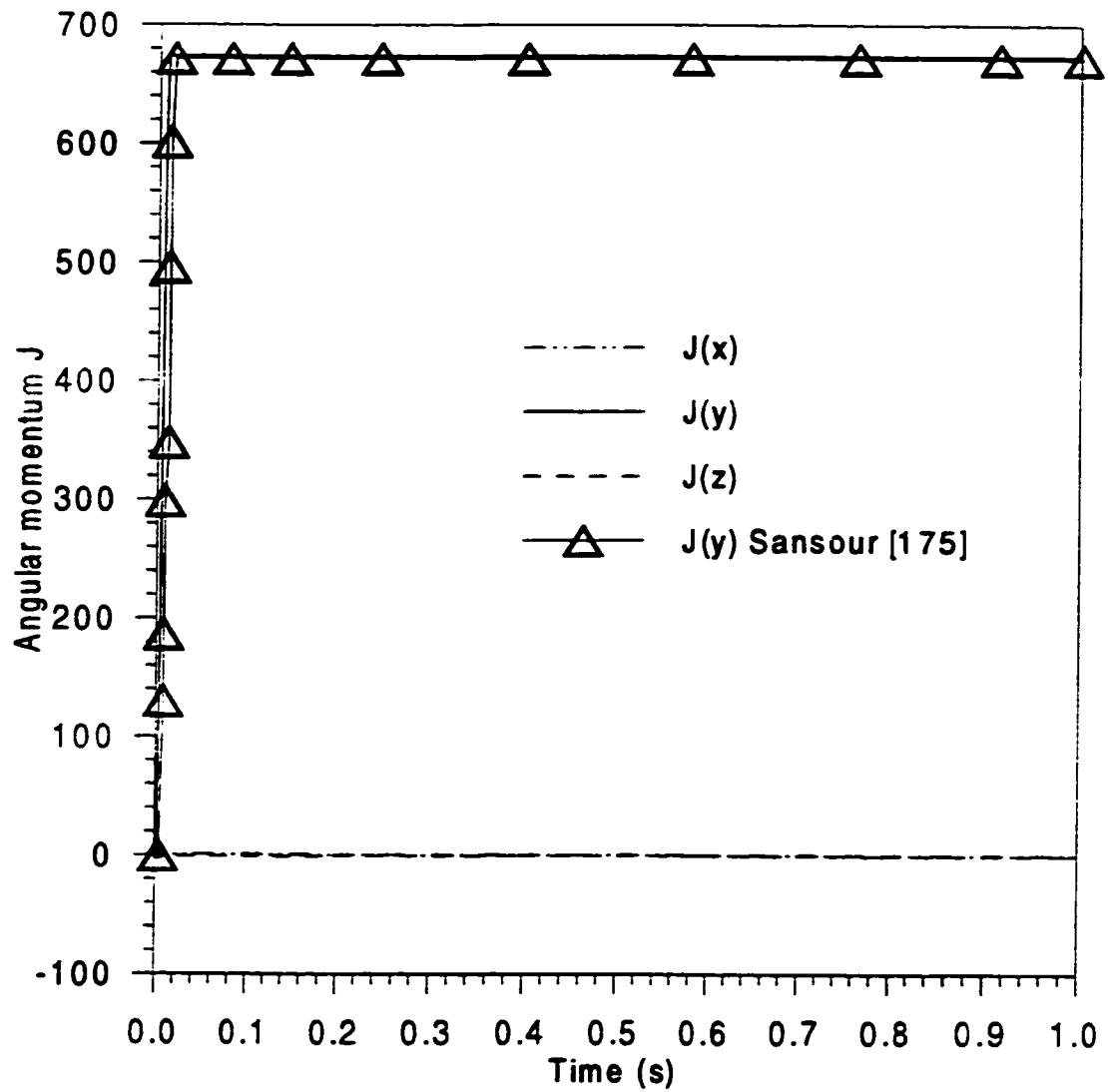


Figure 7.55 Free cylindrical panel: Time history of the total angular momentum

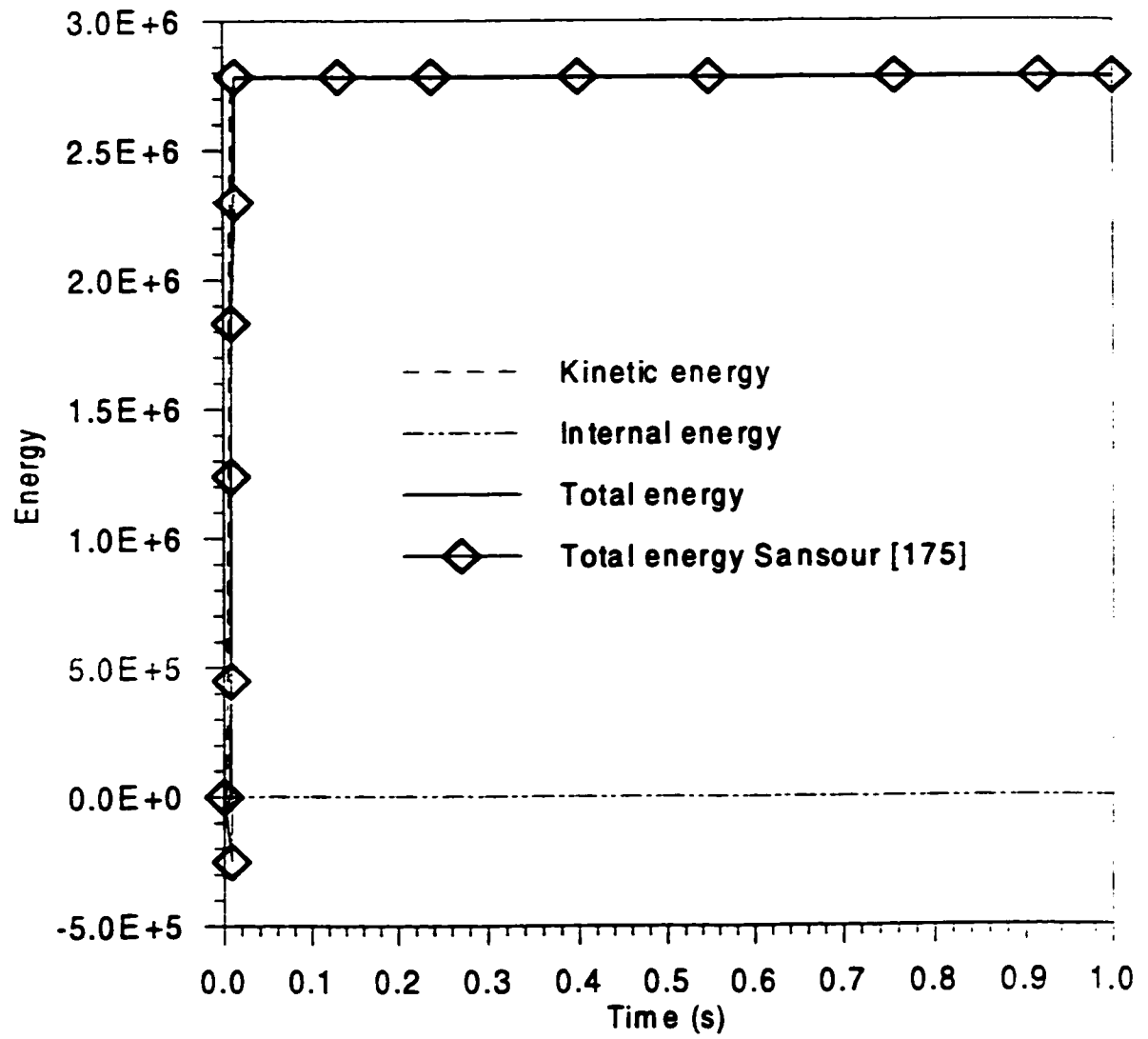


Figure 7.56 Free cylindrical panel: variation of kinetic, internal and total energies

This pseudo-spherical cap is, as shown in Figure 7.57, based on half of a sphere with radius $R = 10$ containing a hole with radius $R_{hole} = 3.88$, then the z coordinates of all points of this hemisphere are divided by a factor of 2, thus, it is no longer a sphere. This last piece of information is not indicated in Reference [32] but obtained from a private correspondence with the first author of Reference [32]. The same finite element mesh is adopted here, i.e., 8×32 elements. The top 32 nodes are subjected to equal downward forces. The bottom 32 nodes are restrained from movement in the z direction, but free to move in (x,y) plane. Thus, this example is different from the two previous ones because of the presence of the restraining boundary conditions.

The intensity $P(t)$ of these forces consists of piecewise linear functions in the interval $[0,2s]$. The values at the end points of these segments are given in Table 7.15. After two seconds of loading, the cap is left in free motion.

Table 7.15 Pseudo-spherical cap: Load intensity variation

Time (s)	0.00	1.00	1.07	1.16	1.20	1.94	2.00
P(t)	0.00	1.60	1.65	1.65	1.60	0.05	0.00

The total time of study for this problem is 4.5 s divided into 3000 steps with $\Delta t = 0.0015$ s for each step. Figure 7.58 shows the time variation of the kinetic, internal and total energies predicted by the present model along with the total energy variation obtained by Brank et al.[32]. The same pattern is observed when comparing the total energy variation obtained here with that of Reference [32] but the values predicted in this study are slightly on the lower side.

It can be seen from Figure 7.58 that the kinetic energy of the pseudo-spherical cap

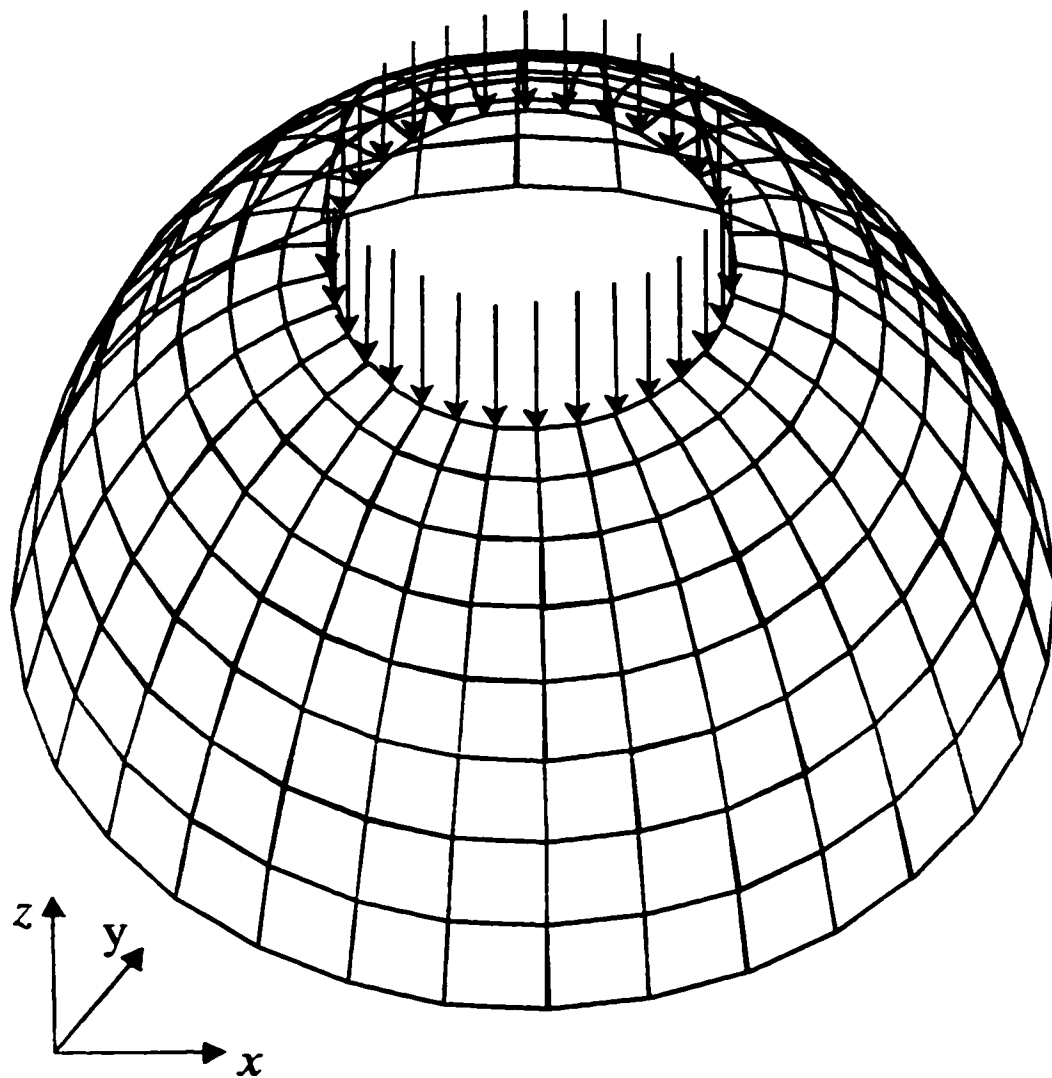


Figure 7.57 Pseudo-spherical cap: Geometry and loading conditions

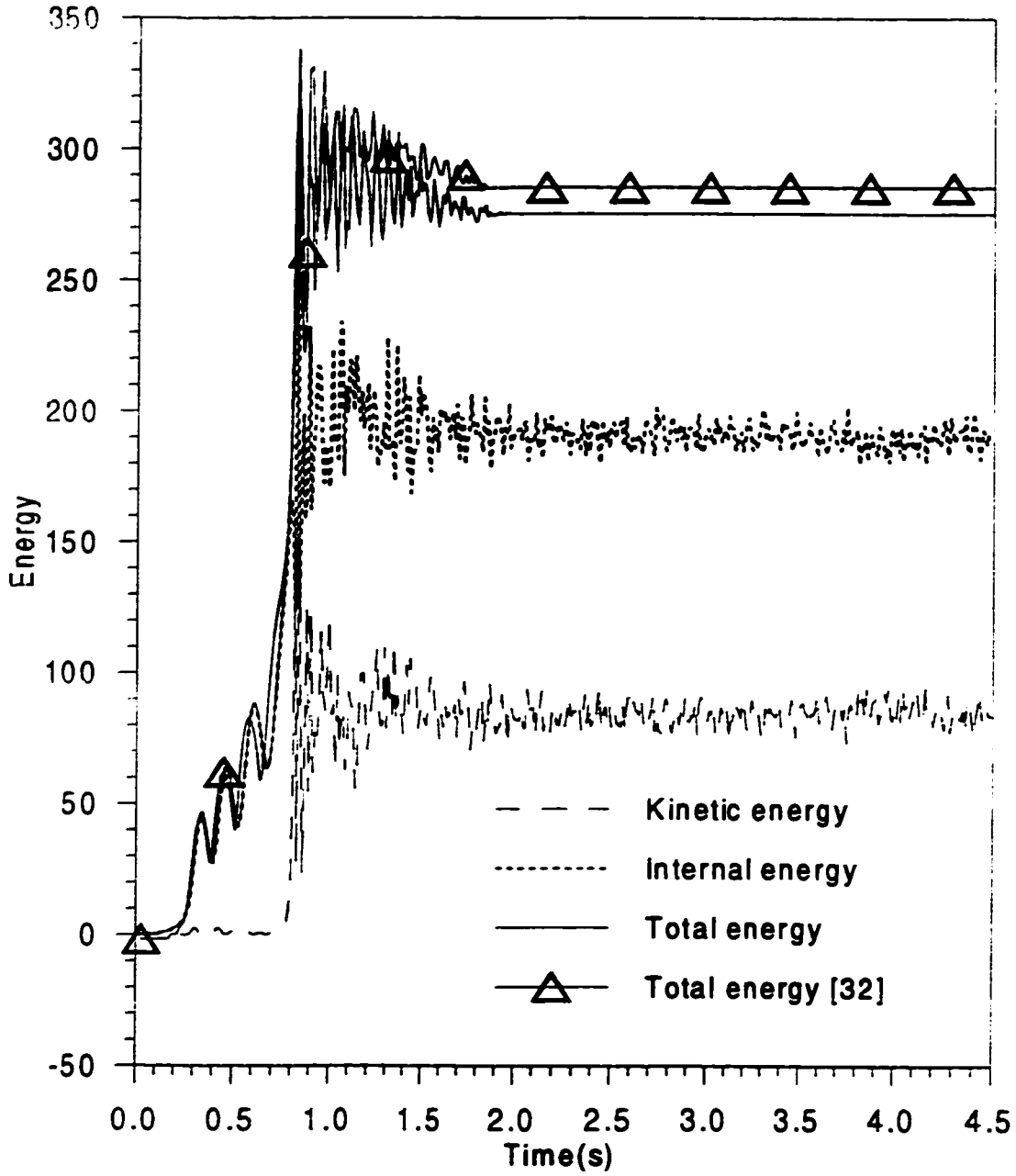


Figure 7.58 Pseudo spherical cap: variation of kinetic, internal and total energies

stays approximately zero until approximately $t=0.8s$ where there is a sharp increase in its value. This reflects the occurrence of the snap through at around this time. Very short wave oscillations of the three energies may be noticed also just after the snap. The oscillation starts with large amplitudes for all energies, then they decrease. For $t>2s$, which represents the end of the impulsive loading, the total energy is exactly conserved, whereas the internal and kinetic energies continue oscillating but with smaller amplitudes. The linear and angular momenta of the system are not conserved during the free motion phase because of the presence of zero-displacement boundary conditions which induce non-zero reactive forces that are not self equilibrated, as was the assumption for the conservation of linear momenta.

7.3.4 ‘Snap-Through’ of a Cylindrical Shell under a Concentrated Vertex Load

This problem was studied by Kuhl and Ramm [33] using the so-called ‘constraint energy momentum algorithm’ (CEMA). The geometry and the loading are shown in Figure 7.59. This cylindrical shell has two simply supported straight (no translation allowed) edges with a length of five meter each and two free curved edges. The panel has a thickness of 0.1m and a radius $R=5m$. The material properties are

$$E=2 \times 10^{11} \text{ N/m}^2 \quad \nu=0.25 \text{ and} \quad \text{Density}=10^4 \text{ kg/m}^3$$

The vertical central force $R(t)$ applied to this panel is given by

$$R(t)(MN) = \begin{cases} 1000t & \text{for } 0 \leq t \leq 0.2 \text{ s} \\ 200 & \text{for } t \geq 0.2 \text{ s} \end{cases} \quad (7.9)$$

This force increases linearly from zero to its final value of 200 MN, then it stays constant

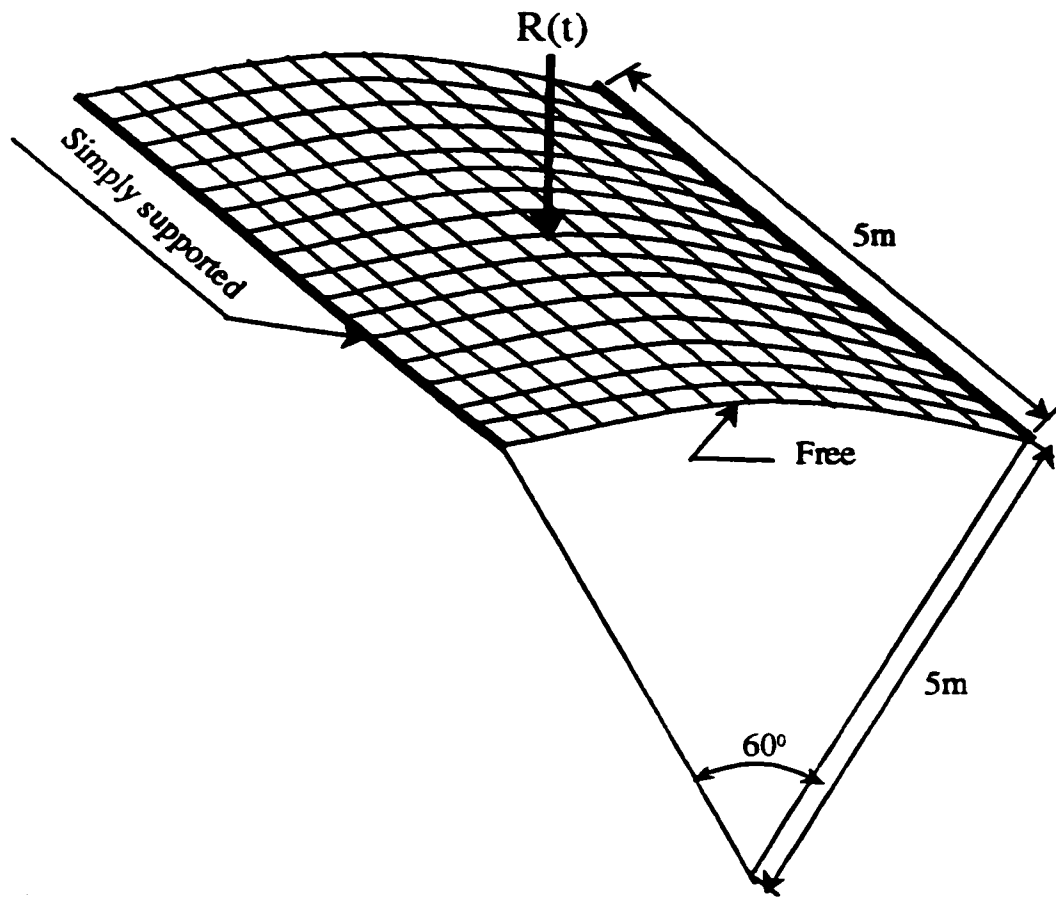


Figure 7.59 Cylindrical shell 'Snap-through': Geometry and loading conditions

for the rest of the time. The force $R(t)$ described in Reference [33] is for one fourth of the panel only, therefore the total load $R(t)$ is obtained by multiplying the given values by 4, as is done in Equation (7.9).

By exploiting symmetry conditions, Kuhl and Ramm [33] discretized one fourth of the panel using 4×4 eight-noded shell elements. Their simulation was carried out for a total time of 0.3 s by using a time step $\Delta t = 0.001$ s. The same parameters are used here, except for the mesh which is of 8×8 four-noded elements. The time variation of the vertex displacement (displacement of the center of the panel along the direction of the applied load) obtained from this analysis along with those of Reference [33] are shown in Figure 7.60. Two simulations are conducted for this example. In the first one, the warping degrees of freedom (ΔD_3) are restrained, leading to a first order shear deformation (FOSDT) model. In the second one, ΔD_3 degrees of freedom are left unrestrained, therefore, representing the TOSDT model.

From Figure 7.60, it can be seen that the two models considered in this simulation are predicting almost the same displacement up to $t = 0.25$ s. After this time, a slight difference appears and at $t = 0.284$ s the FOSDT model did not converge. The TOSDT model did not experience this problem and the solution, in this case, is converging for the whole interval of time.

The displacement predicted by this study in the pre 'snap-through' phase is closely matching that of CEMA [33] up to approximately $t = 0.145$ s. The 'snap-through' predicted here is at a slightly lower time than that predicted by CEMA. It can also be noticed that the first peak of the vertex displacement while the structure is experiencing

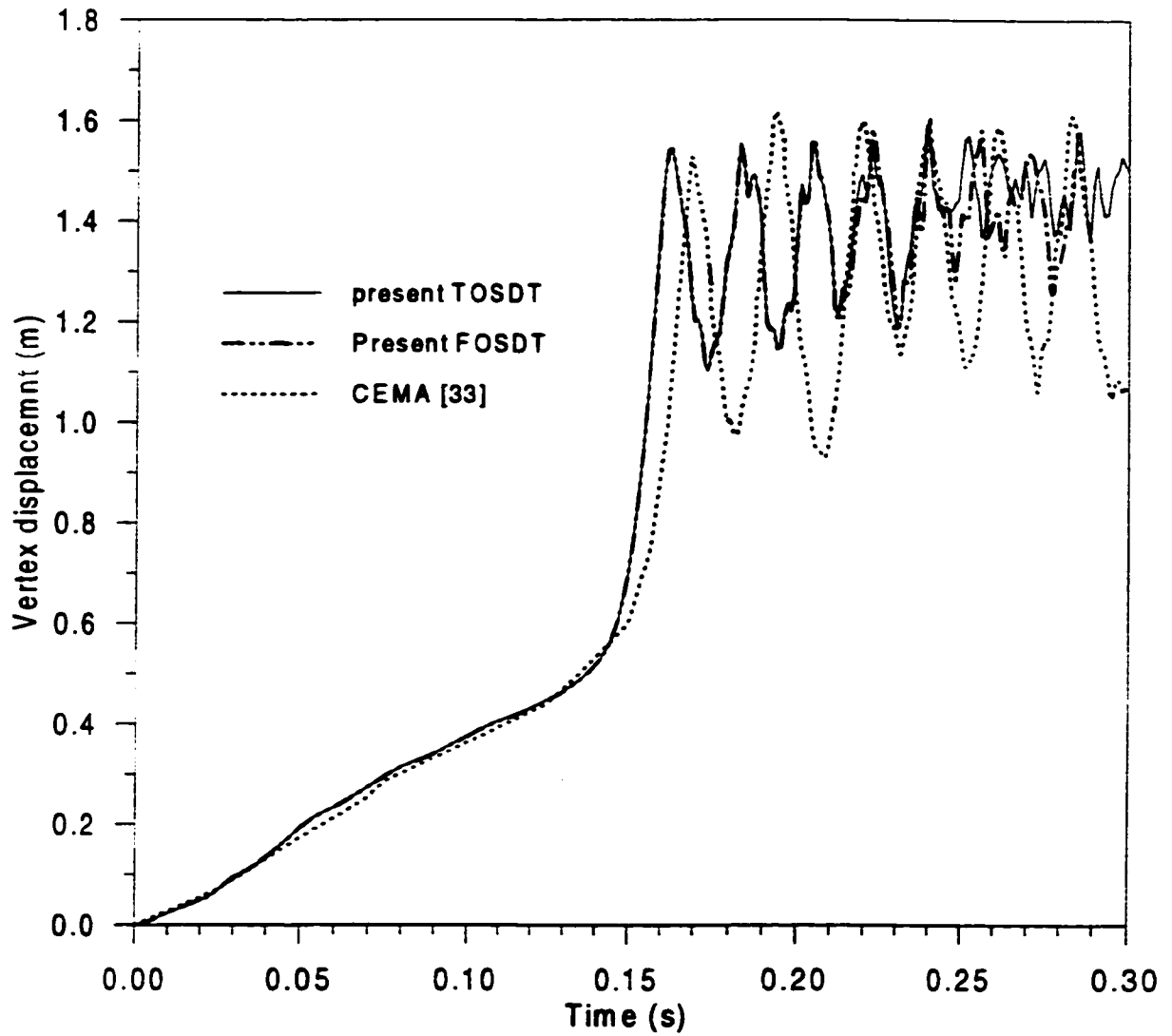


Figure 7.60 Cylindrical shell: vertex displacement before and after 'snap-through'

snap-through is close to that of CEMA. In the post 'snap-through' phase, the amplitudes of oscillation of the vertex displacement found by CEMA are longer than those predicted here by both models.

7.3.5 Ideal Sandwich Cylindrical Shell under Impulsive Load

Here, a cylindrical shell that has a wall made of a soft-core layer and very thin but stiff outer layers is considered. The material properties adopted for this problem are similar to those reported in Reference [176] concerning ideal sandwich beams and frames. This cylindrical shell represents one fourth of a cylinder with one straight edge clamped, the other three edges are free. A vertical impulsive force $P(t)$ is applied at the middle of the cylindrical. Due to symmetry conditions, only half of this cylinder with the applied force $P(t)/2$ are shown in Figure 7.61. The geometric parameters, which are not shown in Figure 7.61, are

$$h_f = 0.05 \quad h_c = 1.0$$

where h_f and h_c are, respectively, the thickness of the face sheet and that of the core material which constitute the cylinder wall as shown in Figure 7.61.

The material properties representing the face sheet and core, which are isotropic, are

$$E_f = 4 \times 10^5 \quad G_f = 1.92 \times 10^5 \quad E_c = 1 \times 10^3 \quad G_c = 480 \quad \text{Density} = 50$$

where the subscript 'f' refers to face sheet and 'c' to the core.

The force $P(t)$, which is applied for 0.2 s, is given by

$$P(t) = \begin{cases} 40000 t & \text{for } 0 \leq t \leq 0.1 \\ 8000 (1 - 5t) & \text{for } 0.1 \leq t \leq 0.2 \\ 0 & \text{for } t \geq 0.2 \end{cases} \quad (7.10)$$

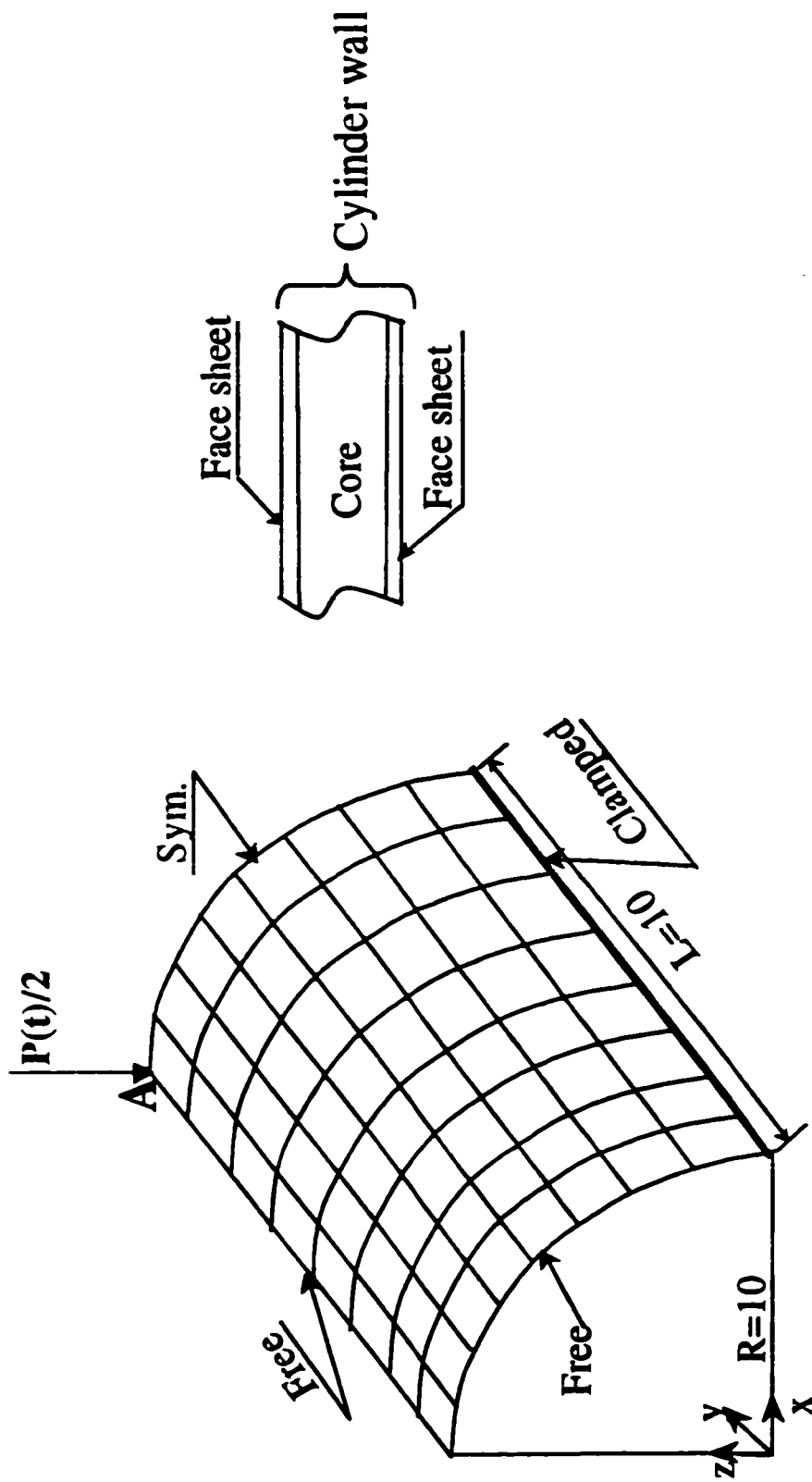


Figure 7.61 Ideal sandwich cylindrical shell : Geometry and loading description

Starting from rest, the cylinder is subjected to an impulsive load $P(t)$ during 0.2 s, then the load is removed and the structure is left in free motion. Since the bottom straight edge is fixed, the linear and angular momenta will not be conserved; however, the total energy will be conserved after $t = 0.2$ s. Due to symmetry conditions, only half of the cylindrical shell is discretized, as shown in Figure 7.61, using 8×8 four-node elements.

The purpose of this example is to show the discrepancy between the predictions of the FOSDT and TOSDT models. The dynamic response is analyzed for 6 seconds with a time step $\Delta t = 0.001$ s. The results predicted by the two models concerning the time variation of the displacement of point A (location where the load is applied) and that of the different energies are plotted in Figures 7.62 through 7.65. These figures show clearly the difference in prediction between the FOSDT and TOSDT models. It was shown from the linear static analysis of the sandwich plate, carried out in this study, as well as from the results of other researchers [19,69] that the predictions of the TOSDT models are superior than those based on the FOSDT. Thus, this discrepancy in prediction can be attributed to the poor performance of FOSDT models in case of thick sandwich laminates with soft core.

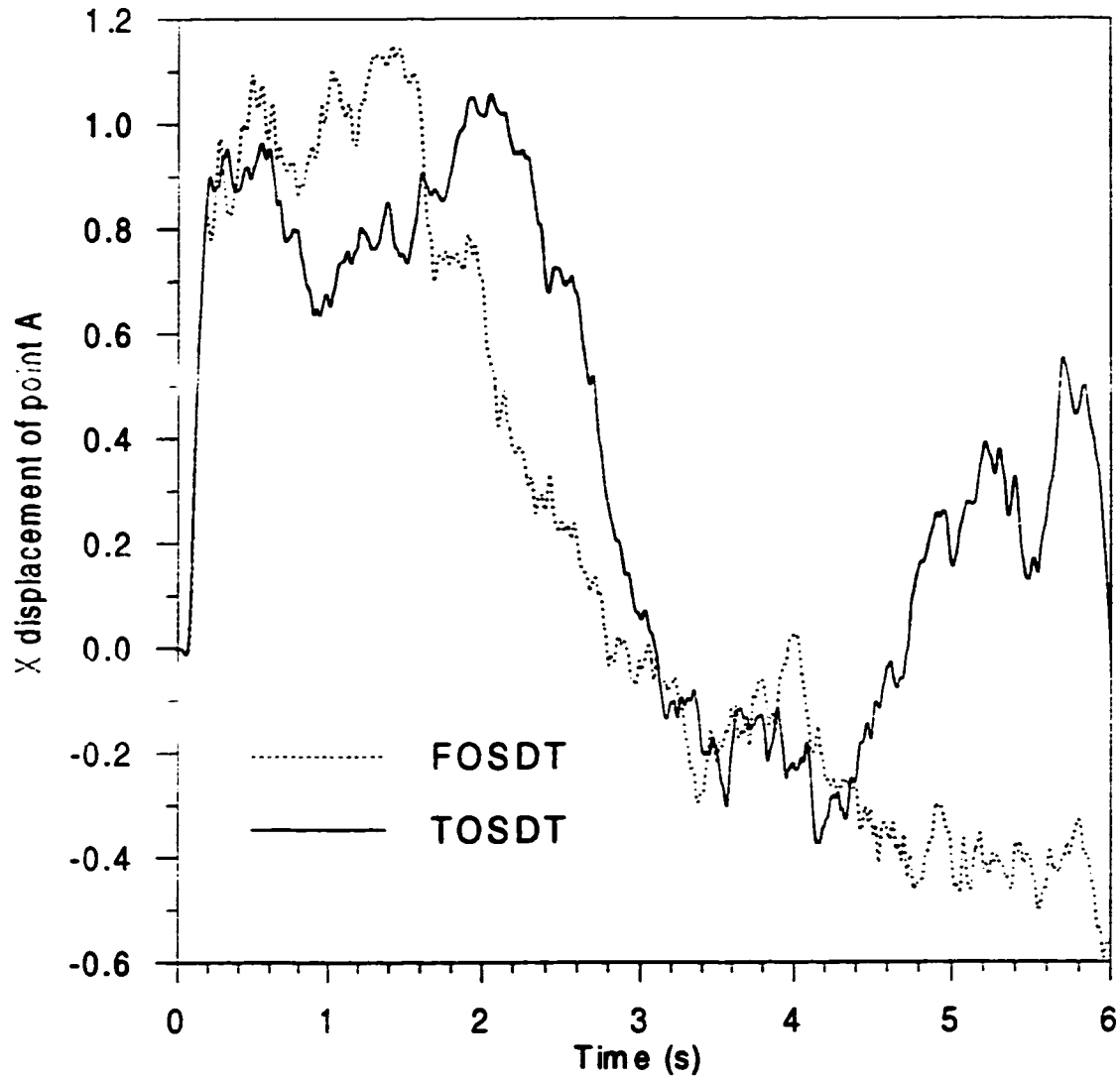


Figure 7.62 Ideal sandwich cylindrical shell : Displacement of A along X axis (TOSDT and FOSDT models)

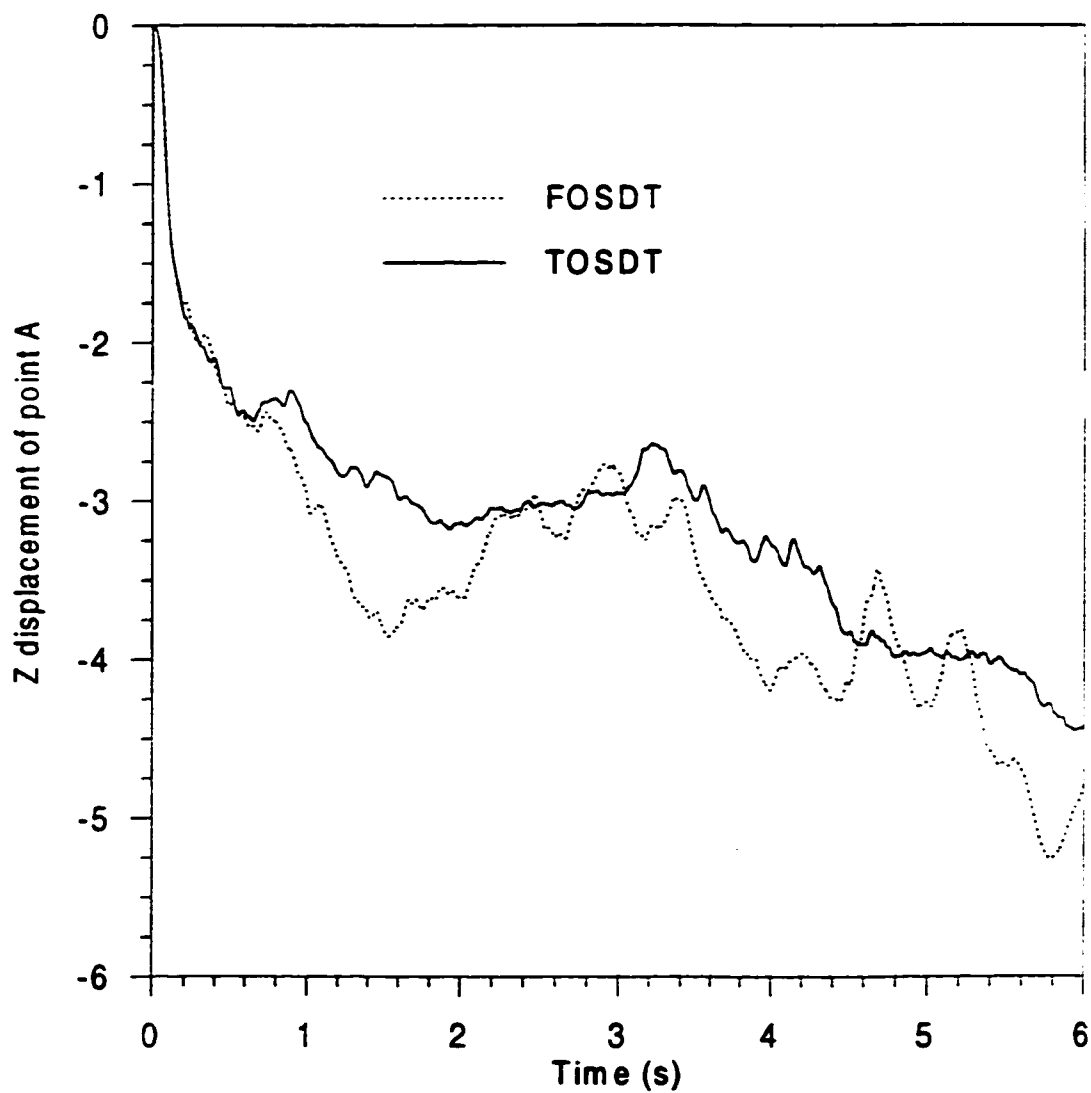


Figure 7.63 Ideal sandwich cylindrical shell : Displacement of A along Z axis (TOSDT and FOSDT models)

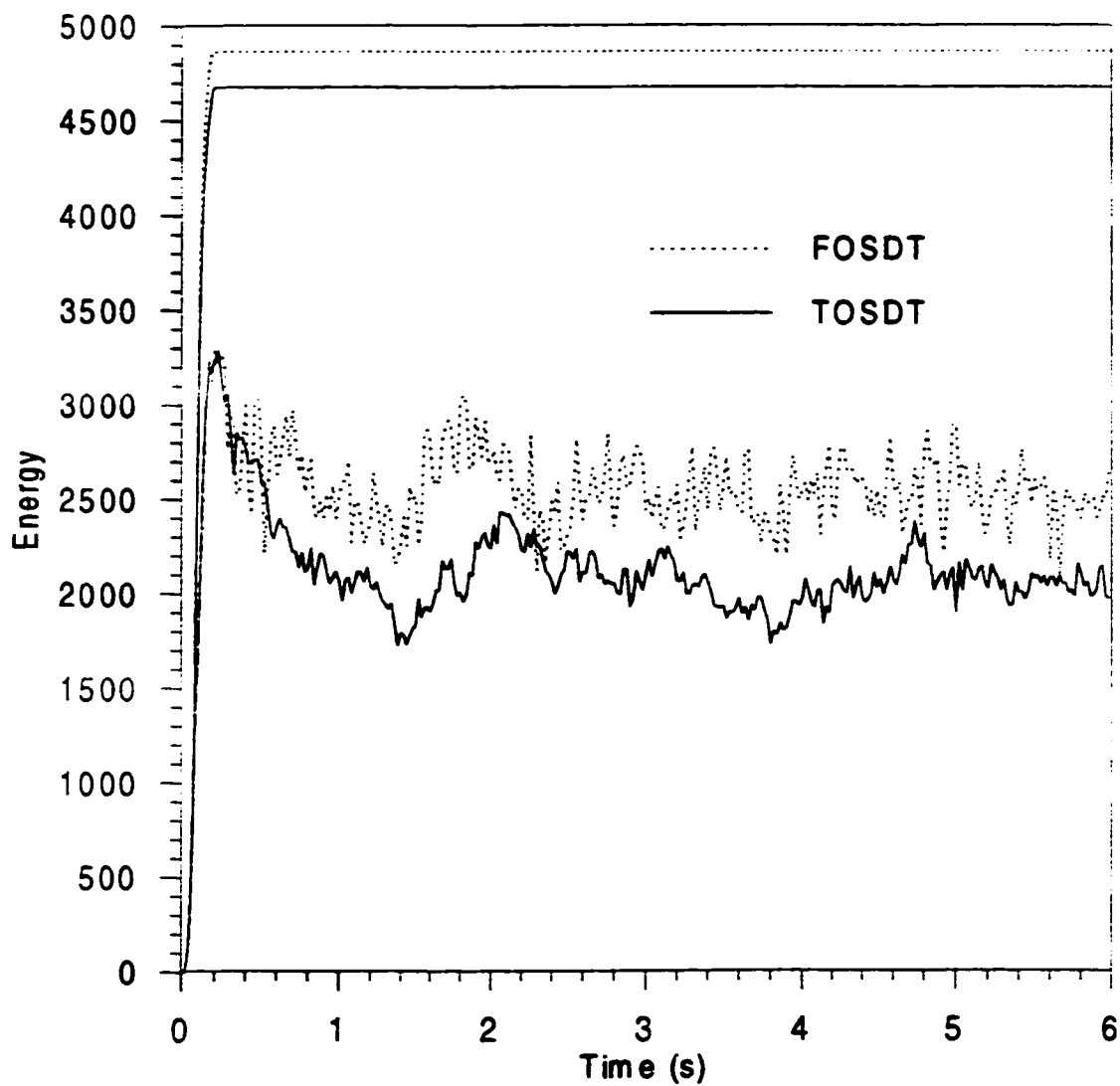


Figure 7.64 Ideal sandwich cylindrical shell : Kinetic and total energies (TOSDT and FOSDT models)

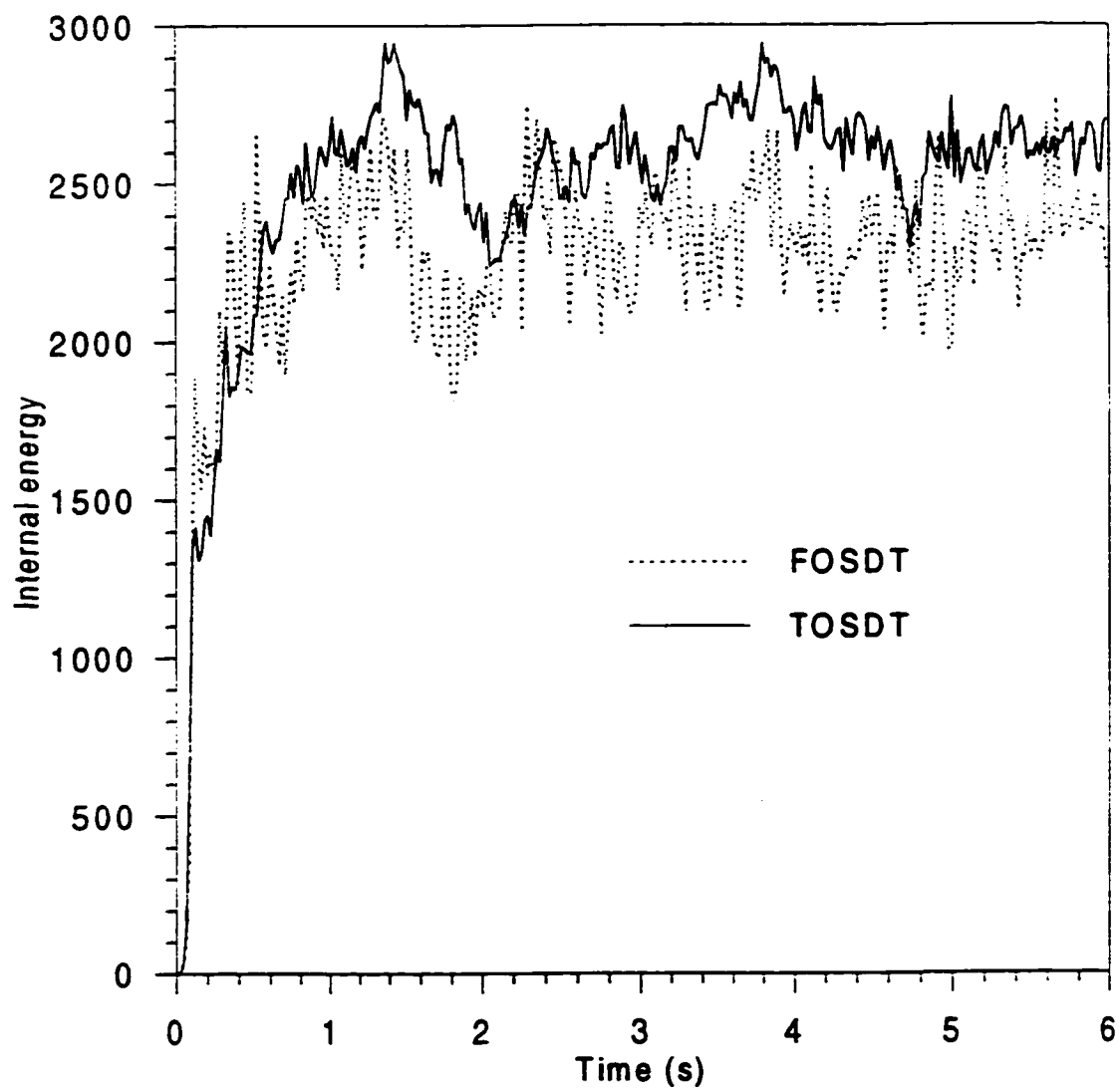


Figure 7.65 Ideal sandwich cylindrical shell : Internal energy (TOSDT and FOSDT models)

CHAPTER 8

CONCLUSIONS AND RECOMMENDATIONS

The primary objective of this dissertation is the development of a laminated finite shell element and its implementation for the nonlinear static and dynamic analysis of general laminated composite shell structures undergoing finite (unlimited in size) rotations and large overall motion.

The present chapter summarizes the main features of the developed finite shell element, then it outlines the conclusions drawn from the numerical simulations using the formulated element, and finally it recommends some directions for future research.

8.1 Summary

The following points are considered during the formulation of the present finite shell element:

1. A kinematic model leading to TOSDT with finite rotations is proposed using the material frame approach. This model results in a quadratic variation of the transverse shear strains across the shell thickness; therefore circumventing the need for a shear correction factor typical of FOSDT.

2. The theoretical formulation of the shell element considers the shell body as three-dimensional continuum and uses convective general curvilinear coordinates to derive Green-Lagrange strains which are based on the current and reference configurations.
3. The introduction of shell assumptions, i.e., fiber inextensibility and zero normal stress leads, respectively, to the reduction of the kinematic model from nine to seven parameters and condensation of the constitutive equations.
4. A singularity free parameterization of the rotation field, based on the rotational vector, is adopted along with the elimination of the drilling rotation from the onset.
5. The constitutive equations, derived with respect to the laminate general curvilinear coordinates, allow for the variation of reinforcing fiber directions in an arbitrary way from layer to layer. Furthermore, the reference axis, used to define the angles of the stacking sequence, is allowed to vary spatially in an arbitrary way. This is achieved by providing nodal directions for the reference axis and then using interpolation functions to find the direction of this axis within the finite element.
6. The thickness integration for obtaining the different contributions to shell element stiffness matrix is performed analytically and prior to the numerical in-plane integration. This leads to considerable saving in computer time during the incremental/iterative static and dynamic analyses.
7. A detailed finite element formulation is presented and implemented in a four-noded isoparametric assumed natural strain laminated shell element. This element has seven degrees of freedom per node with clear physical meaning.
8. In the static formulation, the interpolation functions are applied to the spatial

incremental directors Δd_1 and Δd_3 . Thus, the unit norm of d_1 and the orthogonality between d_1 and d_3 are preserved inside the element. However, in the dynamic formulation the interpolation is applied to the directors themselves, which is a condition to preserve the properties of the continuum and time discretized equations of motion. This leads to simpler expressions from one side and a relaxation of the unit norm and orthogonality conditions away from the nodal points.

9. The transverse shear locking problem is avoided by adopting the assumed natural strain method to the constant part of the transverse shear strain.
10. A geometrically exact procedure, based on the exponential mapping, is used for the element configuration update regardless of the magnitude of the incremental rotations.
11. A general methodology for the design of energy-momentum conserving time stepping algorithms, recently reported in the literature, is adopted. The formulated algorithm, applicable to laminated shells based on TOSDT including finite rotations, is new since all previous algorithms were restricted to shells based on FOSDT.
12. The dynamic finite element model is not merely an extension of the static one which can be obtained just by adding the inertia effects. The main characteristics of the dynamic model are stated in the following points:
 - a) The weak form of the equations of motion is evaluated at an intermediate configuration $\Phi_{n+1/2}$ at time $t_{n+1/2} = \frac{1}{2}(t_n + t_{n+1})$ which represents the middle of the time interval $[t_n, t_{n+1}]$, whereas the weak form in the static formulation is

- evaluated at configuration Φ_{n+1} corresponding to time t_{n+1} (virtual time).
- b) The algorithmic variables corresponding to configuration $\Phi_{n+1/2}$ are taken as the average of the corresponding counterparts at, respectively, t_n and t_{n+1} .
 - c) The Green-Lagrange strain tensor entering in the definition of the second Piola-Kirchhoff stress tensor corresponding to configuration $\Phi_{n+1/2}$ is taken as the average of the corresponding strains at t_n and t_{n+1} rather than the strain obtained from configuration $\Phi_{n+1/2}$.
 - d) In contrast to the static model which leads to a symmetric tangent stiffness matrix, the dynamic model, with the strain variations at configurations $\Phi_{n+1/2}$ and Φ_{n+1} , leads to unsymmetrical tangent operator. Non-symmetry is present in all three contributing matrices, i.e., The tangent consistent mass, the tangent material stiffness and the tangent geometric stiffness matrices.
- 13 A consistent linearization of the fully discrete form of the equation of motion (dynamic) and equilibrium equations (static), which is important in the numerical solution using the Newton-Raphson method, is carefully derived in order to achieve quadratic rate of convergence typical for the Newton-Raphson solution procedure.
 - 14 The arc-length method is adopted in the global solution procedure of the static formulation in order to trace very complex equilibrium paths present in the postbuckling of shell type structures.
 - 15 The above mentioned theoretical fundamentals are successfully implemented through the design of two separate computer programs for nonlinear static and dynamic

analyses for laminated shell structures.

- 16 Several numerical simulations representing test problems, recently reported in the literature, are conducted to assess the performance of the developed static and dynamic finite shell models. Some of these test problems involve severe geometric nonlinearities, very large rotations and large overall rigid body motion. Conclusions regarding the performance of the developed models are discussed in the following section.

8.2 Conclusions

The main conclusions that can be drawn from the numerical simulations conducted in this study are as follow:

1. The present element shows very good rate of convergence with mesh refinement in the linear analysis. This convergence rate is comparable to the best four-node shell elements available in the literature. In some cases, it shows a better performance especially for coarse meshes.
2. The parametric studies show the higher predictive capability of TOSDT models over FOSDT ones for the case of moderately thick to thick plates, cylindrical and spherical shells. For thick panels, TOSDT models still yield good to satisfactory results especially for the deflections and the in-plane stresses; however the predictions of FOSDT models in this range are poorer in the case of laminates and completely erroneous in the case of sandwich panels.
3. The non-enforcement of zero transverse shear stress condition at the bounding surfaces makes the TOSDT model unreliable in predicting transverse shear stresses,

especially in the case of laminates with an increasing number of layers.

4. In the case of thin plates and curved panels, the predictions of TOSDT and FOSDT models are excellent especially concerning the deflection. This performance is due to the fact that the shear deformation is negligible in such situations. On the other hand, it shows the efficiency of the ANS method in alleviating the shear locking phenomenon.
5. Very severe nonlinear static test problems are passed successfully by this model and its predictions are matching those present in the literature. Among these tests, it is noteworthy to mention the large deformations and rotations leading to shape change exhibited by the composite hyperboloidal shell, especially for the weak stacking sequence, and the complex postbuckling load deflection path experienced by the composite shallow cylindrical shell.
6. Some dynamic problems involve unrestrained structures subjected to impulsive loading after which they undergo large rigid body motion accompanied by large deformations. Again the predictions of the present study are closely matching those of the literature, and the shell momenta and total energy are exactly conserved after the end of the impulsive loading.
7. Other dynamic test problems are used to simulate 'snap-through' for a pseudo-spherical cap and a shallow cylindrical panel. The pattern of the response is similar to those of the literature; however, a slight difference appeared in the predicting values between this model and those reported in the literature.
8. The example concerning the ideal sandwich panel, is designed to show the

discrepancy in the prediction of the TOSDT and FOSDT models. It demonstrates clearly the poor performance of FOSDT models in case of thick sandwich laminates with soft core.

9. All the previously cited numerical tests elucidate the good performance and robustness of the presented laminated shell model, both in its static and dynamic form without forgetting the time stepping algorithm, developed in this study, which proved to be very stable and suitable for long-term dynamics.

8.3 Recommendations

Although this study has achieved the goal of developing a new refined finite rotation laminated finite shell element, and a time stepping algorithm which conserves exactly momenta and energy for this element, the following points are recommended for future research in order to enhance the present model and make it more fruitful.

1. A simpler interpolation scheme, similar to that used for directors in dynamics, can be adopted in the static case and a comparison can be carried out to assess the model while using this simpler interpolation scheme.
2. A higher order assumed natural strain laminated shell element can be formulated based on the shell theory presented in this study and a comparison of the efficiency of the four-noded and higher order elements in terms of response prediction and computational time can be performed.
3. At shell intersections where the smoothness assumption of the middle surface, as assumed in this study, no longer holds, the shell director must be described by three degrees of freedom instead of two as used in this study. This element can be

- extended to model shell intersections by adding one degree of freedom to the nodes on the shell intersections and using the full rotation tensor for these nodes while the nodes which belong to the smooth surfaces are kept unchanged.
4. This formulation can be modified to include thermal effects which are of important practical relevance to laminated composite structures.
 5. The present model can be extended to include inelastic materials within small strain assumptions. This can be done by substituting, in the material characterization, the second Piola-Kirchhoff stresses and Green-Lagrange strains by the small displacement engineering stress and strain measures.
 6. The metric tensor is assumed to be constant in the present study and it is equated to that of the middle surface. Other alternatives, as mentioned in the dissertation, can be used to derive different models and parametric studies can be conducted to investigate the influence of different assumptions on the predicted results especially for thick shells.
 7. The kinematic constraint of fiber inextensibility, introduced at the beginning of this study, can be relaxed, thus leading to a shell element with nine degrees of freedom per node where the transverse normal strain is included.
 8. Since FOSDT models are cheaper than TOSDT ones in terms of computational time and storage requirements, a quantitative assessment of the range of applicability of FOSDT models is needed. This can be achieved by a parametric study, involving both models, of structures with different geometrical shapes, loading conditions, and boundary conditions.

9. This model can be degenerated to develop a curved laminated beam element which can be useful in modeling stiffeners. While the development of plane curved laminated beam element using the TOSDT developed here is straightforward, the extension of such element to three dimensional situations requires a special treatment of the torsional modes.
10. The element presented here can be adopted as a basis for a layerwise theory especially for sandwich shells where the core material can be modeled using the present theory and the facings utilizing the FOSDT.
11. The high cost of layerwise theory models limit their use in large scale structures. Their simultaneous combination with refined ESLT models such as the one developed here lead to time saving and better modeling of local effects in predefined subregions where a significant three-dimensional stress field exists. Using this global-local approach will result in different regions modeled with different mathematical models. The incompatibility at the interface between different subregions can be handled using transition elements. Thus, this theory can be used to design a transition element that couples the developed element with layerwise elements.
12. This element can be extended to include delamination initiation and propagation and this by using a more accurate model for predicting transverse shear stresses.
13. The kinematic description used in the formulation of the present element is very general and admits large strains. Thus, the choice of an appropriate constitutive for large strains will lead to the inclusion of this effect.

Appendix I

Geometric Stiffness Matrices

Details concerning submatrices $[KG]_{IJ}^N$

Before giving the detailed expressions for $[KG]_{IJ}^N$, Equations (4.115) need to be rewritten after the introduction of the discrete strain displacement operators.

$${}^{(o)}m^{\alpha\beta} \Delta\delta E_{\alpha\beta} = \sum_{I=1}^4 \sum_{J=1}^4 \delta u_I^T [{}^{(o)}m^{\alpha\beta} N_{,\alpha}^I N_{,\beta}^J I_{3 \times 3}] \Delta u_J \quad (\text{I-1-a})$$

$$\begin{aligned} {}^{(1)}m^{\alpha\beta} \Delta\delta E_{\alpha\beta} &= \sum_{I=1}^4 \sum_{J=1}^4 \delta u_I^T [{}^{(1)}m^{\alpha\beta} N_{,\alpha}^I N_{,\beta}^J \bar{R}_J] \Delta D_{1(J)} + \sum_{I=1}^4 \sum_{J=1}^4 \delta D_{1(I)}^T [{}^{(1)}m^{\alpha\beta} N_{,\alpha}^I N_{,\beta}^J \bar{R}_I^T] \Delta u_J \\ &\quad - \sum_{I=1}^4 \delta D_{1(I)}^T [{}^{(1)}m^{\alpha\beta} N_{,\alpha}^I (d_{1(I)} \cdot \varphi_{,\beta}) I_{2 \times 2}] \Delta D_{1(I)} \end{aligned} \quad (\text{I-1-b})$$

$$\begin{aligned} {}^{(2)}m^{\alpha\beta} \Delta\delta E_{\alpha\beta} &= \sum_{I=1}^4 \sum_{J=1}^4 \delta D_{1(I)}^T [{}^{(2)}m^{\alpha\beta} N_{,\alpha}^I N_{,\beta}^J \bar{R}_I^T \bar{R}_J] \Delta D_{1(J)} \\ &\quad - \sum_{I=1}^4 \delta D_{1(I)}^T [{}^{(2)}m^{\alpha\beta} N_{,\alpha}^I (d_{1(I)} \cdot d_{1,\beta}) I_{2 \times 2}] \Delta D_{1(I)} \end{aligned} \quad (\text{I-1-c})$$

$$\begin{aligned} {}^{(3)}m^{\alpha\beta} \Delta\delta E_{\alpha\beta} &= - \sum_{I=1}^4 \sum_{J=1}^4 \delta u_{(I)}^T [{}^{(3)}m^{\alpha\beta} N_{,\alpha}^I N_{,\beta}^J (d_{1(I)} \otimes d_{3(J)}) \bar{R}_J] \Delta D_{1(J)} \\ &\quad + \sum_{I=1}^4 \sum_{J=1}^4 \delta u_{(I)}^T [{}^{(3)}m^{\alpha\beta} N_{,\alpha}^I N_{,\beta}^J \bar{R}_J] \Delta D_{3(I)} - \sum_{I=1}^4 \sum_{J=1}^4 \delta D_{1(I)}^T [{}^{(3)}m^{\alpha\beta} N_{,\alpha}^I N_{,\beta}^J \bar{R}_I^T (d_{3(I)} \otimes d_{1(I)})] \Delta u_J \\ &\quad + \sum_{I=1}^4 \delta D_{1(I)}^T \bar{R}_I^T [{}^{(3)}m^{\alpha\beta} N_{,\alpha}^I [(d_{1(I)} \cdot \varphi_{,\beta})(d_{1(I)} \otimes d_{3(I)} + d_{3(I)} \otimes d_{1(I)}) \\ &\quad - \frac{1}{2}(d_{3(I)} \otimes \varphi_{,\beta} + \varphi_{,\beta} \otimes d_{3(I)})] \bar{R}_I \Delta D_{1(I)} - \sum_{I=1}^4 \delta D_{1(I)}^T [{}^{(3)}m^{\alpha\beta} N_{,\alpha}^I (d_{1(I)} \cdot \varphi_{,\beta}) I_{2 \times 2}] \Delta D_{3(I)} \end{aligned}$$

$$+ \sum_{I=1}^4 \sum_{J=1}^4 \delta D_{3(I)}^T [m^{\alpha\beta} N'_\alpha N'_\beta \bar{R}_I^T] \Delta u_J - \sum_{I=1}^4 \delta D_{3(I)}^T [m^{\alpha\beta} N'_\alpha (d_{1(I)} \cdot \varphi_\beta) I_{2 \times 2}] \Delta D_{1(I)} \quad (\text{I-1-d})$$

$$\begin{aligned} 2 Q^\alpha \Delta \delta E_{\alpha 3} = & - \sum_{I=1}^4 \sum_{J=1}^4 \delta u_{(I)}^T [3 Q^\alpha N'_\alpha N'_J (d_{1(J)} \otimes d_{3(J)}) \bar{R}_J] \Delta D_{1(J)} \\ & + \sum_{I=1}^4 \sum_{J=1}^4 \delta u_{(I)}^T [3 Q^\alpha N'_\alpha N'_J \bar{R}_J] \Delta D_{3(I)} - \sum_{I=1}^4 \sum_{J=1}^4 \delta D_{1(I)}^T [3 Q^\alpha N'_\alpha N'_\beta \bar{R}_I^T (d_{3(I)} \otimes d_{1(I)})] \Delta u_J \\ & + \sum_{I=1}^4 \delta D_{1(I)}^T \bar{R}_I^T \{3 Q^\alpha N'_\alpha [(d_{1(I)} \cdot \varphi_\alpha) (d_{1(I)} \otimes d_{3(I)} + d_{3(I)} \otimes d_{1(I)}) \\ & - \frac{1}{2} (d_{3(I)} \otimes \varphi_\alpha + \varphi_\alpha \otimes d_{3(I)})]\} \bar{R}_I \Delta D_{1(I)} - \sum_{I=1}^4 \delta D_{1(I)}^T [3 Q^\alpha N'_\alpha (d_{1(I)} \cdot \varphi_\alpha) I_{2 \times 2}] \Delta D_{3(I)} \\ & + \sum_{I=1}^4 \sum_{J=1}^4 \delta D_{3(I)}^T [3 Q^\alpha N'_\alpha N'_\beta \bar{R}_I^T] \Delta u_J - \sum_{I=1}^4 \delta D_{3(I)}^T [3 Q^\alpha N'_\alpha (d_{1(I)} \cdot \varphi_\alpha) I_{2 \times 2}] \Delta D_{1(I)} \quad (\text{I-1-e}) \end{aligned}$$

$2 Q^1 \Delta \delta E_{13}$ and $2 Q^2 \Delta \delta E_{23}$ are obtained using the assumed natural strain concept.

After straight manipulations, the following equations are obtained

$$\begin{aligned} 2 Q^1 \Delta \delta E_{13} + 2 Q^2 \Delta \delta E_{23} = & \begin{Bmatrix} \delta u_1 \\ \delta u_2 \\ \delta u_3 \\ \delta u_4 \end{Bmatrix}^T [MAT1] \begin{Bmatrix} \Delta D_{1(1)} \\ \Delta D_{1(2)} \\ \Delta D_{1(3)} \\ \Delta D_{1(4)} \end{Bmatrix} + \begin{Bmatrix} \delta D_{1(1)} \\ \delta D_{1(2)} \\ \delta D_{1(3)} \\ \delta D_{1(4)} \end{Bmatrix}^T [MAT1]^T \begin{Bmatrix} \Delta u_1 \\ \Delta u_2 \\ \Delta u_3 \\ \Delta u_4 \end{Bmatrix} \\ & - \begin{Bmatrix} \delta D_{1(1)} \\ \delta D_{1(2)} \\ \delta D_{1(3)} \\ \delta D_{1(4)} \end{Bmatrix}^T [MAT2] \begin{Bmatrix} \Delta D_{1(1)} \\ \Delta D_{1(2)} \\ \Delta D_{1(3)} \\ \Delta D_{1(4)} \end{Bmatrix} \quad (\text{I-2}) \end{aligned}$$

where

$$[MAT1] = \frac{1}{8} \begin{bmatrix} [-Q^{(0)}(1-\eta) - Q^{(0)2}(1-\xi)]\bar{R}_1 & -Q^{(0)}(1-\eta)\bar{R}_2 & 0 & 0 \\ Q^{(0)}(1-\eta)\bar{R}_1 & [Q^{(0)}(1-\eta) - Q^{(0)2}(1+\xi)]\bar{R}_2 & 0 & 0 \\ 0 & Q^{(0)2}(1+\xi)\bar{R}_2 & 0 & 0 \\ Q^{(0)2}(1-\xi)\bar{R}_1 & 0 & -Q^{(0)2}(1-\xi)\bar{R}_4 & 0 \\ 0 & -Q^{(0)2}(1+\xi)\bar{R}_3 & 0 & 0 \\ [Q^{(0)}(1+\eta) + Q^{(0)2}(1+\xi)]\bar{R}_3 & Q^{(0)}(1+\eta)\bar{R}_4 & 0 & 0 \\ -Q^{(0)}(1+\eta)\bar{R}_3 & [-Q^{(0)}(1+\eta) + Q^{(0)2}(1-\xi)]\bar{R}_4 & 0 & 0 \end{bmatrix} \quad (I-3)$$

$$[MAT2] = \frac{1}{4} \begin{bmatrix} [(1-\eta)(d_{1(1)} \cdot \varphi_1^A) + (1-\xi)(d_{1(1)} \cdot \varphi_2^A)]I_{2 \times 2} & 0 & 0 & 0 \\ 0 & [(1-\eta)(d_{1(2)} \cdot \varphi_1^B) + (1+\xi)(d_{1(2)} \cdot \varphi_2^B)]I_{2 \times 2} & 0 & 0 \\ 0 & 0 & [(1+\eta)(d_{1(3)} \cdot \varphi_1^D) + (1+\xi)(d_{1(3)} \cdot \varphi_2^D)]I_{2 \times 2} & 0 \\ 0 & 0 & 0 & [(1+\eta)(d_{1(3)} \cdot \varphi_1^D) + (1+\xi)(d_{1(3)} \cdot \varphi_2^D)]I_{2 \times 2} \end{bmatrix} \quad (I-4)$$

Submatrices $[KG]_{IJ}^N$ are further divided into smaller submatrices $[KG]_{IJ}^{kl}$ ($k=1,3, l=1,3$)

where the superscript N has been omitted for simplification. The superscripts k and l

correspond to the partitioning of the vectors $\delta\varphi = [\delta u \quad \delta D_1 \quad \delta D_3]$ or

$\Delta\varphi = \{\Delta u \quad \Delta D_1 \quad \Delta D_3\}^T$ (i.e., for example $k=1$ corresponds to δu , and $l=3$ corresponds to

ΔD_3 etc..) and the subscripts IJ correspond to the node numbers

$$[KG]_{UV}^N = \begin{bmatrix} [KG]_{UV}^{1,1} & [KG]_{UV}^{1,2} & [KG]_{UV}^{1,3} \\ [KG]_{UV}^{2,1} & [KG]_{UV}^{2,2} & [KG]_{UV}^{2,3} \\ [KG]_{UV}^{3,1} & [KG]_{UV}^{3,2} & [KG]_{UV}^{3,3} \end{bmatrix} \quad (I-5)$$

The contribution to the geometric tangent stiffness matrix is split in two parts. The first part $[KG1]_{UV}^N$ is provided by the inplane, bending and higher order transverse shear terms and the second part $[KG2]_{UV}^N$ is obtained from the contribution of the constant transverse shear terms which are obtained using the assumed natural strain concept. In matrix notation, we have

$$[KG]_{UV}^N = [KG1]_{UV}^N + [KG2]_{UV}^N \quad (I-6)$$

where $[KG1]_{UV}^N$ and $[KG2]_{UV}^N$ are partitioned following equation (I-5). The details of the smaller submatrices are given below starting by the elements of $[KG1]_{UV}^N$

$$[KG1]_{UV}^{1,1} = \sum_{G=1}^{NG-pE} [m^{\alpha\beta} N'_{,\alpha} N'_{,\beta}] W_G \sqrt{A_G} I_{3 \times 3}$$

$$[KG1]_{UV}^{2,2} = \sum_{G=1}^{NG-pE} W_G \sqrt{A_G} [(m^{\alpha\beta} N'_{,\alpha} N'_{,\beta}) I_{2 \times 2} - (3Q^{\alpha} N'_{,\alpha} N'_{,\beta} + m^{\alpha\beta} N'_{,\alpha} N'_{,\beta}) (d_{1(J)} \otimes d_{3(J)})] \bar{R}_J$$

$$[KG1]_{UV}^{3,3} = \sum_{G=1}^{NG-pE} W_G \sqrt{A_G} [m^{\alpha\beta} N'_{,\alpha} N'_{,\beta} + 3Q^{\alpha} N'_{,\alpha} N'_{,\beta}] \bar{R}_J$$

$$[KG1]_{UV}^{2,1} = \sum_{G=1}^{NG-pE} \bar{R}_I^T [(m^{\alpha\beta} N'_{,\alpha} N'_{,\beta}) I_{3 \times 3} - (3Q^{\alpha} N'_{,\alpha} N'_{,\beta} + m^{\alpha\beta} N'_{,\alpha} N'_{,\beta}) (d_{3(I)} \otimes d_{1(I)})] W_G \sqrt{A_G}$$

$$[KG1]_{UV}^{2,2} = \sum_{G=1}^{NG-pE} W_G \sqrt{A_G} (m^{\alpha\beta} N'_{,\alpha} N'_{,\beta}) \bar{R}_I^T \bar{R}_J, \quad (\text{Add the following terms in case } I=J)$$

$$\begin{aligned}
& + \sum_{G=1}^{NG-pis} W_G \sqrt{A_G} \{ (-m^{\alpha\beta} N'_{\alpha} (d_{1(l)} \cdot \varphi_{\beta}) - m^{\alpha\beta} N'_{\alpha} (d_{1(l)} \cdot d_{1,\beta})) I_{2 \times 2} \\
& + \bar{R}_l^T (m^{\alpha\beta} N'_{\beta} + 3Q^{\alpha} N') (d_{1(l)} \otimes d_{3(l)} + d_{3(l)} \otimes d_{1(l)}) \bar{R}_l \\
& - \frac{1}{2} \bar{R}_l^T (m^{\alpha\beta} N'_{\beta} + 3Q^{\alpha} N') (d_{3(l)} \otimes \varphi_{\alpha} + \varphi_{\alpha} \otimes d_{3(l)}) \bar{R}_l \}
\end{aligned}$$

$$[KG1]_{IJ}^{2,3} = - \sum_{G=1}^{NG-pis} W_G \sqrt{A_G} (m^{\alpha\beta} N'_{\beta} + 3Q^{\alpha} N') (d_{1(l)} \cdot \varphi_{\alpha}) I_{2 \times 2} \text{ (if } I=J \text{ or } [0] \text{ otherwise)}$$

$$[KG1]_{IJ}^{3,1} = \sum_{G=1}^{NG-pis} W_G \sqrt{A_G} (m^{\alpha\beta} N'_{\alpha} N'_{\beta} + 3Q^{\alpha} N' N'_{\alpha}) \bar{R}_l^T$$

$$[KG1]_{IJ}^{3,2} = - \sum_{G=1}^{NG-pis} W_G \sqrt{A_G} (m^{\alpha\beta} N'_{\beta} + 3Q^{\alpha} N') (d_{1(l)} \cdot \varphi_{\alpha}) I_{2 \times 2} \text{ (if } I=J \text{ or } [0] \text{ otherwise)}$$

$$[KG1]_{IJ}^{3,3} = [0] \tag{I-7}$$

The subscripts IJ are stated explicitly for the elements of $[KG2]_{IJ}^N$. The submatrices, which are not given in the following expressions, are equal to zero. Since $[KG2]^N$ is symmetric, only submatrices belonging to the upper triangular part will be expressed.

$$[KG1]_{11}^{1,2} = -\frac{1}{8} [Q^1(1-\eta) + Q^2(1-\xi)] \bar{R}_1$$

$$[KG1]_{12}^{1,2} = -\frac{1}{8} Q^1(1-\eta) \bar{R}_2$$

$$[KG1]_{14}^{1,2} = -\frac{1}{8} Q^2(1-\xi) \bar{R}_4$$

$$[KG1]_{11}^{2,2} = -\frac{1}{4}[\overset{(0)}{Q}^1(1-\eta)(d_{1(1)} \cdot \varphi_1^B) + \overset{(0)}{Q}^2(1-\xi)(d_{1(1)} \cdot \varphi_2^A)]I_{2 \times 2}$$

$$[KG1]_{12}^{2,1} = \frac{1}{8}\overset{(0)}{Q}^1(1-\eta)\bar{R}_1^T$$

$$[KG1]_{14}^{2,1} = \frac{1}{8}\overset{(0)}{Q}^2(1-\xi)\bar{R}_1^T$$

$$[KG1]_{22}^{1,2} = \frac{1}{8}[\overset{(0)}{Q}^1(1-\eta) - \overset{(0)}{Q}^2(1+\xi)]\bar{R}_2$$

$$[KG1]_{23}^{1,2} = -\frac{1}{8}\overset{(0)}{Q}^2(1+\xi)\bar{R}_3$$

$$[KG1]_{22}^{2,2} = -\frac{1}{4}[\overset{(0)}{Q}^1(1-\eta)(d_{1(2)} \cdot \varphi_1^B) + \overset{(0)}{Q}^2(1+\xi)(d_{1(2)} \cdot \varphi_2^C)]I_{2 \times 2}$$

$$[KG1]_{23}^{2,1} = \frac{1}{8}\overset{(0)}{Q}^2(1+\xi)\bar{R}_2^T$$

$$[KG1]_{33}^{1,2} = \frac{1}{8}[\overset{(0)}{Q}^1(1+\eta) + \overset{(0)}{Q}^2(1+\xi)]\bar{R}_3$$

$$[KG1]_{34}^{1,2} = \frac{1}{8}\overset{(0)}{Q}^1(1+\eta)\bar{R}_4$$

$$[KG1]_{33}^{2,2} = -\frac{1}{4}[\overset{(0)}{Q}^1(1+\eta)(d_{1(3)} \cdot \varphi_1^D) + \overset{(0)}{Q}^2(1+\xi)(d_{1(3)} \cdot \varphi_2^C)]I_{2 \times 2}$$

$$[KG1]_{34}^{2,1} = -\frac{1}{8}\overset{(0)}{Q}^1(1+\eta)\bar{R}_3^T$$

$$[KG1]_{44}^{1,2} = \frac{1}{8}[-\overset{(0)}{Q}^1(1+\eta) + \overset{(0)}{Q}^2(1-\xi)]\bar{R}_4$$

$$[KG1]_{44}^{2,2} = -\frac{1}{4}[\overset{(0)}{Q}^1(1+\eta)(d_{1(4)} \cdot \varphi_1^D) + \overset{(0)}{Q}^2(1-\xi)(d_{1(4)} \cdot \varphi_2^A)]I_{2 \times 2}$$

(I-8)

REFERENCES

- [1] Noor, A.K. and Burton, W.S., "Assessment of computational models for multilayered composite shells," *Appl. Mech. Rev.*, Vol. 43 , 1990, pp.67-96.
- [2] Reddy, J.N. On refined computational models of composite laminates, *Int. J. Numer. Meth. Engrg.*, Vol.27, 1989, pp.361-382.
- [3] Bose, P. and Reddy, J.N., "analysis of composite plates using various plate theories Part1: Formulation and analytical solutions," *Struct. Engng. Mech.*, Vol.6(6), 1998, pp.583-612.
- [4] Dvorkin, E. N. and Bathe, K.J. "A continuum mechanics based four-node shell element for general nonlinear analysis," *Engng. Comput.*, Vol.1, 1984, pp.77-88.
- [5] Bathe, K. J. and Dvorkin, E. N. "A formulation of general shell elements- The use of mixed interpolation of tensorial components," *Int. J. Numer. Meth. Engrg.*, V.22, 1986, pp.697-722.
- [6] Simo, J. C. and Tarnow, N. "A new enrgy and momentum conserving algorithm for the nonlinear dynamics of shells", *Int. J. Numer. Meth. Engrg.*,Vol.37(15), 1994, pp.2527-2549.
- [7] Gadala, M.S., Dokainish, M.A. and Oravas, G. AE., "Formulation methods of geometric and material nonlinearity problems," *Int. J. Numer. Meth. Engrg.*,Vol.20, 1984, pp.887-914.
- [8] Bathe, K. J. "Finite element procedures in engineering analysis", Prentice-Hall, Upper Saddle River, NJ, 1996.
- [9] Mattiasson, K., Bengtsson, A. and Samuelsson, A., "On the accuracy an efficiency of numerical algorithms for geometrically nonlinear structural analysis," in Bergan, P. G., Bathe, K. J., and Wunderlich, W.(eds.), *finite Element Method for Nonlinear Problems*, Springer Heidelberg, 1986, pp.3-23
- [10] Atluri, S.N., "Alternate stress and conjugate strain measures, and mixed variational formulations involving rigid rotations, for computational analyses of finitely deformed solids, with application to plates and shells-I Theory," *Comput. Struct.*, Vol. 18, No.1, 1984, pp. 93-116

- [11] Betsch, P., Menzel, A. and Stein, E., "On the parametrization of finite rotations in computational mechanics. A classification of concepts with application to smooth shells," *Comput. Meth. Appl. Mech. Engng.*, Vol. 155, 1998, pp.273-305.
- [12] Lee, S. J. and Kanok-Nukulchai, W., "A nine-node assumed strain finite element for large-deformation analysis of laminated shells," *Int. J. Numer. Meth. Engng.*, Vol.42, 1998, pp.777-798.
- [13] Bischoff, M. and Ramm, E., "Shear deformable shell elements for large strains and rotations," *Int. J. Numer. Meth. Engng.*, Vol.40, 1997, pp.4427-4449.
- [14] Brank, B., Peric, D. and Damjanic, F.B., "On large deformations of thin elasto-plastic shells: Implementation of finite rotation model for quadrilateral shell element," *Int. J. Numer. Meth. Engng.*, Vol.40, 1997, pp.689-726.
- [15] Brank, B., Peric, D. and Damjanic, F.B., "On implementation of a nonlinear four node shell finite element for thin multilayered elastic shells," *Comput. Mech.*, Vol. 16, 1995, pp.341-359.
- [16] Braun, M., Bischoff, M. and Ramm, E., "Nonlinear shell formulations for complete three-dimensional constitutive laws including composites and laminates," *Comput. Mech.*, Vol.15, 1994, pp.1-18.
- [17] Wagner, W. and Gruttmann, F., "A simple finite rotation formulation for composite shell elements," *Engng. Comput.*, Vol.11, 1994, pp.145-176.
- [18] Basar, Y., "Finite-rotation theories for composite laminates," *Acta Mechanica*, Vol.98, 1993, pp.159-176.
- [19] Basar, Y., Ding, Y. and Schultz, R., "Refined shear deformation models for composite laminates with finite rotations," *Int. J. Solids Struct.*, Vol. 30(19), 1993, pp.2611-2638.
- [20] Basar, Y., Montag, U. and Ding, Y., "On an isoparametric finite element for composite laminates with finite rotations," *Comput. Mech.*, Vol. 12, 1993, pp.329-348
- [21] Basar, Y. And Ding, Y., "Finite-rotation elements for the non-linear analysis of thin shell structures," *Int. J. Solids Struct.*, Vol. 26, No.1, 1990, pp.83-97
- [22] Buechter, N. and Ramm, E., "Shell theory versus degeneration – A comparison in large rotation finite element analysis," *Int. J. Numer. Meth. Engng.*, Vol. 34, 1992, pp.39-59.

- [23] Parisch, H. "An investigation of finite rotation four node assumed strain shell element," *Int. J. Numer. Meth. Engng.*, Vol.31, 1991, pp.127-150
- [24] Dennis, S. T. and Palazotto, A. N., "Large displacement and rotational formulation for laminated shells including parabolic transverse shear," *Int. J. Non-linear Mech.*, Vol.25(1), 1990, pp.67-85.
- [25] Stander, N., Matzenmiller, A. and Ramm, E. "An assessment of assumed strain methods in finite rotation shell analysis," *Engng. Comput.*, Vol.6, 1989, pp.58-66
- [26] Milford, R.V., "Degenerated isoparametric finite elements using explicit integration," *Int. J. Numer. Meth. Engng.*, Vol. 23, 1986, pp.133-154
- [27] Chao, W. C. and Reddy, J. N. "Analysis of laminated composite shells using a degenerated 3-D element," *Int. J. Numer. Meth. Engng.*, Vol.20, 1984, pp.1991-2007
- [28] Oliver, J. and Onate, E., "A total Lagrangian formulation for the geometrically nonlinear analysis of structures using finite elements. Part I. Two-dimensional problems: Shell and plate structures," *Int. J. Numer. Meth. Engng.*, Vol. 20, 1984, pp.2253-2281
- [29] Bathe, K.J. and Bolourchi, S. "A geometric and material nonlinear plate and shell element," *Comput. Struct.*, V.11, 1980, pp.23-48
- [30] Parisch, H. "Geometrical nonlinear analysis of shells," *Comput. Meth. Appl. Mech. Engng.*, Vol.14, 1978, pp.159-178
- [31] Gummadi, L.N.B. and Palazotto, A.N., "Nonlinear dynamic finite element analysis of composite cylindrical shells considering large rotations," *AIAA journal*, Vol. 37(11), 1999, pp.1489-1494.
- [32] Brank, B., Briseghella, L., Tonello, N. And Damjanic, F. B., "On non-linear dynamics of shells: Implementation of energy-momentum conserving algorithm for finite rotation shell model," *Int. J. Numer. Meth. Engng.*, Vol. 42,1998, pp. 409-442.
- [33] Kuhl, D. and Ramm, E., "constraint energy momentum algorithm and its application to non-linear dynamics of shells," *Comput. Meth. Appl. Mech. Engng.*, Vol.136, 1996, pp.293-315.
- [34] Saleeb, A. F., Chang, T. Y., Graf, W. and Yingyeunyoung, S., "A hybrid/mixed model for nonlinear shell analysis and its application to large-rotation problems," *Int. J. Numer. Meth. Engng.*, Vol.29, 1990, pp.407-446.

- [35] Stanley, G. "Continuum-based shell elements," *Ph.D. Dissertation*, Applied Mechanics Division, Stanford University, Stanford, CA, 1985
- [36] Chang, T.Y. and Sawamiphakdi K. "large deformation analysis of laminated shells by finite element method," *Comput. Struct.*, Vol.13, 1981, pp.331-340
- [37] Crisfield, M.A. and Moita, G.F., "A unified co-rotational framework for solids, shells and beams," *Int. J. Solids Struct.*, Vol.33, 1996, pp.2969-2992
- [38] Jiang, L. and Chernuka, M.W., "A simple four-noded corotational shell element for arbitrary large rotations," *Comput. Struct.*, Vol. 53, No5, 1994, pp.1123-1132
- [39] Nour-Omid, B. And Rankin, C.C., "Finite rotation analysis and consistent linearization using projectors," *Comput. Meth. Appl. Mech. Engng.*, Vol. 93, 1991, pp.353-384
- [40] Hsiao, K.M., and Hung, H.C., "Large deflection analysis of shell structure by using corotational total lagrangian formulation," *Comput. Meth. Appl. Mech. Engng.*, Vol. 73, 1989, pp. 209-225.
- [41] Rankin, C.C. and Brogan, F.A., "An element independent corotational procedure for the treatment of large rotations," *ASME J. Pressure Vessel Technol.*, Vol.108, 1986, pp.165-174
- [42] Horrigmoe, G. and Bergan, P. G., "Nonlinear analysis of free form shells by flat finite elements," *Comput. Meth. Appl. Mech. Engng.*, Vol.16, 1978, pp.11-35
- [43] Belytschko, T. and Hsieh, B.J. , "Non-linear transient finite elements analysis with convected coordinates," *Int. J. Numer. Meth. Engng.*, Vol.7, 1973, pp.255-271
- [44] Barut, A., Madenci, E. and Tessler, A. "nonlinear elastic deformations of moderately thick laminated shells subjected to large and rapid rigid-body motion," *Finite El. Anal. Des.*, V.22, 1996, pp.41-57
- [45] Madenci, E. and Barut, A., "Dynamic response of thin composite shells experiencing non-linear elastic deformations coupled with large and rapid overall motions," *Int. J. Numer. Meth. Engng.*, Vol.39, 1996, pp.2695-2723
- [46] Carrera, E., "Multilayered shell theories accounting for layerwise mixed description, Part 1: Governing equations," *AIAA journal*, Vol.37 (9), 1999, pp.1107-1124.

- [47] Wempner, G. A. *Mechanics of solids with applications to thin bodies*. Sijthoff & Noordhoff Int. publishers, 1981
- [48] Reddy, J.N. and Liu, C.F., "A higher-order shear deformation theory of laminated elastic shells," *Int. J. Engrg. Sci.*, Vol.23 , 1985, pp.319-330.
- [49] Reddy, J.N., "An evaluation of equivalent-single-layer and layerwise theories of composite laminates," *Compos. Struct.*, Vol. 25, 1993, pp.21-35
- [50] Noor, A.K., Burton, W.S. and Peters, J. M., "Assessment of computational models for multilayered composite cylinders," *Int. J. Solids Struct.*, Vol. 27, No. 10, 1991, pp.1269-1286
- [51] Reddy, J.N., "A review of refined theories of laminated composite plates," *Shock & Digest*, Vol. 22 (7), 1990, pp.3-17
- [52] Reddy, J.N., "A general non-linear third-order theory of plates with moderate thickness," *Int. J. Non-linear Mech.*, Vol.25 (6), 1990, pp.677-686
- [53] Kapania, R.K., "A Review on the analysis of laminated shells," *ASME J. Pressure Vessel Technol.*, Vol.111, 1989, pp.88-96
- [54] Palmerio, A. F., Reddy, J. N. and Schmidt, R., "On a moderate rotation theory of laminated anisotropic shells – Part 1. Theory," *Int. J. Non-linear Mech.*, Vol.25(6), 1990, pp.687-700.
- [55] Reissner, E. "The effect of transverse shear deformation on the bending of elastic plates," *J. Appl. Mech.*, Vol.12, 1945, pp.A69-A77
- [56] Reddy, J.N., "Energy and Variational Methods in Applied Mechanics.". John Wiley & sons, NY, 1984
- [57] Noor, A.K. and Mathers, M.D., "Shear flexible finite element models of laminated composite plates and shells," 1975, NASA TN D8044
- [58] Ahmad, S., Irons, B. And Zienkiewicz, "Analysis of thick and thin shell structures by curved finite elements," *Int. J. Numer. Meth. Engng.*, Vol.2, 1970, pp.419-451.
- [59] Mahe, M., Sourisseau, J.C. and Ohayon, R., "Explicit thickness integration for three-dimensional shell elements applied to non-linear analysis," *Int. J. Num. Meth. Engng.*, Vol. 36, 1993, pp.1085-1993.
- [60] Vlachoutsis, S., "Explicit integration for three-dimensional degenerated shell finite elements," *Int. J. Numer. Meth. Engng.*, Vol.29, 1990, pp.861-880

- [61] Palmerio, A. F., Reddy, J. N. and Schmidt, R., "On a moderate rotation theory of laminated anisotropic shells – Part 2. Finite-element analysis," *Int. J. Non-linear Mech.*, Vol. 25(6), 1990, pp.701-714.
- [62] Hughes, T.J.R. and Liu, W. K., "Nonlinear finite element analysis of shells: Part I, Three dimensional shells," *Comput. Meth. Appl. Mech. Engng.*, Vol.26, 1981, pp.331-362.
- [63] Hughes, T.J.R. and Liu, W. K., "Nonlinear finite element analysis of shells: Part II, Two dimensional shells," *Comput. Meth. Appl. Mech. Engng.*, Vol. 27, 1981, pp.167-181.
- [64] Simo, J. C., Fox, D. D., "On a stress resultant geometrically exact shell model: Part I, Formulation and optimal parametrization," *Comput. Meth. Appl. Mech. Engng.*, Vol.72, 1989, pp.267-304.
- [65] Simo, J. C., Fox, D. D. and Rifai, M. S., "On a stress resultant geometrically exact shell model. Part II: The linear theory; Computational aspects", *Comput. Meth. Appl. Mech. Engng.*, Vol.73, 1989, pp.53-92.
- [66] Simo, J. C., Fox, D. D. and Rifai, M. S., "On a stress resultant geometrically exact shell model: Part III, Computational aspects of the nonlinear theory", *Comput. Meth. Appl. Mech. Engng.*, Vol.79, 1990, pp.21-70.
- [67] Sansour, C. and Bufler, H. "An exact finite rotation shell theory, its mixed variational formulation and its finite element implementation," *Int. J. Num. Meth. Engng.*, Vol.34, 1992, pp.73-115
- [68] Dörninger, K. and Rammerstorfer, F.G., "A layered composite shell element for elastic and thermoelastic stress and stability analysis at large deformations," *Int. J. Numer. Meth. Engng.*, Vol. 30, 1990, pp.833-858
- [69] Pandya, B. N. and Kant, T., "Higher-order shear deformation theories for flexure of sandwich plates – Finite element evaluations," *Int. J. Solids Struct.*, Vol. 24(12), 1988, pp.1267-1286.
- [70] Vlasov, B.F., "Ob uravneniakh izgiba plastinok (On equations of bending of plates)", *Dokla Ak. Nauk Azerbejianskoi SSR* 03, 1957, pp.955-959 (in Russian)
- [71] Jemielita, G., "Techniczna Teoria Płyty Sreniej Grubbosci (Technical theory of plates with moderate thickness)., *Rozprawy Inzynierskie (Engng. Trans.) Polska Akademia Nauk*, Vol. 23, 1975, pp.483-499

- [72] Schmidt, R., "A refined theory of plates with transverse shear deformation theory." *The J. Ind. Math. Soc.*, Vol. 27, 1977, pp.23-38
- [73] Lo, K. H., Christensen, R. M. and Wu, E. M. "A higher order theory of plate deformation, Part1: Laminated plates," *J. Appl. Mech.*, Vol.44(4), 1977, pp.663-668
- [74] Lo, K. H., Christensen, R. M. and Wu, E. M. "A higher order theory of plate deformation, Part2: Laminated plates," *J. Appl. Mech.*, Vol.44(4), 1977, pp.669-676
- [75] Krishna Murty, A.V., "Higher order theory for vibration of thick plates." *AIAA journal*, Vol. 15, 1977, pp.1823-1824
- [76] Levinson, M., "An accurate simple theory of the statics and dynamics of elastic plates," *Mech. Res. Commun.*, Vol.7, 1980, pp.343-350
- [77] Murthy, M.V.V., "An improved transverse shear deformation theory for laminated anisotropic plates," NASA-TP-1903, 1981, pp.1-37
- [78] Reddy, J.N., "A simple higher order theory for laminated composite plates," *J. Appl. Mech.*, Vol.51, 1984, pp.745-752.
- [79] Bhimaraddi, A. and Stevens, L.K., "A higher order theory for free vibration of orthotropic, homogeneous, and laminated rectangular plates," *J. Appl. Mech.*, Vol. 51, 1984, pp.195-198
- [80] Reddy, J.N. "On the generalization of displacement-based laminate theories." *J. Appl. Mech. Rev.*, Vol.42, 1989, pp.5213-5222.
- [81] Phan, N. D. and Reddy, J. N. "Analysis of laminated composite plates using a higher order shear deformation theory," *Int. J. Numer. Meth. Engng.*, Vol.21, 1985, pp.2201-2219
- [82] Kwon, Y. W. and Akin, J. E., "Analysis of layered composite plates using a higher-order deformation theory," *Comput. Struct.*, Vol.27, 1987, pp.619-623
- [83] Bicos, A. S. and Springer, G. S. "Analysis of free damped vibration of laminated composite plates and shells," *Int. J. Solids Struct.*, Vol.25, 1989, pp.129-149
- [84] Palazotto, A. N. and Linnemann, P. E. "vibration and buckling characteristics of composite cylindrical panels incorporating the effects of a higher order shear theory," *Int. J. Solids Struct.*, Vol.28, 1991, pp.341-361

- [85] Shalev, D. and Aboudi, J. "Postbuckling analysis of viscoelastic laminated plates using higher order theory", *Int. J. Solids Struct.*, Vol. 27, 1991, pp. 1747-1755.
- [86] Soldatos, K. P., "Buckling of axially compressed antisymmetric angle ply laminated circular cylindrical panels according to a refined shear deformable shell theory," *Press. Vess. Piping*, Vol. 124, 1987, pp. 63-71
- [87] Soldatos, K. P., "Stability and vibration of thickness shear deformable cross-ply laminated non-circular cylindrical shells", *Press. Vess. Piping*, Vol. 115, 1986
- [88] Kumar, V. and Singh, A. V., "Geometrically non-linear dynamic analysis of laminated shells using Bezier functions," *Int. J. Non-Linear Mechanics*, Vol. 32, No. 3, 1997, pp. 425-442
- [89] Di Sciuva, M. "An improved shear-deformation theory for moderately thick multilayered anisotropic shells and plates," *J. Appl. Mech.*, Vol. 54, 1987, pp. 589-596
- [90] Librescu, L. and Schmidt, R., "Substantiation of a shear-deformable theory of anisotropic composite laminated shells accounting for interlaminar continuity conditions," *Int. J. Engng. Sci.*, Vol. 29, 1991, pp. 669-683
- [91] Di Sciuva, M. "Multilayered anisotropic plate models with continuous interlaminar stresses", *Compos. Struct.*, Vol. 22, 1992, pp. 149-167
- [92] He, L., "A linear theory of laminated shells accounting for continuity of displacements and transverse shear stresses at layer interfaces," *Int. J. Solids Struct.*, Vol. 31(5), 1994, pp. 613-627
- [93] Gruttmann, F., Wagner, W., Meyer, L. and Wriggers, P., "A nonlinear composite shell element with continuous interlaminar shear stresses," *Comput. Mech.*, Vol. 13, 1993, pp. 175-188.
- [94] Basar, Y. and Ding, Y. "Interlaminar stress analysis of composites: layerwise shell finite elements including transverse strains," *Compos. Engng.*, Vol. 5(5), 1995, pp. 485-499
- [95] Gruttmann, F. and Wagner, W. "Coupling of two- and three-dimensional composite shell elements in linear and non-linear applications," *Comput. Meth. Appl. Mech. Engng.*, Vol. 129, 1996, pp. 271-287
- [96] Epstein, M. and Glockner, P.G., "Nonlinear analysis of multilayered shells," *Int. J. Solids Struct.*, Vol. 13, 1977, pp. 1081-1089

- [97] Epstein, M. and Huttelmaier, H.P., "A finite element formulation for multilayered and thick plates," *Comput. Struct.*, Vol. 16(5), 1983, pp.645-650
- [98] Huttelmaier, H.P. and Epstein .M. "A finite element formulation for multilayered and thick shells," *Comput. Struct.*, Vol. 21(6), 1985
- [99] Huttelmaier, H.P. and Epstein .M. "A large displacement finite element for multilayered plates," *Finite element in analysis and design*, Vol. 6, 1990, pp.189-196
- [100] Simo, J. C., Rifai, M. S. and Fox, D. D., "On a stress resultant geometrically exact shell model. Part IV: Variable thickness with through-the-thickness stretching.", *Comput. Meth. Appl. Mech. Engng.*, Vol.81, 1990, pp.91-126.
- [101] Robbins, D.H., Jr. And Reddy, J.N., "Variable kinematic modeling of laminated composite plates," *Int. J. Numer. Meth. Engng.*, Vol.39(13), 1996, pp.2283-2317.
- [102] Goldstein, H., "Classical mechanics," Addison-Wesley Publishing Company, Inc., 1980.
- [103] Altmann, S.L., "Rotations, Quaternions and Double Groups," 1st edition, Clarendon Press, Oxford, 1986
- [104] Angeles, J., "Rational Kinematics," 1st edition, Springer-Verlag, New York, 1988
- [105] Beatty, M.F., "Vector analysis of finite rigid rotations," *J. Appl. Mech.*, Vol. 44, 1977, pp.501-502
- [106] Argyris, J.H., "An excursion into large rotations," *Comput. Meth. Appl. Mech. Engng.*, Vol. 32, 1982, pp. 85-155.
- [107] Pietraszkiewicz, W. And Badur, J., "Finite rotations in the description of continuum deformation," *Int. J. Engng. Sci.*, Vol. 21, No.9, 1983, pp. 1097-1115.
- [108] Spring, K. W., "Euler parameters and the use of quaternion algebra in the manipulation of finite rotations: A review," *Mechanism and Machine Theory*, Vol.21, No.5, 1986, pp.365-373.
- [109] Cheng, H. And Gupta, K.C., "An historical note on finite rotations," *J. Appl. Mech.*, Vol.56, 1989, pp.139-145
- [110] Argyris, J.H. and Poterasu, V.F., "Large rotations revisited application of Lie algebra," *Comput. Meth. Appl. Mech. Engng.*, Vol. 103, 1993, pp.11-42

- [111] Geradin, M. and Rixen, D., "Parametrization of finite rotations in computational dynamics: a review," *Revue europeenne des elements finis*, Vol.4, No.5-6, 1995, pp.497-553.
- [112] Atluri, S.N. and Cazzani, A., "Rotations in Computational Solid Mechanics." *Arch. Comput. Meth. Engng.*, Vol. 2, 1995, pp.49-138
- [113] Ibrahimbegovic, A., Frey, F. and Kozar, I., "Computational aspects of vector like parametrization of three-dimensional finite rotations," *Int. J. Numer. Meth. Engng.*, Vol. 38, 1995, pp.3653-3673.
- [114] Ibrahimbegovic, A., "On the choice of finite rotation parameters," *Comput. Meth. Appl. Mech. Engng.*, Vol.149, 1997, pp.49-71.
- [115] Hughes, P.C., "Space Attitude Dynamics," John Wiley & Sons, 1986
- [116] Nikravesh, P.E., Computer Aided Analysis of Mechanical Systems, Prentice-Hall International, Inc., 1988.
- [117] Shabana, A. A. "Dynamics of multibody systems", John Wiley & Sons, 1989
- [118] Simo, J.C. "On finite strain beam formulation – the three-dimensional dynamic problem. Part1," *Comput. Meth. Appl. Mech. Engng.*, Vol. 49, 1985, pp.55-70
- [119] Simo, J.C. and Vu-Quoc, L., "A three-dimensional finite strain rod model, Part2: Computational aspects, *Comput. Meth. Appl. Mech. Engng.*, Vol.58, 1986, pp.79-116
- [120] Marsden, J. E. and T.J.R. Hughes, Mathematical foundations of elasticity, Prentice-Hall, Inc., New Jersey, 1983.
- [121] Ramm, E., "A plate/shell element for large deflections and rotations', in *Formulations and Computational Algorithms in Finite Element Analysis*, Bathe, K. J., Oden, J. T. and Wunderlick, W. (eds.), MIT Press, Cambridge, MA, 1977.
- [122] Surana, K. S. and Sorensen, R. M., "Geometrically non-linear formulation for three dimensional curved beam elements with large rotations," *Int. J. Numer. Meth. Engng.*, Vol.28, 1989, pp.43-73.
- [123] Rodrigues, O. "Des lois geometriques qui regissent les déplacements d'un solide dans l'espace, et la derivation des coordonnees provenant de ces déplacements consideres independamment des causes qui peuvent les produire, *Journal de Mathematiques pures et appliques*, Vol.5(1), 1840, pp.380-440

- [124] Simo, J. C., Fox, D. D. and Rifai, M. S. "On a stress resultant geometrically exact shell model. Part VI: Conserving algorithms for nonlinear dynamics," *Int. J. Numer. Meth. Engng.*, Vol.34, 1992, pp.117-164
- [125] Yang, H.T.Y., Saigal, S. And Liaw, D.G., "Advances in thin shell finite elements and some applications-Version I," *Comput. Struct.*, Vol.35(4), 1990, pp.481-504
- [126] Zienkiewicz, O.C. and Cheung, Y.K. "Finite element procedures in the solution of plate and shell problem," In stress Analysis, Edited by Zienkiewicz, O.C. and Holister, G.S., Chap.8, John Wiley, New York, 1965
- [127] Clough, R.W. and Johnson, C.P., "A finite element approximation for the analysis of thin shells," *Int. J. Solids Struct.*, Vol. 4, 1968, pp.43-60
- [128] Dawe, D.J., "Shell analysis using a facet shell element," *J. Strain Anl.*, Vol.6, 1972, pp.266-270
- [129] Argyris, J.H., Dunne, P.C. , Malejannakis, G.A. and Schelke, E, "A simple triangular facet shell element with application to linear and nonlinear equilibrium and elastic stability problems," *Comput. Meth. Appl. Mech. Engng.*, Vol. 10, 1977, pp.97-131 (1977)
- [130] Meek, J.L. and Tan H.S., "A faceted shell element with loof nodes," *Int. J. Numer. Meth. Engng.*, Vol.23, 1986, pp.49-67
- [131] Knowles, N.C., Razzaque, A. and Spooner, J.B., "Experience of finite element analysis of shell structures," In finite elements for thin shells and curved members, Edited by Gallagher, R.H. and Ashwell, D.G., pp.245-262, John Wiley, New York. 1976.
- [132] Hansen, J.S. and Heppler, G.R., "A mindlin shell element which satisfies rigid body requirements," *AIAA journal*, Vol. 22, 1985, pp.288-295
- [133] Sander, G. and Idelsohn, S., "A family of conforming finite elements for deep shell analysis," *Int. J. Numer. Meth. Engng.*, Vol.18, 1982, pp.363-380
- [134] Harte, R. And Eckstein, U., "Derivation of geometrically nonlinear finite shell elements via tensor notation," *Int. J. Numer. Meth. Engng.*, Vol. 23, 1986, pp.367-384
- [135] Jang, J. and Pinsky, P.M., "An assumed covariant strain based 9-node shell element," *Int. J. Numer. Meth. Engng.*, Vol.24, 1987, pp.2389-2411

- [136] Yang, T.Y., and Wu, Y.C., "A geometrically non-linear tensorial formulation of a skewed quadrilateral thin shell finite element," *Int. J. Numer. Meth. Engng.*, Vol. 28, 1989, pp. 2855-2875
- [137] Irons, B.M., and Draper, K.J., "inadequacy of nodal connections in a stiffness solution for plate bending," *AIAA*, Vol.3, 1965, pp.961
- [138] Hughes, T.J.R., "The Finite Element Method," Prentice-Hall, Englewood Cliffs, NJ, 1987
- [139] Newmark, N. M. "A method of computation for structural dynamics," *J. Eng. Mech. Div.*, Vol.85, 1959, pp.67-74
- [140] Simo, J. C. and Tarnow, N. "The discrete energy momentum method. Conserving algorithms for nonlinear elastodynamics" *J. Appl. Mech.*, Vol.43, 1992, pp.757-792
- [141] Simo, J. C., Tarnow, N. and Doblare, M., "On non-linear dynamics of three-dimensional rods: exact energy and momentum conserving algorithms," *Int. J. Numer. Meth. Engng.*, Vol.38, 1995, pp.1431-1474.
- [142] Simo, J. C. And Wong, K.K., "Unconditionally stable algorithms for rigid body dynamics that exactly preserve energy and momentum," *Int. J. Numer. Meth. Engng.*, Vol.31, 1991, pp.19-52
- [143] Hughes, T.J.R., Caughey, T.K. and Liu, W.K., "Finite-element methods for nonlinear elastodynamics which conserve energy," *J. Appl. Mech.*, Vol.45, 1978, pp.366-370
- [144] Galvanetto, U. and Crisfield, M.A., "An energy conserving co-rotational procedure for the dynamics of planar beam structures," *Int. J. Numer. Meth. Engng.*, Vol.39, 1996, pp.2265-2282.
- [145] Flugge, W., *Tensor analysis and continuum Mechanics*, Springer-Verlag, Germany, 1972.
- [146] Jones, R.M., "Mechanics of Composite Materials," McGraw-Hill Book Company, 1975.
- [147] Gibson, R.F., *Principles of composite material mechanics*, McGraw-Hill, Inc., 1994.
- [148] Zienkiewicz, O.C. and Taylor, R.L., *The finite element method*, 4th ed., Vol.1: Basic formulations and linear problems, McGraw-Hill, London, 1989; Vol.2: Solid and Fluid Mechanics, Dynamics and Non-linearity, McGraw-Hill, London, 1991.

- [149] Zienkiewicz, O.C., Taylor, R.L. and Too, J.M., "Reduced integration techniques in general analysis of plates and shell," *Int. J. Numer. Meth. Engng.*, Vol. 3, 1971, pp.275-290
- [150] Pawsey, S.F. and Clough R.W., "Improved numerical integration of thick shell finite elements," *Int. J. Numer. Meth. Engng.*, Vol.3 , 1971, pp.575-586
- [151] Hughes, T.J.R., Cohen, M. and Haroun, M., "Reduced and selective integration techniques in the finite element analysis of plates," *Nucl. Engng. Des.*, Vol. 46, 1975, pp.445-450
- [152] Hughes, T.J.R., Taylor, R.L. and Kanoknukulchai, W., "A simple and efficient element for finite element bending," *Int. J. Numer. Meth. Engng.*, Vol.11, 1977, pp.1529-1543
- [153] Pugh, E.D.L., Hinton, E. and Zienkiewicz, O.C., "A study of quadrilateral plate bending elements with reduced integration," *Int. J. Numer. Meth. Engng.*, Vol.12, 1978, pp.1059-1079
- [154] Liu, W.K., Belytschko, T and Ong, J.S.J., "The use of stabilization matrices in nonlinear analysis," In Proc. International conference on innovative methods for nonlinear analysis, Edited by Liu W.K., Belytschko, T and Park, K.C., Pinneridge Press, Swansea, U.K., 1984
- [155] Riks, E., "An incremental approach to the solution of snapping and buckling problems," *Int. J. Numer. Meth. Engng.*, Vol 15, 1979, pp.524-551
- [156] Riks, E., "The application of Newton's method to the problem of elastic stability," *J. Appl. Mech.*, Vol. 39, 1972, pp.1060-1066
- [157] Wempner, G. A., "Discrete approximations related to nonlinear theories of solids," *Int. J. Solids Struct.*, Vol. 7, 1971, pp. 1581-1599
- [158] Crisfield, M.A., "A fast incremental/iterative solution procedure that handles snap-through", *Comput. Struct.*, Vol 13, 1981, pp.55-62
- [159] Crisfield, M. A., "An arc-length method including line searches and accelerations," *Int. J. Numer. Meth. Engng.*, Vol. 19, 1983, pp.1269-1289
- [160] Ramm, E., "Strategies for tracing the non-linear response near limit points, In *Non-linear finite element analysis in structural mechanics*, pp.63-89, ed. W. Wunderlich, Springer-Verlag, Berlin, 1981

- [161] Ramm, E., "the Riks/Wempner approach-an extension of the displacement control method in non-linear analysis, In *Non-linear computational mechanics*, pp.63-86, ed. Hinton et al., Pineridge, Swansea, 1982
- [162] Schweizerhof, K. and Wriggers, P., "Consistent linearization for path following methods in nonlinear finite element analysis," *Comput. Meth. Appl. Mech. Engng.*, Vol. 59, 1986, pp.261-279
- [163] Forde, B.W.R. and Stemer, S.F., "Improved arc length orthogonality methods for nonlinear finite element analysis," *Comput. Struct.*, Vol. 27, 1987, pp.625-630
- [164] Gierlinski, J.T. and GravesSmith, T.R., "A variable load iteration procedure for thin-walled structures," *Comput. Struct.*, Vol.21, 1985, pp.1085-1094
- [165] Bellini, P.X. and Chulya, A., "An improved automatic incremental algorithm for the efficient solution of nonlinear finite element equations," *Comput. Struct.*, Vol. 26, 1987, pp.99-110
- [166] Simo, J.C., Wriggers, P. Schweizerhof, K.H. and Taylor, R.L., "Finite deformation postbuckling analysis involving inelasticity and contact constraints," In *Innovative methods for nonlinear problems*, pp.365-388, ed. W.K. Liu et al., Pineridge Press, Swansea, 1984
- [167] Crisfield, M.A., "Non-linear Finite Element Analysis of Solids and Structures. Volume1: Essentials," John Wiley & Sons, West Sussex, UK, 1991
- [168] Berthelot, J.M., *Composite materials: Mechanical behavior and structural analysis.* Springer-Verlag New York, Inc., 1999.
- [169] Al-Ghamedy, H.N., "Nonlinear finite element analysis of inelastic structures with application to reinforced concrete," Ph.D. Thesis, Dept. Of Civil, Environment and Architecture Engng., Univ. of Colorado, Boulder, CO, 1986
- [170] Borri, M. and Botasso, C., "A general framework for interpreting time finite element formulations." *Comput. Mech.*, Vol.13, 1993, pp.133-142
- [171] Pagano, N. J., "Exact solutions for rectangular bidirectional composites and sandwich plates." *J. Compos. Mater.*, Vol.4, 1970, pp.20-34.
- [172] Huang, N.N., "Influence of shear correction factors in the higher order shear deformation laminated shell theory, " *Int. J. Solids Struct.*, Vol.31(9), 1994, pp.1263-1277.

- [173] Laschet, G. and Jeusette, J. P., "Postbuckling finite element analysis of composite panels," *Compos. Struct.*, Vol. 14, 1990, pp.35-48.
- [174] Reddy , J.N. and Chandrashekhara. K., "Nolinear analysis of laminated shells including transverse shear strains," *AIAA journal*, Vol. 23(3), 1985, pp.440-441
- [175] Sansour, C., Wriggers. P. and Sancour, J., "Nonlinear dynamics of shells: Theory, Finite element formulation, and integration schemes," *Nonlinear Dynamics*, Vol.13,1997, pp.279-305
- [176] Deng, H. and Vu-Quoc, L., "Dynamics of geometrically exact sandwich structures,"*Int. J. Mech. Sci.*, Vol.40, No.5, 1998, pp.421-441